UNIVERSIDAD COMPLUTENSE DE MADRID
FACULTAD DE CIENCIAS FÍSICAS

TESIS DOCTORAL

Efecto campo ferroeléctrico en interfases conductoras iónicas de óxidos

Ferroelectric field effect at ionically conducting oxide interfaces

MEMORIA PARA OPTAR AL GRADO DE DOCTOR

PRESENTADA POR

David Hernández Martín

Directores

Juan Ignacio Beltrán Fínez
Jacobo Santamaría Sánchez-Barriga

Madrid 2019

© David Hernández Martín, 2019

EFECTO CAMPO FERROELECTRICO EN INTERFASES CONDUCTORAS IONICAS DE OXIDOS

FERROELECTRIC FIELD EFFECT AT IONICALLY CONDUCTING OXIDE INTERFACES

Memoria presentada por

David Hernández Martín

para optar al grado de Doctor en Ciencias Físicas

Directores:

JUAN IGNACIO BELTRÁN FÍNEZ

JACOBO SANTAMARÍA SÁNCHEZ-BARRIGA

FACULTAD DE CIENCIAS FISICAS

MADRID, 2018

Agradecimientos

En primer lugar, quisiera pedir disculpas por si hubiese alguna omisión en la mención de las personas que me han ayudado en el desarrollo de mi tesis doctoral.

Sin más dilación, quiero agradecer a mi director de tesis, el profesor Jacobo Santamaría, por haberme dado la oportunidad de unirme a su grupo de investigación (GFMC); así como por su enorme paciencia conmigo. Por su actitud de entereza ante las dificultades, por su espíritu de ingente esfuerzo y sacrificio, por su magnífica labor de asesoramiento a la hora de diseñar y realizar los experimentos, por transmitirme su dilatada experiencia, por su gran disponibilidad para poder analizar y discutir los resultados experimentales obtenidos del laboratorio y que figuran en esta tesis; por todo el tiempo que ha dedicado a mi formación, por todo ello y más, afirmo que su constante estímulo ha sido para mí una gran fuente de infinita inspiración.

Asimismo, quiero agradecer a mi director de tesis, el Dr. Juan Ignacio Beltrán, por su inmensa bondad, por la enorme labor que ha realizado de introducirme hacia la simulación en DFT a través del paquete de software VASP, su asistencia a la hora de aprender a usar el citado software ha sido clave en mi formación; incluso careciendo inicialmente de una base previa funcional de conocimientos de programación por mi parte, mi codirector tuvo la habilidad de seleccionar lo sustancial e indispensable a fin de que yo pudiera utilizar el paquete de software VASP para realizar los cálculos en DFT que se mostrarán en esta tesis doctoral.

Al profesor Carlos León, por su asesoramiento con el puente impedancias y su asistencia en el tratamiento de los datos experimentales en el software OriginLab que se mostrarán en esta tesis, por su paciencia y dedicación, por sus grandes esfuerzos para dar visibilidad a nuestro grupo, por su disponibilidad siempre que lo he necesitado en cualquier momento, muchas gracias, profesor.

Al profesor Zouhair Sefrioui, por transmitirme su tenacidad, por la enorme influencia que ha tenido sobre mí en mis primeros pasos por este laboratorio, por todo ello y más, muchas gracias, profesor.

A la profesora María Varela, por su increíble destreza con la microscopia electrónica y lo mucho que se ha involucrado con mi formación teórica y experimental. Espero que tras esta etapa, estés orgullosa de mí, muchas gracias por todo.

Al profesor Alberto Rivera, por su gran pericia con los equipos del laboratorio, pues no funcionarían correctamente sin su debida supervisión. Su experiencia con el analizador de impedancias fue clave para la correcta resolución de este trabajo que voy a presentar.

No quisiera olvidarme de nuestro profesor visitante Diego Arias, a quien agradezco sus brillantes consejos, y todos los buenos momentos que hemos pasado juntos fuera del laboratorio.

Asimismo, quiero dedicar unas palabras de agradecimiento a Neven, Norbert y a Rainer, por su constante apoyo a lo largo de mi paso por el GFMC; así como a mis compañeros de laboratorio: Fabián, Gabriel, Tornos, Mirko, Mariona, Ana, Gloria, Fernando y David Sánchez, por su infinita paciencia conmigo, por su excelente acogida y por facilitar mi integración en el grupo.

Además, en ningún caso podemos olvidarnos de los grupos colaboradores externos, sin los cuales nuestro grupo no ostentaría la relevancia que actualmente posee. Por ello, desde estas líneas quiero dedicar unas especiales palabras de agradecimiento a la profesora Mª Carmen Muñoz, Mar García Hernández y Federico Mompeán (ICMM, CSIC); así como a los profesores Manuel Bibes, Javier Villegas y a la profesora Barthèlemy (CNRS, THALES).

Para finalizar, quiero expresar mi profundo agradecimiento a toda mi familia, por su apoyo incondicional en todos estos años, especialmente a mis padres, con quienes tengo una deuda impagable. A mis amigos y conocidos, así como a todas aquellas personas de las cuales he podido

aprender algo, espero que esta disertación refleje todas esas sutiles contribuciones, muchas gracias.

Index

Resumen

Summary

Motivation and Outline **0"**

References 3

Chapter 1: Introduction **6"**

1.1 Colossal Magneto Resistance (CMR) Manganites 8"

1.2 Doped Cobaltites 9"

1.3 Cuprates 10"

1.4 Ferroelectrics 12"

1.5 Memristor 12"

1.6 Tunnel Junction and other Spintronic Devices 13"

1.6.1 MgO dielectric tunnel barrier 16"

1.6.2 $SrTiO_3$ dielectric tunnel barrier 19"

1.7 Spin Filtering Effect 23"

1.7.1 Europium chalcogenides 24"

1.8 Tunnelling through Ferroelectric Barriers 26"

1.9 Magneto-electric Effects at Interfaces 27"

1.10 References 29

Chapter 2: Experimental and Simulation Techniques **37**

2.1 Sample growth: Sputtering 37

2.2 Structural characterization: XRR, XRD 38

2.2.1 X-ray reflectivity 38

2.3 Scanning Transmission Electron Microscopy 41

2.4 Tunnel junction patterning 44

2.4.1 Optical Lithography 44

2.4.2 From bilayer to tunnel junction device 45

2.5 Resistance Measurements 46

2.5.1 Direct Current 46

2.5.2 Impedance Spectroscopy. Alternating Current 47

2.6 Density Functional Theory 48

2.6.1 Introduction 48

2.6.2 Quantum mechanical Many-Body problem 48
2.6.3 Density Functional Theory 49
2.6.4 Exchange and correlation 50
2.6.5 Method of solving: self-consistency 51
2.6.6 Basis sets 53
2.6.7 Pseudo-Potentials 54
2.6.8 Density of States 56
2.6.9 Hubbard correction 57
2.6.10 VASP code 57
2.7 References 58
Chapter 3: High On/Off Ratio Memristive Switching of Manganite Cuprate Bilayer by Interfacial Magnetoelectricity 62
3.1 Methods 62
3.2 Experimental Results 63
3.3 Impedance Spectroscopy Measurements 78
3.4 Appendix. Derivation of Child–Langmuir Law 82
3.5 References 85
Chapter 4: Density functional theory calculations of BTO-metal interfaces, and related materials 91
4.1 Bulk Properties: 92
4.1.1 Metals: 92
4.1.1.1 Ag: 92
4.1.1.2 Co: 94
4.1.1.3 LSMO: 96
4.1.2 Bulk BTO: 97
4.1.2.1 Born Charges: 102
4.2 Most typical chemical modifications. 103
4.2.1 Ag: Oxygen interstitials. 104
4.2.2 Co: Oxidation of the outer monolayer 104
4.2.3 LSMO: La/Sr ratio. 105
4.2.4 BTO: Oxygen vacancies. 107
4.3 BTO-Metal super-lattices: 111

4.3.1 BTO/$La_{1-x}Sr_xMnO_3$ super-lattices: 112
4.3.2 BTO/Ag (001) super-lattices: 123
4.3.3 BTO/Co (0001) super-lattices: 127
4.4 References 133

Chapter 5: Resonant Tunnelling across Ferroelectric Quantum Wells in Charged Domain Walls 138

5.1 Methods 138
5.2 Experimental Results 139
5.3 Quantum oscillations in tunnelling conductance 140
5.4 Appendix. Fitting of tunnelling conductance peaks 144
5.5 Measurement of ferroelectric polarization 146
5.6 Revealing the presence of a charged H-to-H DW 148
5.7 Screening of the DW charges by oxygen vacancies 150
5.8 Discussion 153
5.9 References 155

Chapter 6: Oxygen Vacancy Control of a Ferroelectric Memristor 160

6.1 Introduction 160
6.2 Experimental Results 162
6.3 Discussion 172
6.4 Ferroelectric Memristor in other Top Electrodes 177
6.4.1 LSMO/BTO/Cobalt 177
6.4.2 LSMO/BTO/Ta 194
6.4.3 LSMO/BTO/Pt 201
6.5 References 204

Chapter 7: Final Conclusions and Prospective Research Lines 210

Appendix 1. Surfaces: 214

A.1.1 BTO-surfaces 215

Appendix 2. ABF BTO3/Ag interfase 220

Resumen en español

En este trabajo, realizamos un análisis de la interacción entre la ferroelectricidad, las paredes de dominio ferroeléctrico cargadas y el memristor en las dimensiones reducidas de una unión túnel. Para alcanzar este objetivo, crecemos bicapas de heteroestructuras epitaxiales de manganitas ferromagnéticas $La_{0.7}Ca_{0.3}MnO_3$ (LCMO), $La_{0.7}Sr_{0.3}MnO_3$ (LSMO) a fin de ser utilizadas como electrodo inferior; el aislante de Mott/Anderson $PrBa_2Cu_3O_{7-\delta}$ (PBCO) y el titanato de bario ferroeléctrico $BaTiO_{3-\delta}$ para su uso como barrera túnel; así como distintos metales (Ag, Co, Ta, Pt) con la finalidad de ser depositados como electrodo superior. Hemos encontrado curvas de histéresis de la intensidad de corriente y la Resistencia de lectura en función del voltaje de escritura aplicado que podrían no ser fácilmente explicadas con el modelo de Schottky porque la ferroelectricidad y la barrera de Schottky interactúa con otros defectos interfaciales como las vacantes de oxígeno entre otros muchos. A fin de esclarecer el comportamiento histerético memristivo, se han empleado técnicas experimentales de diversa índole; así como cálculos con la teoría del funcional de densidad por el software VASP, aportando resultados relevantes que pueden ser enumerados a continuación para abordar el problema fundamental:

- El comportamiento histerético resistivo de la union túnel LCMO/PBCO/Ag sondea directamente las rutas de conducción túnel a través de los planos CuO_2 proporcionando una conexión directa al modelo de Fehrenbacher y Rice para los cupratos. Hemos encontrado pruebas de un gap aislante de 4 eV anteriormente mencionado entre los estados Pr^{IV} y Cu^{III}. Esto concuerda con el modelo de Fehrenbacher y Rice para los cupratos, el cual afirma que la ausencia de conductividad de las cadenas Cu–O es debida a las vacantes de oxígeno excluyendo la posibilidad de sortear los planos CuO_2 mediante el túnel de los portadores de carga a través de las cadenas Cu–O.
- El mecanismo de conducción de las uniones túnel LCMO/PBCO/Ag es preferentemente el efecto túnel de los electrones asistido por las trampas localizadas en las cadenas Cu–O de la barrera de cuprato PBCO. El estado de baja resistencia de la unión túnel LCMO/PBCO/Ag ha sido examinado por el ajuste de las curvas IV a la ley de Child-Langmuir (análogo a la conducción de electrones en régimen balístico en un diodo de vacío plano-paralelo) y la conducción túnel por campo eléctrico intenso (régimen de Fowler-Nordheim).
- Encontramos un gas de electrons libres en las paredes de dominio cargadas enfrentadas (Head-to-Head) 180º en la barrera de $BaTiO_3$ de las uniones

túnel LSMO/BTO/LSMO. Obtenemos evidencias de estados electrónicos confinados, que habilitan el transporte túnel resonante entre los electrodos. La conductancia túnel a baja temperatura muestra pronunciadas oscilaciones indicando transporte resonante a través de niveles discretos desocupados del gas de electrones confinados, los cuales están modulados por el fuerte campo eléctrico desarrollado en una barrera ultra-delgada a voltajes moderados en un experimento de transporte.

- Encontramos un débil comportamiento Mem-Capacitivo en las uniones túnel memristor LSMO/BTO/Ag que ocurren como consecuencia de una reacción química interfacial reversible controlada por un campo eléctrico. En el caso del memristor LSMO/BTO/Ag, el campo eléctrico crea intersticiales de oxígeno en el electrodo de plata dejando vacantes de oxígeno en la barrera de titanato de bario. La diferencia en la movilidad de ambos portadores de carga, las vacantes y los intersticiales de oxígeno, da origen a defectos localmente cargados, que garantiza el efecto Mem-Capacitivo.
- Encontramos pruebas de un acoplamiento de las vacantes de oxígeno a la polarización ferroléctrica en las uniones túnel memristor LSMO/BTO/Co. Esto da origen a un estado electrónico localizado t_{2g} resultado del apantallamiento de la polarización ferroeléctrica por el Bloqueo de Coulomb. Las evidencias experimentales son obtenidas de la altamente anómala disminución de la capacidad al aumentar la temperatura correlacionada con el aumento de la conductancia al aumentar la temperatura. Además, la curva plana de la tangente del ángulo de pérdidas con la frecuencia a baja temperatura respaldan el mecanismo puramente electrónico del régimen del Bloqueo de Coulomb (T = 50K).
- Las uniones túnel LSMO/BTO/Co muestran cambio de signo en la magneto-resistencia túnel, impulsado por el cambio de la polarización ferroeléctrica. Esto refleja el cambio de signo en la polarización de spin (en el nivel de Fermi) de la interfaz BTO/Co desencadenada por la polarización ferroeléctrica y la distribución de defectos. Los cálculos de DFT enseñan que dicho cambio de signo es fruto de la competición entre la interacción de canje de los átomos de Co suprimida por la monocapa de óxido CoO ($U - J = 6.0\ eV$) y la interacción de canje de los centros de color de las vacantes de oxígeno mediadas por los iones Ti^{3+} ($U - J = 4.4\ eV$). El transporte túnel mediado por centros de vacantes de oxígeno parece una interacción de doble canje extrapolada a una barrera ferroeléctrica aislante de BTO.

- Los experimentos llevados a cabo utilizando distintos electrodos superiores con diferentes funciones de trabajo no mostraban una relación lineal entre la altura de la barrera y la función de trabajo de los metales implicados (Ag, Co, Ta y Pt). La barrera Schottky detectada en las curvas IV se encuentra en la intercara BTO/LSMO y está causada por efectos de dopado asociados a la acumulación de vacantes de oxígeno. La formación de vacantes de oxígeno está controlada por la oxidación del electrodo impulsada por el campo eléctrico aplicado. Las uniones túnel memristor LSMO/BTO/Ta acoplan la ferroelectricidad y la formación de vacantes de oxígeno a las reacciones químicas de Ta metálico a sus óxidos nativos TaO_2 y Ta_2O_5. La heterogeneidad debida a las capas de óxido formadas causa que el memristor muestre el efecto de relajación de Maxwell-Wagner-Sillars. Finalmente, encontramos que el campo eléctrico necesario para aniquilar las vacantes de oxígeno (coercitividad positiva de los ciclos de histéresis de la conductancia) escala con la entalpía de oxidación del electrodo superior, indicando que el proceso está limitado por la reducción inducida por campo eléctrico del óxido del electrodo interfacial.
- Como pronóstico final a experimentos futuros, sería altamente interesante trabajar con el recientemente desarrollados porta-muestras para microscopios de transmisión y barrido (STEM) que permiten aplicar pulsos de campo eléctrico in situ además de tomar imágenes de campo claro (ABF) y medidas de espectroscopia de pérdida de energía de los electrones (EELS) combinadas para examinar los cambios de valencia en tiempo real y eventualmente también las consiguientes modificaciones estructurales las reacciones químicas REDOX asociadas, las cuales controlan la histéresis resistiva.

SUMMARY

The main findings of this dissertation are summarized here. We performed an analysis of the interplay between ferroelectricity, ferromagnetism, domain structure and memristive response in magnetic tunnel junctions. In order to reach this objective, we grew epitaxial heterostructures combining ferromagnetic manganites $La_{0.7}Ca_{0.3}MnO_3$ (LCMO), $La_{0.7}Sr_{0.3}MnO_3$ (LSMO) to be used as bottom electrode; the Mott/Anderson insulator $PrBa_2Cu_3O_{7-\delta}$ (PBCO) and ferroelectric barium titanate $BaTiO_{3-\delta}$ for use as a tunnel barrier and different metals (Ag, Co, Ta, Pt) to be deposited as top electrodes. We found hysteretic response in transport properties which may not be explained with the Schottky model in simple terms because the ferroelectricity interacts with interface defects such as oxygen vacancies modifying their ionization and changing and the Schottky barrier. To gain more insight into the understanding of the hysteretic memristive behaviour, several experimental techniques were combined with density functional theory simulations by VASP. The main findings of this work can be summarized as follows:

- The LCMO/PBCO/Ag tunnel junction resistive switching behaviour directly probe the tunneling routes across the CuO_2 planes providing a direct connection to the Fehrenbacher and Rice model for cuprates. We have found evidence for the presence of the insulating gap of 4 eV mentioned above between the Pr^{IV} states and the Cu^{III} states. This is in agreement with the Fehrenbacher and Rice model stating that the absence of conductivity of the Cu–O chains is due to the O vacancies excluding the possibility to circumvent the CuO_2 planes via the tunneling of charge carriers through the Cu–O chains.

- The conduction mechanism of the LCMO/PBCO/Ag tunnel junctions is predominantly the tunneling of electrons assisted by traps localized in the CuO chains in the PBCO barrier. The Low Resistance State of the LSMO/PBCO/Ag tunnel junction was examined by fitting IV curves to the Child-Langmuir law (analogous to the electron conduction in a plane parallel vacuum diode in the ballistic conduction regime) and to the Fowler-Nordheim quantum tunneling.

- We found a free-electron gas in 180º Head-to-Head charged domain walls (CDW) in $BaTiO_3$barriers in LSMO/BTO/LSMO tunnel junctions. We obtained evidence for confined electronic states which enable resonant tunnelling transport between the electrodes. Low temperature tunnelling conductance (measured using a dc current set up) exhibits pronounced oscillations indicating resonant transport through discrete unoccupied states of the confined electron gas, which is modulated by the strong electric field developing in an ultrathin barrier at moderated voltages in a transport experiment.

- We found a weak Mem-Capacitor behavior in LSMO/BTO/Ag memristor tunnel junctions occurring as a consequence of reversible interfacial chemical reaction controlled by an electric field. In the particular LSMO/BTO/Ag memristor, the electric field create interstitial oxygen atoms in the face-centered cubic silver electrode leaving behind oxygen vacancies in the Barium Titanate barrier. The different charge carrier

mobilities of the interstitial oxygen atoms and the oxygen vacancies, give rise to locally charged defects giving rise to the mem-capacitor effect.

- We found evidence of the coupling of oxygen vacancies to ferroelectric polarization in LSMO/BTO/Co memristor tunnel juntions. This gives rise to a t_{2g} localized electronic state resulting from the Coulomb-Blockade-like screening of the ferroelectric polarization. Experimental evidence is obtained from the highly anomalous decrease of the capacitance while increasing temperature which correlates with the increase of conductance when temperature is increased. Furthermore, the flat shape of the loss tangent vs frequency further support the purely electronic Coulomb-Blockade-like regime (T = 50K).

- The LSMO/BTO/Co memristor tunnel junction exhibits sign change in the tunnel magneto-resistance (TMR) driven by the switching of the ferroelectric polarization. This reflects the sign change in the spin polarization (at the Fermi level) in the BTO/Co interface triggered by the ferroelectric polarization and the defect distribution. DFT calculations show that the sign change in BTO/Co interface stems from the competition between the Co atoms exchange interaction suppressed by the CoO monolayer ($U - J = 6.0$ eV) and the oxygen vacancies colour centres exchange interaction mediated by Ti^{3+} ions ($U - J = 4.4$ eV). Tunnel transport mediated by the oxygen vacancy centers resemble a double exchange interaction in an insulator ferroelectric BTO barrier.

- Experiments conducted using top electrodes with different work functions did not show not a linear relationship between the barrier height and the work function of the transition metals involved (Ag, Co, Ta and Pt). The Schottky barrier detected in IV curves is at the BTO/LSMO interface and it is caused by doping effects associated to the accumulation of oxygen vacancies. Oxygen vacancy formation is controlled by the oxidation of the electrode driven by the applied electric field. The LSMO/BTO/Ta memristor tunnel junction couple ferroelectricity and oxygen vacancy formation to two consecutive REDOX chemical reactions of metallic Ta to TaO_2 oxide and Ta_2O_5 oxide. Heterogeneity due to the formed oxide layers caused the memristor to display Maxwell-Wagner-Sillars relaxation effect. Finally, we found the electric field necessary to annihilate oxygen vacancies (positive coercivity of conductance hysteresis loops) scales with the (absolute value of the) oxidation enthalpy of the top electrode, indicating that the process is limited by the electric field induced reduction of the interfacial electrode oxide. This constitutes a first evidence of memristive response governed by electric field controlled electrochemical reactions at the interface with the electrode.

As a final outlook into future experiments, it would be highly interesting to work with the recently developed scanning transmission electron microscope (STEM) sample holders which allow applying electric field pulses in situ and take annular bright field (ABF) images and electron energy loss spectroscopy (EELS) measurements combined to examine real time valence changes and eventually also ensuing structural modifications associated to the REDOX chemical reactions controlling resistive switching.

Motivation and Outline

The discovery of the conducting state at the interface between $LaAlO_3$ and $SrTiO_3$, two band insulators, [1, 2] has generated a lot of interest aimed at exploring new electronic states at oxide interfaces but also driven to functionalize them into novel device concepts. The technological opportunities can be dramatically expanded if instead of the (in principle) relative inert band insulators one combines transition metal oxides with correlated electrons. Complex transition metal oxides are a wide family of materials which contain elements with incomplete d shells. The localized d bands poorly screen the Coulomb interaction and give rise to electron correlations responsible for a strong entanglement between the various electronic and lattice degrees of freedom. This is at the origin of the rich phase diagrams of these compounds where the different electronic states with similar characteristic energies compete fiercely. Materials of this family can be found in almost every electronic or lattice ground state of the solid matter including superconductivity, ferromagnetism, antiferromagnetism, ferroelectricity, multiferroicity, etc , [3–5] and thus display a wide variety of properties and responses.

Many complex oxides share a common perovskite structure with similar lattice parameters which allows the growth of heterostructures which grow cube on cube preserving a high degree of crystalline perfection. Oxygen octahedra surrounding the transition metal ion arranged in the cubic sites are the basic building block of the structure. Distortions and rotations of the octahedra determine the degree of hybridization between 3d and oxygen bands and modify the hierarchy of the crystal field e_g and t_{2g} levels which result from the Coulomb interaction with the oxygen ions. Moreover, distortions can be artificially manipulated through strain engineering, opening a path for the design of the electronic states happening at the interfaces [6, 7].

The fabrication techniques have reached a level of control comparable to the semiconductor technology and interfaces can be engineered with atomic precision allowing to combine the lattices of dissimilar materials with very good crystalline matching. In analogy to the (relative inert) semiconductor interfaces where interesting phenomena and even novel states of matter have been found, the delicate entanglement between the various degrees of freedom across the oxide interfaces, along with the possibility of coupling different order parameters is entitled to be the source of emergent electronic states with exciting properties.

Orbital reconstruction resulting from structural (lattice distortions) and electronic processes occurring at interfaces stabilize novel electronic phases. Emergent electronic states may nucleate at the interface between dissimilar oxides [9, 10] as the result of the broken symmetry and of the discontinuity in important quantities such as charge density *n*, repulsion energy *U*, and band width *W*, which govern the correlated electronic states [4, 13, 14]. In addition charge is known to leak across the interfaces due to the difference in the electrochemical potentials [15], what in the case of correlated electron systems may have deeper consequences on the electronic states than in the case of conventional semiconductors which admit a description in terms of single electron schemes [11]. New forms of couplings between different long range orders with high technological potential for new device concepts [9–11] thus appear. This is the arena of the emerging "oxide electronics", an actively pursued strategy based on exploiting the technological opportunities offered by devices based on correlated oxides [9–12]. This is in fact one of the alternative routes being sought to enable a higher density of information storage or capable of more efficient computation speed that the current 2-bits based von Neumann architectures, which is having difficulties to maintain Moore´s law pace of increase of the computing speed. However, the challenge of oxide electronics has so far not been fulfilled, partly due to the incomplete understanding of the complex physics involved but also to the lack of simple device concepts with externally tunable responses. In addition, the complexity of the electronic interactions has prevented the possibility of designing oxide interfaces with the same ease as for semiconductor interfaces [11].

The electronic and orbital reconstructions occurring at oxide interfaces offer highly efficient avenues to tailor their magnetic states. In perovskite oxides with the orbital moment quenched by the octahedral crystal field, magnetism is largely determined by the spin-spin interaction [1, 2]. Spin interaction is governed by charge transfer processes which can be real as in double exchange or virtual as in superexchange. The sign (ferromagnetic or antiferromagnetic) of the superexchange interaction is captured by the Goodenough Kanamori rule [16], as a function of filling and overlap in a way determined by Pauli exclusion principle. Thus, charge transfer processes, structural distortions (Jahn Teller) and rotations of the oxygen octahedra, with a direct effect on band filling and orbital polarization, provide direct access to the magnetic interactions [8, 17]. Furthermore, the bond reconstruction occurring at the atomically sharp oxide interfaces may draw new superexchange paths (B-O-B') between different B-site cations at a ABO_3 / $A'B'O_3$ interface, which may trigger magnetic interactions not existing in either of

the original compounds. This magnetic interaction can in turn be manipulated through the control of the bond angle by strain engineering.

This project is focused in the study of emergent phenomena at the interfaces of magnetic tunnel junctions. The aim is to manipulate these states externally to in the tunnel junction device scale, by means of which it is possible to tailor the tunnel barrier oxide characteristic. By generating point defects (oxygen vacancies) and controlling their concentration profile we will modify the height and the width of the tunnelling barrier. Furthermore, the effect of oxygen vacancies on doping will allow modifying doping of the electrodes thus providing access to the spin degree of freedom and consequently to the spin polarization of the tunnelling current. One of the main objectives to cover in this project is to study the impact of oxygen vacancies in the emergent quantum phases aforementioned because this issue has been ignored for many decades. Thus, the memristive tunnel junction is the most suitable device to achieve this aim.

This PhD dissertation, has a unique physical approach combining experimental and first principles simulation techniques to explore the subtle mechanisms playing in the electronic reconstruction at oxide interfaces. Pioneer work of M. Bibes et al. [17, 18] open relevant questions about the real nature of the ferroelectric polarization and the role of oxygen vacancies in memristive tunnel junctions. In response, direct current (DC) perpendicular measurements, impedance spectroscopy (AC) measurements combined with density functional theory (DFT) calculations were combined to gain insight on the interplay between the ferroelectricity, the ferromagnetism and the oxygen vacancies and its influence on the metal-insulator transition. We will examine memristive effects with potential applications in analogue memory devices and emulation of neuron activity as well as its integration in neuromorphic computing networks [19]. Motivated by these potential applications, we will examine the singular memristive response to electric and magnetic fields [20, 21] of tunneling devices based on correlated oxides.

The manuscript is organized as follows.

Chapter 1 is a review of the state-of-the-art in the field of strongly correlated electronic materials such as manganites, doped cobaltites and cuprates, emphasizing the spintronic effects inherent to this family of materials.

Chapter 2 describes the experimental techniques to produce and characterize the different tunnel junctions as well as the simulation methods to elucidate the subtle

physical mechanisms underlying the complex phenomena studied in this PhD dissertation.

Chapter 3 describes the experiment in the tunnel junctions LCMO/PBCO/Ag intending to understand the interfacial magneto-electric coupling in the LCMO/PBCO interface.

Chapter 4 describes the preliminary density functional theory (DFT) calculations performed by VASP software package in order to address the interfacial implications of structural properties (ferroelectric distortions) into electronic properties (DOS) in LSMO/BTO/LSMO heterostructures. Also, BTO/Ag and BTO/Co interfaces will be simulated using first principles tools.

Chapter 5 addresses the problem of resonant tunnelling through charged domain walls and the role of the oxygen vacancies in the compensation of the charged domain wall.

Chapter 6 tackles the memristive tunnel junction problem displaying the hysteretic experimental measurements of the tunnel junctions LSMO/BTO/Metal. The metals deposited in this tunnel junctions were Ag, Co, Ta and Pt. In addition, for each metal, the interplay between ferroelectricity and oxygen vacancies is examined. New scenarios on interplay between ferroelectricity and the defect concentration profile will be examined, such as the Coulomb Blockade and Maxwell-Wagner polarization effect.

Chapter 7 summarises the main conclusions of this work.

References

[1] A. Ohtomo, D. A. Muller, J. L. Grazul, H. Y. Hwang, Artificial charge-modulation in atomic-scale perovskite titanate superlattices. Nature 419, 378-380 (2002).

[2] A. Ohtomo, H. Hwang, A high-mobility electron gas at the LaAlO3/SrTiO3 heterointerface. Nature 427, 423-426 (2004).

[3] M. Imada, A. Fujimori, Y. Tokura, Metal-Insulator Transitions. Rev. Mod. Phys. 70, 1039 (1998).

[4] E. Dagotto, Y. Tokura, Strongly Correlated Materials: Present and Future. MRS Bull. 33, 1037 (2008).

[5] Khomskii, D. Transition Metal Compounds (Cambridge Univ. Press, (2014).

[6] Tokura, Y. & Nagaosa, N. Orbital physics in transition-metal oxides. Science 288, 462–468 (2000).

[7] J. M. Rondinelli, N. A. Spaldin. Structure and Properties of Functional Oxide Thin Films: Insights From Electronic-Structure Calculations. Adv. Mater. 23 3363 (2011)

[8] Bhattacharya, A. & May, S. J. Magnetic oxide heterostructures. Annu. Rev. Mater. Res. 44, 65–90 (2014).

[9] Mannhart, J. & Schlom, D. G. Oxide Interfaces An Opportunity for Electronics. Science 327, 1607 (2010).

[10] Hwang, H. Y. et al. Emergent phenomena at oxide interfaces. Nat. Mater. 11, 103-113 (2012).

[11] J. Chakhalian, A.J. Millis and J. Rondinelli Nat. Mater. 11, 92-94 (2012), also Editorial Nat. Mater. 11, 91 (2012).

[12] Ngai, J. H., Walker, F. J. & Ahn, C. H. Correlated oxide physics and electronics. Annu. Rev. Mater. Res. 44, 1–17 (2014).

[13] Ahn, C. H. et al. Electrostatic modification of novel materials. Rev. Mod. Phys. 78, 1185–1212 (2006).

[14] Zubko, P., Gariglio, S., Gabay, M., Ghosez, P. & Triscone, J. Interface physics in complex oxide heterostructures. Annu. Rev. Condens. Matter Phys. 2, 141–165 (2011).

[15] S. Okamoto, A. Millis, Electronic reconstruction at an interface between a Mott insulator and a band insulator. Nature 428, 630-633 (2004).

[16] J. B. Goodenough, Theory of the Role of Covalence in the Perovskite-Type Manganites [La, M(II)]MnO3. Phys. Rev. B 100, 564-573 (1955). J. Kanamori, Superexchange interaction and symmetry properties of electron orbitals. J. Phys. Chem. Solids 10, 87-98 (1959).

[17] Coey, J. M. D., Ariando & Pickett, W. E. Magnetism at the edge: new phenomena at oxide interfaces. MRS Bull. 38, 1040–1047 (2013) V. Garcia, M. Bibes, L. Bocher, S. Valencia, F. Kronast, A. Crassous, X. Moya, S. Enouz-Vedrenne, A. Gloter, D. Imhoff, C. Deranlot, N. D. Mathur, S. Fusil, K. Bouzehouane, A. Barthélémy. "Ferroelectric Control of Spin Polarization". Science, 327 (2010).

[18] André Chanthbouala, Vincent Garcia, Ryan O. Cherifi, Karim Bouzehouane, Stéphane Fusil, Xavier Moya, Stéphane Xavier, Hiroyuki Yamada, Cyrile Deranlot, Neil D. Mathur, Manuel Bibes, Agnès Barthélémy and Julie Grollier. "A ferroelectric memristor". Nat. Mater. 11 (2012).

[19] Duygu Kuzum, Shimeng Yu, and H-S PhilipWong. "Synaptic electronics: materials, devices and applications". Nanotechnology 24 (2013) 382001.

[20] Zheng-Dong Luo, Geanina Apachitei, Ming-Min Yang, Jonathan J. P. Peters, Ana M. Sanchez, and Marin Alexe. "Bi-ferroic memristive properties of multiferroic tunnel junctions". Appl. Phys. Lett. 112, 102905 (2018).

[21] Weichuan Huang, Yue-Wen Fang, Yuewei Yin, Bobo Tian, Wenbo Zhao, Chuangming Hou, Chao Ma, Qi Li, Evgeny Y. Tsymbal, Chun-Gang Duan, and Xiaoguang Li. "Solid-State Synapse Based on Magnetoelectrically Coupled Memristor". ACS Appl. Mater. Interfaces 2018, 10, 5649−5656.

Chapter 1: Introduction

Over the last decades, one of the most interesting areas of research in condensed-matter physics is the field of correlated electronic materials [1, 2]. However the great complexity of strongly correlated materials in cases leaves the experimental results non-conclusive against the entanglement between competing mechanisms. In this PhD Thesis, we will apply state-of-the-art experimental and simulation characterization to understand, tune, and predict the emergent complexity of correlated electron systems at it is one of the most foremost challenges in condensed-matter physics at present [3].

The fundamental parameters for tuning the behaviour of correlated electrons are the tunnelling electron hopping amplitude *t* and the band filling [4]. The hopping amplitude *t* competes with the on-site electron–electron Coulomb repulsion energy *U* and the outcome of this competition is the Mott transition, namely, an insulator–metal transition that occurs in correlated-electron systems. As a function of *U*/*t*, the system undergoes several changes in spin and charge dynamics. In the limit of large *U*/*t*, every electron localizes on an atomic site when the number of electrons precisely equals the number of atomic sites. Another route to the Mott transition is by changing the filling (charge doping) of the correlated Mott insulator. Ideally, a minute deviation from half- filling (or from an integer number of conduction electrons per atomic site in the *d*-electron system) leads to a paramagnetic metallic state with a divergently large effective mass of conduction electrons. In most actual cases, however, a finite amount of filling change (doped charge) is necessary to realize the metallic state, which is free of the self-localization of conduction carriers caused by the interactions with the lattice, spins, and so on.

These fundamental parameters, and other related quantities, in correlated-electron oxides can be well controlled typically by the crystal engineering of a perovskite with the formula $(RE,AE)MO_3$, where RE, AE, and M represent the trivalent rare-earth and divalent alkaline-earth ions, which can be in solid solution, and the transition-metal element, respectively. The ideal perovskite (AMO_3) exhibits a simple cubic structure, but the lattice distortions, usually referred to as $GdFeO_3$-type distortions (Figure 1.1 (b)), are governed by the size mismatch of the ionic radii of A and M, or by the so-called tolerance factor *f*, defined as

$$f = \frac{(r_A + r_O)}{\sqrt{2}(r_M + r_O)}$$

Where r_i (i = A, M, or O) represents the ionic size of each element i. When *f* is close to 1, the cubic perovskite structure is realized. As r_A, or equivalently *f*,

decreases, the lattice structure transforms first to the rhombohedral and then to the orthorhombic ($GdFeO_3$-type) structure, in which the M–O–M bond is bent and the angle deviates from 180°. This bond-angle distortion decreases the one-electron bandwidth *W*, because the effective *d*-electron transfer amplitude *t* between the neighbouring M sites is ruled by the *d*-electron hybridization with the intervening O 2*p* state. If the tolerance factor is close to unity [5], a metallic paramagnetic behaviour is displayed. Otherwise, smaller *f* values (or decreasing RE ionic size) exhibit antiferromagnetic insulating ground states and undergo a thermally induced insulator–metal transition (IMT) with increasing temperature.

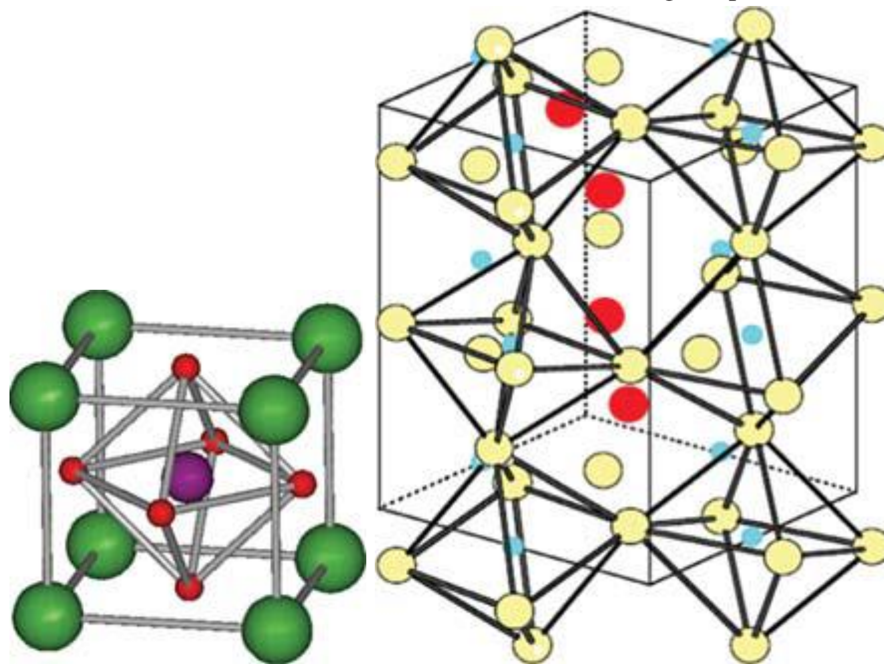

Figure 1.1 (a) Perovskite structure, $(RE, AE)MO_3$, with trivalent (3+) rare-earth (RE) ions and divalent (2+) alkaline-earth (AE) ions at the perovskite A site and the transition-metal element on the perovskite B site. (b) Orthorhombically distorted (GdFeO3-type) structure of perovskites. E. Dagotto and Y. Tokura. "Strongly Correlated Electronic Materials: Present and Future". MRS Bull. 33 (2008) [3].

Another important advantage of perovskites or related structures is the ease of chemical control of the band filling. Using the solid solution $RE_{1-x}AE_x$ at the perovskite *A* site AMO_3, see Figure 1.1 (a), the effective valence of the transition metal (M) becomes 3 + *x*. In analogy to doped semiconductors, the increase (decrease) of *x* is typically called "hole doping" ("electron doping"). In fact, this change in *x* reflects a decrease (increase) of the band filling or the chemical potential. As a result, we tune the metallic or insulating character of the perovskite

by the chemical doping. At this stage, explanations about the most representative doped transition metal oxides will be developed:

1.1 Colossal Magneto Resistance (CMR) manganites

Doped manganites $R_{1-x}A_xMnO_3$ (being R^{3+} a rare earth such as La, Pr, etc… and A^{2+} Ca or Sr) with the perovskite structure exhibit varied properties, mainly colossal magnetoresistance (CMR). They display an astonishing wide ranging of different types of ordering: orbital, spin and charge ordering; they have insulating and metallic phases, they are very sensitive to external influences such as electric and magnetic fields, irradiation, etc. [6]
These systems have very complicated and rich phase diagrams, for instance, the detailed phase diagram for $La_{1-x}Sr_xMnO_3$ [7]. Undoped $LaMnO_3$, containing Jahn–Teller ions Mn^{3+} $\left(t_{2g}^3 e_g^1\right)$ with $S = 2$ is a Mott insulator which undergoes the cooperative Jahn–Teller transition at the critical temperature $T_{O.O.}$~$800K$ and a much lower critical Néel temperature $T_N \approx 140K$, $LaMnO_3$ turns into type A antiferromagnetic.
With hole doping by cations Ca^{2+} or Sr^{2+}, we introduce ions Mn^{4+} $\left(t_{2g}^3 e_g^0\right)$ with $S = \frac{3}{2}$ which makes orbital ordering temperature $T_{O.O.}$ and Néel temperature T_N decreases. Nevertheless, the magnetic ordering change into a spin-glass-like state, which is also rather spatially inhomogeneous, there may be a phase separation.
Likely, the most interesting phase is reached in both $La_{1-x}Sr_xMnO_3$ and $La_{1-x}Ca_xMnO_3$ at concentrations ranging between $0.2 < x \leq 0.5$; this is the ferromagnetic phase in which the phenomenon of colossal magnetoresistance arises. In other words, ferromagnetism ordering makes electron hopping easier, and this electron hopping, in turn, promotes ferromagnetism.
The formation of inhomogeneous states due to phase separation in low doped manganites, might exist at higher doping too. There are relevant arguments, see [8], to discuss the phenomenon of colossal magnetoresistance in these systems.
For higher doping, the phase of $La_{1-x}Ca_xMnO_3$ change again. At $x = 0.5$ there is checkerboard type charge ordering in the system. In the over-doped regime, the charge ordering is incommensurate, in the form of Charge Density Waves (CDW) or stripes of zigzag type. Every phases for $x \geq 0.5$ are insulating because the transition to a charge-ordered state is usually accompanied by an enhanced resistivity.
Nevertheless, $Pr_{1-x}Ca_xMnO_3$ remains insulating at all x. In particular, at concentrations ranging between $0.3 < x \leq 0.5$; this system display the

checkerboard pattern charge ordering with extra Mn^{3+} occupying random sites or with a larger-scale phase separation.
The system $Nd_{1-x}Sr_xMnO_3$ displays an exotic novel phase, for $x \geq 0.5$ it turns the charge-ordered insulating phase into metallic phase endowed with A-type magnetic ordering. The mentioned metallic behaviour is due to the partially filled two-dimensional band constructed of $x^2 - y^2$ orbitals.
Thus we show that CMR manganites display a wide variety of different phases, all this diversity being based on the interplay between different degrees of freedom: charge, spin, and orbital. In many such phases one also observes phase separation, especially close to (usually quite sharp) transitions between charge ordered insulating antiferromagnets and ferromagnetic metallic states which lie close in energy; these transitions can be triggered by temperature, by magnetic field, and even by isotope substitution [9].
There are also layered manganite perovskites of Ruddlesden-Popper series presenting a wide spectrum of properties. For instance, the bilayer "327" manganite $La_{2-2x}Sr_{1+2x}Mn_2O_7$ has a very rich phase diagram, endowed with a ferromagnetic (CMR) metallic phase, an A-type antiferromagnetic ordering which is also metallic, a phase with charge ordering, etc. Note that a similar layered "214" perovskite $La_{2-x}Sr_xMnO_4$ remains insulating at all x concentration values. This could be generalized for many other systems: for example single layer compounds (with Mn, Co, Fe) have a stronger tendency to remain insulating even when doped in comparison with double layer perovskite structures.

1.2 Doped Cobaltites

The system $La_{1-x}Sr_xCoO_3$ exhibits possible effects of doping. It is well known that Co^{3+} (d^6) can exist in different spin configurations: the high spin (HS), the intermediate spin (IS), and low spin (LS) states. At low temperatures, the undoped $LaCoO_3$ presents the LS state as the most stable state, being an nonmagnetic insulator because the LS state of Co^{3+} has spin $S = 0$. Whenever temperature increases, both magnetic states (HS and IS) are thermally populated, leading to the appearance of magnetic states with $S = 2$ (HS) or $S = 1$ (IS).
Separately the temperature-induced transition, the transition to magnetic and metallic state can be triggered by hole doping. Replacing La^{3+} by Sr^{2+} gives rise to such a transition.
By analogy with doped manganites, phase separation also takes place [10] enhancing x concentration of cation dopants. Thus, the system undergoes transition to ferromagnetic metallic state through inhomogeneous states. Their presence was

observed by different experimental techniques, including local probes such as NMR and ESR, and is confirmed by neutron scattering [11–13].

1.3 Cuprates

After the discovery of high–T_C superconductors in 1986 [14], the doped cuprates attracted huge interest and have been investigated with various experimental techniques, accumulating a lot of information about them. However, relevant open questions still remain. For instance, there is a lack of understanding of the detailed microscopic mechanism of superconductivity; but there are a wide variety of theoretical explanations [15–17]. We will introduce the main ideas because the whole detailed theoretical ideas are beyond the scope of this dissertation.

The first material discovered for high– T_C cuprates was the "214" layered perovskite $La_{2-x}Sr_xCuO_4$, composed of CuO_2 layers as building blocks, also characteristic in other high– T_C materials of the same class.

Undoped La_2CuO_4 $(x = 0)$ is a Mott insulator provided with Cu^{2+} $\left(t_{2g}^6 e_g^3\right)$ ions, whose d-shell hole has spin $\left(S = \frac{1}{2}\right)$, set in CuO_2 layers in a simple square lattice; endowed with G-type antiferromagnetic ordering (checkerboard alternations of spin ↑ and ↓) and Néel temperature $T_N = 317K$. Thus, Cu^{2+} is a Jahn–Teller ion with one hole in the doubly degenerate e_g orbitals. It triggers strong tetragonal distortion (elongation of the surrounding ligand octahedral), which sets two e_g electrons on the z^2 orbital, leaving a hole in the $(x^2 - y^2)$ orbital. The splitting of e_g levels is quite large, on the order of $\geq 1eV$. In the process of this JT distortion, the two apical oxygens move away from the basal plane. In the "infinity limit", Cu^{2+} may be left in a fivefold coordination. If both apex oxygens are distorted to the "infinity limit" regime, Cu^{2+} will remain square–coordinated. Particularly, the high–T_C superconductor $YBa_2Cu_3O_{7-\delta}$ $(T_C = 90K)$ has the Cu ions belonging to CuO_2 planes arranged in square pyramids (provided with fivefold coordination and Cu^{1+} ions in linear chains). Furthermore, there are also superconductors endowed with square coordination, such as electron-doped superconductors $Nd_{2-x}Ce_xCuO_4$.

Despite the common trend of hole occupation in the $(x^2 - y^2)$ orbital, the axis of the distorted CuO_6 octahedra (pyramid or square coordinaton) is not necessarily along the z–direction. For instance, $KCuF_3$, whose "cross-shaped " hole orbitals alternate in such a way that local tetragonal axes lie in x- and y- directions.

However, the situation in this sense is simpler in the oxide La_2CuO_4 because this material has its distorted axis of the CuO_6 octahedra parallel along the z- axis. Therefore, the hole orbitals belong to the $(x^2 - y^2)$ type. In addition, the Jahn–Teller splitting between $(x^2 - y^2)$ and z^2 orbitals is very large, and we can consider z^2 bands contribution negligible. Thus, the holes are located in nondegenerate $(x^2 - y^2)$ levels or bands, and the later kind of cuprates may be described approximately by the simple nondegenerate Hubbard model, or more precisely, including also the oxygen p orbitals, by the three-band (or d-p) model, only for nondegenerate d-electrons.
One can discuss [18] that it is plausible to reduce the three-band or d-p model to the nondegenerate Hubbard model; but the state Cu^{3+}, which is obtained formally by hole doping, corresponds to a very small charge-transfer gap. As a result, the doped holes would occupy the p orbitals of oxygen. Thus, instead of the state Cu^{3+} (d^8), we would rather have $Cu^{2+}(d^9)\bar{L}$, where $\bar{L}$ is the ligand (oxygen) hole. The "core" state $Cu^{2+}(d^9)$ has spin $\left(S = \frac{1}{2}\right)$ and the ligand hole surrounding it has also unpaired spin $\left(S = \frac{1}{2}\right)$. Therefore, the strong d–p hybridization results in the creation of a bound singlet state between Cu^{2+} and the aforementioned ligand hole. This state is known as the *Zhang–Rice singlet*. In other words, when we set a hole into La_2CuO_4 the hole would create a singlet state at a given Cu site (in analogy with the hole doping or electron removing in the Hubbard model). At this stage we take into consideration that *Zhang–Rice singlets* have its holes delocalized over four oxygens around the Cu ion belonging to its basal plane. This approximation is approximately valid in the theoretical description of high–T_C cuprates, although there are some arguments [19] that this approximation can sometimes fails.
When doping the Mott insulator La_2CuO_4 using Sr ion, the antiferromagnetic order is quenched swiftly, turning the material into metallic and also a high–T_C superconductor. The characteristic function of the critical temperature T_C with the concentration of hole dopants x, is a dome-shaped function: First at all, the critical temperature T_C enhances initially with x doping, reaches a maximum value, and then begins to decrease until quenching in the overdoped regime. Regarding the quantum states above the critical temperature T_C, the overdoped regime is well described by the Fermi-liquid theory. But, for the moderate concentration range, there is another exotic state, the so-called *pseudogap phase*, whose transport and magnetic properties exhibit anomalous behaviour. At present, there is an open controversy about the true nature of this pseudogap phase (it might be a precursor

to the superconducting phase, maybe it could be triggered by charge ordering, which competes with superconductivity).
The other high–T_C cuprates, such as $YBa_2Cu_3O_7$, $Bi_2Sr_2CaCu_2O_{8+x}$, or other materials in the same family provided with Hg or Tl, whose maximum superconducting transition temperatures are higher than 150K, share in common the CuO_2 basal planes endowed with $(x^2 - y^2)$ hole orbitals. The main difference is based on the nature of the "charge reservoirs" which supply dopant charge carriers in these CuO_2 basal planes.

1.4 Ferroelectrics

The Goldschmidt´s tolerance factor might be a useful parameter to find perovskite structures prone to ferroelectricity. If tolerance factor is smaller than $f \leq 0.71$, the octahedral-rotation-like distortions inhibits the ferroelectric distortion, easier to fulfill in cubic perovskite structures.
Over the last decades, there have been an increasing interest to the electrical measurement of the ferroelectric distortion contribution in thin film ferroelectrics (in spite of the spurious contributions unrelated to ferroelectricity due to electrical measurement "artifacts" [20]) in order to patent Ferroelectric Random Access Memories (FRAMs) [85]. Furthermore, the domain walls in ferroelectric and multiferroic materials have gained relevance [21] due to the experimental observation of charged domain walls [22]: which are subsequently classified as Head-to-Head domain walls and Tail-to-Tail domain walls, depending on the electrostatic repulsion to be between the cations or the anions, respectively.

1.5 Memristor

At this stage, a fundamental question arises if the electronic correlations involves ionic transport. The memristance behaviour stems naturally from nanoscale systems in which solid-state electronic and ionic transport are coupled under an external bias voltage [23]. The concept of memristor was coined by Leon Chua in 1971 [24] based on six mathematical relations between the electric current, voltage, charge and magnetic flux. Nevertheless, the memristance effect was not experimentally observed until 2008 by Dr. Stanley Williams et al. [23] in 10 nm thick TiO_{2-x} between Pt metal electrodes. Furthermore, there are several efforts to accommodate the Hodgkin-Huxley model for spike voltage signal of biological neurons [25] to inorganic memristor devices [26]. The memristor device is based

on a reversible REDOX reaction controlled by electric fields [27]. Because of this, there were several attempts to extend the traditional memristor concept to nanobatteries [28].

1.6 Tunnel Junction and other Spintronics Devices

The necessity of miniaturization of electronic components last decades lead to take into consideration the quantum tunnelling effect in the design of electronic devices [29, 30]. The electron tunnelling is a quantum mechanical effect by which an electrical current may flow from one metallic electrode, across a thin insulating barrier, into another metallic electrode. The easiest way to understand how tunnelling is possible is by considering an electron wave that encounters a potential step. For enough thin barriers (customarily a few nanometers thick), some intensity remains on the other side of the potential step, and therefore, the electron will have a finite probability of being found on the other side of the tunnel barrier [31]. The current across the structure is given by the product of the density of states (η) in the electrodes, multiplied by the square of the tunnelling matrix elements M (being M related to the transmission coefficient $T \equiv |M|^2$) and the thermal occupation probability of the quantum states involved in the process:

$$I_{1\to 2}(V) = \int_{-\infty}^{+\infty} \eta_1(E)\eta_2(E+eV)|M|^2 f(E)[1-f(E+eV)]dE \qquad (1)$$

Specifically, for non-magnetic identical electrodes, and a diamagnetic insulating barrier, the current density J can be expressed as given by Simmons [32], who determined the tunneling matrix elements in the Wentzel–Kramers–Brillouin (WKB) approximation:

$$J(V) = \frac{J_0}{d^2}\left(\phi - \frac{eV}{2}\right) exp\left[-Ad\sqrt{\phi - \frac{eV}{2}}\right] - \frac{J_0}{d^2}\left(\phi + \frac{eV}{2}\right) exp\left[-Ad\sqrt{\phi + \frac{eV}{2}}\right]$$

Where $A = 4\pi\sqrt{2m^*}\hbar$ and $J_0 = \frac{e}{2\pi\hbar}$ are characteristic constants with m^* being the electron effective mass, d the dielectric tunnel barrier thickness, ϕ the barrier height and eV the applied voltage bias.

In fact, the tunnel current has an exponential dependency on the barrier thickness, the square root of the effective mass and the square root of the barrier height. The most direct and natural consequence consists that the smallest perturbation in any of these three parameters will trigger a strong influence on the tunnel current.

Amongst other relevant traits, the tunnel current, at moderate voltage regime, adopts the general form:

$$J \propto \alpha V + \beta V^3 \qquad (2)$$

If the applied voltage bias is larger than ϕ/e, the tunnelling effect is no longer direct; adopting the Fowler–Nordheim tunnelling regime whose current density may be approximated by:

$$J = \frac{e^3V^2}{16\pi^2 d^2 \hbar\phi} exp\left(-\frac{\pi d\sqrt{m^*}\phi^{\frac{3}{2}}}{2\sqrt{2}e\hbar V}\right) \qquad (3)$$

In the direct (elastic) tunnelling case of Equation (1), the final state of an electron tunnelling from the Fermi level in the first electrode is a state at an energy eV above the Fermi level in the second electrode. Nevertheless, in non-idealized cases, the electron may be able to interact with phonons or, when the ultrathin dielectric barrier separating the electrodes is not perfect, with defect states within the bandgap of the insulator. The physics of defect-assisted tunnelling is very rich, especially when spin-dependent processes come into play. See model of Glazman and Matveev [33, 34] for assisted tunnelling through several localized states whose prediction is a $V^{4/3}$ trend of the tunnelling conductance G. when tunnelling is assisted by defects, the conductance of the junction strongly decreases as temperature decreases. For more details, the reader may consult [35].

In the original description of direct tunnelling by Simmons, the effects of the density of states (DOS) on the tunnel current was neglected. However, the research of tunnel junctions provided with superconducting electrodes (Al, Pb or Sn at very low temperatures), showed that the superconductor density of states (DOS) is significantly relevant. Below the critical temperature, the opening of a quasiparticle gap bring about strong variations in the density of states (DOS) close to the Fermi level as demonstrated in $I(V)$ and $G(V)$ curves [36].

The use of ferromagnetic metals as electrodes create non-equivalent density of states (DOS) for spin-up and spin-down electron states. According to the assumption that the spin is conserved during the tunnel process so that the total tunnel current is the superposition of spin-up and spin-down currents. Then, the conductance of a magnetic tunnel junction (MTJ, a trilayer in which two ferromagnetic electrodes sandwich a diamagnetic-dielectric tunnel barrier) in the parallel (P) and antiparallel (AP) configurations of the electrodes' magnetization is given by the product of the density of states (DOS) of the electrodes:

$$G_P \propto G_{\uparrow\uparrow} + G_{\downarrow\downarrow} \propto N_{1\uparrow}N_{2\uparrow} + N_{1\downarrow}N_{2\downarrow} \qquad (4)$$

$$G_{AP} \propto G_{\uparrow\downarrow} + G_{\downarrow\uparrow} \propto N_{1\uparrow}N_{2\downarrow} + N_{1\downarrow}N_{2\uparrow} \qquad (5)$$

Being $N_{1\uparrow(\downarrow)}$ and $N_{2\uparrow(\downarrow)}$ the density of states (DOS) of both ferromagnetic electrodes at the Fermi level energy for majority (↑) and minority (↓) spin

electrons. Therefore, the tunnel resistance adopts different values in function of the relative orientation of the ferromagnetic electrodes magnetization: Parallel (P) or Antiparallel (AP) magnetization states (see Figure 1.2). Consequently, the tunnel magnetoresistance effect (TMR) is defined by virtue of the Jullière's equation for the TMR ratio [29]:

$$TMR = \frac{R_{AP} - R_P}{R_P} = \frac{G_P - G_{AP}}{G_{AP}} = \frac{2P_{spin}^1 P_{spin}^2}{1 - P_{spin}^1 P_{spin}^2} \qquad (6)$$

Being P_{spin} the spin polarization of the electrodes whose equation is given as

$$P_{spin}^i = \frac{N_{i\uparrow} - N_{i\downarrow}}{N_{i\uparrow} + N_{i\downarrow}} \qquad (8)$$

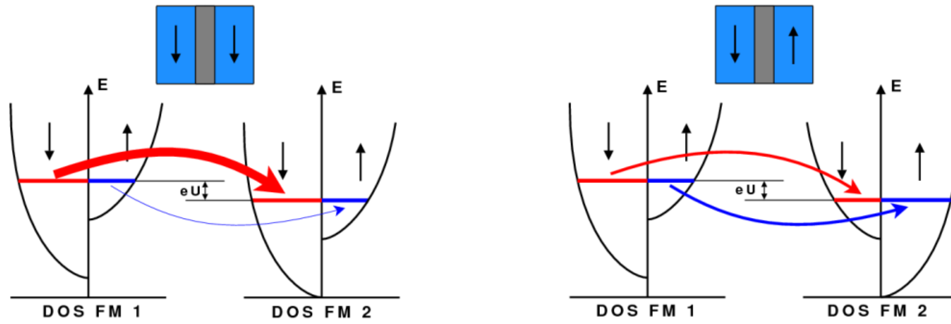

Figure 1.2 Schematic of the spin-dependent tunnelling process through an insulating barrier when the magnetizations of the ferromagnetic electrodes are aligned parallel (left) and antiparallel (right) to one another. In this case the tunnelling current is larger in the parallel state. J. Tornos, "Spin-dependent transport in oxide multiferroic tunnel junctions", Ph. D. Thesis, Universidad Complutense de Madrid (2014) [98].

The first TMR experiment (at low temperature) dates back to 1975 [29]; but only until 1995 [37, 38] this research restarted to blast off because of the observation of large and reproducible tunnel magnetoresistance (TMR) effect at room temperature in $Fe/Al_2O_3/Fe$ and $Co/Al_2O_3/CoFe$ (depicted in Figure 1.3). Non-volatile magnetic random access memories (MRAMs) [39] based on the TMR effect. For instance, arrays of MTJs, have been commercialized since 2007 [40].

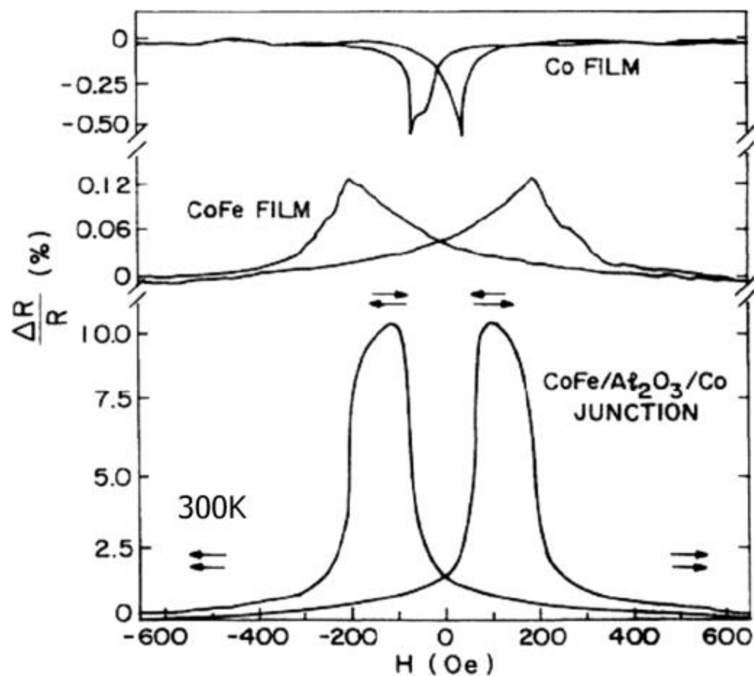

Figure 1.3 Field dependence of the resistance of a Co/Al2O3/CoFe tunnel junction, defining a TMR effect of about 10%. The intrinsic magnetoresistance of each electrode (anisotropic magnetoresistance) is also shown for comparison. J.S. Moodera *et al.*, Physical Review Letters, 74, p. 3273, 1995 [38].

In order to increase the TMR ratio, it is necessary to find materials endowed with the highest P_{spin}, which are called half-metals [41], whose DOS is metallic for one spin direction and almost zero for the other. The most successful example are the tunnel junctions based on manganite electrodes such as $La_{2/3}Sr_{1/3}MnO_3$ (LSMO) or $La_{2/3}Ca_{1/3}MnO_3$ (LCMO), displaying TMR values of several hundred per cent [42–46]. However, the TMR of manganite-based MTJs is only large at low temperature and vanishingly small at 300K [47]. More detailed references could be provided [48]. Several tunnel dielectric barriers will be explained in subsequent sections.

1.6.1 MgO dielectric tunnel barrier

MgO adopts the rocksalt crystalline structure with a lattice constant $a = 4.203$Å and a bulk optical bandgap of 7.8 eV. In 2001, ab initio calculations on tunnel junctions with MgO dielectric barriers that a deeper determination of the band structures of both electrodes and dielectric barrier would be necessary to shed more

light over the true nature of spin-polarized tunnelling in the case of epitaxial tunnel junctions [49, 50]. An intuitive description of these theoretical results [51], in the case of large tunnel barrier thicknesses, for instance, when the tunnel current is primarily carried by states with wave-vector perpendicular to the interface $\left(k_{||} = 0\right)$, considering the band structure of $b.c.c. Fe$ in the ΓH direction depicted in Figure 1.4 (a) (associated to electrons propagating perpendicularly to the interface), one can see that at the Fermi level states of Δ_1, (spd-like character), Δ_5 (pd), and $\Delta_{2'}$ (d) symmetries coexist for the majority spin electrons. Opposite to this, Δ_1 is absent in the minority spin band structure. The Bloch state of electrons of Δ symmetry stemming from a Fe electrode will decay with different rates in the epitaxially grown MgO barrier. In fact, the *ab initio* calculations of the complex band structure of MgO (see Figure 1.4 (b)), it is worth noting that the decay rate Δ_1 is much smaller than Δ_5 which is in turn smaller than $\Delta_{2'}$ at the Fermi level.

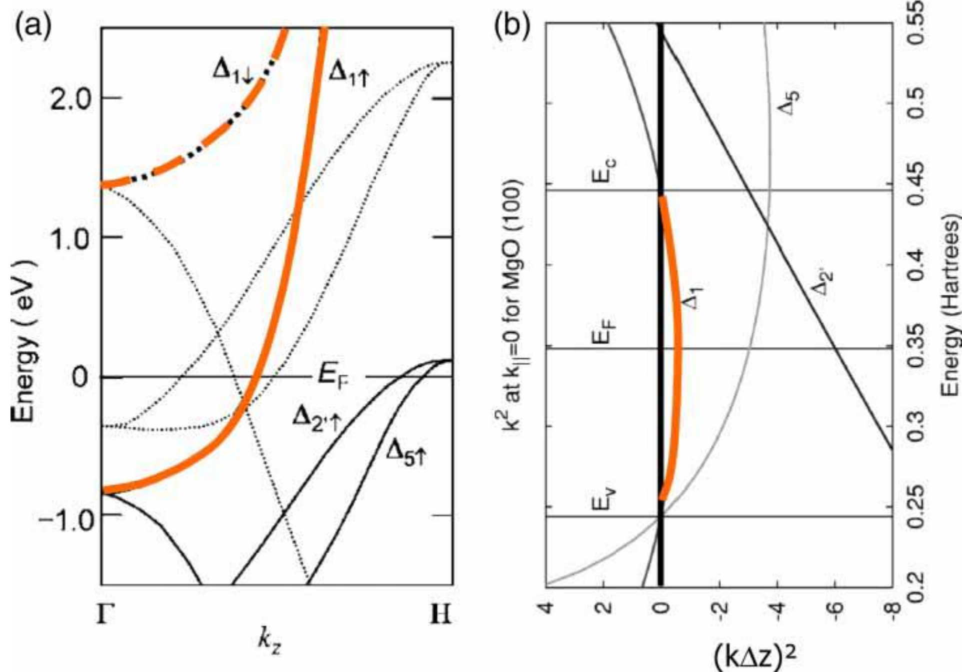

Figure 1.4 (a) Band structure of b.c.c. Fe in the H direction corresponding to electron propagating perpendicularly to the interface for majority spin and minority spin states. Due to the exchange interaction, the spin-up and spin-down bands are shifted in energy. S. Yuasa *et al.* Applied Physics Letters, 89, P. 042505, 2006 [52]. (b) Complex band structure of MgO in the vicinity of the gap along (100) Negative values of $k^2 = -\kappa$ determine the exponential decay rates for various Bloch states. E_v is the top of the valence band. E_C is the bottom of the conduction band. W.H. Buttler *et al*., Physical Review B 63, p. 054416, 2001 [49].

In fine, given the different symmetries of the Bloch states in the electrodes, the transmission coefficient at the interface, and the different decay rates of the evanescent charge density waves inside the barrier in Fe-b.c.c.(001)/MgO/Fe-b.c.c.(001) tunnel junctions, Butler *et al.* [49] estimated the tunnelling DOS in the parallel and antiparallel configuration of the magnetizations in the large thickness regime (see Figure 1.5). Thus, in the parallel configuration, the tunnelling is regulated by Δ_1 states of majority spin endowed with small decay rate that gives rise to a high conductance state. In the antiparallel configuration, the tunnelling is regulated by Δ_5 and $\Delta_{2'}$ states endowed with large decay rates and giving rise to a small conductance state.

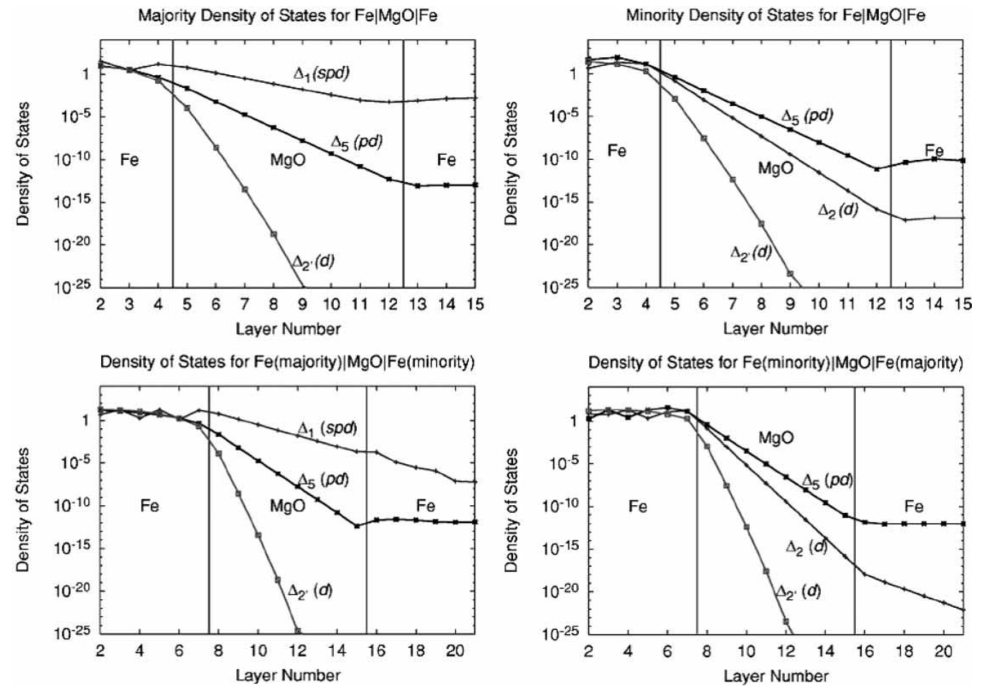

Figure 1.5 Tunnelling DOS for $k_{||} = 0$ for Fe(100)/MgO(8ML)/Fe(100). The four panels show the tunnelling DOS for majority spins (upper left) and minority spins (upper right) in the parallel configuration, and antiparallel alignment of the moments in the two electrodes (lower panels). W.H. Butter et al., Physical Review B 63, p. 054416, 2001 [49].

Experimentally, tunnel magnetoresistance (TMR) values more than 200% were reported by Parkin et al. [53] and Yuasa et al. [54]. Several researchers have published very large TMR results in Co/MgO/Co (410%) [52], CoFe/MgO/CoFe (290%) [53] and CoFeB/MgO/CoFeB (1144% at low temperature and 604% at room temperature [55]). This last result is reported in Figure 1.6 (c).

In Co/MgO/Co tunnel junctions, we can assert the TMR varies weakly with temperature but more strongly with voltage bias compared to case of Fe/MgO/Fe. This has been attributed to the influence of the band structure of b.c.c. Co [52, 56]. In Fe/MgO/Fe MTJs, Yuasa *et al.* [57] reported oscillations of the TMR as a function of the MgO thickness (Figure 1.6 (b)) and ascribed them as the signature of interferences between evanescent waves of different symmetry (different metal-induced gap states), required in a coherent tunnel regime.

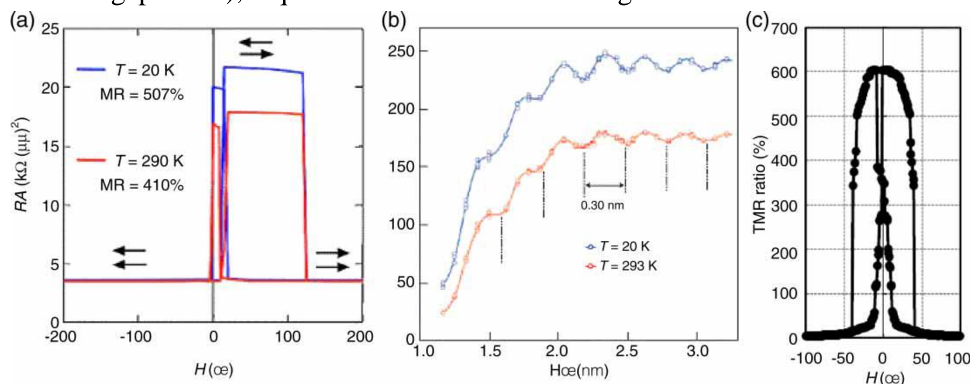

Figure 1.6 (a) Magnetoresistance curves at bias voltage of 10 mV for the Co(001)/MgO(001)/Co(001) MTJ with MgO thickness of 2.2 nm. The red and blue curves represent magnetoresistance curves at 290 and 20 K, respectively. Arrows represent magnetization alignments. (b) MR ratio at *T* = 293 and 20K (measured at a bias voltage of 10 mV) versus t_{MgO} (a) and (b). Nature Materials 3, p. 868, 2004. [54] (c) *R(H)* curve of a CoFeB/MgO/CoFeB tunnel junction, showing a TMR of 600% at room temperature. S. Ikeda *et al.*, Applied Physics Letters 93 (2008), 082508 [55].

1.6.2 $SrTiO_3$ dielectric tunnel barrier

$SrTiO_3$ adopts the perovskite structure ABO_3 with a lattice constant $a = 3.905$ Å and a bandgap of 3.2 eV [58, 59]. The valence band is formed by $O\ 2p$ states and the conduction band by $Ti\ t_{2g}$ (as depicted in Figure 1.7 (a)). Opposite to the case of MgO, the quantum states at the top of the valence band do not share the same symmetry as those of the bottom of the conduction band [60], which consequently affects tunnelling effects. The complex band structure of $SrTiO_3$ has been estimated by Bowen et al. [61] and Velev et al. [62] as depicted in Figure 1.7 (b). Opposite to MgO, the hierarchy of decaying states has a nontrivial dependency on energy. For instance, Δ_2 and $\Delta_{2'}$ decay faster than both Δ_1 and Δ_5, and note the intersection between Δ_1 and Δ_5 symmetry κ loops at the Fermi level and therefore accessible in tunnelling experiments.

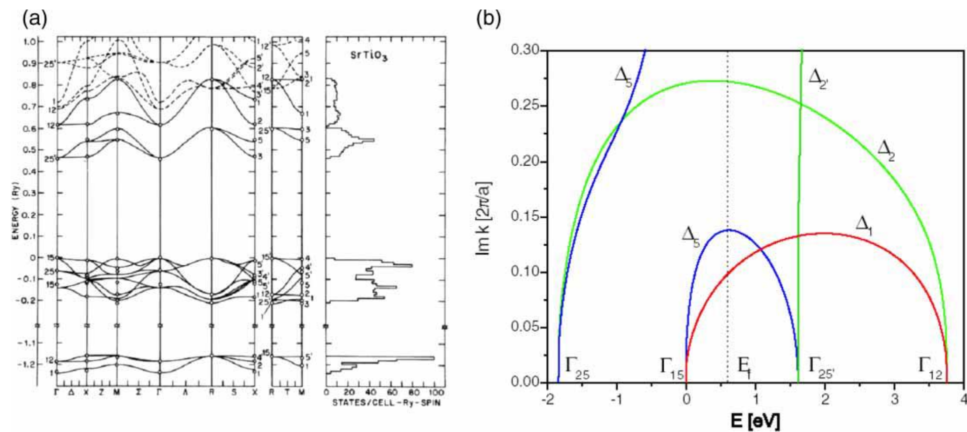

Figure 1.7 (a) Band structure of SrTiO3. L.F. Mattheiss, Physical ReviewB, 6, p. 4718, 1972 [60]. (b) Complex band structure of $SrTiO_3$ at the $\overline{\Gamma}$ point. J.P. Velev et al., Physical Review Letters, 95, p. 216601, 2005 [62].

In order to gain deeper insights into the role of the barrier on the tunnelling process, transport experiments were carried out in $La_{0.7}Sr_{0.3}MnO_3\,/\,SrTiO_3\,/\,Co$ tunnel junctions [63–66]. The mentioned results are depicted in Figure 1.8. In particular, LSMO/Al_2O_3/Co junctions (Figure 1.8 (b)) have a positive TMR (the resistance is larger in the antiparallel state than in the parallel one) which indicates a positive spin polarization for Co at the interface with Al_2O_3, as always found with Al_2O_3 barriers and transition metal electrodes [67]. Conversely, LSMO/ $SrTiO_3$ /Co junctions have a negative TMR (Figure 1.8 (a)) which indicates a negative spin polarization for Co at the interface with $SrTiO_3$. The aforementioned results give evidences about the role played by the barrier [63].
Furthermore, by inserting an ultrathin Al_2O_3 layer at the interface between $SrTiO_3$ and Co in LSMO/ $SrTiO_3$/Co tunnel junctions, De Teresa *et al.* [64] have demonstrated that a positive TMR is restored (Figure 1.8 (d)).

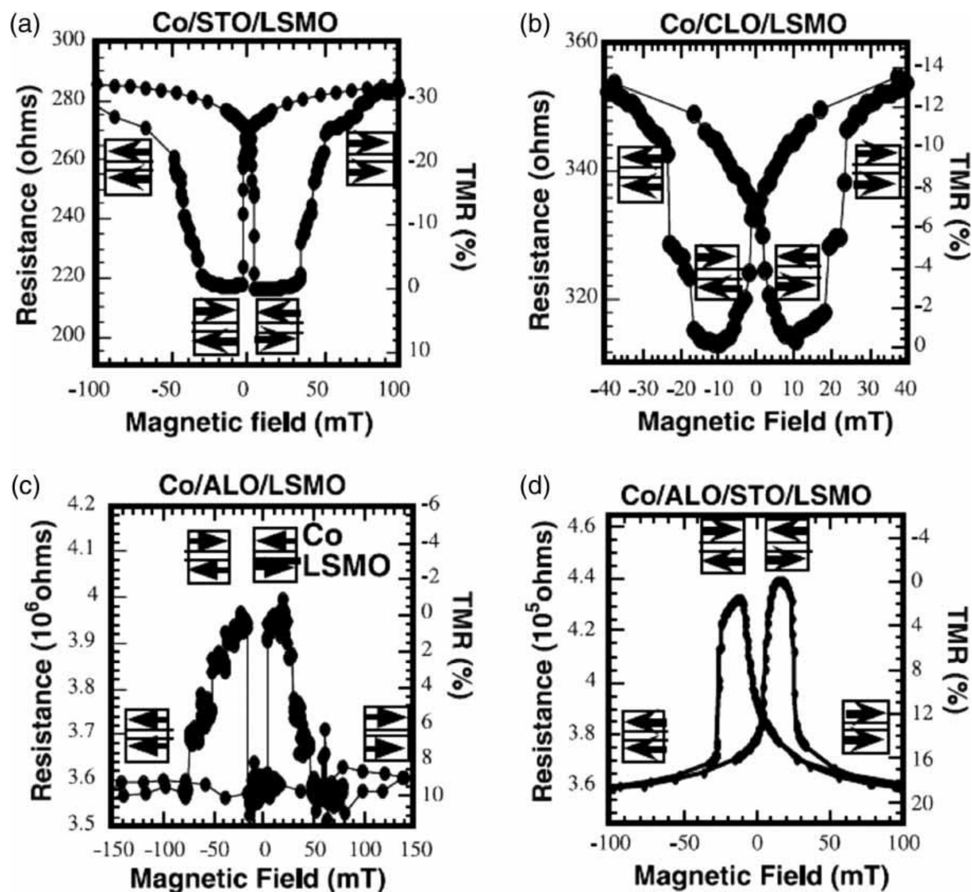

Figure 1.8 TMR curves recorded at 40K and 10mV for (a) Co/SrTiO3/LSMO, (b) Co/(Ce,La)O2/LSMO, (c) Co/Al2O3/LSMO and (d) Co/Al2O3/SrTiO3/LSMO junctions. J.M. De Teresa et al., Science, 286, p. 507, 1999 [64].

This last result shows that interfacial bonding nature is a critical parameter in the determination of spin polarization, in agreement with the theoretical work of Tsymbal and Pettifor [68]. The different bias dependences of the TMR found in $SrTiO_3$ or Al_2O_3 is understood in terms of the d-character, or s-character respectively, of the tunnelling electrons through the barrier. The TMR maximum absolute value in LSMO/$SrTiO_3$/Co tunnel junctions at negative bias, (for example, when electrons are injected into the Co electrode) is ascribed to the DOS of d character of the Co electrodes. First-principles density functional studies of the Co/Al_2O_3 and Co/ $SrTiO_3$ interface by Oleinik and coworkers [69–71] suggested the same interpretation, i.e. the inversion of the Co spin polarization for $SrTiO_3$ (depicted in Figure 1.9) or thick Al_2O_3 tunnel barriers. Furthermore, they predicted a moment of $0.25\mu_B$ on the Ti atom at the interface due to an antiferromagnetic

exchange coupling between Co and Ti mediated by oxygen atoms. Results in the case of SrTiO3 barriers are presented in Figure 1.8 [70].

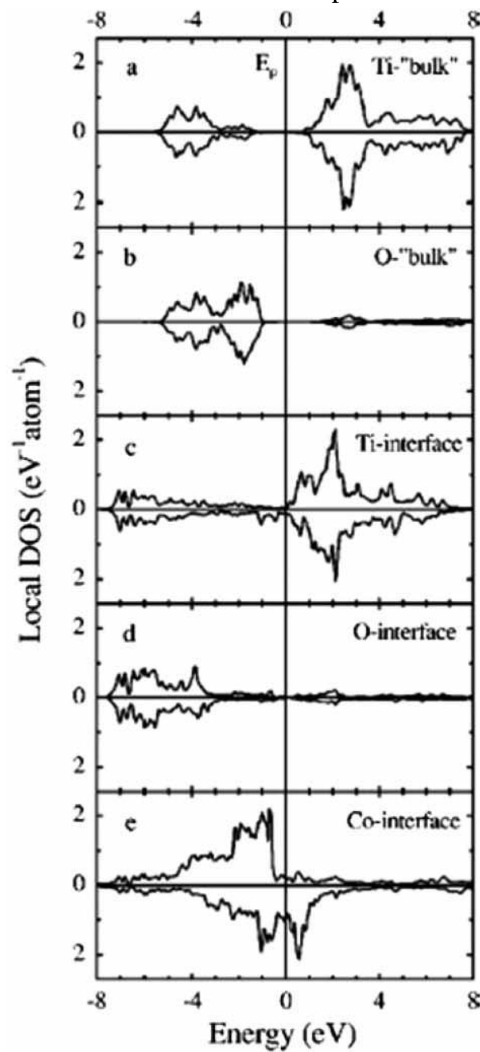

Figure 1.9 Local densities of states for the majority-(top panels) and minority-(bottom panels) spin electrons for the TiO_2-terminated $Co/SrTiO_3/Co$ tunnel junctions: (a) Ti and (b) O in the third TiO_2 layer from the interface; (c) Ti and (d) O in the interfacial TiO_2 layer, (e) Co at the interface. The vertical line indicates the position of the Fermi level. I.I. Oleinik et al., Physical Review B, 65, p. 020401, 2001 [70].

Note also that Bibes *et al.* and Garcia *et al.* also found a negative spin polarization for Co at the interface with epitaxial TiO_2 [72] and $LaAlO_3$ [73] barriers, respectively.

As a parenthetical remark, we are going to explain the spin filtering effect [74].

1.7 Spin Filtering Effect

Spin filtering effect consists on the spin-dependent tunnelling through a ferromagnetic or ferromagnetic insulating barrier. Because of the exchange splitting, the bottom of the conduction band in the barrier material divides in two different energies for spin-up and spin-down electrons, yielding two different tunnel barrier heights for spin-up and spin-down electrons. According to the free electron model, the tunnel transmission has an exponential dependence with the tunnel barrier height. As a result, electrons from a non-magnetic electrode will be transmitted differently depending on their spin. If the bottom of the conduction band is at a lower energy for spin-up than for spin-down, therefore a large positive spin polarization is expected for the current emerging from the barrier. The spin polarization of this current, or spin filtering efficiency of the barrier, follows the equation:

$$P_F^{spin} = \frac{J_\uparrow - J_\downarrow}{J_\uparrow + J_\downarrow} \qquad (9)$$

Where $J_\uparrow$ ($J_\downarrow$) is the spin-up (spin-down) current that satisfies the Simmons model at small voltage bias [32]:

$$J_\uparrow = \sqrt{\phi_0 - \frac{\Delta\phi}{2}}\, exp\left(-A\sqrt{\phi_0 - \frac{\Delta\phi}{2}}\, d\right) \qquad (10)$$

$$J_\downarrow = \sqrt{\phi_0 + \frac{\Delta\phi}{2}}\, exp\left(-A\sqrt{\phi_0 + \frac{\Delta\phi}{2}}\, d\right) \qquad (11)$$

Being ϕ the averaged barrier height, $\Delta\phi$ the spin-splitting of the bottom of the conduction bands and d the thickness of the tunnel barrier. If the spin-splitting $\Delta\phi$ and the thickness of the barrier are risen, the spin filtering efficiency P_F^{spin} will clearly rise. For the purpose of measuring the spin filtering efficiency, a ferromagnetic counter-electrode is used, defining a spin-filter tunnel junction. The relative orientations of the magnetizations of the barrier and the counter-electrode will determine the current intensity. As an extrapolation of the Jullière model, the TMR of a spin filter satisfies the equation:

$$TMR = \frac{2P_1^{spin} P_F^{spin}}{1 - P_1^{spin} P_F^{spin}} \qquad (12)$$

The dependence of the TMR on the thickness of the barrier and with the bias applied to the junction has been calculated by Saffarzadeh [75]. In general, the TMR is expected to increase with bias voltage, which is a typical signature of spin-

filtering. Nevertheless, the problem is more complex for an epitaxial spin filter and the role of wave-function symmetry has to be considered [76]. There have been several estimations of spin filtering in europium chalcogenides.

1.7.1 Europium chalcogenides

EuS and EuO are ferromagnetic semiconductors with Curie temperatures of 16 and 69 K, respectively [77]. Moodera et al. [78, 79] performed spin-polarization measurements at 400mK using the Meservey–Tedrow technique in tunnel junctions with EuS barriers, a normal metal electrode (typically Ag or Au) and a superconducting Al counter-electrode (Figure 1.10). This technique consists in measuring the bias dependence of the tunnel conductance in tunnel junctions in which one electrode is superconducting, in a large magnetic field [80]. The field spin splits the DOS of the superconductor by Zeeman effect, which in turn selectively collects tunneling electrons according to their spin orientation. Fitting the obtained *G(V)* curves with Maki equations [81] yields the value of the tunnel current spin polarization. By virtue of this technique, very large spin-polarization values were found with Eu chalcogenide barriers, e.g. $P_F^{spin} = 0.85$ for EuS (see Figure 1.10 (d)). By applying a large magnetic field on Ag/EuSe/Al junctions, turning the EuSe into ferromagnetic, an even larger value of 97% was found [82]. The fabrication of high-quality EuO tunnel barriers is more complicated than that of EuS and EuSe, because Eu2O3 is more stable than EuO. Nevertheless, $P_F^{spin} = 0.29$ was reported in Al/EuO/Y junctions [83] (see Figure 1.10 (e)).
An intricate analysis of the bias dependence of the TMR (see Figure 1.10 (d)) demonstrated that after a decrease at low bias, the TMR increased again in the high bias range, as expected for spin-filter junctions from a simple tunnelling model (see e.g. [75] or the model included in [84]).

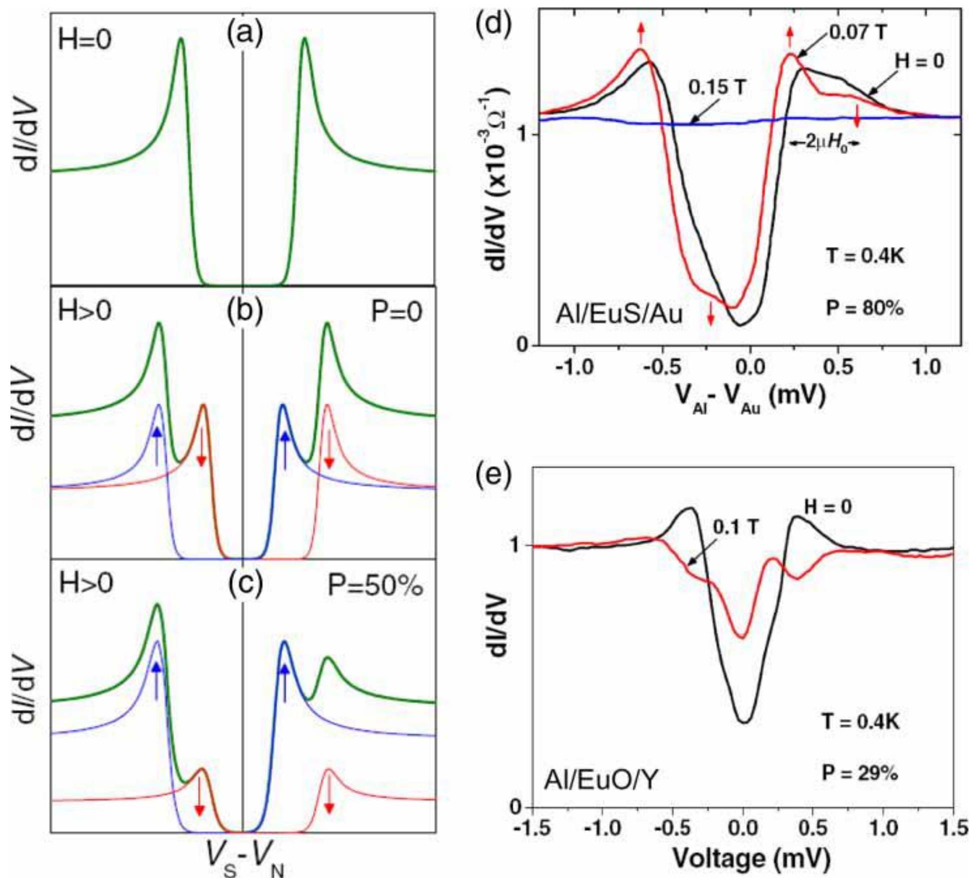

Figure 1.10 Meservey–Tedrow method. (a) Conductance (dI/dV) versus bias at zero field for a superconductor/insulator/metal tunnel junction. The superconducting energy gap is centred at $V=0$. There are two peaks at finite bias, corresponding to the quasiparticle DOS. (b) dI/dV in an applied field, showing Zeeman splitting of the DOS. The deconvolved spin-up (blue) and spin-down (red) DOS are shown, as well as the resulting measured curve (green), which is completely symmetric when $P = 0$, for a non-magnetic metal counter-electrode. (c) dI/dV in an applied field with $P = 50\%$, when the counter-electrode is a ferromagnet. The spin-up DOS is greater than the spin-down DOS, resulting in an asymmetric curve. Meservey–Tedrow mesaurements on (d) Au/EuS/Al junctions and (e) Y/EuS/Al junctions. J.S. Moodera et al., Journal of Physics: Condensed matter, 19, p. 165202, 2007 [74].

At this stage, we will explain the physics concerning tunnelling through ferroelectric insulator barriers.

1.8 Tunnelling through Ferroelectric Barriers

The main potential applications expected for ferroelectric barriers are the following, namely: Ferroelectric random access memories (FRAMs) [85] (whose information readout is destructive, and consequently, the initial orientation of ferroelectric polarization must be restored after reading, being time- and power-consuming) and ferroelectric tunnel junctions (FTJ), which is expected to yield exotic physical phenomena because of the interplay/coupling between tunnelling and ferroelectricity at the nanoscale.

Tsymbal and Kohlstedt [86] have proposed several possible theoretical mechanisms by means of which the tunnel current would be tuned by the reversal of polarization in the ferroelectric barrier (Figure 1.11).

The first theoretical mechanism proposes that the charges built up at the ferroelectric/electrode interface are only partially compensated by the electrodes in the order of the Thomas–Fermi screening length of the two different metals involved, causing an asymmetric variation of the electrostatic potential along the ferroelectric tunnel barrier (`1´ in Figure 1.11). Thereby, the screening and electrostatic variation are different at the two interfaces owing to the different metals employed as electrodes. The aforementioned situation can be modelled as a shift of the average barrier height in the order of $\phi \pm \Delta\phi$ due to the ferroelectric polarization switching [87–89], satisfying the equation:

$$\Delta\phi = \frac{dP(\delta_1 - \delta_2)}{2\epsilon_0\epsilon(\delta_1 + \delta_2)} \qquad (13)$$

Being P the remanent ferroelectric polarization, $\delta_{1,2}$ the Thomas–Fermi screening lengths of the different metallic electrodes, ϵ_0 the vacuum permittivity and ϵ the relative dielectric permittivity of the ferroelectric.

The second theoretical mechanism states that the interfacial density of states (DOS) is altered corresponding to the position of the ions situated in the last atomic layer in the ferroelectric, which in turn changes the tunnel current [90].

The third theoretical mechanism refers to the converse piezoelectric effect by means of the effective tunnel barrier width would be modified upon flipping the polarization vector direction. Due to the fact that the tunnel current has an exponential dependency on the barrier thickness, a significant change of the tunnel current is assumed [87–89, 91].

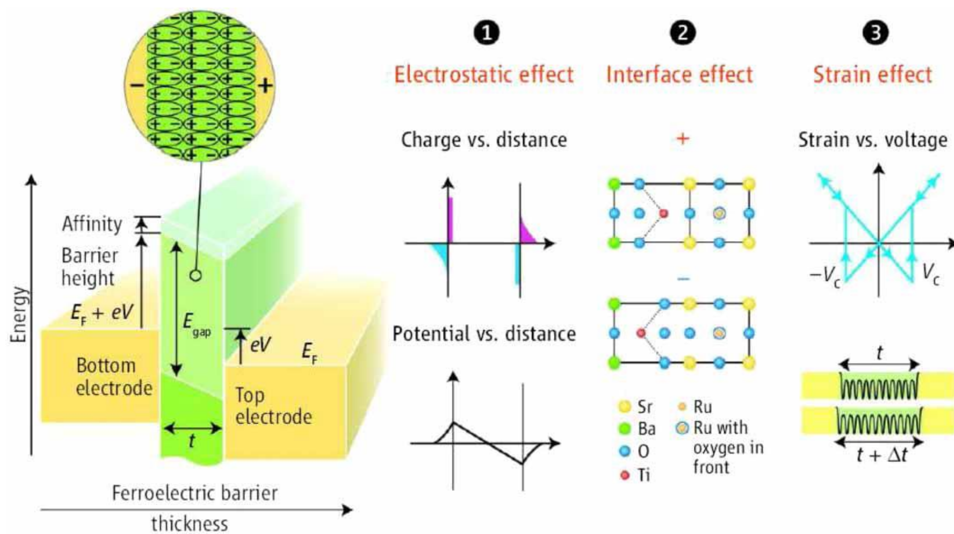

Figure 1.11 Schematic diagram of a tunnel junction, which consists of two electrodes separated by a nanometer-thick ferroelectric barrier (E_{gap} is the energy gap, E_F is the Fermi level, V is the applied voltage, V_C is the coercive voltage, t is the barrier thickness and Δt is the thickness variation under an applied electric field). E.Y. Tsymbal and H. Kohlstedt, Science, 313, p. 181, 2006 [86].

1.9 Magneto-electric Effects at Interfaces

Over the last decades, there have been theoretical predictions about the huge variations of magnetic properties which would take place at interfaces between ferroelectric and ferromagnetic materials. In other words, the ferroelectric polarization flipping can produce modifications of the spin polarization [92] (Figure 1.12). Extrapolated to tunnel junctions, ferroelectric controllable variations in the spin-dependent density of states (DOS) is supposed to tune the TMR or the spin injection efficiency [93].

In order to gain experimental insights in this interfacial magneto-electric coupling, professor Garcia et al. [94] made multiferroic tunnel junctions based on LSMO/BTO (1nm)/Fe. At temperatures of 4K, they measured huge negative TMR, corresponding to a negative spin polarization for the BTO/Fe interface. By performing short voltage pulses of $\pm 1V$, they measured reversible changes of the tunnel resistance provided with a TER of approximately 30%, showing a change of the tunnel current by the switch of the ferroelectric polarization of BTO. In addition, the TMR magnitude strongly varies in function of the direction of the ferroelectric polarization. Since the half-metallic LSMO/BTO spin-polarization is

hardly sensitive to the ferroelectric polarization switching [95], it is natural to think that only the BTO/Fe spin polarization is sensitive enough to the ferroelectric polarization switching. In order to quantify the aforementioned magneto-electric interplay, the researchers defined a term called "tunnel electro-magneto-resistance (TEMR)" with the following expression:

$$TEMR = \frac{TMR_{high} - TMR_{low}}{TMR_{low}} \qquad (14)$$

Being TMR_{high} and TMR_{low} the high and low absolute values of the TMR. To sum up, this interfacial magneto-electric coupling offers a low-power approach to control spintronic sources.

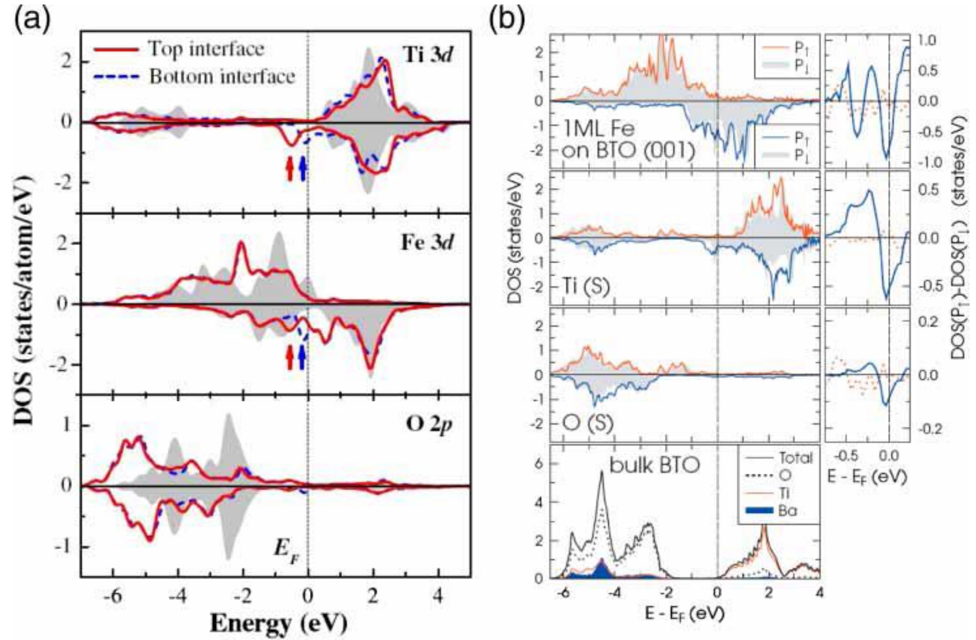

Figure 1.12 (a) Orbital-resolved DOS for interfacial atoms in a Fe = BaTiO3 multilayer for *m* = 4: (top) Ti 3d, (middle) Fe 3d and (bottom) O 2p. Majority- and minority-spin DOS are shown in the upper and lower panels, respectively. The solid and dashed curves correspond to the DOS of atoms at the top and bottom interfaces, respectively, with the ferroelectric polarization in the BTO pointing to the top. C.G. Duan et al., Physical Review Letter, 97, p. 047201, 2006 [92]. (b) Main panels on the left: electronic structure at the surface of Fe/BaTiO3(001): spin-resolved DOS of Fe in layer $S + 1$ (top) as well as of Ti (second from top) and O (third from top) in layer S for ferroelectric polarization pointing up (lines) and down (gray). Bottom: total and partial DOS of bulk BaTiO3, with the bottom of the conduction band taken as energy reference. The small panels on the right show the spin-resolved difference of the DOS for ferroelectric polarization pointing up and down of Fe, Ti and O (majority: dotted; minority: solid). M. Fechuer et al., Physical Review B, 78, p. 212406, 2008 [96].

Updating to nowadays, one of the most successful attainments was realized by professor Bibes et al. [97], the so-called “Ferroelectric Memristor”, which relies on the correlation between junction resistance and ferroelectric domain structure. Due to this fact, they were able to model the resistive switching behaviour using a simple model of domain nucleation and growth in a heterogeneous medium, qualifying the ferroelectric tunnel junctions (FTJ) as memristive devices.

The foremost motivation of this research is the possibility of integration given by the interplay between the electronic correlations, the ferroelectricity and the memristance effect in the tunnel junction device scale. This will bring about emergent chemical and physical properties which are not present in the above mentioned effects separately. The coupling regimes of the above mentioned effects (electronic correlations, ferroelectricity, memristance and tunnelling effects) will be discussed below in this PhD dissertation.

1.10 References

[1] Y. Tokura, N. Nagaosa. “Orbital physics in transition-metal oxides”. *Science* 288, 462 (2000).
[2] E. Dagotto. “Complexity in Strongly Correlated Electronic Systems”. *Science* 309, 257 (2005).

[3] E. Dagotto and Y. Tokura. “Strongly Correlated Electronic Materials: Present and Future”. MRS Bull. 33 (2008).

[4] M. Imada, A. Fujimori, Y. Tokura. “Metal-insulator transitions”. *Rev. Mod. Phys*. 70, 1039 (1998).
[5] J.B. Torrance, P. Lacorre, A.I. Nazzal, E.J. Ansaldo, Ch. Niedermayer. “Systematic study of insulator-metal transitions in perovskites RNiO3 (R = Pr, Nd, Sm, Eu) due to closing of charge-transfer gap”. *Phys. Rev. B* **45**, 8209 (1992).
[6] Transition Metal Compounds. Daniel I. Khomskii.
[7] Hemberger, J. Hemberger, A. Krimmel, T. Kurz, H.-A. Krug von Nidda, V. Yu. Ivanov, A. A. Mukhin, A. M. Balbashov, and A. Loidl. “Structural, magnetic, and electrical properties of single-crystalline $La_{1-x}Sr_xMnO_3$ ($0.4<x<0.85$)”. *Phys. Rev.* B 66, 094410 (2002).
[8] Dagotto, E. (2003), *Nanoscale Phase Separation and Colossal Magnetoresistance: The Physics of Manganites and Related Compounds*. Berlin: Springer-Verlag.

[9] N. A. Babushkina, L. M. Belova, O. Yu. Gorbenko, A. R. Kaul, A. A. Bosak, V. I. Ozhogin & K. I. Kugel. “Metal–insulator transition induced by oxygen isotope exchange in the magnetoresistive perovskite manganites”. *Nature* 391, 159, (1998).
[10] Wu, J. and Leighton, C. "Glassy ferromagnetism and magnetic phase separation in $La_{1-x}Sr_xCoO_3$”. *Phys. Rev.* B 67, 174408. (2003).
[11] Phelan, D. Despina Louca, S. Rosenkranz, S.-H. Lee, Y. Qiu, P. J. Chupas, R. Osborn, H. Zheng, J. F. Mitchell, J. R. D. Copley, J. L. Sarrao, and Y. Moritomo “Nanomagnetic Droplets and Implications to Orbital Ordering in $La_{1-x}Sr_xCoO_3$”. *Phys. Rev. Lett.* 96, 027201 (2006). D. Phelan, Despina Louca, K. Kamazawa, S.-H. Lee, S. N. Ancona, S. Rosenkranz, Y. Motome, M. F. Hundley, J. F. Mitchell, and Y. Moritomo. “Spin Incommensurability and Two Phase Competition in Cobaltites”. *Phys. Rev. Lett.* 97, 235501 (2006).
[12] A. Podlesnyak, S. Streule, J. Mesot, M. Medarde, E. Pomjakushina, K. Conder, A. Tanaka, M. W. Haverkort, and D. I. Khomskii. “Spin-State Transition in LaCoO3: Direct Neutron Spectroscopic Evidence of Excited Magnetic States”. *Phys. Rev. Lett.* 97, 247208 (2006).
[13] A. Podlesnyak, M. Russina, A. Furrer, A. Alfonsov, E. Vavilova, V. Kataev, B. Büchner, Th. Strässle, E. Pomjakushina, K. Conder, and D. I. Khomskii. “Spin-State Polarons in Lightly-Hole-Doped $LaCoO_3$”. *Phys. Rev. Lett.* 101, 247603. (2008).
[14] Bednorz, J. G. and Müller, K. A. “Possible highTc superconductivity in the Ba−La−Cu−O system”. *Zeitschr. für Physik B: Condens. Matter.* 64, 189. (1986).
[15] Anderson, P. W. (1997), *The Theory of Superconductivity in the High-Tc Cuprate Superconductors*. Princeton, NJ: Princeton University Press.
[16] Norman, M. R. and Pepin, C. “The electronic nature of high temperature cuprate superconductors”. *Rep. Progr. Phys.* 66, 1547 (2003).
[17] Plakida, N. (2010), “High-Temperature Cuprate Superconductors: Experiment, Theory and Applications”. Berlin: Springer-Verlag.
[18] Zhang, F. C. and Rice, T. M. “Effective Hamiltonian for the superconducting Cu oxides”. *Phys. Rev.* B37, 3759 (1988).
[19] Emery, V. J. and Reiter, G. “Mechanism for high-temperature superconductivity”. *Phys. Rev.* B 38, 4547 (1988).
[20] Dawber, Rabe, and Scott. Physics of thin-film ferroelectric oxides. Rev. Mod. Phys. 77 (2005).
[21] G. Catalan et al. Domain wall nanoelectronics. Rev. Mod. Phys. 84 (2012).

[22] Chun-Lin Jia, Shao-Bo Mi, Knut Urban, Ionela Vrejoiu, Marin Alexe and Dietrich Hesse. Atomic-scale study of electric dipoles near charged and uncharged domain walls in ferroelectric films. Nat. Mater. 7 (2008).
[23] Dmitri B. Strukov, Gregory S. Snider, Duncan R. Stewart & R. Stanley Williams. The missing memristor found. Nature 453 (2008).
[24] Chua, L. O. Memristor - the missing circuit element. IEEE Trans. Circuit Theory 18, 507–519 (1971).
[25] Hodgkin, A. L. & Huxley, A. F. A quantitative description of membrane current and its application to conduction and excitation in nerve. J. Physiol. 117, 500_544 (1952).
[26] Chua, L., Sbitnev, V. & Kim, H. Hodgkin Huxley axon is made of memristors. Int. J. Bifur. Chaos 22, 1_48 (2012).
[27] Waser, R. & Aono, M. Nanoionics-based resistive switching memories. Nat. Mater. 6, 833–840 (2007).
[28] I. Valov, E. Linn, S. Tappertzhofen, S. Schmelzer1, J. van den Hurk, F. Lentz & R. Waser. Nanobatteries in redox-based resistive switches require extension of memristor theory. Nat. Comm. (2013).
[29] M. Julliere. Tunneling between ferromagnetic films. Phys. Lett. A, 54, 3, 8, pp. 225-226 (1975).

[30] Manuel Bibes, Javier E. Villegas & Agnès Barthélémy (2011) Ultrathin oxide films and interfaces for electronics and spintronics, Advances in Physics, 60:1, 5 84, DOI: 10.1080/00018732.2010.534865.
[31] P. LeClair, *Fundamental aspects of spin polarized tunneling: Magnetic tunnel junctions and spin filters*, Eindhoven University of Technology, Eindhoven, the Netherlands, 2002.
[32] J.G. Simmons. “Generalized Formula for the Electric Tunnel Effect between Similar Electrodes Separated by a Thin Insulating Film”. J. Appl. Phys. 34 (1963), pp. 1793–1803.
[33] L. Glazman and K. Matveev. Inelastic tunneling across thin amorphous films. Sov. Phys. JETP 67 (1988), pp. 1276–1282.
[34] Y. Xu, D. Ephron, and M.R. Beasley. “Directed inelastic hopping of electrons through metal-insulator-metal tunnel junctions”. Phys. Rev. B 52 (1995), pp. 2843–2859.
[35] E.L.Wolf, *Principles of Electron Tunneling Spectroscopy*, Oxford University Press, NewYork, 1985.
[36] I. Giaever. “Energy Gap in Superconductors Measured by Electron Tunneling”. Phys. Rev. Lett. 5 (1960), pp. 147–148.

[37] T. Miyazaki and N. Tezuka. “Giant magnetic tunneling effect in Fe/Al_2O_3/Fe junction”. J. Magn. Magn. Mater. 139 (1995), pp. L231–L234.
[38] J.S. Moodera, L.R. Kinder, T.M.Wong, and R. Meservey. “Large Magnetoresistance at Room Temperature in Ferromagnetic Thin Film Tunnel Junctions”. Phys. Rev. Lett. 74 (1995), pp. 3273–3276.
[39] W.J. Gallagher and S.S.P. Parkin. “Development of the magnetic tunnel junction MRAM at IBM: from first junctions to a 16-Mb MRAM demonstrator chip”. IBM J. Res. Dev. 50 (2006), pp. 5–23.
[40] http://www.freescale.com.
[41] R.A. de Groot, F.M. Mueller, P.G. van Engen, and K.H.J. Buschow. “New Class of Materials: Half-Metallic Ferromagnets”. Phys. Rev. Lett. 50 (1983), pp. 2024–2027.
[42] M.H. Jo, N.D. Mathur, N.K. Todd, and M.G. Blamire. “Very large magnetoresistance and coherent switching in half-metallic manganite tunnel junctions”. Phys. Rev. B 61 (2000), pp. R14905–R14908.
[43] J. O’Donnell, A.E. Andrus, S. Oh, E.V. Colla, and J.N. Eckstein. “Colossal magnetoresistance magnetic tunnel junctions grown by molecular-beam epitaxy”. Appl. Phys. Lett. 76 (2000), pp. 1914–1916.
[44] M. Bowen, M. Bibes, A. Barthélémy, J.P. Contour, A. Anane, Y. Lemaître, and A. Fert. “Nearly total spin polarization in $La_{2/3}Sr_{1/3}MnO_3$ from tunneling experiments”. Appl. Phys. Lett. 82 (2003), pp. 233–235.
[45] Y. Ishii, H. Yamada, H. Sato, H. Akoh, Y. Ogawa, M. Kawasaki, and Y. Tokura. “Improved tunneling magnetoresistance in interface engineered (La, Sr)MnO_3 junctions”. Appl. Phys. Lett. 89 (2006), p. 042509.
[46] E.T. Wertz and Q. Li. “Magnetoresistance after initial demagnetization in La0.67Sr0.33MnO3⁄SrTiO3⁄La0.67Sr0.33MnO3 magnetic tunnel junctions”. Appl. Phys. Lett. 90 (2007), p. 142506.
[47] V. Garcia, M. Bibes, A. Barthélémy, M. Bowen, E. Jacquet, J.P. Contour, and A. Fert. “Temperature dependence of the interfacial spin polarization of $La_{2/3}Sr_{1/3}MnO_3$”. Phys. Rev. B 69 (2004), p. 052403.
[48] M. Bibes and A. Barthélémy. “Oxide Spintronics”. IEEE Trans. Electron Dev. 54 (2007), pp. 1003–1023.
[49] W.H. Butler, X.G. Zhang, T.C. Schulthess, and J.M. MacLaren. “Spin-dependent tunneling conductance of Fe|MgO|Fe sandwiches”. Phys. Rev. B 63 (2001), p. 054416.
[50] J. Mathon and A. Umerski. “Theory of tunneling magnetoresistance of an epitaxial Fe/MgO/Fe(001) junction”. Phys. Rev. B 63 (2001), p. 220403.

[51] X.G. Zhang and W.H. Butler. “Band structure, evanescent states, and transport in spin tunnel junctions”. J. Phys., Condens. Matter 15 (2003), pp. R1603–R1639.
[52] S.Yuasa, A. Fukushima, H. Kubota, Y. Suzuku, and K. Ando. ″Giant tunneling magnetoresistance up to 410% at room temperature in fully epitaxial Co⁄MgO⁄Co magnetic tunnel junctions with bcc Co(001) electrodes”. Appl. Phys. Lett. 89 (2006), p. 042505.
[53] S.S.P. Parkin, C. Kaiser,A. Panchula, P.M. Rice, B. Hughes, M. Samant, and S.-H.Yang. ″Giant tunnelling magnetoresistance at room temperature with MgO (100) tunnel barriers”. Nat. Mater. 3 (2004), pp. 862–867.
[54] S.Yuasa, T. Nagahama, A. Fukushima, Y. Suzuki, and K. Ando. “Giant room-temperature magnetoresistance in single-crystal Fe/MgO/Fe magnetic tunnel junctions”. Nat. Mater. 3 (2004), pp. 868–871.
[55] S. Ikeda, J. Hayakawa,Y. Ashizawa,Y. Lee, K. Miura, H. Hasegawa, M. Tsunoda, F. Matsukura, and H. Ohno. “Tunnel magnetoresistance of 604% at 300K by suppression of Ta diffusion in CoFeB⁄MgO⁄CoFeB pseudo-spin-valves annealed at high temperature”. Appl. Phys. Lett. 93 (2008), p. 082508.
[56] X.-G. Zhang and W.H. Butler. “Large magnetoresistance in bcc Co⁄MgO⁄Co and FeCo⁄MgO⁄FeCo tunnel junctions”. Phys. Rev. B 70 (2004), p. 172407.
[57] S. Yuasa, A. Fukushima, T. Nagahama, K. Ando, and Y. Suzuki. ″High Tunnel Magnetoresistance at Room Temperature in Fully Epitaxial Fe/MgO/Fe Tunnel Junctions due to Coherent Spin-Polarized Tunneling”. Jpn. J. Appl. Phys. 43 (2004), pp. L588– L590.
[58] K. Benthemvan, C. Elsasser, and R.H. French, “Bulk electronic structure of $SrTiO_3$: Experiment and theory”. J. Appl. Phys. 90 (2001), pp. 6156–6164.
[59] D. Kan, T. Terashima, R. Kanda, A. Masuno, K. Tanaka, S. Chu, H. Kan, A. Ishizumi, Y. Kanemitsu, Y. Shimakawa and M. Takano. “Blue-light emission at room temperature from Ar^+-irradiated $SrTiO_3$”. Nat. Mater. 4 (2005), pp. 816–819.
[60] C. Tiusan, J. Faure-Vincent, C. Bellouard, M. Hehn, E. Jouguelet, and A. Schuhl. “Interfacial Resonance State Probed by Spin-Polarized Tunneling in Epitaxial Fe/MgO/Fe Tunnel Junctions”. Phys. Rev. Lett. 93 (2004), p. 106602.
[61] M. Bowen, A. Barthélémy, V. Bellini, M. Bibes, P. Seneor, E. Jacquet, J.P. Contour, and P.H. Dederichs. “Observation of Fowler–Nordheim hole tunneling across an electron tunnel junction due to total symmetry filtering”. Phys. Rev. B 73 (2006), p. 140408.
[62] J.P. Velev, K.D. Belashchenko, D.A. Stewart, M. Schilfgaardevan, S.S. Jaswal, and E.Y. Tsymbal. “Negative Spin Polarization and Large Tunneling

Magnetoresistance in Epitaxial Co|$SrTiO_3$|Co Magnetic Tunnel Junctions”. Phys. Rev. Lett. 95 (2005), p. 216601.
[63] J.M. De Teresa, A. Barthélémy, A. Fert, J.P. Contour, R. Lyonnet, F. Montaigne, P. Seneor, and A. Vaurès. “Inverse Tunnel Magnetoresistance in Co/SrTiO3/La0.7Sr0.3MnO3: New Ideas on Spin-Polarized Tunneling”. Phys. Rev. Lett. 82 (1999), pp. 4288–4291.
[64] J.M. De Teresa, A. Barthélémy,A. Fert, J.P. Contour, F. Montaigne, and P. Seneor. “Role of metal-oxide interface in determining the spin polarization of magnetic tunnel junctions”. Science 286 (1999), pp. 507–509.
[65] J. Hayakawa, S. Kokado, K. Ito, M. Sugiyama, H. Asano, M. Matsui, A. Sakuma, and M. Ichimura. “The origin of bias-voltage dependence in CoFe/$SrTiO_3$/$La_{0.67}Sr_{0.33}MnO_3$ magnetic tunnel junctions”. Jpn. J. Appl. Phys. 41 (2002), pp. 1340–1342.
[66] I.J. Vera Marún, F.M. Postma, J.C. Lodder, and R. Jansen. “Tunneling magnetoresistance with positive and negative sign in $La_{0.67}Sr_{0.33}MnO_3$/$SrTiO_3$/Co junctions”. Phys. Rev. B 76 (2007), p. 064426.
[67] R. Meservey and P.M. Tedrow. “Spin-polarized electron tunnelling”. Phys. Rep. 238 (1994), pp. 173–243.
[68] E.Y. Tsymbal and D.G. Pettifor, J. Phys., Condens. Matter 9 (1997), pp. L411–L417.
[69] I.I. Oleinik, E.Y. Tsymbal, and D.G. Pettifor. “Structural and electronic properties of Co/Al_2O_3/Co magnetic tunnel junction from first principles”. Phys. Rev. B 62 (2000), pp. 3952–3959.
[70] I.I. Oleinik, E.Y. Tsymbal, and D.G. Pettifor. “Atomic and electronic structure of Co/$SrTiO_3$/Co magnetic tunnel junctions”. Phys. Rev. B 65 (2001), p. 020401.
[71] I.I. Oleynik and E.Y. Tsymbal. “Atomic, electronic, and magnetic properties of magnetic tunnel junctions”. J. Appl. Phys. 93 (2003), pp. 6429–6431.
[72] M. Bibes, M. Bowen,A. Barthélémy,A.Anane, K. Bouzehouane, C. Carrétéro, E. Jacquet, J.P. Contour, and O. Durand. “Growth and characterization of TiO_2 as a barrier for spin-polarized tunnelling”. Appl. Phys. Lett. 82 (2003), pp. 3269–3271.
[73] V. Garcia, M. Bibes, J.L. Maurice, E. Jacquet, K. Bouzehouane, J.P. Contour, and A. Barthélémy. “Spin-dependent tunneling through high-k $LaAlO_3$”. Appl. Phys. Lett. 87 (2005), p. 212501.
[74] J.S. Moodera, T.S. Santos, and T. Nagahama. “The phenomena of spin-filter tunnelling”. J. Phys., Condens. Matter 19 (2007), p. 165202 (24 pp.).
[75] A. Saffarzadeh. “Spin-filter magnetoresistance in magnetic barrier junctions”. J. Magn. Magn. Mater. 269 (2004), pp. 327–332.

[76] U. Lüders, M. Bibes, S. Fusil, K. Bouzehouane, E. Jacquet, C. B. Sommers, J.-P. Contour, J.-F. Bobo, A. Barthélémy, A. Fert and P. M. Levy. "Bias dependence of tunnel magnetoresistance in spin filtering tunnel junctions: Experiment and theory". Phys. Rev. B 76 (2007), p. 134412.
[77] A. Mauger and C. Godart. "The magnetic, optical, and transport properties of representatives of a class of magnetic semiconductors: The europium chalcogenides". Phys. Rep. 141 (1986), pp. 51–176.
[78] J.S. Moodera, X. Hao, G.A. Gibson, and R. Meservey. "Electron-Spin Polarization in Tunnel Junctions in Zero Applied Field with Ferromagnetic EuS Barriers". Phys. Rev. Lett. 61 (1988), pp. 637–640.
[79] X. Hao, J.S. Moodera, and R. Meservey. "Spin-filter effect of ferromagnetic europium sulfide tunnel barriers". Phys. Rev. B 42 (1990), pp. 8235–8243.
[80] R. Meservey and P.M. Tedrow. "Spin-polarized electron tunneling". Phys. Rep. 238 (1994), pp. 173–243.
[81] K. Maki. "The Behavior of Superconducting Thin Films in the Presence of Magnetic Fields and Currents". Prog. Theor. Phys. 31 (1964), pp. 731–741.
[82] J.S. Moodera, R. Meservey, and X. Hao. "Variation of the electron-spin polarization in EuSe tunnel junctions from zero to near 100% in a magnetic field". Phys. Rev. Lett. 70 (1993), pp. 853–856.
[83] T.S. Santos and J.S. Moodera. "Observation of Spin-Filtering with Ferromagnetic Europium Monoxide Tunnel Barrier". Phys. Rev. B 69 (2004), p. 241203.
[84] T. Nagahama, T.S. Santos, and J.S. Moodera. "Enhanced Magnetotransport at High Bias in Quasimagnetic Tunnel Junctions with EuS Spin-Filter Barriers". Phys. Rev. Lett. 99 (2007), p. 016602.
[85] J.F. Scott and C.A. Paz de Araujo. "Ferroelectric memories". Science 246 (1989), pp. 1400–1405.
[86] E.Y. Tsymbal and H. Kohlstedt. "Tunneling Across a Ferroelectric". Science 313 (2006), pp. 181–183.
[87] H. Kohlstedt, N.A. Pertsev, J. Rodríguez Contreras, and R.Waser. "Theoretical current-voltage characteristics of ferroelectric tunnel junctions". Phys. Rev. B 72 (2005), p. 125341.
[88] M.Y. Zhuravlev, R.F. Sabirianov, S.S. Jaswal, and E.Y. Tsymbal. "Giant electroresistance in ferroelectric tunnel junctions". Phys. Rev. Lett. 94 (2005), p. 246802.
[89] K.M. Indlekofer and H. Kohlstedt. "Simulation of quantum dead-layers in nanoscale ferroelectric tunnel junctions". Europhys. Lett. 72 (2005), pp. 282–286.

[90] J.P.Velev, C.G. Duan, K.D. Belashchenko, S.S. Jaswal, and E.Y. Tsymbal. “Effect of Ferroelectricity on Electron Transport in Pt/BaTiO3/Pt Tunnel Junctions”. Phys. Rev. Lett. 98 (2007), p. 137201.
[91] Y. Zheng and C.H. Woo. “Giant piezoelectric resistance in ferroelectric tunnel junctions”. Nanotechnology 20 (2009), p. 075401 (6 pp.).
[92] C.G. Duan, S.S. Jaswal, and E.Y. Tsymbal. “Predicted Magnetoelectric Effect in Fe/BaTiO3 Multilayers: Ferroelectric Control of Magnetism”. Phys. Rev. Lett. 97 (2006), p. 047201.
[93] M.Y. Zhuravlev, S.S. Jaswal, E.Y. Tsymbal, and R.F. Sabirianov. “Ferroelectric switch for spin injection”. Appl. Phys. Lett. 87 (2005), p. 222114.
[94] V. Garcia, M. Bibes, L. Bocher, S. Valencia, F. Kronast, A. Crassous, X. Moya, S. Enouz-Vedrenne, A. Gloter, D. Imhoff, C. Dernalot, N.D. Mathur, S. Fusil, K. Bouzehouane, and A. Barthélémy. “Ferroelectric Control of Spin Polarization”. Science 327 (2010), pp. 1106–1110.
[95] J.D. Burton and E.Y. Tsymbal. “Prediction of electrically induced magnetic reconstruction at the manganite/ferroelectric interface”. Phys. Rev. B 80 (2009), p. 174406.
[96] M. Fechner, I.V. Maznichenko, S. Ostanin, A. Ernst, J. Henk, P. Bruno, and I. Mertig. “Magnetic phase transition in two-phase multiferroics predicted from first principles”. Phys. Rev. B 78 (2008), p. 212406.
[97] André Chanthbouala, Vincent Garcia, Ryan O. Cherifi, Karim Bouzehouane, Stéphane Fusil, Xavier Moya, Stéphane Xavier, Hiroyuki Yamada, Cyrile Deranlot, Neil D. Mathur, Manuel Bibes, Agnès Barthélémy and Julie Grollier. “A ferroelectric memristor”. Nat. Mater. 11 (2012).
[98] J. Tornos, “Spin-dependent transport in oxide multiferroic tunnel junctions”, Ph. D. Thesis, Universidad Complutense de Madrid (2014).

Chapter 2: Experimental and Simulation Techniques

2.1 Sample growth: Sputtering

Samples are prepared by sputter deposition in high O_2 pressure. This method is based on the ballistic impact of atoms against a substrate after being removed from a material source. The sputtered ions come from targets made of the stoichiometric compound while the oxygen plays the role of the sputtering element. In our case the substrate is placed on a heater plate below the targets. The growth takes place inside a chamber in which a high vacuum of about 10^{-6} mbar is previously realized. The chamber, shown in Fig. 2.1, is connected to a turbo-molecular pump supported by a membrane pump. A constant oxygen flow is injected and controlled by a system of needle valves. Since the sputter yield depends on the energy of the incoming O_2 ion and the source atom species, the material removed from the target will deposit on the substrate in a manner, which strongly depends on several controllable parameters such as the temperature of the substrate, the applied radio frequency power and the pressure inside the chamber. In order to grow epitaxial oxide heterostructures, high temperature and pressure are usually required. All the samples studied in this work have been grown on $SrTiO_3$ substrate (100)-oriented. The high oxygen pressure (3.2 mbar) applied during the deposition, favours a complete thermalization of the extracted species and at the same time prevents them from back-sputtering and loss of oxygen in the final crystal structure. The substrate temperature is kept at 900º C. Under these conditions the deposition rate is slow (0.3nm/min) and ensures the epitaxial growth of the sample. To preserve the optimal oxygen content of the structure an *in-situ* annealing at 900 mbar O_2 pressure is necessary. The chamber is oxygenated at 800º C and the annealing is made at 750º C during 1 hour.

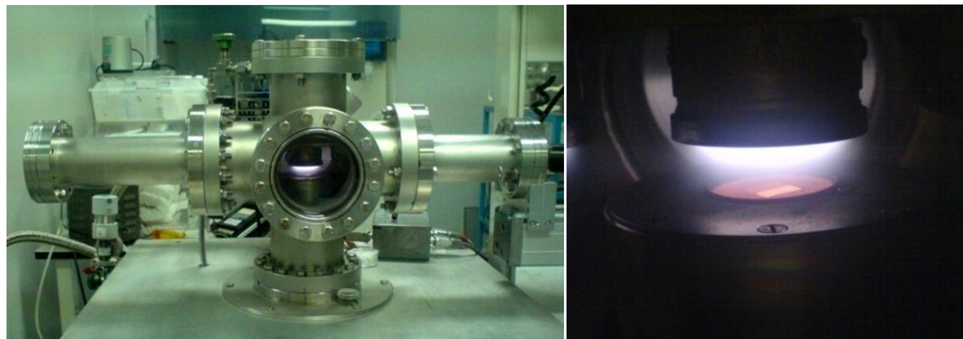

Fig. 2.1 (Left) View of the sputtering chamber. The targets are mounted on a remote controlled arm to switch between the different materials. (Right) Enlarged view of the powered target on the substrate.

2.2 Structural characterization: XRR, XRD

X-ray reflectivity (XRR) and diffraction (XRD) patterns allowed determining the thickness and the structural quality of our samples. XRR and XRD measurements have been carried out at CAI de Difracción de Rayos-X (UCM), with a Philips X'pert MRD diffractometer, using a Cu tube as X-ray source (λx = 0.15418 nm) operating at 45 kV and 40 mA. All the measurements of XRR and XRD were performed by Fernando Gallego and Javier Tornos.

2.2.1 X-ray reflectivity

The coherent and collimated radiation coming from an X-ray source is reflected at the interface between layers with different electronic densities (the substrate, the film). The different refractive indexes induce a change in the path length of the X-ray and consequently a constructive/destructive interference of the different reflected beams. In an analogous way, the interference resulting from a layered structure produces oscillation in the reflectivity pattern. This pattern is obtained by measuring the reflected intensity as a function of the incident angle (2θ) through a detector which is set in θ-2θ (Bragg) geometry with respect to the source (See Figures 2.2 and 2.3).

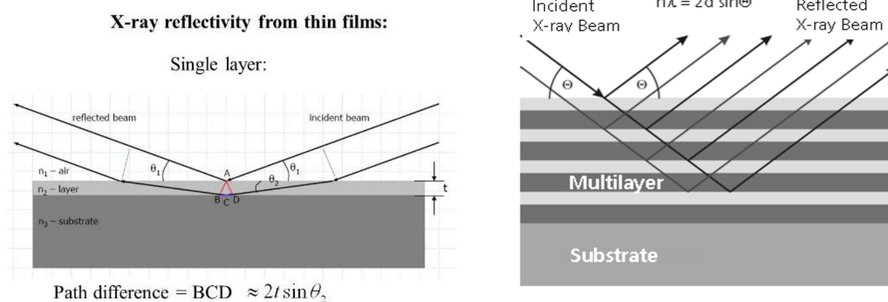

Fig. 2.2 Schematic diagram of the θ-2θ geometry

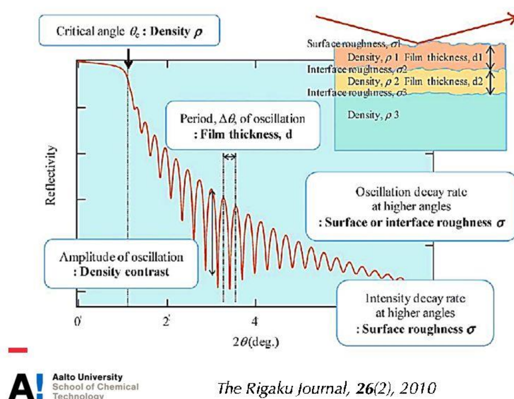

Fig. 2.3 Information collected by X ray reflectivity

Reflectivity scans showed in this work are usually taken up to an angle of $2\theta \sim 10$ degrees. In this range of angle we are able to see finite size oscillations ($2\theta < 7º$), related to the total thickness of the sample, and the first order Bragg (diffraction) peak of the YBCO, centered around $2\theta = 7.5º$, accompanied by satellite diffraction peaks, as shown in Fig. 4. The period of the finite size oscillations is inversely related to the thickness d of the whole sample. By indexing the position of the maxima and minima (n = 1, 2, ...) we can calculate the total thickness using the formula:

$$(sin\theta)^2 = \left[\frac{(n-k)\lambda_X}{2d}\right]^2 + 2\delta$$

Where k=0 correspond to a minimum and k=1/2 to a maximum. δ is the real part of the refraction index:

$$n = 1 - \frac{\rho_n r_e \lambda_X}{2\pi}(f_0 + \Delta f' - i\Delta f'') = 1 - \delta + i\beta$$

Where ρ_n is the electronic density, r_e is the electron radius, f_0 is the atomic dispersion factor, $\Delta f'$ and $\Delta f''$ are corrections due to the anomalous dispersion [1, 2]. In Fig. 2.4 we show some representative curves of thin films. The width of the diffraction peak is inversely proportional to its thickness, so thinner sample will show a wide less intense peak. The thickness can be calculated using the Scherrer´s formula:

$$\xi = \frac{0.9\lambda_X}{b\cos\theta}$$

Where λ_X is the X-ray wavelength, b is the peak width at half maximum (FWHM) and θ the corresponding angle.

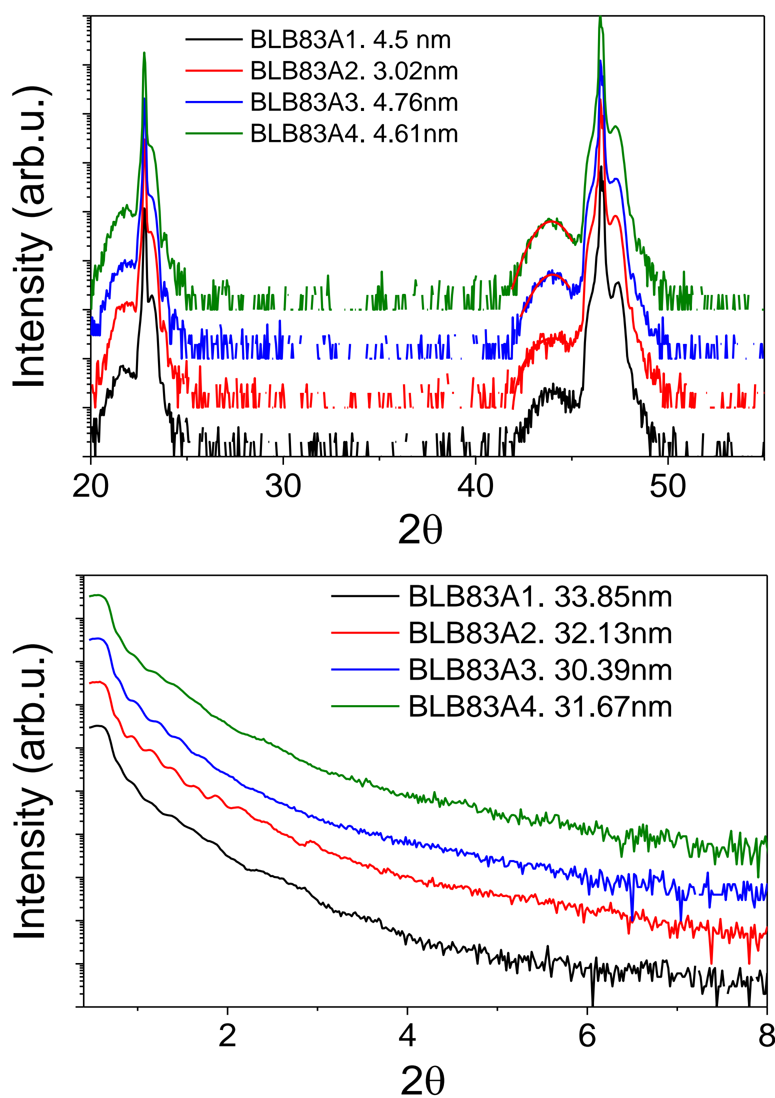

Fig. 2.4 XRD and XRR representative curves of thin films.

2.3 Scanning Transmission Electron Microscopy

Scanning transmission electron microscopy (STEM) is a powerful technique which can map the atomic and electronic structure of complex oxides with sub-Ångstrom spatial resolution and sub-eV energy resolution. All the STEM measurements in this thesis were done at the S.J. Pennycook group (STEM Group)

of the Oak Ridge National Laboratory by Gabriel Sánchez-Santolino, Mariona Cabero and Maria Varela, using an aberration corrected Nion UltraSTEM100 and a Nion UltraSTEM200 equipped with GatanEnfina and Enfinium spectrometers, respectively.

In the scanning-transmission electron microscope (see Figure 2.5), a field-emission source and strong electromagnetic lenses are used to form a small probe that can be raster-scanned across the specimen [5]. Images are obtained serially as the probe is scanned pixel-by-pixel using a number of detectors with different geometries. The key advantage of STEM is the ability to detect multiple signals simultaneously.

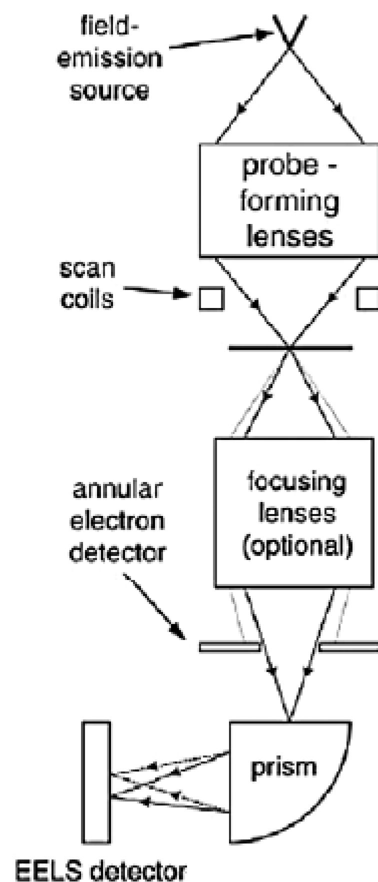

Figure 2.5 Schematic of a scanning-transmission electron microscopy system. From ref [3].

A high angle annular dark field (HAADF) detector is normally used for Z-contrast imaging. A dark-field image, representing transmitted electrons scattered through relatively large angles, is formed by feeding the signal from a ring-shaped (annular) detector to a display device scanned in synchronism with the probe scan (Figure 2.6). Simultaneously, electron energy-loss spectra (EELS) can be read out at each probe position (pixel), resulting in a large spectrum-image data set that can be processed off-line [7]. The dark field images, collected over a wide range of scattering angles, show strong atomic number contrast. The fact that the Z-contrast images are directly interpretable makes this technique very appealing.

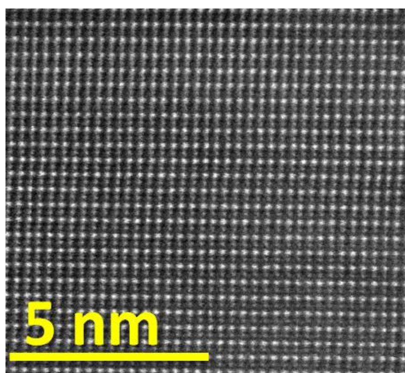

Fig. 2.6 High magnification HAADF image of a LSMO/BTO heterostructure.

The STEM geometry can also provide atomic resolution EELS [4-5]. In many ways, EELS is formally equivalent to X-ray absorption spectroscopy. Electrons scattered through smaller angles enter a single prism spectrometer, which produces an energy-loss spectrum (EEL spectrum) for any given position of the probe on the specimen [6]. With modern microscopes it is possible to obtain an EEL spectrum from each atomic column (Figure 2.7); this makes this technique a powerful tool to investigate the chemical composition of interfaces. EELS provides a tool to map terminations or inter-diffusion between different interfaces of an oxide thin-film or multilayer. The high energy resolution of this technique (0.3 eV for a cold field emission gun) also allows the study of the fine structure of the absorption edges. This way, we can investigate electronic properties. EELS edges are a result of the excitations of inner shell electrons into occupied levels above the Fermi level. Therefore, the EELS fine structure ensues from the material's unoccupied density of states and it can be used to probe electronic properties. In complex oxides, properties such as the transition metal oxidation state can be measured from the EELS fine structure of the transition metal L2,3 edge and the O K edge [7-9].

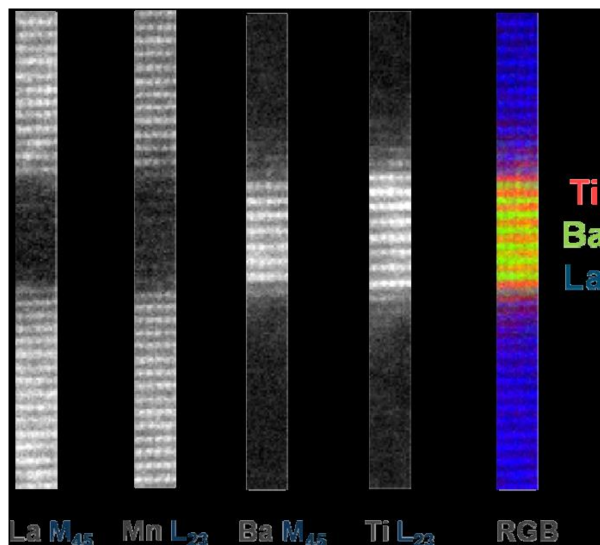

Figure 2.7 (from left to the right) Atomic elemental maps corresponding to the La M4,5, Mn L2,3, Ba M4,5, Ti L2,3 signal, and false color image where three atomic resolution images have been overlayed: a Ti L2,3 image in red, a La M4,5 image in blue, and Ba M4,5,image in green (RGB).

2.4 Tunnel junction patterning

Thin-films must be geometrically defined laterally or patterned in the layer plane in order to obtain tunnel junction devices.

2.4.1 Optical Lithography

Photolithography is a technique used to produce high precision two-dimensional patterns in the microscopic scale on a photoresist material [10], it is the equivalent to the negative used in photography. These patterns are optically projected from a master pattern in a photo-mask, which are generally made of a thin chromium or ferrite layer on a glass or quartz plate. Masks patterns commonly fabricated using high resolution lithography process using electron beam lithography. Printing of this negative mask requires physical transference of the pattern to the film surface in question through the use of a photo-resist which is sensible to the UV radiation. Two types of photo-resist are available and their behaviours are distinguished in the effect of the light. The positive photoresist faithfully reproduces the opaque

mask pattern; in this case light exposure causes scission of polymerized chains rendering the resist soluble in the developer. Alternatively, negative resists reproduce the transparent portion of the mask pattern because photon-induced polymerization leaves a chemically inert resist layer behind [11]. The resist layer deposited on the sample surface must be thin enough to obtain high lateral resolution. This thickness should be near few microns or less. To obtain these thicknesses a spinner system, which achieves high speeds near 6000 rpm, is used.

Figure 2.8 Photograph of a Karl Suss alignment equipment.

The core of the microlithography process is the exposure system. Figure 2.8 shows the alignment and exposure system, it consists of a lithographic lens system to collimate UV light from a Hg lamp, a mask holder, an optical microscope, and a sample positioning system with micrometers screws.

2.4.2 From bilayer to tunnel junction device

In order to increase the number of measureable tunnel junction per sample we have reduced the number of technological steps comparing with previous work in our

group [12]. It also reduces the time of patterning process allowing us to measure more samples.

First at all, we clean the sample surface with subsequent ultrasonic baths of acetone and propanol, after that, we deposit SPR-700 Photo-Resist to cover the sample surface. Then, we spin the sample to near 6000 rpm in a spinner system in order to distribute the SPR-700 Photo-Resist homogeneusly and expose the sample to UV radiation protected with the mask where the junction patterns are to be transferred to the sample. Finally, we develop the sample with the junction pattern using "MF319 Developer" solvent.

2.5 Resistance Measurements

For our low temperature resistance measurements we used a closed-cycle Cryophysics helium refrigerator which works with the expansion of highly-pure He-gas compressed in a Gifford McMahon cycle. The expansion through the capillaries undergoes two steps at 50 K and at 8.5 K. The sample is mounted onto a cooled copper piece in contact with the second cooling step. The system is evacuated by a rotary pump capable of a pressure down to 10 mTorr, measured with a Pirani vacuum sensor. The best temperature was 14 K. A silicon diode thermometer is in contact with the sample holder calibrated for measuring between 10 and 325 K. The system is also equipped with a heater controlled by a Lake Shore 330-11 temperature controller which permits to control the sample's temperature between room temperature and 14 K with 10 mK accuracy. Microcoaxial wires connect the different parts for low noise measurements. For magnetoresistance measurements we used an electromagnet (with a 10cm separation between the magnetic cores) which provided a magnetic field in the range of ± 4200Oe.

2.5.1 Direct Current

In the case of tunnel junctions (current perpendicular to plane) measurement we use a 2-points method because the junction resistance are much higher than the electrode, and the silver/manganite is an ohmic contact. The main instrument used was a Keithley 2400 sourcemeter, capable of apply voltage between 5μV and 210V and measure current from 10pA to 1.055A.

2.5.2 Impedance Spectroscopy. Alternating Current

The impedance analyser [13] used in these experiments is HP 4284 model (Figure 2.9). The measurement principle of the electrical impedance is the following:
First of all, we apply to the sample a sinusoid (f frequency) voltage input signal, whose amplitude is V_{osc}. Afterwards, we measure the intensity current output signal whose amplitude is I_{osc}. Considering the linear response and neglecting superior harmonics, the output signal is a sinusoid (f frequency) current endowed with a phase difference θ angle respect to the sinusoid voltage. The electrical impedance is a complex number whose module is the amplitude ratio and angle the phase difference voltage-current:

$$|Z| = \frac{V_{osc}}{I_{osc}} \ ; \ \frac{Z''}{Z'} = tan\theta$$

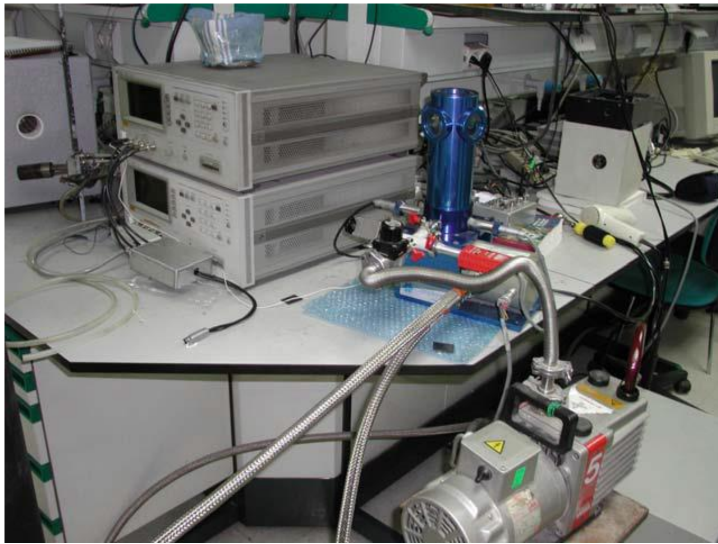

Figure 2.9 Impedance Analyser.

The derivative of the current and the charge respect to the voltage gives the differential conductance and differential capacitance in our samples, which are tunnel junctions endowed with memristive properties.
In particular, the memristor measurements consists of DC voltage bias hysteresis with a sweep in frequencies (20 Hz to 1 MHz) and temperatures (50 K to 260 K) in addition to the oscillation voltage V_{osc} required to measure the electrical impedance.

2.6 Density Functional Theory

2.6.1 Introduction

The electron correlation phenomena that occur when two dissimilar materials are brought into contact in an interface, result in emergent electronic properties that are not present in the separated bulk materials, such as tunnel conduction and spin filtering to name a few. This involves processes at the atomic length scale which are ruled by quantum mechanics laws. The Schrödinger equation is the simplest expression that compiles all the relevant interactions, and even in this simplest case, the solution may be extraordinarily complex when a large number of atoms need to be considered [14].

Although Schrödinger equation was formulated early in the 20th century, at present there is still a large effort to obtain new solutions. One of the most extended and successful solutions of the Schrödinger equation was developed in 1964 when Hohenberg and Kohn postulated the two theorems [15] which constitute the basis of the Density Functional Theory (DFT) [16]. Despite DFT has been a very popular method for calculations in solid state physics since the 1970s, it was not increasingly employed until the 1990s when it started to be applied in quantum chemistry, mainly due to the refinements introduced to better model the exchange-correlation interactions.

The calculations presented here are based on DFT. In the following the state of art of DFT calculations is discussed and explained in terms of the approximations that are considered.

2.6.2 Quantum mechanical Many-Body problem

The Schrödinger equation expresses within a Quantum Mechanics framework the solution of the Hamiltonian (H) of a system formed by electrons and ionic nuclei mutually interacting. This equation has the following expression [17]:

$$H\Psi = E\Psi$$

Where the wave function (WF) $\Psi = \Psi(x_1, \dots, x_N; R_1, \dots, R_M)$ depends on the coordinates of the N electrons x_i $(i < N)$ and M ions x_j $(j < M)$, and E is the

system energy, Ψ and E are the solutions of the Schrödinger equation, while H contains both electronic and ionic terms, satisfying the equation:

$$H = T_e + T_I + C_I + C_e + V$$
$$= -\frac{1}{2}\sum_{i=1}^{N} \nabla_i^2 - \frac{1}{2}\sum_{A=1}^{M} \frac{\nabla_A^2}{M_A} + \sum_{A,B} \frac{(Z_A Z_B)}{R_{AB}} + \sum_{i,j} \frac{1}{r_{ij}} - \sum_{i,A} \frac{Z_A}{r_{iA}}$$

Where the first two terms are the kinetic energies of the electrons and the ions, respectively, the third and fourth terms are the Coulomb repulsions between ions and between electrons respectively and the fifth term is the Coulomb attraction between electrons and ions.

The situation, as described above, express a many body problem that was simplified by Born and Oppenheimer [18], considering the nucleus stationary, so that the nuclear contributions can be solved by classical expressions, while the electrons are mobile and treated quantum-mechanically. This is justified by the big difference of mass and mobility between them. Thus, the quantum mechanical problem of nuclei and electrons is reduced from 3N+3M to 3N coordinate variables describing the stationary electronic state.

Thus, the Schrödinger equation can be written as a set of electronic terms in the following way:

$$H\Psi = [T + V + U]\Psi = -\frac{1}{2}\sum_{i=1}^{N} \nabla_i^2 + \sum_{i=1}^{N} V(r_i) + \sum_{i,j} U(r_i, r_j) = E\Psi$$

Where T and U are the kinetic and e-e interaction universal operators, while V is system dependent or non-universal term.

2.6.3 Density Functional Theory

DFT provided a way to systematically map the many-body problem, with U, onto a single-body problem without U, which was based on the introduction of the density variable:

$$n = |\Psi * \Psi^*| = N \int d^3r_2 \int d^3r_3 \int d^3r_N \, \Psi(r_1, \ldots, r_N) * \Psi^*(r_1, \ldots, r_N)$$

Hohenberg and Kohn proved in 1964 [15] with their first DFT theorem, by virtue of which the former expression can be reversed and write Ψ as a functional of the electronic density $\Psi(n)$. In consequence, any other observable is also a functional of n. In particular, Hohenberg and Kohn's second theorem states that the total energy of an electronic system is an universal functional of the density $E\{n(r)\}$, and that the global energy minimum E_0 corresponds to the ground state charge density $n_0(r)$ [19].

This new theory was just previous to what Kohn and Sham (1965) [20] proposed, in order to change from a many-body electron interacting problem, with an external potential, onto a non-interacting electron problem with an effective potential. The Kohn-Sham equation is a density functional expression of a non-interacting system with the same solutions than the Schrödinger equation only when the energy is minimized. The Kohn-Sham equation is written as [19]:

$$[T_S + V_S]\Psi = E\Psi = \mathrm{V} + \int \frac{n_S(r')}{|r - r'|} d^3r' - V_{XC}[n_S(r)]$$
$$= V + U + U_{NCL} - (T_S - T) = T + U + V_{XC}$$

Where V_S is the effective potential constituted by the nucleus-electron potential V, the classical Coulomb term of the e-e interaction (Hartree term) U, and V_{XC} is the sum of the non-classical Coulomb term (U_{NCL}) plus the residual factor of the kinetic energy ($-T_S + T$), which supplies information about the kinetic interaction between electrons. The exchange-correlation (XC) term V_{XC}, is the sum of all unknown terms and must be treated generally by some approximation [19]. This treatment is exact only in the simplest systems, like the free electron gas case.

2.6.4 Exchange and correlation

By defining the XC energy density per electron $\varepsilon_{XC}[n(r)]$, E_{XC} can be analytically defined as:

$$E_{XC} = \int \varepsilon_{XC}[n_-, n_+] d^3r$$

If, with this linear density dependence of the E_{XC}, we use the $\varepsilon_{XC}[n(r)]$ value from the free electron gas, we are considering the local (spin) density approximation [19] for the XC term. By virtue of this approximation, the electron density is

constant so the XC effects stem predominantly from the immediate vicinity and are not dependent on inhomogeneities of the electron density away from the reference point “r”. The calculations we have performed with L(S)DA are based on parameterizations [21] of exact many-body calculations performed by Ceperley and Alder (CA) [22].

If we consider L(S)DA, and its linear density dependence, as the first term of a Taylor series expansion of the energy density, we can go one step further in the XC approximation including also some gradient corrections of the density. This is the generalized gradient approximation (GGA), introduced by Becke [23], Perdew [24] and Perdew and Wang [25] which adopts a gradient expansion from the LDA to account the inhomogeneities of the electron density, leading to the following equation:

$$E_{GGA}(n) = \int \varepsilon_{XC}(n_-, n_+; \nabla n_-, \nabla n_+) d^3 r$$

Nevertheless, the GGA functional generally offered improved accuracy over the LDA, they are prone to underestimate binding energies and failed in those cases where the electrons are delocalized in the uniform gas, such as metal oxides. To account for these failures Perdew, Burke and Ernzenhof constructed from first principles a numerical GGA functional called PBE [26], which constitutes the scheme we are using in our GGA calculations [26-29]. This functional involves a second-order density gradient expansion for the XC hole surrounding the electron in a system of slowly varying density. In condensed matter calculations, the GGA is known to provide an improved description of cohesive energies and magnetic properties over LDA [30]. In our calculations, GGA approximation have been used to describe bulk and interface properties.

2.6.5 Method of solving: self-consistency

Even though U and V_{XC} depends on the electronic density, they are also solution dependent, which entails that we have to proceed in a self-consistent (SCF) way to solve the Kohn–Sham equations [19, 20]. First, an initial guess for the density is

used to obtain H, and the resulting solution of this H provides the next guess for the density in an iterative way until the solution for the density is close, measured by some tolerance parameter, to the last guess density used [31]. The whole process, including SCF, to obtain the ground state of a quantum mechanical system is schematically depicted in the flux diagram:

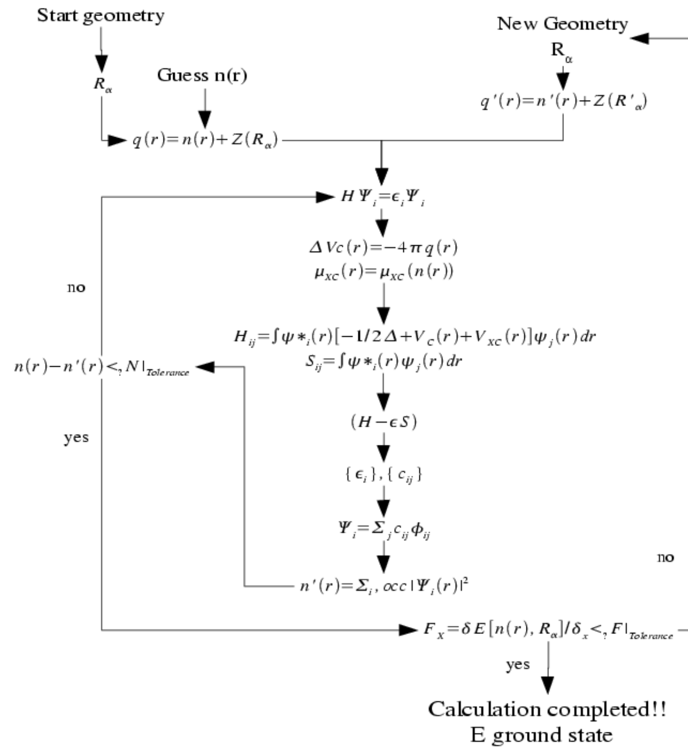

Figure 2.10 Computational process in DFT calculations from the electronic density guess and initial ionic geometry to the electronic density self consistently calculated and the equilibrium geometry.

The procedure employed to calculate the equilibrium atomic distances has been performed with the Hellmann-Feynmann theorem [32, 33]. The theorem states that in the ground state, the partial derivatives of the total energy with respect to the ionic positions result into the force experienced by the ions.

The search for the minimum energy state is achieved in an iterative way as depicted in figure 2.10. First we consider the initial ionic geometry, and start the self-consistent procedure to calculate the electronic density, and then we calculate the

forces and use them to determine the next trial for the ionic geometry by means of the conjugate-gradient algorithm [34]. After an iterative process on the ionic forces, we reach the final situation when the forces on every atom are less than certain tolerance parameter.

2.6.6 Basis sets

There are several types of basis sets in DFT calculations, but mainly two are mostly employed: Plane Waves (PW) and atomic orbitals [19]. The construction of the wave function (WF), and then the density, for different choices of the basis set involves different computational procedures that we describe subsequently.

A plane wave expansion is the most straightforward extension of Bloch theorem with Periodic Boundary Conditions (PBC) [35]. Considering these assumptions, we can model an infinite crystal by the repetition of a periodic cell along the three space directions. This allows us to determine the crystal properties by evaluating them at a finite number of points inside the periodic cell [36, 37]. The Plane Wave (PW) expression of the Wave Function (WF) in a periodic cell satisfies:

$$\Psi_{kn}(r) = e^{(ikr)} U_{kn}(r) = \sum_{G} C_G(kn)\, e^{(i(k+G)r)}$$

Where k is the point in reciprocal space within the Brillouin Zone (BZ) and $U_{kn}(r)$ is the Wave Function (WF) periodic part on the Brillouin Zone (BZ), which can be expressed as a plane waves expansion using the reciprocal lattice vectors (G) as the wave vectors.

The main advantages of PW are: they are simple to implement, the PW basis is an orthonormal and complete set, and the accuracy of the basis set can be systematically improved by simply increasing the number of basis functions; by that means, making it easy to perform convergence checks. However, the main drawback arises from the non-local nature of the PW. PW's basis put weight in regions devoid of charge where no basis is needed (for example the vacuum region in a surface calculation).

There are two main classes of atomic orbitals: Gaussian-type-orbitals (GTO) [38], and Slater-type-orbitals (STO) [39, 40]. GTO are commonly used in calculations involving multicentre integrals because they are less computational expensive [41].

STO orbitals are the most natural choice as they are the closest to the exact wave function (WF) of a solid state problem. In order to have the same accuracy for GTOs than for STOs, three times more functions need to be employed. As STO is one of the basis set type we will use in our calculations, we will briefly discuss their general properties.

The general expression of STOs satisfies:

$$X_{[n,m,l,\xi]}(r,\theta) = NY_{(l,m)}r^{(n-1)}e^{(-\xi r)}$$

Where the parameters n, l and m are quantum numbers, $Y_{l,m}$ are the spherical harmonics and characterizes the size of the basis function [41].

2.6.7 Pseudo-Potentials

The pseudopotential (PP) formalism is an attempt to replace the complicated interactions of the nucleus and the core electrons with the valence electrons by an effective potential [42] or PP, so that the Schrödinger equation contains a modified potential term instead of true Coulomb potential terms.

Thus the core electrons and nucleus potentials are replaced by an equivalent PP, which generates a set of modified valence WF, or “pseudo wave functions” (pWF). Figure 2.11 represents the different spatial dependences derived from the PP with respect to the original potential. The Pseudo-Potential (PP) approach is justified by the fact that most chemical properties are governed by the valence electrons. Thus the tightly bound core electrons are usually shielded from interactions with other species, and they do not change with different atomic environments.

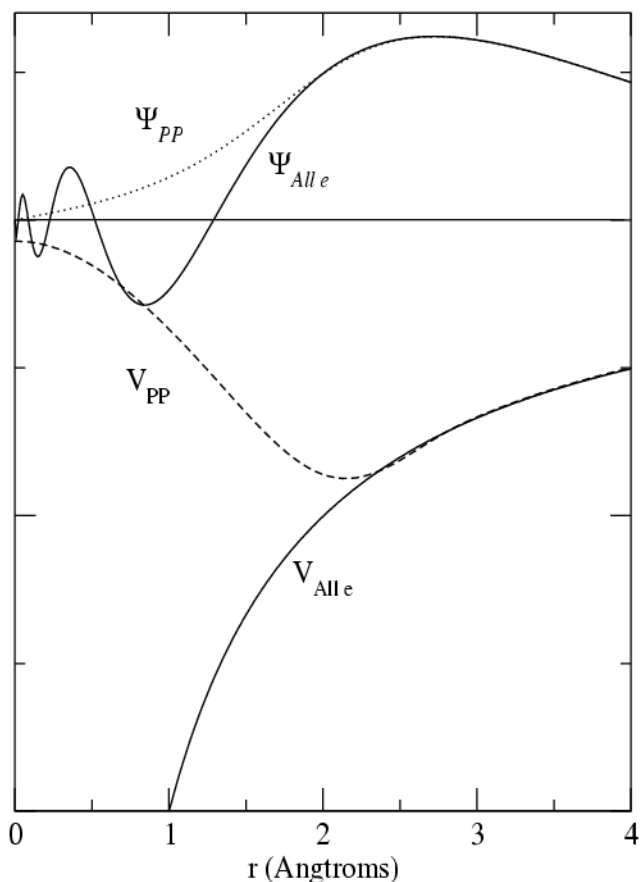

Figure 2.11 Comparison between the wave functions and potentials of the *all electron* calculations and those of the pseudopotentials we have employed for a transition metal.

The use of Pseudo-Potential (PP) reduces the number of terms required in the calculations and hence, the computational cost [43]. The major drawback is that it introduces another approximation to the solution of the Schrödinger equation which can reduce the accuracy of the results [44].

The construction of the more accurate "norm-conserving" PP is based on four conditions due to Troullier and Martins [45]. The first is that the pWF originated from the PP contains no nodes in order to reach maximum smoothness. The second is that the pWF must be the same that the all-electron-WF beyond certain radius cut off, r_{CL}, when both radial parts are normalized. The third is that the charge enclosed within r_{CL} for these two WFs must be equal. And the last is that the

eingenvalues of both potentials (*all-electron* and that related with the pWF) must be the same.

A Pseudo-Potential (PP) is called "local" when there is no distinction among its angular momentum components. But in order to obtain more accurate approximations we can use non-local ones with different scattering behavior for each angular momentum [45].

These concepts have been employed for the pseudopotential generation in codes that employ linear combination of atomic orbitals as the basis set. Nevertheless, when plane waves are used some modifications are required because the calculation of pseudopotentials for first row, transition and rare-earth elements are computationally demanding.

By virtue of the ultrasoft Pseudo-Potential (PP) concept developed by Vanderbilt [46] and combining it with the ideas of the linearized augmented-plane-wave (LAPW) method proposed by Blöchl [47] a so called projected augmented wave (PAW) method was created [48]. These PAW potentials are more accurate that the ultrasoft PP as they deserve smaller radial cutoffs and also provide the solution to the exact valence wave function with all nodes in the core region.

2.6.8 Density of States

The density of states (DOS) provides the number of electronic states as a function of the energy. It is intimately related to the band structure defined as the band energy dispersion along high-symmetry directions in reciprocal space $E(k)$. In general, the DOS is proportional to the inverse of the slope of $E(k)$ [49]. Usually the results are analysed in terms of the partial DOS, which is the projection of the DOS either on selected atoms, angular momentum, spins... etc.

The expression of the DOS satisfies the following equation:

$$D(E, r_\alpha) = \sum_{nk} \int dr \Theta(R_\alpha - |r - r_\alpha|) \Psi_{nk}^*(r) \Psi_{nk}(r) f(E - E_{nk})$$

where r_α is the position of the atom α, R_α is the chosen atomic radius, Θ(x) is the Heaviside function, and $f(E-E_{nk})$ is the occupancy of the state with energy E_{nk}.

In this PhD dissertation, we will make use of the total and partial density of states (DOS) projected on atomic planes to study electronic properties variations per atomic plane.

2.6.9 Hubbard correction

The Hubbard correction involves an on-site Coulomb interaction U-J [50] because the semi-local functional, such as the GGA, usually underestimates the energy band gap. Within the VASP code we will use the Hubbard correction within the Dudarev approximation where only the effective parameter $U_{eff} = U - J$ influences the results. The expresion of the additional term which is included in VASP code using Hubbard correction is the following:

$$E_{\mathrm{LSDA+U}} = E_{\mathrm{LSDA}} + \frac{(U-J)}{2}\sum_{\sigma}\left[\left(\sum_{m_1} n^{\sigma}_{m_1,m_1}\right) - \left(\sum_{m_1,m_2} \hat{n}^{\sigma}_{m_1,m_2}\hat{n}^{\sigma}_{m_2,m_1}\right)\right]$$

Being the first term the energy obtained by the pure Linear Spin Density Approximation while the second term depicts the effective Hubbard correction; written in terms of the electron density matrix:

$$E_{LSDA+U} = E_{LSDA} + \frac{(\bar{U}-\bar{J})}{2}\sum_{\sigma}[Tr\rho^{\sigma} - Tr(\rho^{\sigma}\rho^{\sigma})]$$

Where ρ^{σ} is the density matrix of d electrons.

The above expression penalizes the energy of local/semilocal functional, such as the local spin density approximation (LSDA), and forces the on-site occupancy density matrix is fully occupied or unoccupied by electrons.

2.6.10 VASP code

The Vienna Ab initio Simulation Package (VASP) is a computer program for atomic scale materials modelling, e.g. electronic structure calculations and quantum-mechanical molecular dynamics, from first principles [51].

For our interests, VASP computes an approximate solution to the many-body Schrödinger equation, either within density functional theory (DFT), solving the Kohn-Sham equations [52], or within the Hartree-Fock (HF) approximation, solving the Roothaan equations.

In VASP, central quantities, like the one-electron orbitals, the electronic charge density, and the local potential are expressed in plane wave basis sets. The interactions between the electrons and ions are described using norm-conserving or ultrasoft pseudopotentials, or the projector-augmented-wave method.

To determine the electronic groundstate, VASP makes use of efficient iterative matrix diagonalisation techniques, and a series of algorithms that have allow us to satisfy the required electronic convergence and force tolerance criteria. The tolerance parameters employed for the electronic and ionic convergence are XX and YY respectively. The used values for the k-point mesh and energy cuttoff will be detailed for each of the calculations, in chapter 4.

Our calculations are performed using Generalized Gradient Approximation (GGA) as proposed by Perdew, Burke and Ernzerhof (PBE approximation) [53]. Whenever required an appropriate usage of the Hubbard correction will be performed in order to mimic the bulk properties either from previous experimental or theoretical works.

2.7 References

[1] O. Nakamura, E. Fullerton, J. Guimpel, I. K. Schuller. Appl.Phys.Lett. 60,120, (1992).

[2] D. Kelly, E. Fullerton, J. Santamaría, I. K. Schuller. "A simple closed-form expression for the X-ray reflectivity from multilayers with cumulative roughness". Scripta Metallurgica et Materiala 33, 1603 (1995).

[3] R. Egerton, "Electron energy-loss spectroscopy in the TEM". *Rep. Prog. Phys.*72, 016502 (2009).

[4] N. D. Browing, M. F. Chisholm, and S. J. Pennycook. "Atomic-resolution chemical analysis using a scanning transmission electron microscope". *Nature* 366, 143 (1993).
[5] P. E. Batson. "Simultaneous STEM imaging and electron energy-loss spectroscopy with atomic-column sensitivity". *Nature* 366, 727 (1993).

[6] N. Browning, D. Wallis, P. Nellist, and S. Pennycook. "EELS in the STEM: Determination of materials properties on the atomic scale". *Micron* 28, 333 (1997).
[7] O. L. Krivanek, and J. H. Paterson. "Elnes of 3d transition-metal oxides: I. Variations across the periodic table". *Ultramicroscopy* 32, 313 (1990).

[8] H. Kurata, and C. Colliex. "Electron-energy-loss core-edge structures in manganese oxides". *Phys. Rev. B* 48, 2102 (1993).
[9] J. H. Rask, B. A. Miner, and P. R. Buseck. "Determination of manganese oxidation states in solids by electron energy-loss spectroscopy". *Ultramicroscopy* 21, 321(1987).

[10] I. Brodie, and J. J. Muray, "The Physics of Micro/Nano-Fabrication", (Plenum Press, 1992)
[11] M. Ohring, "The Materials Science of Thin-films" (Academic Press, 1992).

[12] J. Tornos, "Spin-dependent transport in oxide multiferroic tunnel junctions", Ph. D. Thesis, Universidad Complutense de Madrid (2014).

[13] A. Rivera, "Movilidad iónica en conductores superiónicos: movilidad local, percolación y relajación vibracional", Ph. D. Thesis, Universidad Complutense de Madrid (2003).
[14] JUAN IGNACIO BELTRÁN FÍNEZ. "FIRST-PRINCIPLES STUDY OF THE ATOMIC PROPERTIES AND ADHESION AT METAL-CERAMIC INTERFACES." Ph. D. Thesis, Universidad Autónoma de Madrid (2006).
[15] P. Hohenberg and W. Kohn, "Inhomogeneus electron gas". Phys. Rev., 1964. 136(3B): p. B864.
[16] http://en.wikipedia.org/wiki/Density_functional_theory
[17] C. Cohen-Tannoudji, B. Diu and F. Laloe, "Quantum Mechanics". ed. Wiley-VCH. 1976.
[18] M. Born and R. Oppenheimer, "Quantum theory of the molecules". Ann. Physik., 1927. 84: p. 457.

[19] W. Koch and M. C. Holthausen, *A Chemist's Guide to Density Functional Theory*. ed. W. Wiley-VCH. 2001.
[20] W. Kohn and J. Sham, *Self-consistent equations including exchange an correlation effects.* Phys. Rev., 1965. 140(4A): p. A1133.
[21] J. P. Perdew and A. Zunger, “Self-interaction correction to density-functional approximations for many-electron systems.” Phys. Rev. B, 1980. 23(10): p. 5048.
[22] D. M. Ceperley and B. J. Alder, “*Ground state of the electron gas by a stochastic method.”* Phys. Rev. Lett., 1980. 45: p. 566.
[23] A. D. Becke, “Density functional calculations of molecular bond energies.” J. Chem. Phys., 1986. 84: p. 4524.
[24] J. P. Perdew, “*Density-functional approximation for the correlation energy of the inhomogeneous electron gas.”* Phys. Rev. B, 1986. 33 (12): p. 8822
[25] J. P. Perdew and Y. Wang, “*Accurate and simple density funcional for the electronic exchange energy: Generalized gradient approximation”*. Phys. Rev. B, 1986. 33(12): p. 8800.
[26] J. P. Perdew, K. Burke and M. Ernzerhof, “*Generalized gradient approximation made simple.”* Phys. Rev. Lett., 1996. **77**(18): p. 3865.
[27] J. P. Perdew, K. Burke and Y. Wang, “Generalized gradient approximation for the exchange-correlation hole of a many-electron system.” Phys. Rev. B, 1996. 54 (23): p. 16533.
[28] J. P. Perdew, K. Burke and M. Ernzerhof, “Local and gradient-corrected density functionals”. Chemical Applications of Density-Functional Theory, 1996. 629: p. 453.
[29] K. Burke, J. P. Perdew and M. Ernhof, “*Why semilocal functional work: accuracy of the on-top pair density and importance of system averaging.”* J. Chem. Phys., 1998. 109 (10): p. 3760.
[30] J. P. Perdew and K. Burke, *Comparison shopping for a gradient-corrected density functional.* Int. J. Quantum Chem, 1996. 57: p. 309.
[31] P. Pulay, *Ab initio calculation of force constants and equilibrium geometries in polyatomic molecules. I. Theory.* Mol. Phys., 1969. 17(2): p. 197.
[32] H. Hellmann, “*Einfuhrung in die Quantumchemie”*, Deuticke. Leipzig (1937).
[33] R. P. Feynmann, “*Forces in molecules”*. Phys. Rev. B, 1939. 56: p. 340.
[34] M. C. Payne, M. P. Teter, D. C. Allan, T. A. Arias and J. D. Joannopoulos, “*Iterative minimization techniques for ab initio total-energy calculations: molecular dynamics and conjugate gradients”*. Review of Modern Physics, 1992. 64 (4): p. 1045.
[35] N. W. Ashcroft and N. D. Mermin, “Solid State Physics”. Ed. Saunders. 1976

[36] H. J. Monkhorst and J. D. Pack, "*Special points for brillouin-zone integrations*". Phys. Rev. B, 1976. 13: p. 5188.
[37] P. E. Blöchl, O. Jepsen and O. K. Andersen, "*Improved tetrahedron method for brillouin-zone integrations*". Phys. Rev. B, 1994. 49: p. 16223.
[38] S. F. Boys, "*Electronic wave functions I. A general method for calculation of the stationary states or any molecular system*". Proceedings Royal Society London, 1950. A200: p. 542.
[39] J. C. Slater, "*Atomic shielding constants*". Phys. Rev. 1930. 36: p. 57.
[40] J. C. Slater, "*Note on Hartree's method*". Phys. Rev., 1930. 35: p. 210.
[41] J. Simons, "*An experimental chemist's guide to ab initio quantum Chem*". J. Phys. Chem., 1991. 95: p. 1017.
[42] D. R. Hamman, M. Schlüter and C. Chiang, "*Norm-conserving pseudopotentials*". Phys. Rev. Lett., 1979. 43 (20): p. 1494.
[43] A. R. Leach, *Molecular Modelling: Principles and applications*. ed. L. 2ed Prentice Hall, Harlow. 2000, London.
[44] D. Porezag, M. R. Pederson and A. Y. Liu, *The accuracy of the pseudopotential approximation within density functional theory.* Phys. Status Solidi B, 2000. 217: p. 219.
[45] N. Troullier and J. L. Martins, *Efficient pseudopotentials for plane-wave calculations.* Phys. Rev. B, 1991. 43 (3): p. 1993.
[46] D. Vanderbilt, *Soft self-consistent pseudopotentials in a generalized eigenvalue formalism.* Phys. Rev. B, 1990. 41: p. 7892.
[47] P. E. Blöchl, *"Projector augmented-wave method".* Phys. Rev. B, 1994. 50 (24): p. 17953.
[48] G. Kresse and D. Joubert, "*From ultrasoft pseudopotentials to the projector augmented-wave method*". Phys. Rev. B, 1999. 59: p. 1758.
[49] R. Hoffmann, *Solids and Surfaces: A Chemist's View of Bonding in Extended Structures*. ed. W. VCH. 1988.
[50] S. L. Dudarev, G. A. Botton, S. Y. Savrasov, C. J. Humphreys, and A. P. Sutton. *"Electron-energy-loss spectra and the structural stability of nickel oxide: An LSDA+U study".* Phys. Rev. B 57, 1505 – Published 15 January 1998. https://cms.mpi.univie.ac.at/vasp/vasp/On_site_Coulomb_interaction_L_S_DA_U.html

[51] https://www.vasp.at/index.php/about-vasp/59-about-vasp

[52] W. Kohn and L. J. Sham. "Self-Consistent Equations Including Exchange and Correlation Effects". *Phys. Rev.* 140, A1133 (1965).

[53] “Electronic Structure. Basic Theory and Pratical Methods.” Richard M. Martin (2008).

Chapter 3: High On/Off Ratio Memristive Switching of Manganite/Cuprate Bilayer by Interfacial Magnetoelectricity

3.1 Methods

The samples were grown on top of $SrTiO_3$ (001) substrates using a high pressure (3.2 mbar) pure oxygen sputtering deposition system at high temperature (900ºC) [19, 20]. The junctions are fabricated from [PBCO (8 nm)/LCMO (50 nm)] bilayers using standard UV optical lithography and ion milling. Then, the samples are patterned into micron size ($9 \times 18\mu m^2$ and $5 \times 10\mu m^2$) rectangle shape pillars and measured their magnetotransport properties. For transport properties, Ag top contacts were deposited on the PBCO. Typically 40% of patterned junctions were not shunted and could be measured, which represents a large success ratio of the patterning process. IV curves were measured using current source and voltmeter. For all measurements the top contact was grounded such that negative (positive) voltages correspond to electric fields pointing downwards (upwards).

High-angle annular dark field (HAADF) imaging was performed on Nion UltraSTEM 100 and UltraSTEM 200 instruments operated at 100 and 200 kV respectively. Both microscopes use cold field emission electron sources and aberration correctors capable of neutralizing up to fifth order aberrations. Electron energy loss spectroscopy was performed on the Nion UltraSTEM 100 using a Gatan Enfina EEL spectrometer.

For the DFT simulations, Perdew-Burke-Ernzerhof (PBE) [43] flavour of the generalized-gradient approximation (GGA) has used the exchange-correlation functional. Using projector-augmented-wave (PAW) potentials [44] and a plane-wave basis as implemented in the Vienna Ab-initio Simulation Package (VASP) code [45]. The kinetic energy cutoff of the plane wave basis is set to be 368.6 eV. The electronic self-consistent calculations are converged to 10^{-5} eV between two self-consistent steps. The structural relaxations are converged to 10^{-4} eV for the total energy difference between two ionic steps. The simulation cell consists of a layer of $La_{0.67}Sr_{0.33}MnO_3$ of 23 Å and a $PrBa_2Cu_3O_7$ layer of 19 Å, with a total of 104 atoms. Brillouin zone sampling is performed by using the 2x2x1 k-point-mesh. To account for the electron correlations, it is used an implementation [46] of DFT+U methods [47] and apply $U = 2\ eV$ on Mn 3d orbitals. The 4f electrons on Pr atoms are kept frozen at the core.

3.2 Experimental Results

The transistor, a three-terminal device, is the basis unit in modern electronics, which powers information technology. Driven by the approaching limits of transistor scaling, interest in exploring memristors as an alternative has recently surged. Memristors are devices in which the passage of current is controlled by exploiting the defining property of memristive materials, namely a pinched current-voltage hysteresis loop [1, 2]. In a transistor, the different conducting states are achieved by altering the gate voltage that externally modulates the carrier density in the semiconductor. In a memristor, one uses external electric and magnetic fields to generate different conducting states by inducing reversible atomic displacements. Memristors often have the additional property of being continuously tunable, which emulates biological synapses [3, 4].

Many materials have been explored for their memristive behaviour. The most widely studied types are based on the dynamics of defects such as oxygen vacancies or metal ions [5, 6, 7]. Different resistances states are generated by either causing the formation and rupture of a conductive filament or modifying the Schottky barrier at the contacts. High On/Off ratios $(> 10^3)$ are often achieved [8, 9]. Memristors based on other switching mechanisms have also been demonstrated, including molecular memristors [10], ferroelectric memristors [11], and spin-transfer torques (STTs) [12]. These memristors typically have On/Off ratio smaller

than 10^2 with the exception of ferroelectric memristors, which can reach 10^4 [13]. Several recent papers demonstrated that the magnetic polarization in magnetic tunnel junctions (MTJs) [14] and magnetic-metal/ferroelectric junctions [15-17] can be modified by external electric fields, effectively producing memristive behaviour, but the On/Off ratio is typically smaller than 10.

In this PhD dissertation, it is reported that memristive switching with high On/Off ratio in transition-metal-oxide (TMO) interfaces and show that it is unlikely to involve defect motion. Instead, it is more likely that the phenomenon arises from a new type of interfacial magnetoelectricity. It is demonstrated experimentally that the resistance of $La_{0.7}Ca_{0.3}MnO_3/PrBa_2Cu_3O_7$ bilayers can be changed 10^3 – fold by an external electric field. The switching can happen at temperatures as low as 50 K, whereby the underlying mechanism is unlikely to be oxygen-vacancy diffusion. Although other explanations may be possible, results of density functional-theory calculations in terms of which is concluded that the memristive behaviour originates from the switching of a "magnetic dead layer" (MDL) at the LCMO/PBCO interface by the external electric field. A MDL can exist at the interface of ferromagnetic (FM) and non-ferromagnetic TMOs such as $La_{0.7}Ca_{0.3}MnO_3/YBa_2Cu_3O_7$, where the first layer of the FM TMO can be antiferromagnetically (AFM) coupled to bulk FM TMO [18]. Furthermore, first-principles calculations show that the external electric field induces subtle displacements of the interfacial Mn atoms and such displacements control the presence or absence of an MDL, which causes the memristive behaviour for the transport of spin-polarized electrons. The subtle nature of the switching makes the system very energy efficient (~0.1 attoJoule to write/erase a bit). The high On/Off ratio, non-defect based mechanism, and the low switching energy make the LCMO/PBCO bilayer and similar manganite/cuprate systems particularly attractive for memristive devices.

$La_{0.7}Ca_{0.3}MnO_3/PrBa_2Cu_3O_7$ bilayers were grown using a high pressure (3.4 mbar) pure oxygen sputtering technique at elevated temperature (900º C), which is known to yield good epitaxial properties [19]. Standard optical lithography and ion milling by a plasma source or electrically SiO_2 isolated mesas were used to define square micron size ($4x4\ \mu m^2$) pillars to measure perpendicular transport. The top electrode was evaporated with silver. Transport (resistance versus field loops and I-V curves) was measured in a closed-cycle He cryostat equipped with an electromagnet that supplies a magnetic field up to 4000 Oe. For all measurements, the top contact was grounded.

Aberration-corrected scanning transmission electron microscopy (STEM) was employed to determine the atomic scale structure and composition of the LCMO/PBCO bilayer. High-angle annular dark field (HAADF) imaging shows that the layers grow coherently on the $SrTiO_3$ (STO) substrate as seen in Figure 1b. The atomic-number contrast (Z contrast) of HAADF imaging allows the STO, LCMO and PBCO layers to be easily identified. However, because La, Pr and Ba are similarly heavy elements compared to the similarly light Cu and Mn elements the termination of the interface is not clear from the HAADF images alone. Electron-energy-loss spectroscopy (EELS) imaging was therefore performed.

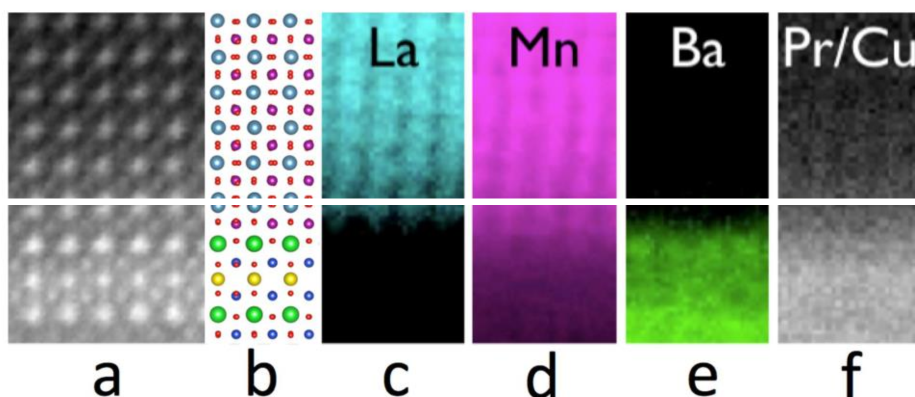

Figure 3.1 (a) Zoomed-in view of the HAADF image of the LCMO/PBCO sample. (b) Atomic-scale model obtained by DFT calculations. It is the same as Figure 3.3, but rotated by 45 degrees and projected along the [110] direction of the underlying perovskite lattice. (c-f) Chemical maps of La, Mn, Ba, and Pr/Cu from EELS measurements

The maps show that the interface consists of a Mn-rich plane terminating the LCMO, adjacent to a single Ba-rich plane terminating the PBCO. Hence, the atomistic model assumes a $MnO_2 - BaO$ termination at the interface.

Electrical measurements in the current-perpendicular-to-plane geometry reveal a memristive hysteresis of the LCMO/PBCO bilayer, as shown in the current-voltage relation in Figure 3.1 (c). Additionally, Figure 3.1 (d) shows the resistance hysteresis of the junction that was read with a voltage of 200 mV at 100 K. Under an external magnetic field of 4 kOe, the resistance (R) of the as-fabricated bilayer junction is about $3 \times 10^5 \Omega$. By applying negative biases greater than -0.5 V, the measured resistance can be increased by more than 3 orders of magnitude, with larger maximum biases resulting in greater R values. Applying a reverse positive

bias switches the bilayer back to the initial low-resistance state. Such a large magnitude of resistance change is not observed in LCMO/PBCO/LCMO trilayer samples, which instead show a smaller factor-two change in resistance [20]. The resistance hysteresis in the LCMO/PBCO bilayers varies with both temperature and magnetic field. The hysteresis window narrows as the temperature increases and vanishes when the temperature is raised to 180 K, which is above the Curie temperature of LCMO films (155 K), as shown in Fig. 3.1 (e). It is noticeable that the critical temperature (T_C) of the thin film is lower than the bulk value of 240 K, which probably is due to the strain effect on the very thin film, X-ray magnetic circular dichroism (XMCD) measurements were carried out, showing that there is exchange coupling between the interfacial Cu and Mn moments. The results included in oxygen vacancies in the switching cannot be ruled out. However, there are several factors that suggest a different mechanism may be at play. First, we observe memristive hysteresis when the temperature is far below room temperature, meaning there may not be sufficient thermal energy to enable the vacancy motion despite the barrier being lowered by the external electric field [4, 5, 7, 25]. More specifically, the diffusion barrier for oxygen-vacancy migration in LCMO is 1.3 eV [26] and the estimated maximum electric field during the experiment is 0.04 $V/Å$ for a 1V bias. For a hopping distance of 2 Å, the barrier lowering effect due to the electric field is 0.04 eV. For such an amount of barrier lowering, the diffusivity increases non-linearly with the electric field [4, 25]. However the overall diffusivity is still too low for vacancy migration. Even if we use a generously overestimated value of 0.1 eV for the diffusion barrier lowering, the resulting diffusion barrier is still 1.2 eV.

Although a diffusion barrier around 1 eV allows detectable vacancy motion at room temperature, [27] such a barrier is quite large for diffusion at 100 K, as a 1 eV at 100 K is equivalent to a 3 eV barrier at 300 K for diffusivity. Furthermore, if the motion of oxygen vacancies is causing the switching, the switching voltage should decrease as the temperature increases. The data do not show any such effect. In Figure 3.1 (e) we see that, on the left, all three temperatures show a switch occurring at about -0.6 V and on the right is at about +0.9 V for all temperatures.

The possibility that Joule heating might raise the temperature of the device to allow vacancy migration can be ruled out. First, junctions with different areas carved out of the sample showed current levels that scale approximately with junction area. Nevertheless, these data indicate that the current flow is homogeneous and exclude Joule heating at filaments.

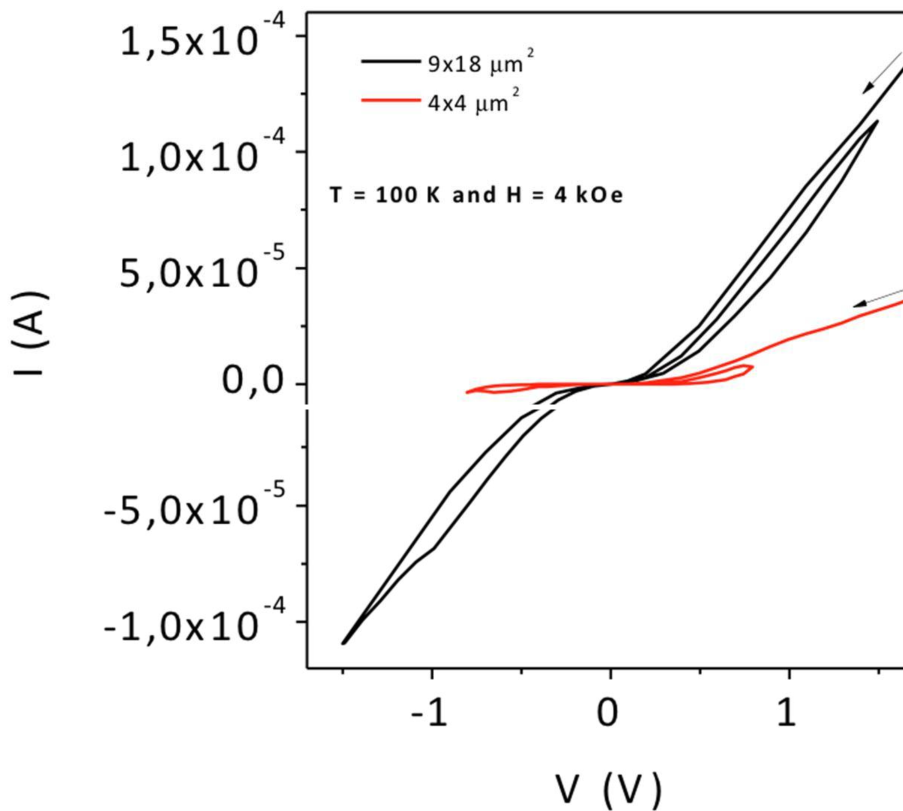

Fig. 3.2 The scaling of current level with the junction area. The current approximately scales with the junction area in both ON and OFF state, which proves a homogeneous current flow and exclude Joule heating at filament.

The possibility that Joule heating in the entire device causes vacancy migration is also not very likely for the following reasons: If Joule heating were sufficient for oxygen vacancies to move by overcoming a barrier of 1.3 eV, the temperature in the active region would be at or above room temperature, which is much higher than Curie temperature of LCMO. As a result, the LCMO would undergo a phase transition and lose its magnetization, and the resistance hysteresis would not occur at all, contrary to observations, which find hysteresis, but only up to the Curie temperature. The lack of hysteresis above Curie temperature suggest that hysteresis is related to the spin-polarization of the current. Meanwhile, the hysteresis window widens as the magnetic field increases, with stronger magnetic fields yielding greater resistance at the high-resistance state (Figure 3.3 (f)). This feature distinguishes the LCMO/PBCO system from other heterostructure systems that use

the spin-filtering effect, such as quasi-magnetic tunnel junctions (QMTJ), which are switched by magnetic fields [21].

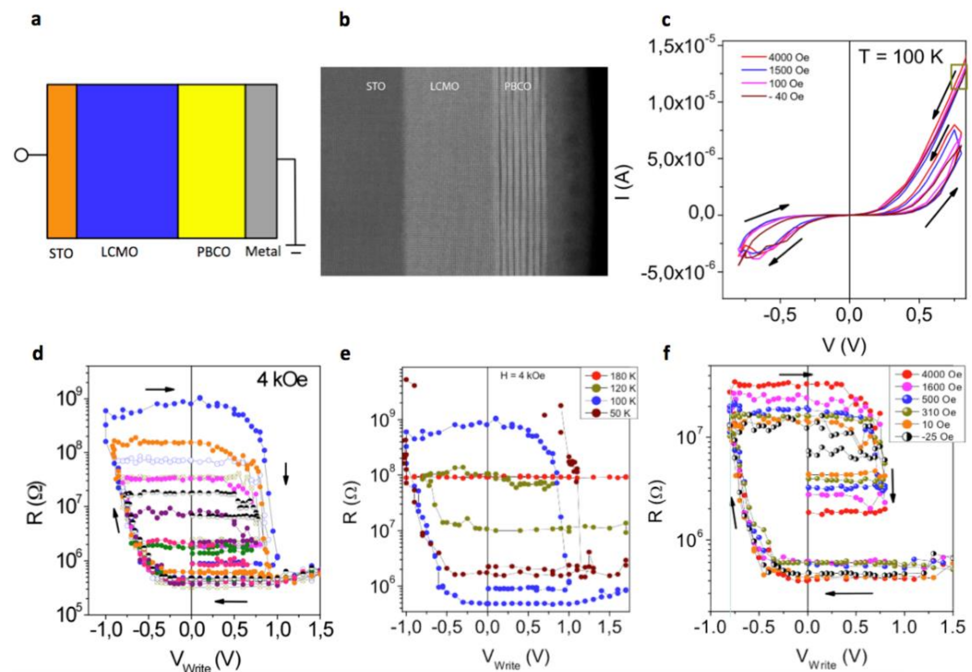

Figure 3.3 (a) The layout of the bilayer structure, where the top electrode (grounded) is shown in the right. (b) HAADF image of the LCMO/PBCO sample. (c) I-V hysteresis of the LCMO /PBCO bilayer recorded at 100 K. (d) Resistance hysteresis at 100 K. The different colors correspond to measurements with different maximum negative voltages. (e) Temperature dependence of the resistance hysteresis. (f) Magnetic field dependence of the resistance hysteresis.

The memristive behaviour of TMO thin films is often attributed to the diffusion of oxygen vacancies [4, 5, 7, 22, 23]. This mechanism has also been invoked in the case of TMO bilayer and trilayer structures such as PCMO/YBCO junctions [24]. A role of quick cool down only happens in cases of very fast switching when the current reaches a compliance value. In spite of using current compliance, the current never reaches compliance value in the experiments. Furthermore, the SET and RESET of the bilayer junction happens at similar voltages but the initial current can differ by 3 orders of magnitude. If Joule heating is moving the defects

then the SET and RESET should occur at similar power, i.e., very different switching voltages, which is contradictory to the experimental observations.

Other mechanism for vacancy diffusion are also likely absent in the bilayers. In a good conductor with high current, electron wind can transfer energy to defects and cause their migration. However this mechanism may be absent as the LCMO is a poor conductor and the PBCO barrier limits the current, which is further reduced when the bilayer is at the high resistance state. Recombination-enhanced diffusion [28, 29] can enable the diffusion at low temperature and also can cause memristive behaviour of oxides, [22, 23] but this effect is also unlikely present in the manganite/cuprate bilayers as there is no non-equilibrium concentration of electrons and holes and thus no carrier recombination.

Besides the vacancy migration mechanism, in some ferromagnet-oxide-ferromagnet MTJs, spin-orbit coupling can rotate the direction of the magnetic moment of one of the ferromagnetic layers through voltage-controlled magnetic anisotropy (VCMA) [30] and cause memristive switching [14] with on/off ratio no greater than 10 [31]. This mechanism, however, does not explain the present observations, as only one magnetic layer is present in the bilayer samples. The diffusion of Ag into the oxide, which is commonly observed in programmable metallization cells (PCMs), is also not likely at-play in the current system. In the Phase Change Memory (PCMs) devices, the host materials are amorphous or polycrystalline, which contain voids or low density regions (amorphous) or grain boundaries (polycrystalline), which act as paths for Ag incorporation from the electrode. In contrast, here we are switching a single-crystalline epitaxial film that contains no voids or grain boundaries for Ag incorporation. Therefore, although we cannot definitively rule out the possible role of oxygen vacancies, a new mechanism may be at play.

It has been shown that at the perovskite manganite/cuprate interface, the magnetic moments on the interfacial Mn layer are significantly different from those in bulk manganite. More specifically, at the LCMO/YBCO interface, a Magnetic Dead Layer (MDL) can form [18] resulting from the interfacial Mn layer being coupled anti-ferromagnetically (AFM) to the ferromagnetic (FM) LCMO bulk (strongly suppressing double exchange transport through the interface). If such a Magnetic Dead Layer (MDL) can be switched on and off in our manganite/cuprate bilayer by an electric field and the states are metastable (metastability in the magnetic states is known to exist in manganites [32]), the junction should also exhibit memristive hysteresis. Figure 3.2 shows schematically how the magnetic dead

layer (MDL) would affect the transport, where the details of the heterostructure, such as band bending and the transport in PBCO, are neglected, as they do not affect the discussion below. In the low resistance state (LRS) the MDL is absent. The spin of the interfacial layer is ferro-magnetically (FM) coupled to the ferromagnetic LCMO bulk as in Figure 3.4a, allowing the majority-spin electrons in the LCMO to tunnel through the PBCO, as shown in Figure 3.4 (b) (the light red area shows the additional barrier from the Magnetic Dead Layer). In this case, the current is large and R is small. In the high resistance state (HRS), the spin of the interfacial layer is anti-ferro-magnetically (AFM) coupled with the LCMO bulk (Figure 3.4c), giving rise to a magnetic dead layer (MDL). This magnetic dead layer (MDL) adds an additional tunnelling barrier to the transport of majority-spin electrons (Figure 3.4d), causing lower current and higher R.

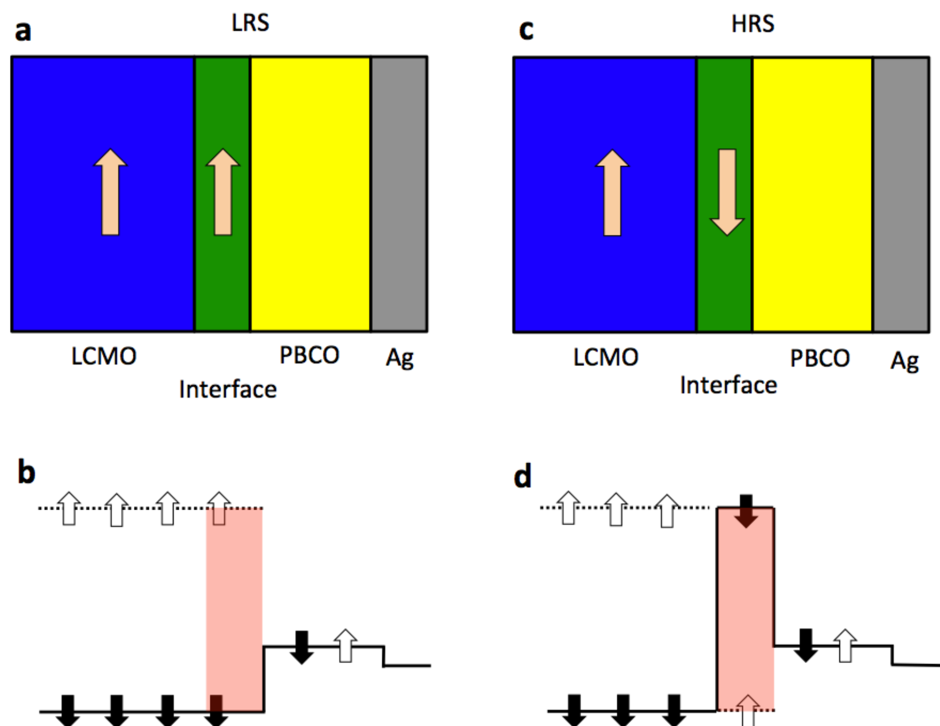

Figure 3.4 The mechanism of memristive switching at LCMO/PBCO interface. (a) The magnetic polarization at LRS, the arrow shows the direction of the magnetic moment. The potential "magnetic dead layer" is marked in green. (b) The band diagram of majority (black) and minority (white) spins at LRS. The light red area is the potential additional tunneling barrier if MDL is present. (c) The magnetic polarization at HRS. (d) The band diagram of majority and minority spins at HRS.

To demonstrate that the above mechanism is in fact active in our LCMO/PBCO bilayers, first-principles density-functional-theory (DFT) calculations are performed by Professor Sokrates Pantelides. In Figure 3.5 (a), it is shown the relaxed structure of the LCMO/PBCO interface and highlighted the position of the interfacial MnO_2 layer. It can be seen that the layer is polarized, with the Mn atoms displaced towards the PBCO. External biases (as illustrated in Figures 3.5 (b), 3.5 (c)) are able to alter the displacements of positively charged Mn atoms. Quantitative results from density functional theory (DFT) calculations are presented below in the discussion of the switching mechanism. As will be shown below, density functional theory (DFT) calculations confirm that such structural changes are indeed coupled to the change of magnetic ground state of the interfacial Mn layer and thus can switch the magnetic dead layer (MDL) on or off and cause the observed memristive hysteresis.

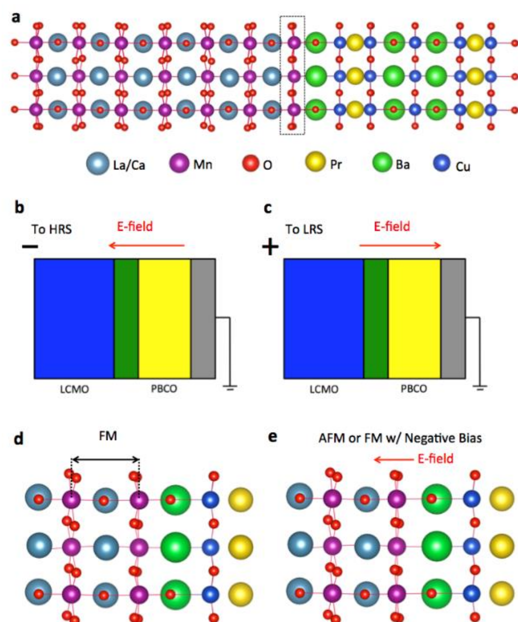

Figure 3.5 (a) The relaxed structure of the LCMO/PBCO interface. The position of possible "magnetic dead layer" is marked in dotted lines. (b, c) The polarities of the applied bias and the directions of the electric field inside the bilayer during the memristive switching. (d) The interface layer at optimized geometry when the interfacial Mn atoms are FM-coupled to bulk LCMO. This is also a zoomed-in view of Fig. 3.5a. The double-head arrow in black marks the distance between interface Mn layer the adjacent Mn layer as described in the text. (e) An exaggerated illustration of the interface layer at optimized geometry when the interfacial Mn atoms are AFM-coupled to bulk

LCMO. It also illustrates the change of Mn displacement from (d) under a negative bias. The change of Mn displacement is magnified by 20 times to 0.2 A for demonstration. The actual change from DFT relaxation is only 0.01 Å as discussed in the text, which is not distinguishable from (d) to the eyes.

Using density functional theory (DFT) calculations (performed by Professor Sokrates Pantelides), structural relaxations were performed for the PBCO/LCMO bilayer with fixed magnetic coupling between the interfacial Mn layer and the bulk in both the AFM and FM configurations. To capture the subtle structural difference, it is used a very tight convergence setting that ensures the electronic self-consistency converges to 10^{-6} eV and the forces converge to 10^{-5} $eV/$Å. The relaxed structure with FM coupling has an energy 0.5 meV lower than the relaxed structure with AFM coupling, meaning the FM state is the ground state of the bilayer. Therefore, in the resting state, the magnetic dead layer (MDL) is not present and the bilayer is at LRS, as shown in Figure 3.4 (a, b), consistent with electrical results shown in Figure 3.3 (c).

The most important result from the calculations is that the displacements of interfacial Mn atoms are different in the cases of FM and AFM coupled states. In the FM coupled case, the distance between the interfacial Mn layer and the adjacent Mn layer (see Figure 3.5 (d)) is 3.946 Å; in the AFM coupled case, the value is 3.937 Å. Although the change of 0.01 Å from FM to AFM coupling seems quite small, it is significant when compared to the change of distances between bulk Mn layers from FM to AFM couplings, which do not exceed 0.002 Å. Multiple structural optimizations with different starting geometries were performed to ensure that these results are consistent and are not from artifacts of structural relaxation. Testing structural relaxations was also repeated at different doping levels and with different numerical setups (k-points, plane-wave cutoff) for the DFT calculations. The $\sim$0.01 Å change in the distance between interfacial and adjacent bulk Mn layers that is much larger than the changes of distances between bulk Mn layers upon changing from FM to AFM coupled states are consistently obtained.

Although the LCMO bulk in the bilayer is nominally metallic at 30% Ca doping [33], an electric field can be sustained at the interfacial MnO_2 layer because the Thomas-Fermi screening length corresponds to one to two units cells of LCMO [34]. Furthermore, as discussed below, the properties of the interface LCMO layer differ from those of the bulk and might be viewed as an insulator. A negative bias

(Figure 3.5 (b)) pulls the interfacial Mn towards the LCMO (Figure 3.5 (e)) and reduces the distance from the adjacent Mn layer. A change of 0.01 Å in the displacements of interfacial Mn layer preconditions the lattice structure to the optimized geometry of the antiferromagnetic (AFM) state. Density Functional Theory (DFT) calculations were performed to obtain the electronic ground states of the FM and AFM coupled states at the displaced configuration.

The results show that the AFM-coupled state has an energy 0.3 meV lower than the FM coupled state. The magnetic moments on the interfacial Mn atoms relax into the AFM coupling state, activating the "magnetic dead layer" (MDL) and switching the bilayer to the HRS. A follow-up positive bias (Figure 3.5c) pushes the interfacial Mn ions back towards the PBCO. Again, a 0.01 Å change in the displacement preconditions the structure to the optimized geometry of the FM state (Figure 3.5d). The magnetic moments on the interfacial Mn atoms then relax into the FM coupling state, deactivating the magnetic dead layer (MDL) and switching the bilayer back to the low resistance state (LRS). The behaviour of "magnetic dead layer" (MDL) in the $La_{0.7}Ca_{0.3}MnO_3/PrBa_2Cu_3O_7$ system and the $La_{0.7}Ca_{0.3}MnO_3/YBa_2Cu_3O_7$ system [18] show that the Magnetic Dead Layer (MDL) is a very subtle effect that comes from very small energy difference (around the order of meV) between FM- and AFM-coupled states. In the reported $La_{0.7}Ca_{0.3}MnO_3/YBa_2Cu_3O_7$ system, the AFM state is the ground state and the FM state is metastable, while in the present $La_{0.7}Ca_{0.3}MnO_3/PrBa_2Cu_3O_7$ system, the FM state is the ground state and the AFM state is metastable.

As mentioned above, a 0.01 Å displacement of the interfacial Mn atoms "preconditions" the geometry of the lattice and facilitate the transition between the magnetic states. The remaining question is whether such displacement can be created by the electric field used in the experiment? Direct calculation of the displacement under the electric field is not feasible due to the complications (doing so would require using a saw-tooth electrostatic potential and periodic replicas of a large supercell containing a bilayer and a vacuum layer, which inevitably has PBCO and LCMO surfaces that would lead to spurious effects). Therefore, an alternative method was adopted: first DFT is used to calculate how much force is needed to create the 0.01 Å displacement, and then compare it to the estimated force from the external electric field. Starting from the relaxed structure of the FM-coupled state and displacing interface Mn ions towards LCMO by 0.01 Å is a good strategy to estimate the forces (and field) required to generate the mentioned displacements. Density Functional Theory (DFT) calculations were performed for

this geometry while keeping the magnetic configuration and other atoms frozen. The calculations show that the forces on the displaced Mn atoms are $0.25\ eV/Å$, which is the magnitude of the opposite force that needs to be generated by the applied electric field.

Now we estimate the forces exerted on the interfacial Mn ions in the experiment and compare them with those calculated with DFT results. Depending on the level of Ca doping, $La_{1-x}Ca_xMnO_3$ can be a ferromagnetic insulator (x<0.2), a ferromagnetic metal (0.2<x<0.5), or an antiferromagnetic insulator (0.5>x) [33]. While the LCMO in our experiment has 30% Ca doping and therefore should be a ferromagnetic metal, the electron density around the Mn atoms at the interfacial Mn atoms is slightly different from the bulk, as illustrated in Figure 3a. For the interfacial Mn atoms, the calculated average electron density within the Wigner-Seitz cell is $11.574\ e$, which is greater than the value of $11.546\ e$ for the Mn atoms inside de LCMO part of the bilayer and is close to the calculated value of $11.579\ e$ for pure $LaMnO_3$. Therefore, it is assumed that the interfacial MnO_2 layer is similar to lightly doped $LaMnO_3$ and thus could be viewed as a ferromagnetic insulator. As a result, when an external bias is applied, the voltage drop is across both the interfacial MnO_2 layer and the PBCO layer. By assigning a thickness of 2 Å to the interface MnO_2 layer (half the spacing between the Mn layers) and combining it with the thickness of the PBCO layer ($\sim 8nm$) and the dielectric constants of lightly doped $LaMnO_3$ ($\varepsilon = 18$) [32] for the interfacial layer and $PrBa_2Cu_3O_7$ ($\varepsilon = 80$) [33], the estimation of the electric field at the interface MnO_2 layer to be about $0.02\ V/Å$. Moreover, the Born effective charge of interfacial Mn atoms from density functional theory (DFT) calculation is 11. If these values are combined together, the conclusion is that an external voltage of 0.5 V generates a force of $0.22\ eV/Å$ on an interfacial Mn atom. Although this estimation is relatively crude, it is in good agreement with the DFT result that a force of $0.25\ eV/Å$ is needed to displace the interfacial Mn atom by 0.01 Å and create a "Magnetic Dead Layer" (MDL).

The On/Off resistance ratio of the bilayer is the inverse of the transmission coefficient T across the magnetic dead layer (MDL). Using the WKB approximation for a rectangular barrier, the transmission coefficient (T) is given by the expression, $T \cong exp\left(-2\sqrt{\frac{2m^*V_0}{\hbar^2}}d\right)$, where m^* is the effective mass of electrons in LCMO, V_0 is the barrier height that equals the splitting between spin-up and spin-down electrons, and d is the barrier width. Making use of $m^* = m_e$

[37], $V_0 = 3.3\ eV$ [38], and $d = 3.9$ Å (MnO_2 layer thickness), the transmission coefficient of $T = 7.5 \times 10^{-4}$ is obtained. Thus, it is obtained an On/Off ratio of $\frac{R_{off}}{R_{on}} = 1.3 \times 10^3$, which is in good agreement with the experimental results shown in Figures 1d and 1e. The large splitting energy between majority and minority spins in LCMO is an important factor in achieving the high On/Off ratio. Other TMO systems would show different On/Off ratios upon the creation and elimination of magnetic dead layer (MDL) depending on the splitting energy between the majority and minority spins.

In addition to the high On/Off ratio, the mechanism described above is in good agreement with several other experimental observations. (1) The density functional density (DFT) calculations are independent of the electrical measurements and predict that negative bias switches the bilayer from the Low Resistance State (LRS) to the High Resistance State (HRS) and that positive bias switches it from the High Resistance State (HRS) to the Low Resistance State (LRS), consistent with the experimental switching directions. (2) Stronger negative bias can cause a more complete formation of the MDL (convert larger portions of the interfacial plane to AFM domains) or make the MDL grow thicker, by propagating it beyond the first interfacial layer, thereby increasing the resistance in the High Resistance State (HRS), as shown in experiments. (3) Meanwhile, once the Magnetic Dead Layer (MDL) is destroyed, the bilayer has only one state, thus the resistance in the Low Resistance State (LRS) is the same regardless of the applied positive bias, which is also observed experimentally. (4) The higher external magnetic field can enhance the degree of spin-polarization of injected current, being "analyzed" by the antiferromagnetic (AFM) aligned interface plane in the "Magnetic Dead Layer" (MDL), therefore causing larger resistance in the High Resistance State (HRS), as the experiment shows. (5) The lack of a high On/Off ratio in LCMO/PBCO/LCMO trilayer in Reference 20 can be understood as the trilayer has two opposing interfacial Mn layers which are coupled by the magnetic moments in PBCO through the antiferromagnetic interaction between Cu and Mn spins at the interfaces [20]. The calculations performed confirm the experimental observations that Cu and Mn at the interface are always antiferromagnetically (AFM) coupled, regardless of whether Mn atoms at the interface are ferromagnetically (FM) or antiferromagnetically (AFM) coupled to Mn in bulk LCMO. In other words, flipping the magnetization of interfacial Mn atoms would cause the flipping of the magnetization of Cu in PBCO. As the two interfacial Mn layers are opposing each other, they cannot be both switched from ferromagnetic (FM) to antiferromagnetic

(AFM) simultaneously by an electric field that produces displacements in the same direction, because the direction of the displacement that favours antiferromagnetic (AFM) coupling in one interface would be "wrong" for the other interface. Therefore, the switching of one side can be suppressed by its coupling to the opposite side through PBCO. The net result is that it is much harder to switch the trilayer and a different mechanism is at play (Reference 20). Indeed, the On/Off ratio in a trilayer is only ~ 2 while in the bilayer it is about $\sim 10^3$, which signals different switching mechanisms.

As already mentioned, alternative explanations of the observed switching may be possible. The mechanism described above, however, explains the experimental data and is backed up by first-principles calculations. The physical phenomenon that underlies the memristive switching mechanism shown here is a new type of interfacial magnetoelectricity. It relies on the dependence of the magnetic coupling on the atomic positions, according to the fact that the magnetic properties in transition metal oxides can be very sensitive to the atomic structures [39]. It bears similarity to the recently observed interfacial magnetoelectricity in magnetic metal/ferroelectric oxide junctions [15-17] where the magnetism at the interface can be controlled by electrically reversing the polarization direction of the ferroelectric. First-principles calculations revealed that in those systems, the change of atomic displacements at the interface upon the switching of the ferroelectric plays the key role in altering the interfacial magnetism [40]. However, even though the magnetic switching in metal/ferroelectric systems only involves the interface, it is necessary to electrically switch the bulk of the ferroelectric. On the contrary, in the LCMO/PBCO bilayer, both magnetic switching and electrical switching are limited to the interface, which potentially offers faster switching and lower energy cost. Using the maximum force around $0.25\, eV/\text{Å}$ and the displacement of 0.01 Å, the energy cost estimated to switch one Mn atom is about $1.3\ meV$. Therefore, the switching energy of a 10 nm by 10 nm area of the bilayer that represents a "bit" is only $0.8\, eV$, in other words, $0.13\ atto\ Joule$. In comparison, switching a $BiFeO_3$ ferroelectric memristor [13] with the same area and a thickness of 4.6 nm would require $470\ atto\ Joule$ at the theoretical limit. Indeed, it takes $0.427\ eV$ to switch one $BiFeO_3$ formula unit [41]. Furthermore, while the switching in magnetic metal/ferroelectric interfaces involves the change of the in-plane magnetic ordering that has a small effect on spin-current, the switching in LCMO/PBCO bilayer involves the activation of a magnetic "dead" layer, which allows high On/Off ratios for applications.

The key factors that enable the type of interfacial magnetoelectricity found in this system are the existence of a polarizable MnO_2 layer at the PBCO/LCMO interface and the modification of the magnetic properties of the Mn atoms by their displacement. As both factors are intrinsic to the perovskite manganite/cuprate interface, these findings should be applicable to other perovskite manganite/cuprate materials systems and possibly other transition metal oxides junctions as well. Further optimization of the materials might result in bilayer junctions with desired electrical properties to be used in a range of applications of memristive devices [4]. One key step would be realizing devices that operate at room temperature. This may be achievable by replacing $La_{0.7}Ca_{0.3}MnO_3$ with $La_{0.7}Sr_{0.3}MnO_3$, whose Curie temperature can be higher than 300 K [42].

3.3 Impedance Spectroscopy Measurements

At this stage, it is necessary to gain deeper insight into the conduction mechanisms in the resistive switching of the LCMO/PBCO/Ag tunnel junction. In order to achieve this goal, additional impedance measurements have been performed.

If a very high negative voltage bias is applied (-8V approximately), Ag electrode creates oxygen vacancies whose electrons left behind are transferred into LCMO electrode, making it more insulator. Thus, conduction is blocked, giving rise to the High Resistance State (HRS).

Conversely, If a very high positive voltage bias is applied (+8V approximately), Ag electrode removes oxygen vacancies, (this leads to the formation of Cu-O chains) collecting electrons from LCMO electrode, making it more conductive. Thus, tunnel conduction is enhanced, giving rise to the Low Resistance State (LRS).

In order to shed more light on the hypothesis mentioned above; we have performed differential conductance measurements applying a wide range of frequencies and voltage bias, showing a clear resistive switching, see figure 3.6

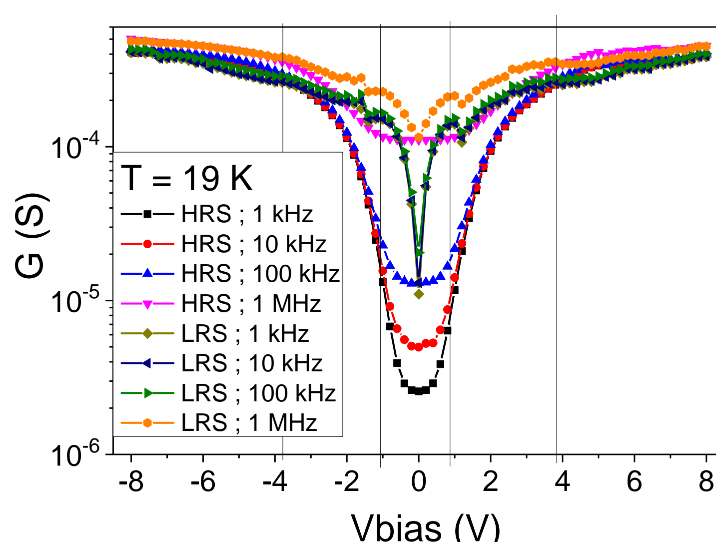

Figure 3.6 Differential conductance hysteresis curve at 19K ranging from 1kHz to 1MHz.

As can be seen from a closer inspection of the figure 3.6, a conductance resonance peak appear at 1 eV in the Low Resistance State (LRS) owing to the energy of the

$Cu - O$ chains required to tunnel electrons between 1D t-J band $Cu - O$ Chain (located in the $O\ 2p_z$ orbitals hybridized with the $Cu\ 3d_{3z^2-r^2}$ orbitals) and $O\ 2p_\pi$ orbitals located in the Pr–O coordination.

Furthermore, an energy gap of 4 eV appear in the High Resistance State (HRS) due to the forbidden gap between Pr^{IV} states (strong hybridization of $4f^2\underline{L}$ and $4f^1$ configurations, where $\underline{L}$ denotes a ligand hole on the O neighbors, in other words, a low-energy hole state as a result of a superposition of $O\ 2p_\pi$ orbitals with the $4f^2\underline{L}$ orbitals of the Pr^{4+} ion) and Cu^{III} states (the last ones located in the $O\ 2p_\sigma$ orbitals hybridized with the $Cu\ 3d_{x^2-y^2}$ orbitals in the CuO_2 planes).

Therefore, the data depicted in figure 3.6 validates the Fehrenbacher and Rice model for cuprates, whose hypothesis states that the absence of conductivity of the Cu–O chains is due to the O vacancies and the possibility to circumvent and oxygen vacancy via the tunneling of charge carriers through the CuO_2 planes is excluded by the insulating gap of 4 eV mentioned above between the Pr^{IV} states and the Cu^{III} states [48].

Another interesting feature in figure 3.6 is the convergence of the conductance at zero voltage bias for both resistance states while increasing the frequency [49]. To gain insight in this effect, we have depicted for the High and Low Resistance States the calculated $\tan\delta$ based on the conductance and capacitance measurements performed previously.

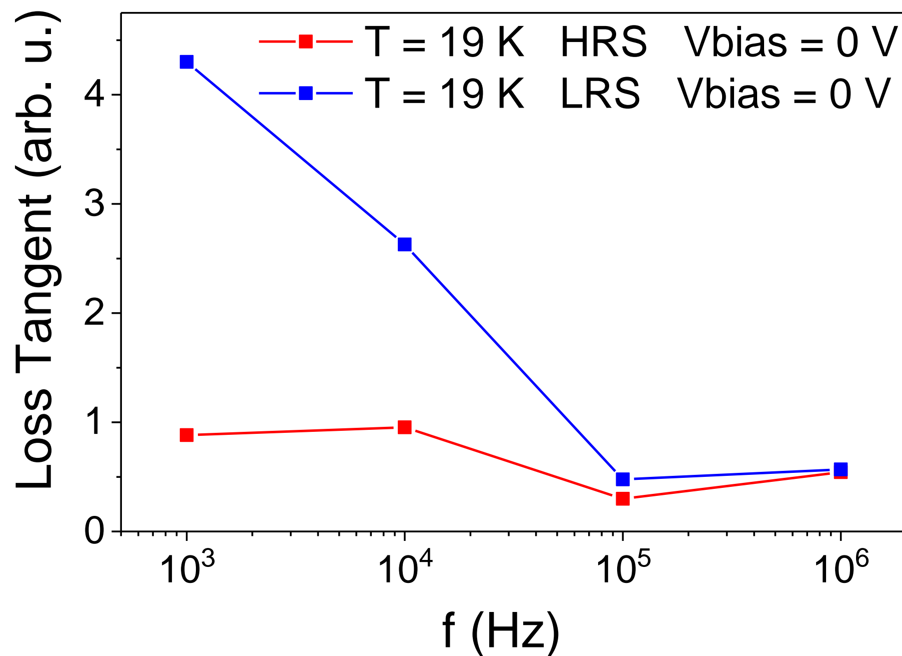

Figure 3.7 tan δ vs frequency in LCMO/PBCO/Ag tunnel junction.

As shown in figure 3.7, the loss tangent converges to the same value at the frequency of 1 MHz for the High Resistance State (HRS) and for the Low Resistance State (LRS). This fact stems from the inertial effects owing to ionization-deionization of the oxygen vacancies acting as interfacial states traps, in other words, at low frequencies the LCMO surface interfacial defects induced in the LCMO/PBCO interface are not relevant for the resistive switching and thus the conduction is dominated by the quantum tunneling through the defects (oxygen vacancies) inside the "bulk" PBCO barrier. Nevertheless, at high enough frequency (around 1 MHz), the LCMO surface states induced by the oxygen vacancies at the LCMO/PBCO interface may play a part in the partial frustration of the resistive switching effect, because of the ionization-deionization of the oxygen vacancies, which are very strong-frequency dependent, which mean to be the main mechanism of this resistive switching phenomenon [49].

Finally, we have performed I-V curves measurements at different temperatures in the range from 30 K to 100 K, depicted in figure 3.8:

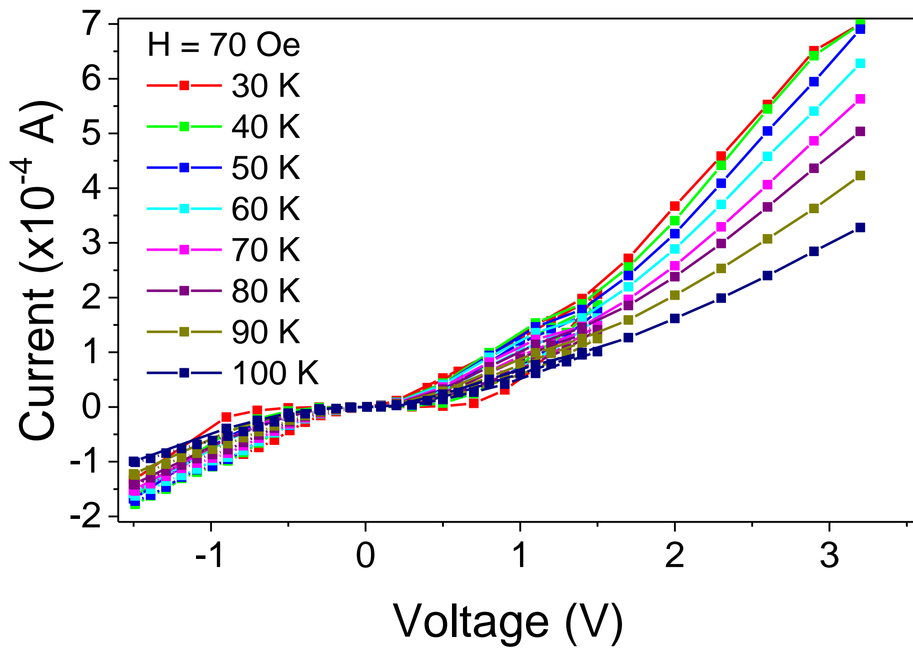

Figure 3.8 I vs V curves at temperatures ranging from 30K to 100K.

As revealed from a deeper inspection of figure 3.8, the Low Resistance State (High Conductive State) data can be fitted to the Child-Langmuir law [50, 51, 52] analogous to the electrons in a plane parallel vacuum diode [53] (ballistic conduction regime), which is a particular case of the Space-Charge Limited Currents (SCLC), whose carrier injection from the electrode is limited by the electric field of the accumulated space charges and the Fowler-Nordheim quantum tunneling in the tunnel junctions LCMO/PBCO/Ag. The Child–Langmuir Law fitting is depicted in figure 3.9:

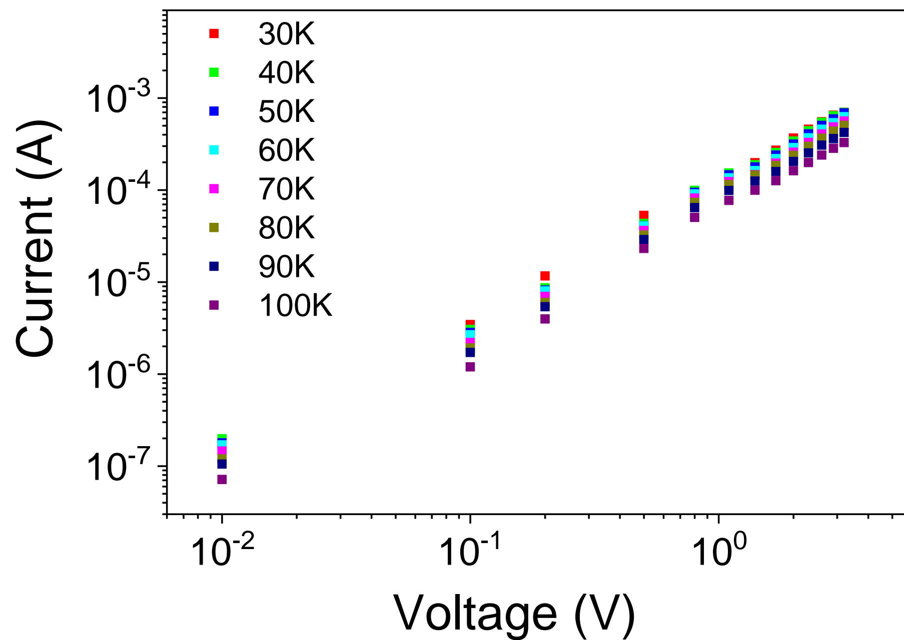

Figure 3.9 Child-Langmuir Law fitting.

$$I = \frac{9}{8}\varepsilon\varepsilon_0\theta\mu\frac{V^{\frac{3}{2}}}{d^2}$$

Equation 1. Child-Langmuir Law in analogy to electrons in a plane parallel vacuum diode [53] (ballistic conduction regime).

3.4 Appendix. Derivation of Child–Langmuir Law

When thermionic electrons are emitted from the metal surface (cathode), setting an anode at a distance $x = b$ at a potential difference V_A in vacuum. This potential attracts electrons from the cathode to the anode and electric current I_A flows from the anode to the cathode and the same holds for the current density J_A $[A/m^2]$. A cloud of thermally escaped electrons is formed on the surface of metal, so that the space around is non-uniformly filled with electrons. Thus, space charge density of electrons $n(x)$ $[m^{-3}]$ vary with x. Positive potential on $x = b$ pulls these electrons towards the anode. Electric current density of electrons is the following equation:

$$J = -en(x)v(x) = -J_A$$

Kinetic energy of electrons equals to:

$$\frac{1}{2}mv^2 = eV(x)$$

Knowing the potential $V(x)$, the velocity of electrons is calculated as the function of distance *x*:

$$v = v(x) = \sqrt{\frac{2}{m}V(x)}$$

Accelerating electrons constitute a steady current J_A so that $n(x)$ is decreasing and $v(x)$ is increasing towards anode. Thus, space charge density affects electric potential between cathode and anode, using Poisson´s equation:

$$\frac{\partial^2 V}{\partial x^2} = -\frac{\rho(x)}{\varepsilon_0}$$

Substituting the previous equations:

$$\frac{\partial^2 V}{\partial x^2} = -\frac{en(x)}{\varepsilon_0} = \frac{J_A}{\varepsilon_0 v(x)} = \frac{J_A}{\varepsilon_0\sqrt{\frac{2}{m}V(x)}}$$

The initial boundary conditions are the following:

$$\left(\frac{\partial V}{\partial x}\right)_{x=0} = 0$$

$$V(0) = 0$$

Solving differential equation, potential $V(x)$ is obtained:

$$V(x) = \left[\frac{9J_A}{4\varepsilon_0\sqrt{\frac{2e}{m}}}\right]^{\frac{2}{3}} \cdot x^{\frac{4}{3}}$$

Substituting the boundary conditions $V(b) = V_A$:

$$J_A = \left[\frac{4\varepsilon_0}{9b^2}\sqrt{\frac{2e}{m}}\right] V_A^{\frac{3}{2}}$$

Equation describes the relation between the current density J_A at any given voltage V_A. This result is known as Child's law or Child-Langmuir law. Extrapolating the Child-Langmuir law to the tunnel junction, the equation is given by:

$$I = \frac{9}{8}\varepsilon_r\varepsilon_0\theta\mu\frac{V^{\frac{3}{2}}}{d^2}$$

Where ε_r is the relative dielectric constant, ε_0 is the vacuum permittivity, μ is the charge mobility, θ is the ratio between free and trapped carriers, V is the voltage applied between the electrodes, d is the thickness of the dielectric. The Child-Langmuir law is, in turn, a particular case ($n = \frac{1}{2}$) of the more general Space Charge Limited Currents (SCLC) [54] where n is a parameter which varies between 0 and 3 depending on charge energy distribution:

$$I = \frac{9}{8}\varepsilon_r\varepsilon_0\theta\mu\frac{V^{n+1}}{d^{2n+1}}$$

To sum up, the conduction mechanism of the LCMO/PBCO/Ag tunnel junctions is predominantly the tunnelling of electrons hindered by traps localized in the CuO chains in the PBCO barrier. Could orbitronics be involved in the conduction through the CuO chains in the PBCO barrier?

In order to gain deeper insight in this kind of issue, it would be highly recommended to perform Ultraviolet Photoelectron Spectroscopy (UPS) and Near Edge X-Ray Absorption Fine Structure (NEXAFS) [55]. Nevertheless, the measurement of the Franz-Keldysh effect [56, 57] would clarify the electrostatic and chemical doping process.

The Franz-Keldysh effect consists of the redshift of the absorption edge in a Mott insulator induced by an electric field.

To start, an electrostatic-doping is induced in the Mott insulator due to the applied electric field. Consequently, the hole doping gives rise to the emergence of new

states within the Charge Transfer gap and the suppression of the spectral weight in the high energy region.

In other words, the Franz-Keldysh effect is the result of wavefunctions "leaking" into the Charge Transfer gap. Owing to the applied electric field, the free electron wavefunction associated to Ag and the free hole wavefunction associated to LCMO become Airy functions whose tails extends into the Charge Transfer gap, the more overlap there is between the free electron and hole wavefunctions, the stronger the optical absorption will be owing to the electron-hole recombination and the higher the tunneling current will be.

In conclusion, if a strong positive bias voltage is applied to our tunnel junction LCMO/PBCO bilayer. The dopants and traps associated with PBCO barrier will be de-ionized (electroforming), increasing the probability of overlap between the free electron and hole wavefunction because the recombined dopants and traps provide empty quantum interface states to make easier the delocalization of free electron and hole wavefunctions "tails" to overlap. So, the electron-hole recombination in the Schottky model framework is no longer necessary.

3.5 References

[1] L. Chua, "Memristor-The missing circuit element". *IEEE Trans. Circuit Theory* 1971, 18, 507.

[2] Y. V. Pershin, M. Di Ventra, "Memory effects in complex materials and nanoscale systems". *Adv. Phys.* 2011, 60, 145.

[3] S. H. Jo, T. Chang, I. Ebong, B. B. Bhadviya, P. Mazumder, W. Lu. "Nanoscale Memristor Device as Synapse in Neuromorphic Systems". *Nano Lett.* 2010, 10, 1297.

[4] J. J. Yang, D. B. Strukov, D. R. Stewart. "Memristive devices for computing". *Nat. Nanotechnol.* 2013, 8, 13.

[5] D. B. Strukov, G. S. Snider, D. R. Stewart, R. S. Williams. "The missing memristor found". *Nature* 2008, 453, 80.

[6] A. Asamitsu, Y. Tomioka, H. Kuwahara, Y. Tokura. "Current switching of resistive states in magnetoresistive manganites". *Nature* 1997, 388, 50.

[7] R. Waser, R. Dittmann, G. Staikov, K. Szot. “Redox-Based Resistive Switching Memories –Nanoionic Mechanisms, Prospects, and Challenges”. *Adv. Mater.* 2009, 21, 2632.

[8] S. H. Jo, W. Lu. “CMOS Compatible Nanoscale Nonvolatile Resistance Switching Memory”. *Nano Lett.* 2008, 8, 392.

[9] L. Goux, J. G. Lisoni, X. P. Wang, M. Jurczak, D. J. Wouters. “Optimized Ni Oxidation in 80-nm Contact Holes for Integration of Forming-Free and Low-Power Ni/NiO/Ni Memory Cells”. *IEEE Tran. Elec. Dev.* 2009, 56, 2363.

[10] A. S. Blum, J. G. Kushmerick, D. P. Long, C. H. Patterson, J. C. Yang, J. C. Henderson, Y. Yao, J. M. Tour, R. Shashidhar, B. R. Ratna. “Molecularly inherent voltage-controlled conductance switching”. *Nat. Mater.* 2005, 4, 167.

[11] A. Chanthbouala, V. Garcia, R. O. Cherifi, K. Bouzehouane, S. Fusil, X. Moya, S. Xavier, H. Yamada, C. Deranlot, N. D. Mathur, M. Bibes, A. Barthélémy, J. Grollier. “A ferroelectric memristor”. *Nat. Mater.* 2012, 11, 860.

[12] X. Wang, Y. Chen, H. Xi, H. Li. "Spintronic Memristor Through Spin-Torque-Induced Magnetization Motion". *IEEE Electron Dev. Lett.* 2009, 30, 294.

[13] H. Yamada, V. Garcia, S. Fusil, S. Boyn, M. Marinova, A. Gloter, S. Xavier, J. Grollier, E. Jacquet, C. Carrétéro, C. Deranlot, M. Bibes, A. Barthélémy. “Giant Electroresistance of Super-tetragonal BiFeO3-Based Ferroelectric Tunnel Junctions”. *ACS Nano* 2013, 7, 5385.

[14] W. G. Wang, M. Li, S. Hageman, C. L. Chien. “Electric-field-assisted switching in magnetic tunnel junctions”. *Nat. Mater.* 2012, 11, 64.

[15] Y.-H. Chu, L. W. Martin, M. B. Holcomb, M. Gajek, S.-J. Han, Q. He, N. Balke, C.-H. Yang, D. Lee, W. Hu, Q. Zhan, P.-L. Yang, A. Fraile-Rodriguez, A. Scholl, S. X. Wang, R. Ramesh. "Electric-field control of local ferromagnetism using a magnetoelectric multiferroic". *Nat. Mater.* 2008, 7, 478.

[16] V. Garcia, M. Bibes, L. Bocher, S. Valencia, F. Kronast, A. Crassous, X. Moya, S. Enouz-Vedrenne, A. Gloter, D. Imhoff, C. Deranlot, N. D. Mathur, S. Fusil, K. Bouzehouane, A. Barthélémy. “Ferroelectric Control of Spin Polarization”. *Science* 2010, 327, 5969.

[17] S. Valencia, A. Crassous, L. Bocher, V. Garcia, X. Moya, R. O. Cherifi, C. Deranlot, K. Bouzehouane, S. Fusil, A. Zobelli, A. Gloter, N. D. Mathur, A. Gaupp, R. Abrudan, F. Radu, A. Barthélémy, M. Bibes. "Interface-induced room-temperature multiferroicity in $BaTiO_3$". *Nat. Mater.* 2011, 10, 753.

[18] W. Luo, S. J. Pennycook, S. T. Pantelides. Magnetic "Dead" Layer at a Complex Oxide Interface. *Phys. Rev. Lett.* 2008, 101, 247204.

[19] M. Varela, Z. Sefrioui, D. Arias, J. Santamaria. "Intracell Changes in Epitaxially Strained $YBa_2Cu_3O_{7-x}$ Ultrathin Layers in $YBa_2Cu_3O_{7-x}/PrBa_2Cu_3O_7$ Superlattices". *Phys. Rev. Lett.* 1999, 83, 3936.

[20] F. A. Cuellar, Y. H. Liu, J. Salafranca, N. Nemes, E. Iborra, G. Sanchez-Santolino, M. Varela, M. Garcia Hernandez, J. W. Freeland, M. Zhernenkov, M. R. Fitzsimmons, S. Okamoto, S. J. Pennycook, M. Bibes, A. Barthélémy, S.G.E. te Velthuis, Z. Sefrioui, C. Leon, J. Santamaria. "Reversible electric-field control of magnetization at oxide interfaces". *Nat. Comm.* 2014, 5, 4215.

[21] J. S. Moodera, T. S. Santos, T. Nagahama. "The phenomena of spin-filter tunnelling". *J. Phys.: Condens. Matter* 2007, 19, 165202.

[22] X. Shen, Y. S. Puzyrev, S. T. Pantelides. "Vacancy breathing by grain boundaries—a mechanism of memristive switching in polycrystalline oxides". *MRS Commun.* 2013, 3, 167.

[23] X. Shen, K. Yin, Y. S. Puzyrev, Y. Liu, L. Sun, R.-W. Li, S. T. Pantelides. "2D Nanovaristors at Grain Boundaries Account for Memristive Switching in Polycrystalline $BiFeO_3$". *Adv. Electron. Mater.* 2015, 1, 1500019.

[24] Z. W. Xing, N. J. Wu, A. Ignatiev. "Electric-pulse-induced resistive switching effect enhanced by a ferroelectric buffer on the $Pr_{0.7}Ca_{0.3}MnO_3$ thin film". *Appl. Phys. Lett.* 2007, 91, 052106.

[25] D. Strukov, F. Alibart, R. S. Williams. "Thermophoresis/diffusion as a plausible mechanism for unipolar resistive switching in metal–oxide–metal memristors". *Appl. Phys. A* 2012, 107, 509.

[26] B. Vengalis, V. Lisauskas, V. Pyragas, K. Sliuziene, A. Oginskis, A. Cesnys, J. Santiso, A. Figueras. "Oxygen diffusion in $La_{2/3}Ga_{1/3}MnO_3$ and Sr_2FeMoO_6 thin films". *J. Phys. IV* 2001, 11, 209.

[27] K. H. Warnick, Y. S. Puzyrev, T. Roy, D. M. Fleetwood, R. D. Schrimpf, S. T. Pantelides. “Room-temperature diffusive phenomena in semiconductors: The case of AlGaN”. *Phys. Rev. B* 2001, 84, 214109.

[28] D. V. Lang. “Recombination-Enhanced Reactions in Semiconductors”. *Ann. Rev. of Mater. Sci.* 1982, 12, 377.

[29] N. Itoh, A. M. Stoneham, “*Materials modification by electronic excitation”*, Cambridge Univ. Press, Cambridge, UK 2001.

[30] D. S. Wang, R. Wu, A. J. Freeman. “First-principles theory of surface magnetocrystalline anisotropy and the diatomic-pair model”. *Phys. Rev. B* 1993, 47, 14932.

[31] S. Ikeda, J. Hayakawa, Y. Ashizawa, Y. M. Lee, K. Miura, H. Hasegawa, M. Tsunoda, F. Matsukura, H. Ohno. “Tunnel magnetoresistance of 604% at 300K by suppression of Ta diffusion in CoFeB/MgO/CoFeB pseudo-spin-valves annealed at high temperature”. *Appl. Phys. Lett.* 2008, 93, 082508.

[32] Y. Tokura, H. Kuwahara, Y. Moritomo, Y. Tomioka, A. Asamitsu. “Competing Instabilities and Metastable States in $(Nd, Sm)_{1/2}Sr_{1/2}MnO_3$”. *Phys. Rev. Lett.* 1996, 76, 3186.

[33] P. Schiffer, A. P. Ramirez, W. Bao, S.-W. Cheong. “Low Temperature Magnetoresistance and the Magnetic Phase Diagram of $La_{1-x}Ca_xMnO_3$”. *Phys. Rev. Lett.* 1995, 75, 3337.

[34] A. Hoffmann, S.G.E. te Velthuis, Z. Sefrioui, J. Santamaria, M. R. Fitzsimmons, S. Park, M. Varela. “Suppressed magnetization in $La_{0.7}Ca_{0.3}MnO_3/YBa_2Cu_3O_{7-\delta}$ superlattices”. *Phys. Rev. B* 2005, 72, 140407R.

[35] J. L. Cohn, M. Peterca, J. J. Neumeier. “Low-temperature permittivity of insulating perovskite manganites”. *Phys. Rev. B* 2004, 70, 214433.

[36] P. J. Hirst, R. G. Humphreys, in *Handbook of Superconducting Materials*, Vol. 1 (Eds. D. A. Cardwell, D. S. Ginley), CRC Press, Boca Raton, FL, USA 2003, p828.

[37] Y. Liu, F. A. Cuellar, Z. Sefrioui, J. W. Freeland, M. R. Fitzsimmons, C. Leon, J. Santamaria, S.G.E. te Velthuis. “Emergent Spin Filter at the Interface between Ferromagnetic and Insulating Layered Oxides”. *Phys. Rev. Lett.* 2013, 111, 247203.

[38] J. Y. T. Wei, N.-C. Yeh, R. P. Vasquez, A. Gupta. “Tunneling evidence of half-metallicity in epitaxial films of ferromagnetic perovskite manganites and ferrimagnetic magnetite”. *J. Appl. Phys.* 1998, 83, 7366.

[39] J. He, A. Borisevich, S. V. Kalinin, S. J. Pennycook, S. T. Pantelides. “Control of Octahedral Tilts and Magnetic Properties of Perovskite Oxide Heterostructures by Substrate Symmetry”. *Phys. Rev. Lett.* 2010, 105, 227203.

[40] G. Radaelli, D. Petti, E. Plekhanov, I. Fina, P. Torelli, B. R. Salles, M. Cantoni, C. Rinaldi, D. Gutiérrez, G. Panaccione, M. Varela, S. Picozzi, J. Fontcuberta, R. Bertacc, “Electric control of magnetism at the Fe/BaTiO3 interface”. *Nat. Comm.* 2014, 5, 3404.

[41] P. Ravindran, R. Vidya, A. Kjekshus, H. Fjellvag, O. Eriksson. “Theoretical investigation of magnetoelectric behavior in $BiFeO_3$”. *Phys. Rev. B* 2006, 74, 224412.

[42] P. Perna, L. Mechin, M. P. Chauvat, P. Ruterana, Ch. Simon, U. Scotti di Uccio. “High Curie temperature for $La_{0.7}Sr_{0.3}MnO_3$ thin films deposited on CeO_2/YSZ-based buffered silicon substrates”. *J. Phys.: Condens. Matter* 2009, 21, 306005.

[43] J. P. Perdew, K. Burke, M. Ernzerhof. “Generalized Gradient Approximation Made Simple”. *Phys. Rev. Lett.* 1996, 77, 3865.

[44] G. Kresse, D. Joubert. “From ultrasoft pseudopotentials to the projector augmented-wave method”. *Phys. Rev. B* 1999, 59, 1758.

[45] G. Kresse, J. Furthmuller. “Efficient iterative schemes for ab initio total-energy calculations using a plane-wave basis set”. *Phys. Rev. B* 1996, 54, 11169.

[46] A. I. Liechtenstein, V. I. Anisimov, J. Zaane. “Density-functional theory and strong interactions: Orbital ordering in Mott-Hubbard insulators”. *J. Phys. Rev. B* 1995, 52, R5467.

[47] S. L. Dudarev, G. A. Botton, S. Y. Savrasov, C. J. Humphreys, A. P. Sutton. “Electron-energy-loss spectra and the structural stability of nickel oxide: An LSDA+U study”. *Phys. Rev. B* 1998, 57, 1505.

[48] R. Fehrenbacher and T. M. Rice. “Unusual Electronic Structure of $PrBa_2Cu_3O_7$”. Phys. Rev. Lett. 70, (1993).

[49] Rickard Fors, Sergey I. Khartsev, and Alexander M. Grishin. “Giant resistance switching in metal-insulator-manganite junctions: Evidence for Mott transition”. Phys. Rev. B 71, 045305 (2005).

[50] Woo-Young Yang, Wan-Gee Kim, Shi-Woo Rhee. “Radio frequency sputter deposition of single phase cuprous oxide using Cu_2O as a target material and its resistive switching properties”. *Thin Solid Films* 517 (2008) 967–971.

[51] S. Tsui, A. Baikalov, J. Cmaidalka, Y. Y. Sun, Y. Q. Wang, and Y. Y. Xue, C. W. Chu, L. Chen and A. J. Jacobson. “Field-induced resistive switching in metal-oxide interfaces”. *Appl. Phys. Lett.*, 85, 317 (2004).

[52] Murray A. Lampert. “Simplified Theory of Space-Charge-Limited Currents in an Insulator with Traps”. *Phys. Rev.* 103, 6, (1956).

[53] http://mafija.fmf.uni-lj.si/seminar/files/2007_2008/Thermionic_emission.pdf

[54] Adam Koszewski, Frederic Souchon. “Conduction and Trapping in RF MEMS Capacitive Switches with a SiN Layer”. IEEE Proccedings 2009.

[55] Hong Sub Lee, Sun Gyu Choi, Hyung-Ho Park & M. J. Rozenberg. “A new route to the Mott-Hubbard metal-insulator transition: Strong correlations effects in $Pr_{0.7}Ca_{0.3}MnO_3$”. Nat. Sci. Rep. (2013).

[56] M. Nakamura, A. Sawa, H. Sato, and H. Akoh, M. Kawasaki, Y. Tokura. “Optical probe of electrostatic-doping in an *n*-type Mott insulator”. Phys. Rev. B 75, 155103 (2007).

[57] Masao Nakamura, Masashi Kawasaki, and Yoshinori Tokura. “*eg*-level splitting in a layered perovskite manganite as revealed by charge modulation spectroscopy”. Phys. Rev. B 86, 125127 (2012).

Chapter 4. Density functional theory calculations of BTO-metal interfaces, and parent compounds

One of the aims in this PhD. thesis is to unravel the complex but rich interactions between $BaTiO_3$ (BTO) and metals (M). These systems bring novel phenomena into play such as resistive switching, inversion of TMR sign, existence of very unstable ferroelectric charged domain walls, etc. There is an inherent complexity in these phenomena since they involve the interplay of different degrees of freedom at different levels such as atomic, electronic, orbital and spin. In order to unravel the mechanisms behind those properties we are going to take advantage of the predicting properties of first principle calculations. In this chapter we compile a systematic density functional theory (DFT) study of BTO-M interfaces for a diverse set of metals: $La_{1-x}Sr_xMnO_3$ (LSMO), Cobalt (Co) and Silver (Ag). First we will describe the structural and electronic properties of ideal bulk crystal of the three metals and the BTO. At this point we will discuss our results at the light of previous works in the literature to quantify the prediction potential of density functional theory (DFT) and characterize about its limitations [1]. Some of them, related to the local or semi-local functionals range, will be partially amended using the Hubbard (U) correction providing the theoretical tools required to study more complex systems, such as moderately correlated oxides [2]. Afterwards we will consider the most frequently observed defects that modify key properties on each bulk system. Then, we will proceed to study low dimensional BTO [001] surfaces which will highlight the type of models we will have to build up when studying the BTO-M [001] heterostructures. Finally we will take advantage of all the knowledge acquired in previous sections of this chapter to describe the main features involved in the phenomena observed in BTO-M complex interfaces with defects, whose experiments will later be discussed in chapters 5 and 6.

Density functional calculations were performed using the Vienna *ab-initio* simulations package (*VASP*) [3-5], within the GGA semi-local exchange correlation functional. Additionally for the purpose of correcting the band gap problem due to correlation deficiencies of DFT we use the Hubbard U correction in the Dudarev implementation [6]. In this rotationally invariant approach Dudarev

perform corrections to the L(S)DA energy only through the effective correction parameter $U_{eff} = U - J$ and not independently on the U and J. The used U_{eff} value will be discussed throughout the text and abbreviated as U. All calculations were relaxed for both atomic positions and lattice parameters, unless otherwise specified, till the Hellmann–Feynman forces on the ions were less than 15 meV/Å. In all the DOS plots, the "a.u." units stands for arbitrary units. Since we are finally interested in performing heterostructures calculations with $SrTiO_3$ (STO) as substrate. The in-plane parameters of related calculations will be constrained to the 3.905 Å bulk STO value. More details about this will be given.

4.1 Bulk Properties:

Unless specified otherwise, for the unit cell bulk calculations of the relaxed structure, we have used 350 eV energy cut off (E_{cut}) and a k-mesh of 8x8x8 in the Monkhorst–Pack grid notation or similar mesh densities for large cells, which have been confirmed to be converged performing calculations with E_{cut} of 450 eV and 18x18x18 meshes. For the electronic properties calculations, such as the density of states, we have used a larger 12x12x12 k-mesh for the unit cell or similarly scaled for larger cells. The calculation size and atom number per unit cell will be specific and clarified for each study performed.

4.1.1 Metals:

4.1.1.1 Ag:

Silver is a noble metal with the electronic configuration given by [Kr] 4d10 5s1, therefore its properties mostly dependent on the s-orbital. Ag has a face centered cubic (FCC) structure with lattice parameter of of 4.07 Å [7], see figure 4.1 for an atomic structure sketch. Due to the fact of its large lattice parameter and a relatively low interaction Ag is a catalytic oxidation reactive which tends to adsorb or oxidize very easily in the closest monolayers to the surface [8]. Such exposed surface provides to the BTO-Ag interfaces a drain of oxygen and therefore in this interface Ag behaves as an oxygen vacancy source. This characteristic of the BTO-Ag interface will be taken into account in our interface models by means of introducing oxygen atoms in the Ag close by the interface. They are the well-known oxygen interstitials which are the most frequent defects one may observe in low dimensional Ag structures [9].

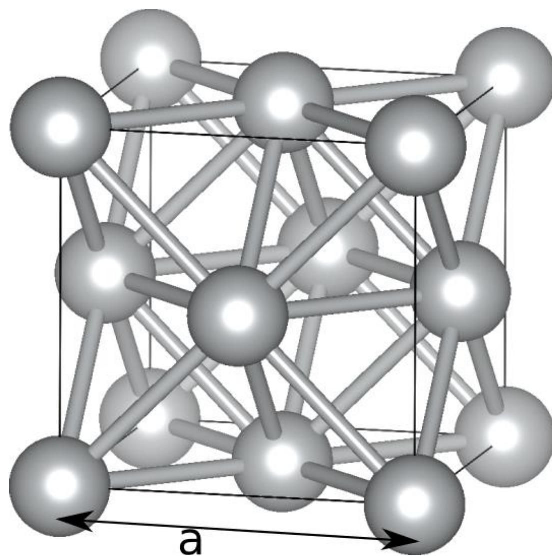

Figure 4.1 Atomic structure sketch of the Ag face centered cubic (fcc) structure.

In the bulk Ag calculation the lattice parameter we obtain is 4.15 Å, which is in agreement with similar DFT calculations [7]. The electronic structure is depicted in figure 4.2 in the form of density of states (DOS).

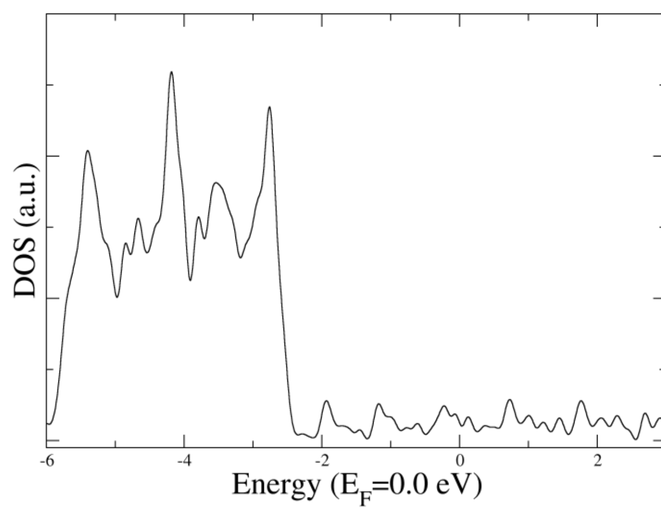

Figure 4.2 Total DOS of fcc Ag bulk.

Notice in figure 4.2 the d-orbitals are fully filled up and they are at -2.5 eV, approximately, below the Fermi level and above the s-orbital extends and influences the Ag properties.

4.1.1.2 Co:

Cobalt's electronic structure is [Ar] 3d7 4s2 and then its electronic properties will be mostly given by the d orbitals. Co is one of the few natural ferromagnets which have the largest Curie temperature, 1388 K [10]. This confers the Co with great potential in magnetic applications such as spintronics, spin-valves, magnets… etc. Co crystallizes in the hexagonal closed packet (HCP) structure. Co is also a catalytic oxidation reactive, therefore attracting the oxygen in the surroundings and generating oxygen vacancies. With large enough acquisition of oxygen Co may generate one or several oxide layers which can critically impact the performance of its electronic and magnetic properties as it will be discussed in the final subsection of chapter 6. Besides the occurrence of reaction-related processes the Co properties depend on the values of the Hubbard (U) parameter.

The experimental lattice parameters of the Co are $a = 2.50$ Å, $c = 4.07$ Å, with a c/a ratio equal to 1.628 [11], very close to the highest density HCP stacking (1.633). The lattice parameters we obtain as a function of the U parameter can be seen in figure 4.3.

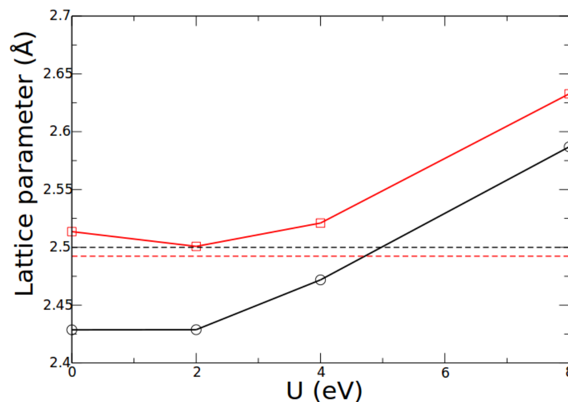

Figure 4.3 Lattice parameters a (black) and c/1.633 (red) as a function of the U value compared to the experimental values (in dashed lines).

From figure 4.3 we can observe that the *a* parameter increases when increasing the U value reaching the experimental one around $U = 5\ eV$. The *c/a* ratio is around 3% larger than the ideal 1.633 factor which is expected from GGA calculations [12]. The value we choose for future calculations is $U = 2.0\ eV$ based on a compromise agreement with the experimental *a* and *c/a* values.

The electronic structure for the ground state with $U = 2\ eV$ is depicted in figure 4.4.

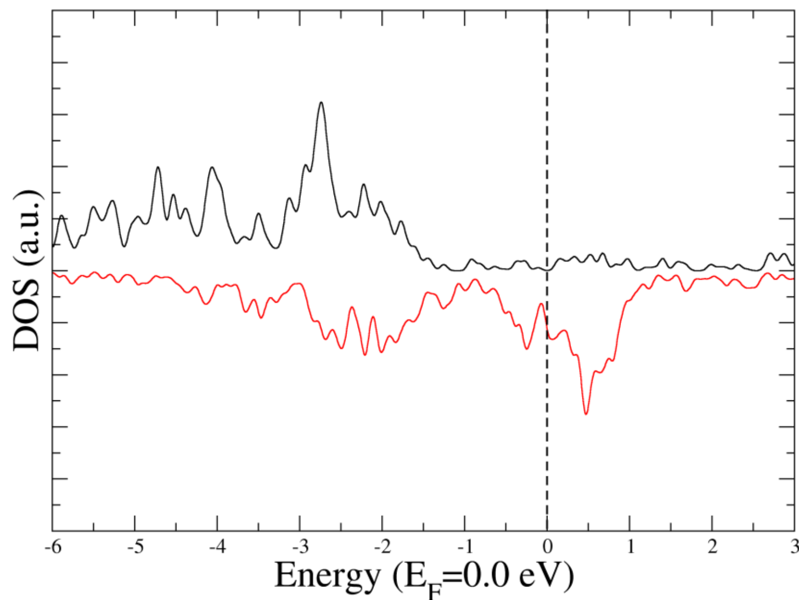

Figure 4.4: Total DOS of Co hcp bulk for U = 2 eV.

The main structural modification which may happen for Co in an oxygen environment is that the outer surface layer(s) becomes CoO, as it was commented and which will be discussed in the next section.

4.1.1.3 LSMO:

The manganites ($La_{1-x}Sr_xMnO_3$) are perovskites compounds (ABO_3) which two cations: La and Sr present in the A position. They are well known compounds used in spintronics since they have a very complex phase diagram which includes diverse magnetic phases accessible either by varying the La/Sr ratio or the temperature [13]. We will be particularly interested in $x = 0.3$ $La_{0.7}Sr_{0.3}MnO_3$ (LSMO) since this compound is a half-metal with only the majority spin contributing to the electronic properties at the Fermi level. The Curie temperature is 378.1 K and its most stable crystal structure (for T<425 K) in bulk is the rhombohedral with space group R3c. However, when grown in thin films and heterostructures on cubic substrates such as $SrTiO_3$ (STO) the LSMO adopts a tetragonal or pseudocubic phase [14].

For the sake of comparison we have computed the rhombohedral and cubic structures and compare their electronic structure to obtain an idea of the electronic variation when structurally constraining the LSMO in-plane.

Pseudo-cubic structure $La_{0.75}Sr_{0.25}MnO_3$ calculations are performed with 8 units cells (2x2x2) and rhombohedral structure with 6 units cells and $La_{0.67}Sr_{0.33}MnO_3$ stoichoimetry, which are large enough supercells that allows for full degrees of freedom in the relaxation and therefore access to realistic ground state properties. We obtain for the rhombohedral structure the lattice parameters $a = 5.54$ Å and $c = 13.41$ Å while for the pseudo-cubic structure $a = 3.87$ Å and $a/c = 0.976$. The density of states comparing the pseudo-cubic $La_{0.75}Sr_{0.25}MnO_3$ and rhombohedral $La_{0.67}Sr_{0.33}MnO_3$ stoichiometries is depicted in figure 4.5.

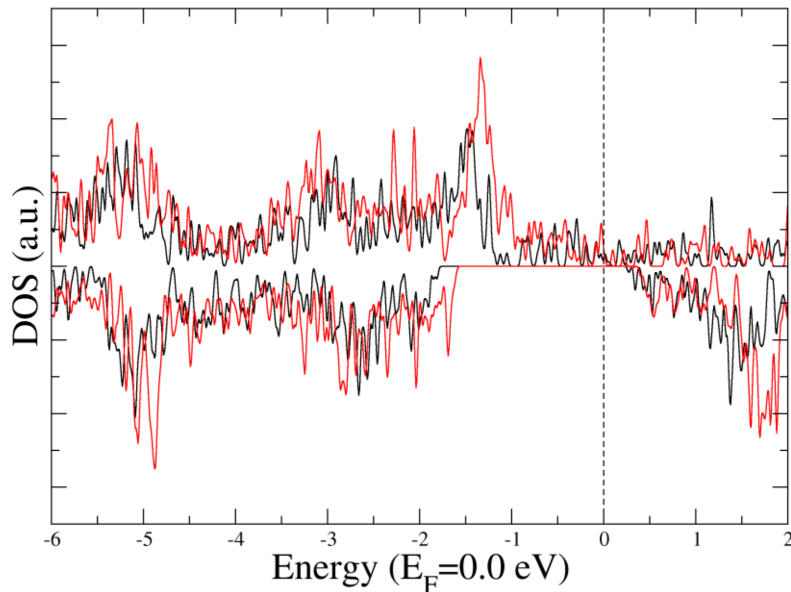

Figure 4.5 DOS for the cubic (red) and rhombohedral (black) phase of LSMO.

From figure 4.5 we can observe that the two structures show very similar electronic features with the rhombohedral structure shifted towards positive energies due to the fact that the La/Sr ratio is larger. This fact is addressed in section 4.2.3 where the role of the La/Sr will be discussed more extensively. The slight electronic differences between both phases support the fact that under epitaxial strains the LSMO adopts the tetragonal or pseudocubic phase.

4.1.2 Bulk BTO:

We have performed DFT calculations in bulk $BaTiO_3$ (BTO) in order to study the relation between the atomic and electronic structure at different configurations such as elastic strain, electronic correlations and structural defects, for that we have varied the in-plane lattice parameter, the U values and the presence of oxygen vacancies.

BTO crystallizes in a cubic structure, which show isotropic properties along x,y and z directions. The Ti-O-Ti bonds orientate along each of the three directions

showing equal atomic distances and so structural and electronic properties [15]. At lower temperature (104 ºC) the most stable symmetry of BTO becomes tetragonal with an elongated c lattice vector versus the a value. For the tetragonal structure the Ti-O-Ti distances along z are larger than along x or y. The degree of tetragonality (*c/a*) is larger for larger differences between the z (c) and the x, y (a) cartesian axes (lattice parameters). The tetragonal structure can be characterized by the *a, c* lattice parameters and a ferroelectric distortion (δ) which is the z displacement between the oxygen and Ti in the TiO_2 plane (also to be referred as O-B distance). Besides those parameters, specially c and d, we will pay particular attention to the role of each of the planes along the (001) which are the BaO and TiO_2 planes. We obtain after BTO relaxation in a 2x2x2 supercell that the crystal structure is tetragonal with $a = 3.99$ Å and $c = 4.14$ Å, which agrees well with other theoretical simulations as well as experimental values [16]. For bulk we obtain that δ is approximately 0.17 Å, which compare well with similar calculations [17] but it is slightly overestimated, as expected using GGA functional for the exchange-correlation, with respect to the bulk value of 0.12 Å [18]. Similarly for thin films of BTO deposited on STO, the δ value is 0.12 Å [19]. In figure 4.6 we can observe the crystal structure together with *a, c* and the δ parameter for the tetragonal phase.

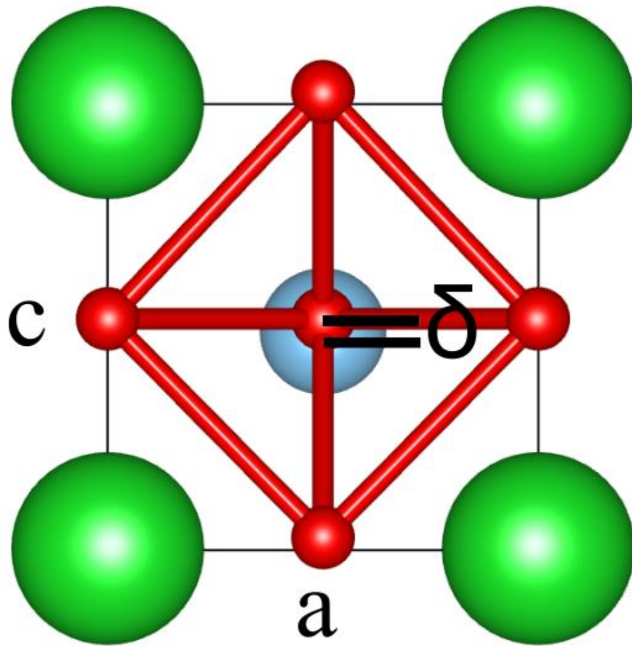

Figure 4.6 Lattice parameters (*c, a*) and δ ferroelectric displacement in the tetragonal unit cell of BTO. Green, blue and red circles corresponds to Ba, Ti and oxygen atoms. This colour coding will be employed throughout the text.

For latter comparison to the relaxation trend observed in surfaces and interfaces we have also considered to set a compressive strain to the BTO corresponding to the structural constraint generated due to the $SrTiO_3$ (STO) substrate, whose experimental cubic lattice parameter is $a = 3.905$ Å [20]. This case will be mostly relevant for the discussion of epitaxial growth of BTO on STO substrate. However the elastic response of the BTO material, e.g. c and δ parameters, depends on the describing theory, which we will focus on the evolution with U values. Such dependency of c and δ vs U is illustrated in figure 4.7.

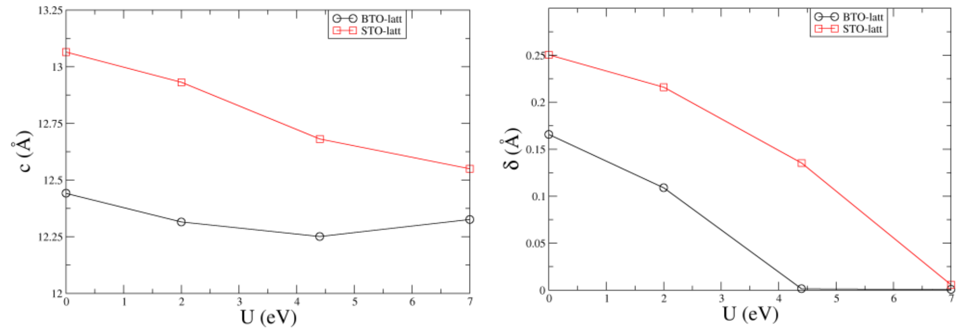

Figure 4.7 c (left) and δ (right graph) of the BTO bulk as a function of the U correction for strain conditions of either BTO or STO in-plane parameters.

The two types of in-plane settings for the calculations, BTO relaxed $(a = 3.94\ \text{Å})$ or in-plane compressed to the STO value $(a = 3.905\ \text{Å})$ will be considered and referred thought-out the text as with BTO or STO lattice parameters, respectively. When setting different *a* values (either BTO or STO), we observe that for higher U values, the parameters c and δ are reduced except for an overcorrection at large U values for BTO lattice parameter which show no meaningful results. δ displacement is on the other hand progressively reduced to zero, which occurs at U = 4.4 or 7.0 for the BTO or STO in-plane respectively. We can observe that the closest δ value to experiments $(\delta = 0.12\ \text{Å})$ result at U = 2.0 or 4.4 for the BTO or STO in-plane, respectively. Therefore depending on the type of calculation we perform, either bulk, surface or interface, we should choose the U value accordingly. For the STO in-plane constraints, such as in surfaces and interfaces, the employed U value is 4.4 eV for Ti 3d electrons, choice which has also been employed in previous works [21] [22].

Although the U parameter also exerts an effect on the atomic structure of the BTO lattices, originally U is included to correct the underestimation of the band gap through increasing the electronic correlation in one-body simulations (such as DFT). In figure 4.8 we include the projected density of states to the BaO and TiO_2 plane, which is further decomposed into orbitals.

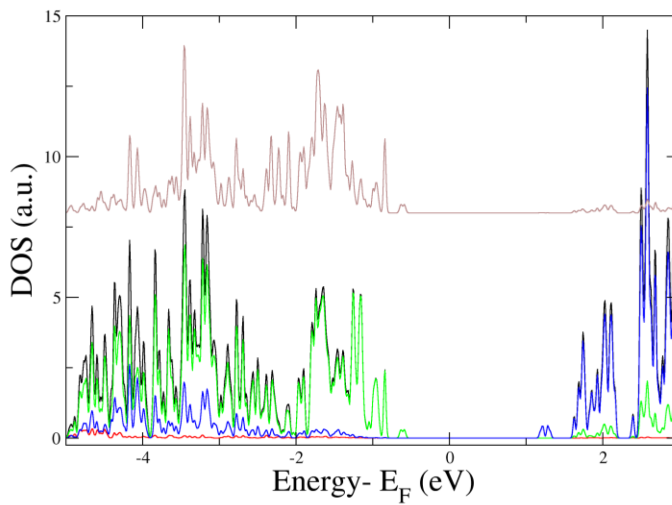

Figure 4.8: Projected DOS to the BaO plane (upper brown curve) and TiO_2 plane (lower curves) which include the total, s, p and d orbitals in black, red, green and blue respectively.

As we observe in figure 4.8, BTO is an insulator with the Fermi level quite centered in the middle of the gap which is just a convention within the calculation. Both BaO and TiO_2 planes have contribution to the valence band while the bottom of the conduction band is mostly located at the Ti-d orbital, with some hybridization to the O-p orbital, specifically in the TiO_2 plane (green curve) and the BaO plane (grey curve). If we apply a correction with U = 0.0, 2.0, 4.4 and 7 eV, we can observe the evolution of the total density of states and band gap in figure 4.9.

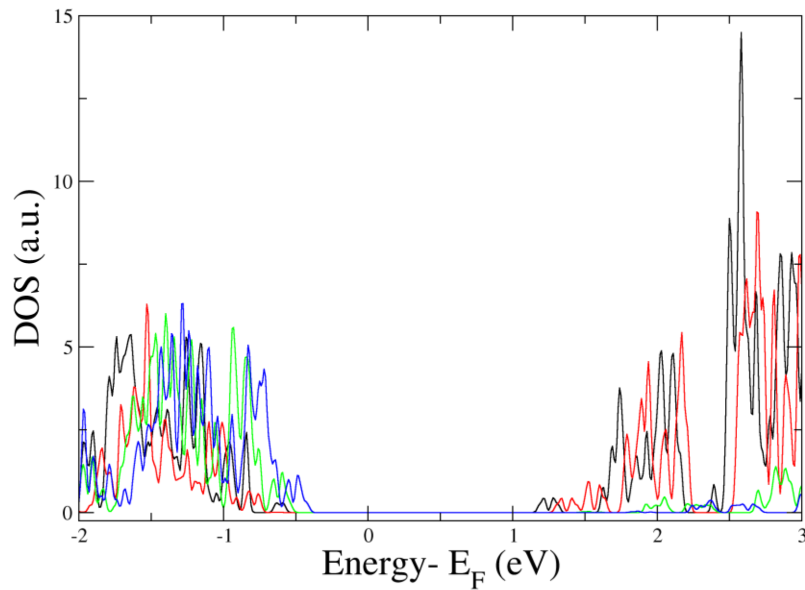

Figure 4.9 Total DOS for the U = 0.0, 2.0, 4.4, and 7 eV, depicted in black, red, blue and green respectively.

As can be observed from figure 4.9 both the valence and conduction band are shifted to larger energy values upon increasing the U value from 0 to 7 eV, however the conduction shift is much larger which efficiently increases the BTO band gap from 1.7 to 2.4 eV respectively.

4.1.2.1 Born Charges:

We have also computed the $BaTiO_3$ Born effective charges [19] in the ferroelectric tetragonal phase at the equilibrium STO in-plane unit cell parameter by relaxing both, the atomic positions and out of plane unit cell parameter. The Born charge components along the ferroelectric direction are 2.74 e^- for Ba, 5.27 e^- for Ti and −1.91 e^- and −4.17 e^- for O ions in the TiO_2 (O⊥) and BaO (O∥) planes respectively, close to the values reported previously [23]. We have also calculated the Born charges corresponding to the tetragonal phase at two different experimental unit cell parameters for a Cartesian axis with the z axis pointing in

the ferroelectric direction. For this choice, all the charge tensors are diagonal. The calculated values, which agree reasonably with those previously reported, are supplied in Table 1. As discussed by Ghosez et al., $BaTiO_3$ Born charges are strongly dependent on the structural features [27]. The charges of Ba and O (at the TiO_2 planes) remain almost unchanged in both structures while strong modifications are observed for Ti and O (at the BaO planes). Similar behavior was reported in the orthorhombic and rhombohedral ferroelectric phases of $BaTiO_3$ [24].

	Exp1 [1]	Exp2 [2]	Theor. [3]
$O_{\parallel}$	(-1.96 -1.96 4.53)	(-2.00 -2.00 4.65)	(-1.99 -1.99 -4.73)
$O_{\perp}$	(-2.07 -5.00 -1.96)	(-2.07 -5.07 -1.98)	(-2.14 -5.53 -1.95)
Ti	(6.31 6.31 5.62)	(6.40 6.40 5.81)	(6.94 6.94 5.81)
Ba	(2.73 2.73 2.81)	(2.75 2.75 2.80)	(2.72 2.72 2.83)
P	0.278	0.252	0.286

Table 4.1 Calculated Born effective charges and Polarization in C/m2, in the tetragonal ferroelectric phase of bulk $BaTiO_3$, for different structural parameters; Exp1 and Exp2 correspond to the experimental parameters of references [25] and [26], respectively and Theor. to previously reported theoretical calculations [27]. Tensors are given in Cartesian coordinates, with the z axis along the ferroelectric direction. For all the atoms the tensors are diagonal. O|| and O⊥ stands for oxygen in the BaO, and TiO_2 planes, respectively.

Local polarization P(z) can be obtained from the atomic displacements measured from annular bright-field images (figure 5.3) and Born charges:

$$P(z) = \frac{e}{V} \sum_{m=1}^{N} Z_m \delta z_m$$

Where Z_m denotes the Born effective charge whose index m runs over the different atoms of the unit cell and δz_m is the displacement of the mth atom respect its centrosymmetric position; z is the position of the Ba-centered unit cell, V is volume and e the electronic charge. Using the effective Born charges obtained from the calculations (Fig. 5.3), resulting in $P = 24\ Cm^{-2}$, which is very close to the bulk polarization of barium titanate (BTO), $P = 26\ Cm^{-2}$.

4.2 Most typical chemical modifications.

While the bulk materials Ag, Co and LSMO exhibit well defined metallic nature, the bulk BTO exhibits well defined dielectric nature. The inclusion of structural defects/dopants makes the parent compound properties may change in

such a way that structural and electronic modifications take place. In this sub-section, we consider the most relevant atomic and electronic perturbations to the parent compounds that may be responsible for specific effects at the more complex interface calculations.

4.2.1 Ag: Oxygen interstitials.

As previously explained, silver is a well known catalytic oxidation reactive which tends to incorporate oxygen within its structure in surfaces and interfaces. We have considered interstitial oxygens in a c(1x1) 9 monolayers (ML) surface calculation by including an oxygen atom between the first and second outermost ML and compared the electronic structure to that of the ideal oxygen-free surface, see figure 4.10.

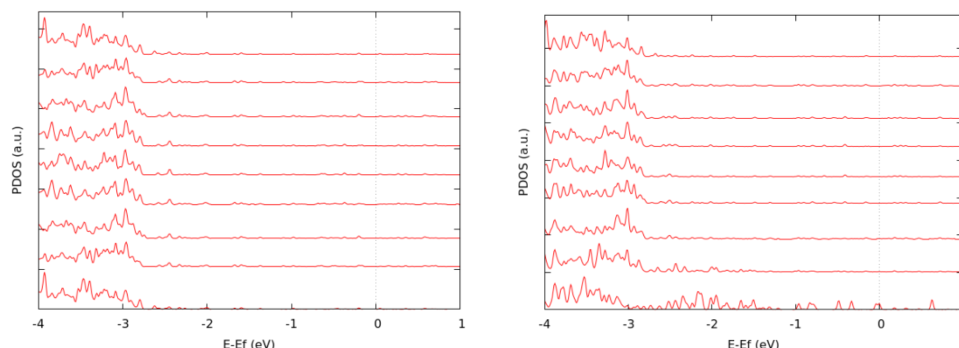

Figure 4.10 d-orbital PDOS projected along the 9 ML of the surface (bottom and top are the most surfacial) for the ideal oxygen-free surface (left) compared to a incorporation of one oxygen atom between the first and the second outermost planes (right).

From Figure 4.10 (left graph) we observe that there are no d-states near the E_F for the pristine Ag surface. However, when one oxygen interstitial is included (bottom plane at the right graph), the hybridization with the O p-orbitals makes the Ag d-orbitals (eg type) populates states at and near the Fermi level. This affects the conduction and excitation properties due to the available states (throughout few hundreds of meV) with a different orbital nature than the s-orbital observed for defect free configurations (left figure 4.10).

4.2.2 Co: Oxidation of the outer monolayer.

When the metal has a strong affinity to the oxygen, as it is the case for

Cobalt, often one can find that the metal layers closest to the surface or interface are structurally modified to accommodate the abundant presence of the oxygen which may end forming the corresponding monoxide (CoO). Cobalt monoxide is a Mott-insulator with a band gap of approximately 2.4 eV [28] showing antiferromagnetic order with a Neel Temperature of 291 K [29].

We calculate the CoO bulk phase to account for the oxidation of Co at the BTO interface. We enforce the STO in-plane lattice parameter, allowing full relaxation of the atomic positions and the out-of-plane direction. We use a U correction of 6 eV obtaining an AFM order with a band gap of 1.0 eV and a Co spin moment of $2.9\mu_B$ which reasonably compares well with previous calculations performed within the VASP code [30] where even higher U values are considered.

4.2.3 LSMO: Sr/La ratio.

$La_{1-x}Sr_xMnO_3$ is a disordered alloy pertaining the La/Sr location. While the size of both cations is very similar, Sr being a slightly larger, the oxidation state varies which consequently alters the Mn oxidation state ranging from +3 to +4 from a Sr-poor $(x = 0)$ to Sr-rich $(x = 1)$ concentrations. Using the above mentioned pseudo-cubic structure we can study how the La/Sr ratio influences the electronic and magnetic properties of the $La_{1-x}Sr_xMnO_3$, ranging from x = 0 to 0.75. It is beyond the scope of this section to investigate the antiferromagnetic orthorhombic phase of $LaMnO_3$ $(x = 0)$, but just get an insight about how the La/Sr ratio modifies the DOS and the spin polarization of the Mn in the ferromagnetic pseudo-cubic $La_{1-x}Sr_xMnO_3$ phase.

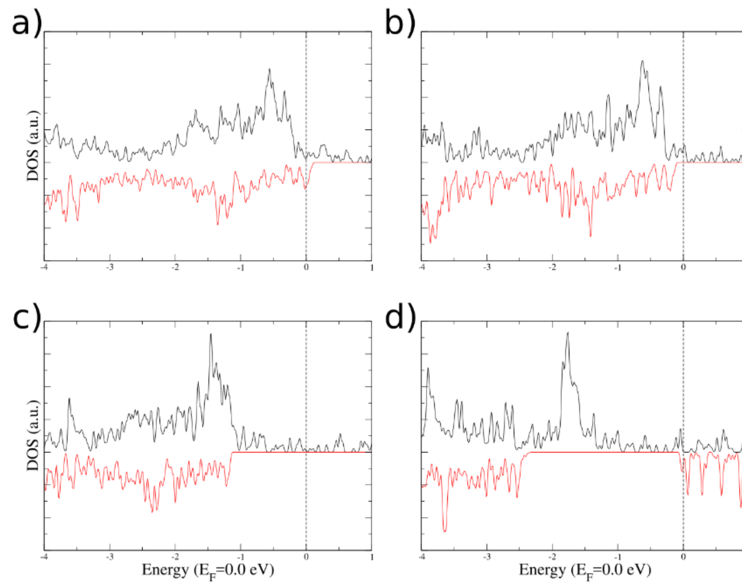

Figure 4.11 DOS for pseudo-cubic $La_{1-x}Sr_xMnO3$ with different Sr concentrations (x values): a) 0.75, b) 0.50, c) 0.25 and d) 0.0.

In figure 4.11, the most important orbital contributing to the electronic structure around the Fermi level is the Mn 3d-orbital. It can be observed that increasing the La (Sr) concentration increases the number of electrons (holes) in the system, as expected from the lower Sr^{2+} oxidation state compared to La^{3+}, populating mostly the majority spin channel. Between x = 0.25 and 0.5, figure 4.11 b and c, notice that the system is half-metal with only the majority spin channel contributing to the conduction. This agree well with the phase diagram of $La_{1-x}Sr_xMnO_3$ which show a half metallic phase around x = 0.33 approximately [31]. We can also observe that since both spin channels are not equivalently populated the value of the Mn spin polarization varies with Sr concentration, which we have depicted in figure 4.12.

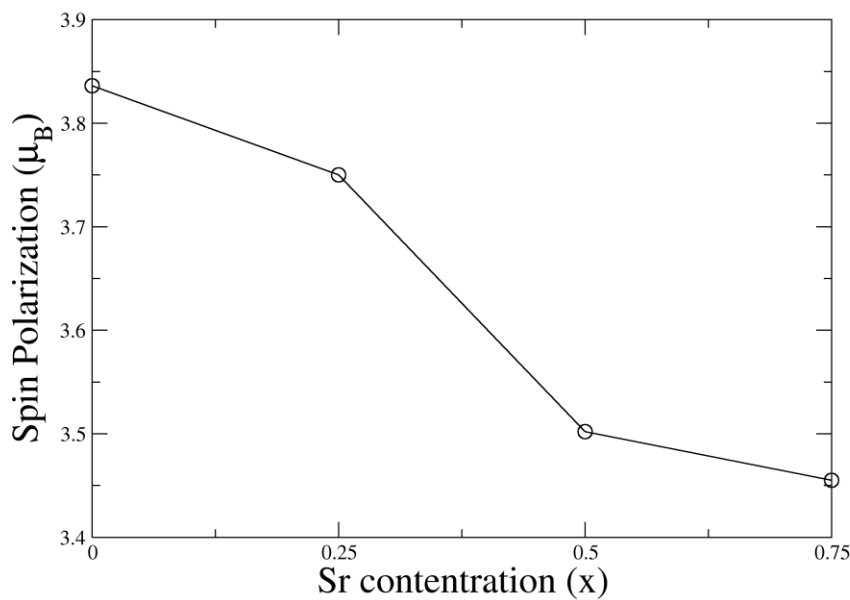

Figure 4.12: Mn spin polarization in pseudo-cubic $La_{1-x}Sr_xMnO_3$ versus the Sr concentration (x).

In figure 4.12 there is a clear relation between the Mn spin polarization and the cation La/Sr ratio. For x between 0.25 and 0.5 there is only Mn spin majoritary contribution so the cation variation implies Mn oxidation state modification that efficiently alters its spin polarization (large negative slope in figure 4.12). For lower and higher values that this interval the minoritary contribution becomes comparable to the majoritary therefore considerably reducing the slope.

4.2.4 BTO: Oxygen vacancies.

It is well known that $BaTiO_3$ properties strongly depends on the growth conditions, in particular to the oxygen partial pressures which generate oxygen vacancies in the dielectric [32]. Realistic vacancy concentrations in $BaTiO_3$ are diluted (around $10^{22}\ vacancies/cm^3$ [33]) so the periodic simulation cell to model oxygen vacancies on BTO have to be large enough for two first neighbours vacancies not to interact with each other, avoiding overlapped structural and electronic effects. We have considered 2x2x2 or 3x3x3 times the primitive cell

resulting in 40 or 135 atoms respectively. Generally the 2x2x2 exhibits qualitative agreement with the 3x3x3 however there are some quantitative differences. If not mentioned otherwise the 3x3x3 cell will be the one discussed for the BTO with vacancies. The oxygen vacancy (OVac) can reside either at the BaO plane or TiO_2 plane, BaO or TiO_2 respectively from now on. The OVac at the TiO_2 (BaO) plane detach the Ti-O-Ti bond line along the x, y (z) directions which are different only due to the tetragonality of the structure, compared to the isotropic cubic structure. We include in figure 4.13 the c and δ as a function of the U value for the two oxygen vacancy location, both the BaO and TiO_2 plane.

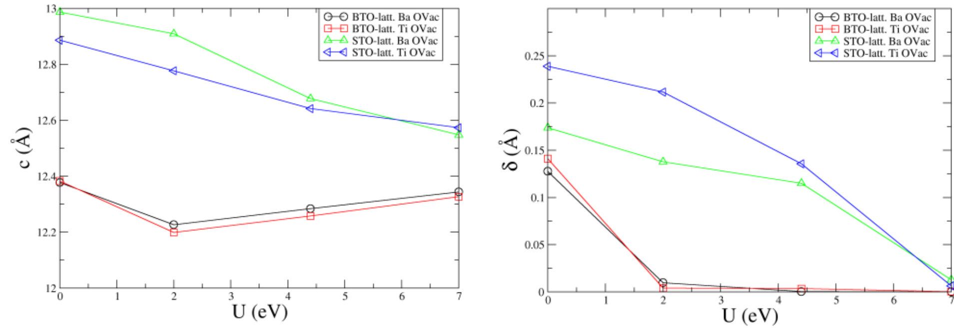

Figure 4.13 c (left) and δ (right graph) of the BTO bulk with OVac as a function of the U correction for strain conditions of either BTO or STO in-plane parameters.

We observe that increasing the U value gradually decreases the c lattice parameter similar to the pristine BTO. However, for large values ($U \geq 4.4\ eV$) and BTO in-plane conditions, there is an overcorrection indicating that these are non-realistic results. The δ value continuously decreases to zero at U= 2.0 or 7.0 for the BTO or STO in-plane lattice parameters respectively. These same trends were exhibited by the BTO in the case without vacancies, showing the overcorrection and zero δ value at higher U, where we again evidence the different appropriate value for BTO or STO constrained calculations. The appropriate value for STO-constrained calculations is U = 4.4 eV, as it was without the oxygen vacancies (see figure 4.7). Besides, the role of the OVac location (either at the Ti or Ba plane) is not relevant for BTO in-plane configurations (bulk calculations) while it is for STO in-plane configurations (surfaces and heterostructures calculations) especially in the low U range, see differences between green and blue curves in figure 4.13. An insight of

how the atoms relax around the vacancy can be gained from figure 4.14.

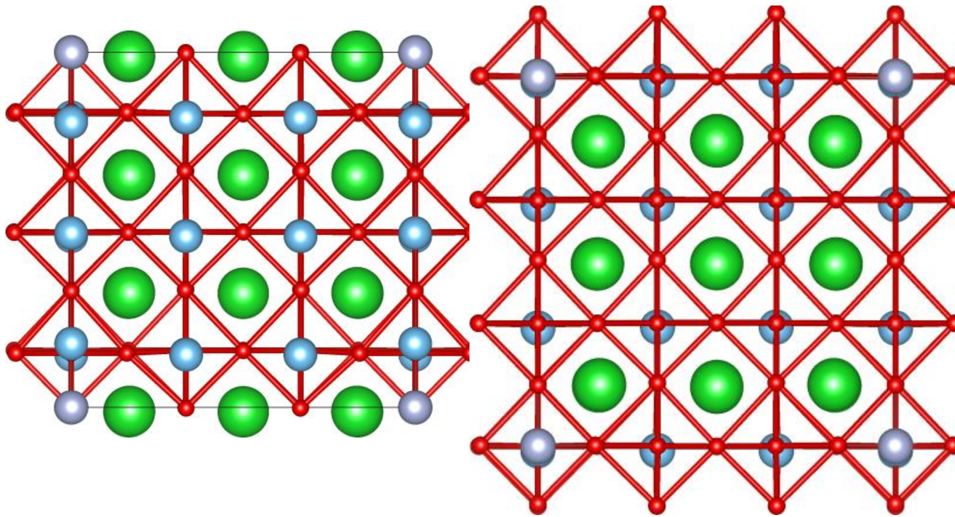

Figure 4.14: Atom relaxation around the oxygen vacancy (grey circle) located at the a) Ba plane, b) Ti plane. Blue, red, green and grey circle corresponds to Ti, oxygen, Ba atoms and OVac respectively.

Besides, we include in figure 4.15 the total energy of the OVac at the TiO_2 plane minus the total energy at the BaO plane as a function of the U value for the BTO and STO in-plane which can be related to the most stable location of the OVac in the bulk or thin film configurations respectively.

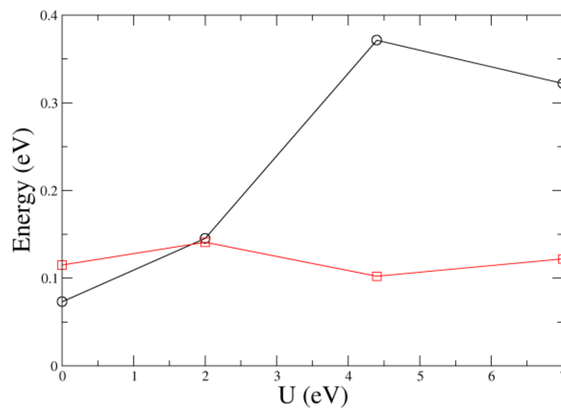

Figure 4.15: BTO energy difference between the OVac located at the TiO_2 minus the BaO location for the BTO in-plane (black curve) or STO-constrained in-plane (red curve) as a function of the U in

the Ti 3d-orbitals.

In figure 4.15, we observe that the most stable location is at the BaO plane being the value almost constant and close to 100 meV in the STO in-plane constraint. For the BTO there is an appreciable stabilization of the oxygen vacancy at the BaO when increasing the U beyond 2.0 eV, however for U = 2.0 eV (reasonable value) is around 150 meV. For the BTO in-plane at the U = 0 eV case the most stable OVac location is the Ba plane by 73 meV over the Ti plane. This compares well with the results from Nieminen et al. but is slightly lower than its 110 meV value [34]. As we saw in figure 4.7 increasing the U values reduces the tetragonality (c and δ) but still do not approach the cubic situation in which both the δ value is zero and c is either 12.0 or 11.7 Å for the BTO or STO in-plane lattice configurations respectively. While the U is effectively reducing the δ value to zero, the c lattice parameter is far from the value 12 and 11.7 Å as we can see in figure 4.7. The persistence of certain tetragonality through the c lattice implies an anisotropy between z out-of-plane and x, y in-plane directions which makes that the OVac is always more stable at the BaO plane than at the TiO_2 plane. The two are equally stable on the perfectly cubic isotropic symmetry.

Inclusion of the oxygen vacancies generates an off-stoichiometry relation which shows up as an electron doping at the bottom of the conduction band, as can be seen in figure 4.16 for both the OVac location at the BaO or TiO_2 plane.

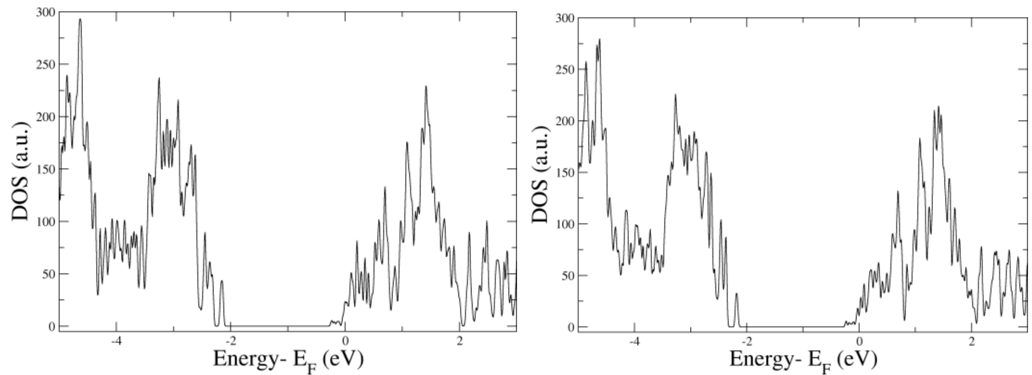

Figure 4.16: Total DOS for the oxygen vacancy at the Ba and Ti plane.

In figure 4.16 we observe, in contrast to the case without vacancies, the appearance of a contribution at the Fermi level associated mostly to the Ti d orbital and coming from the conduction band.

Therefore, we conclude that while U value effectively reduces the δ value although the c value is not reduced. Such anisotropy creates a situation in which the oxygen vacancy is always more stable located at the Ba plane although the electronic structure is not altered and the DOS in both locations are very similar. This suggests that the energy imbalance is mostly due to the atomic structure and strain conditions.

4.3 BTO-Metal super-lattices:

In this section we study the BTO-metal (001) heterostructures distinguishing two kinds of metals: one is the pseudo-cubic LSMO and the second are Co and Ag due to their high oxidation tendencies. All interfaces will be modeled as super-lattices (SLs) with the minimum number of planes in each compound required to observe the relevant phenomena. The mechanisms at the interface will partially rely on the bulk and on the surface properties of the BTO as well as on its interaction with the metal. This among other magnitudes will depend on its electronic affinity and elastic strain due to the structure commensurability between both constituents. The BTO-LSMO interface grows epitaxially and it has been microscopically characterized, see figure 5.3, to be TiO_2/La(Sr)O terminated in both interfaces so a symmetric configuration will be considered. This termination agrees with the first principles calculations of other groups in similar conditions [35]. However Co and Ag do not grow epitaxially but as polycrystals on the BTO so the plane termination may vary depending on the interface region. For a STEM micrography of BTO-Ag highlighting the non-epitaxial growth see figure A5. Such degree of inhomogenity will be taken into account in the simulations by calculating the asymmetric BTO cell, highlighting that the real interface may contain n- and p-type interfaces, and not only one kind as for BTO-LSMO.

For both the symmetric and asymmetric BTO-metal interface terminations the metal is on-top to the oxygen of the TiO_2 plane, since metal-oxygen bond distance is typically lower than the Ti-metal bond. This configuration where the Ti-metal distance is not first neighbour typically offers more degrees of freedom

to the BTO since the oxygen can be accommodated depending on the interaction strength to the metal rather than influencing the oxygen-metal distances and so its interactions. Unless stated otherwise, the employed U_{eff} for the 3d orbitals of Ti is 4.4 eV.

4.3.1 BTO/$La_{1-x}Sr_xMnO_3$ super-lattices:

The BTO/$La_{1-x}Sr_xMnO_3$ calculations are performed in a c(1x1) in-plane u.c., using 350 eV cut-of-energy and 4x4x1 kpoint mesh for ionic relaxation and 6x6x1 for electronic structure calculations, respectively. However, results convergence has been checked against larger 450 eV and 8x8x1 k-meshes obtaining the same results. The SLs contains 8 units cells + 1 TiO_2 layer (8.5 u.c.) and 6 units cells + 1 La(Sr)O layer (6.5 u.c.) of BTO and La1-xSrxMnO3 respectively to impose a symmetric supercell, see figure 4.17. Besides, as commented above, the most frequently found defects in $La_{1-x}Sr_xMnO_3$ may be the chemical modification La/Sr ratio near by the interface. We will calculate the effect of La/Sr concentration (ranging from x = [0, 0.56]) and its localization over the 7 La(Sr)O focusing on experimental concentrations of $x = 0.3$ which provides the interesting half-metal properties to the manganite. This is best obtained with 2 Sr and 5 La, out of the 7 La(Sr)O planes, which corresponds to a simulated x = 0.28.

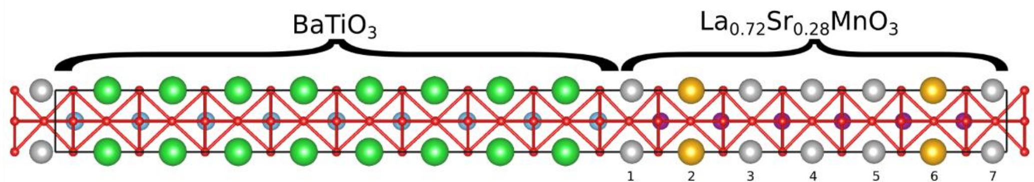

Figure 4.17: Atomic sketch of the c(1x1) $LaSr_xMnO_3$/BTO calculation, where the La(Sr)O planes of the manganite are labeled from 1 to 7 to help describe the concentration and distribution models of La/Sr ratio. E.g. the depicted BTO-LSMO interface corresponds to 2 Sr planes at the position 2 and 6.

Similarly to the BTO surfaces at the $La_{1-x}Sr_xMnO_3$/BTO calculations the interface chemical configurations sets an electrostatic boundary which ultimately influence the electronic and structural properties of the calculations. We will discuss in the BTO the electric polarization O-B, distance between the oxygen and the Ti atom in the TiO_2 plane, similarly to the δ parameter for the BTO bulk and

surface properties, in order to analyse also the role of the La/Sr ratio in the $La_{1-x}Sr_xMnO_3$/BTO interfaces.

The O-Ti values for $La_{1-x}Sr_xMnO_3$/BTO interface for varying La/Sr ratios in the [0, 0.56] range are shown in figure 4.18.

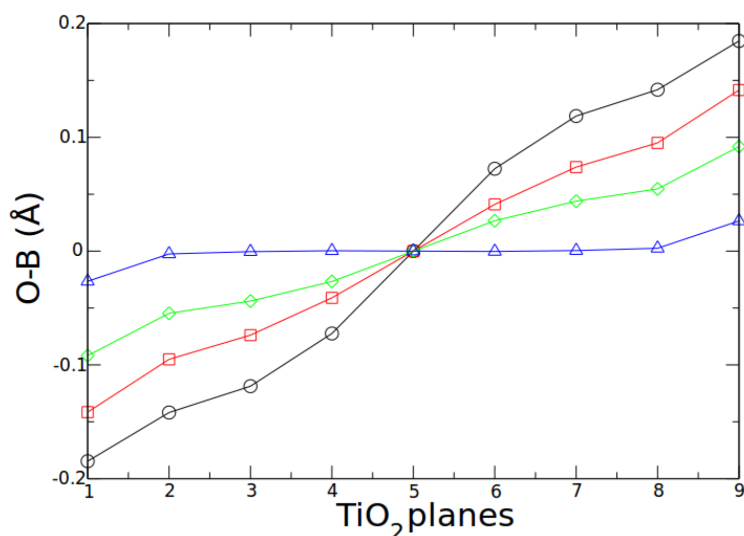

Figure 4.18 O-B distance within the BTO when interfaced to LSMO with Sr atom number (location) in each calculation 0, 2 (at positions 3, 5), 3 (2,4,6) and 4 (1,3,5,7) respectively out of the 7 La(Sr)O planes in the $La_{1-x}Sr_xMnO_3$/BTO interfaces, see figure 21. The symbols and curves denoting each case corresponds to x=0 (black circles), 0.28 (red square), 0.42 (green diamond) and 0.56 (blue triangle).

In figure 4.18, we can observe that for all x values the calculation is perfectly symmetric at the TiO_2 central plane, as imposed by the interfaces, indicating that the oxygen atoms are moving towards the $La_{1-x}Sr_xMnO_3$ side; while the Ti is moving opposite to it. The displacement follows almost a linear relation as we go from the central plane to the interface plane and it also varies with x. The larger the x (Sr concentration), the smaller the O-Ti distance till the case of $x = 0.56$ where there is no TiO_2 electric polarization but only a minor value at the most interfacial TiO_2 plane. This suggest that the there is a clear and almost linear

relation between the number of electron/holes (Sr concentration) in the system vary and the system structural properties.

Beside the role of the Sr/La ratio we have also found that for the closest Sr concentration to the experiments (x = 0.28), the location of the Sr also influences the ferroelectric distortion of the system, again depicted as O-B in figure 4.19.

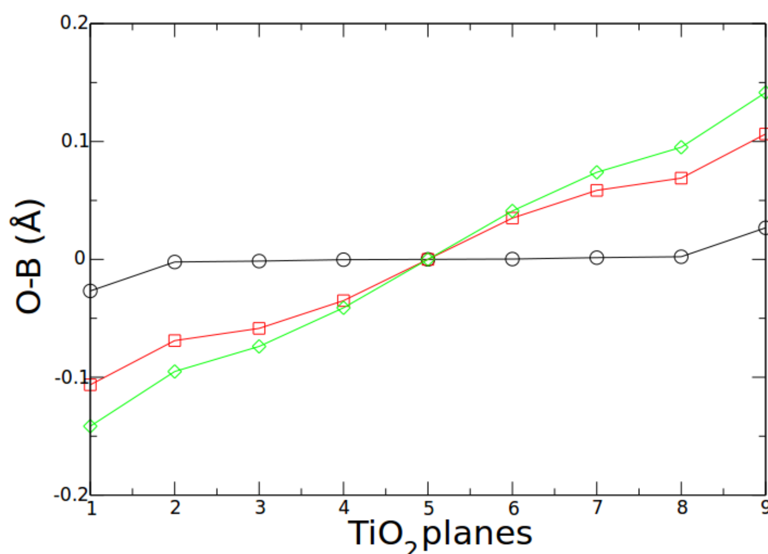

Figure 4.19 O-B within the BTO for x=0.28 in $La_{1-x}Sr_xMnO_3$/BTO interfaces, with the Sr located at the planes 1-7 (black) 2-6 (red) and 3-5 (green). See figure 4.21 for an atomic sketch of the interface and Sr location configurations.

The dependence of the BTO ferroelectric distortion as a function of the Sr location in figure 4.19 indicates a similar variation of the O-B values than that obtained in figure 4.18 for the Sr concentration. While in this case the amount of electron/holes in the system is preserved we modify the electrostatic interface configuration increasing/reducing the polar discontinuity at the LSMO/BTO interfase. The polar discontinuity occurs at the interface when the nominal oxidation states of one compound do not follow the value sequence of the other compound therefore developing an electrostatic potential which eventually makes the system unstable when the polar compound is thick enough. The polar discontinuity is a well-known mechanism in oxide based heterostructures in which the alteration from the bulk coordination generates an exotic phenomenon such as

the two-dimensional electron gas (2DEG) at the interface environment [38]. The first system in which this 2DEG was observed was LAO-STO (100) heterostructure residing in the Ti d-orbitals [37]. This 2DEG appears as a stabilizing mechanism to compensate the polar discontinuity when the LAO is larger than 4 ML [38], thickness at which the electrostatic potential would be too high for the heterostructure to form without 2DEG.

However Stengel et al. have discussed that certain oxide-metal heterostructures are wrongly described using DFT-based methods due to the band gap problem, which induce fictitious interactions between the metal and the oxide [39]. A structural feature they claim it evidences the problem is a linear ramp in the electric polarization, such as that we obtain in figure 4.18 for high La concentrations and in figure 4.19 for LaO-terminated interface configurations. To be on the safe side from this parasitic effect we will consider from now on the SrO termination of the LSMO-BTO heterostructure with 28% Sr concentration, case a) from figure 4.19, which shows a flat O-B value with a slight modification at the interface. In order to show the influence of two different Sr location at the interface on the electronic properties, the PDOS for SrO- and LaO-terminated BTO are included in figure 4.20

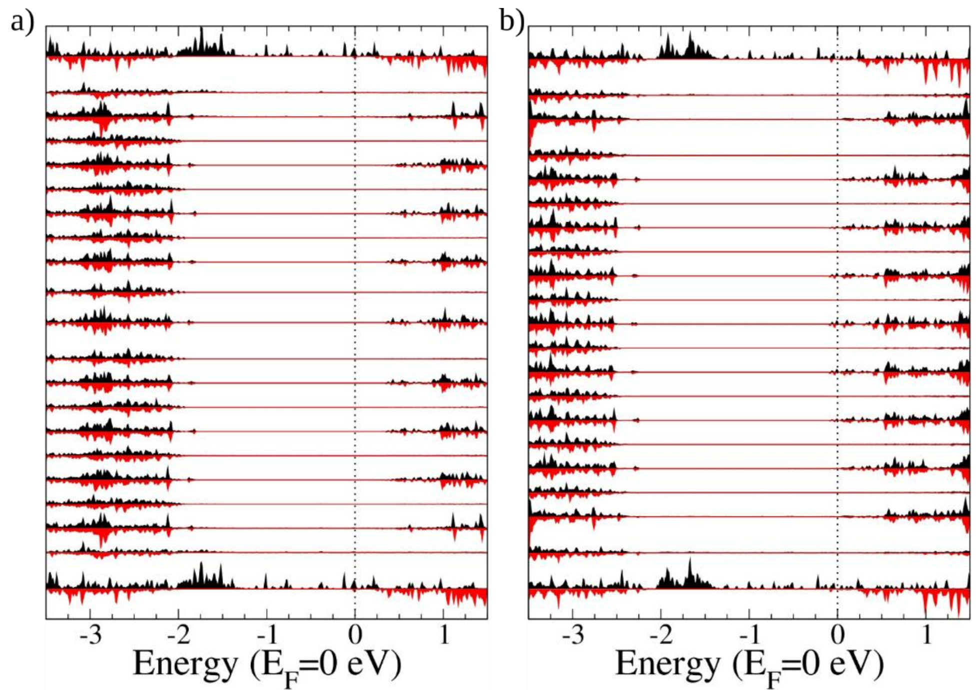

Figure 4.20 Calculated layer-resolved density of states in the BTO region and the two first LSMO planes at each interface for the SrO- (left) and LaO-terminated (right) configurations. Black curves in the density-of-states plots indicate the majority spin and red curves indicate the minority spin.

In figure 4.20 for the SrO-termination the BTO conduction band show a dielectric barrier of around 0.5 eV while for the LaO-termination the conduction band aligns along the Fermi level contributing slightly at the central plane and in the rest just on a verge to become metallic. As stated before the largest difference between the two configurations is structural and corresponds in figure 4.19 to a paraelectric O-B distribution (black curve) and a head-to-head charged domain wall (H-to-H DW) (red curve) corresponding to the left and right cases of figure 4.20 respectively. However BTO is a ferroelectric with an electric O-Ti displacement of around 0.12 Å which will not result in our BTO/LSMO calculations as a consequence of the symmetric super-lattice of our model. Still one relevant interface configuration is a constant 0.12 Å O-Ti displacement at each

half of the super-lattice meeting a charged ferroelectric domain wall, the so called H-to-H DW forced configuration at the center, see figure 4.21 for an atomic sketch.

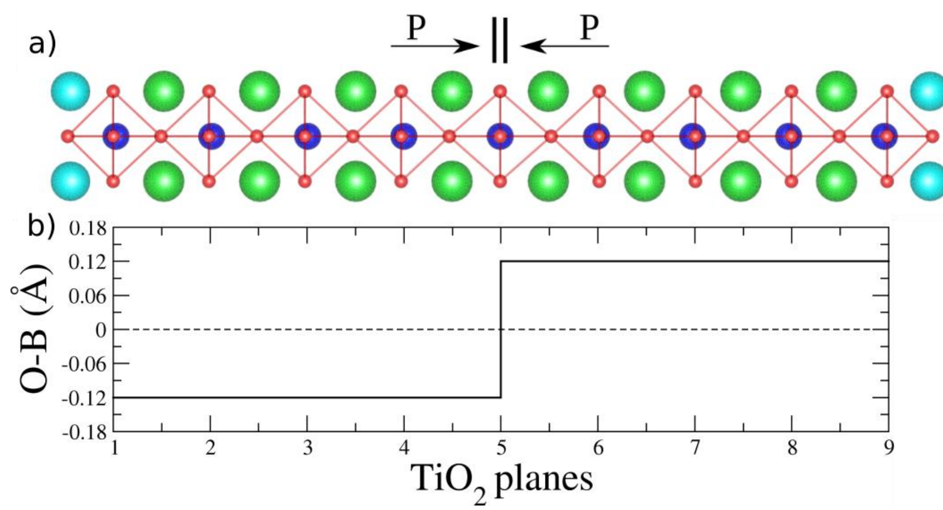

Figure 4.21: (a) Atomic sketch H-t-H DW forced configuration of the BTO/LSMO calculation with 0.12 Å (bulk) BTO constant ferroelectric displacement at each BTO half-side meeting a H-to-H DW wall at the center. (b) Step-like electric polarization profile along the BTO.

The electronic properties of the unrelaxed configuration of figure 4.21 depicted as PDOS are shown in figure 4.22.

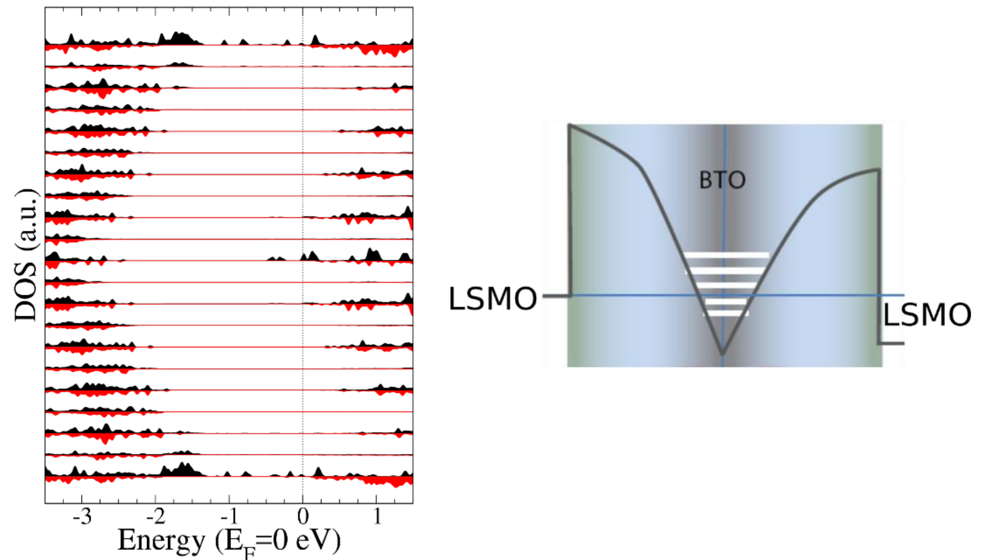

Figure 4.22: Left. Calculated layer-resolved density of states in the BTO region and the two first LSMO planes at each interface for the H-to-H DW forced-configuration. Black curves in the density-of-states plots indicate the majority spin and red curves indicate the minority spin. Right: Sketch for the band bending of the LSMO/BTO calculations.

In figure 4.22, we can observe that the dielectric barrier that forms at the interface with the LSMO (almost 1 eV) is continuously reduced due to a band bending throughout the BTO till a localized metallic region by the center where it resides the H-to-H DW. The conduction band is characterized by Ti 3d-orbitals whose region lay below the Fermi level forming a free electron gas confined to one or two BTO unit cells from the domain wall. In figure 4.22, it is shown a sketch for the band bending which gradually makes that the band offset at the interface become a metallic dip at the center of the BTO.

However the total energy of this configuration is 1100 erg/cm^2 less stable than the paraelectric configuration. This energy difference compare to 10 erg/cm^2 for non-charged ferroelectric domain walls. Therefore, the charged ferroelectric domain wall configuration is very unstable and unlikely to be observed in ideal BTO/LSMO heterostructures.

We extend the study of atomically relevant configurations in BTO/LSMO heterostructures by including the most common defects present in BTO, these are oxygen vacancies. We consider the previous paraelectric interface calculation with oxygen vacancies in the BTO at the third most interfacial plane and we let the

system relax. The corresponding PDOS of its ground state is depicted in figure 4.23.

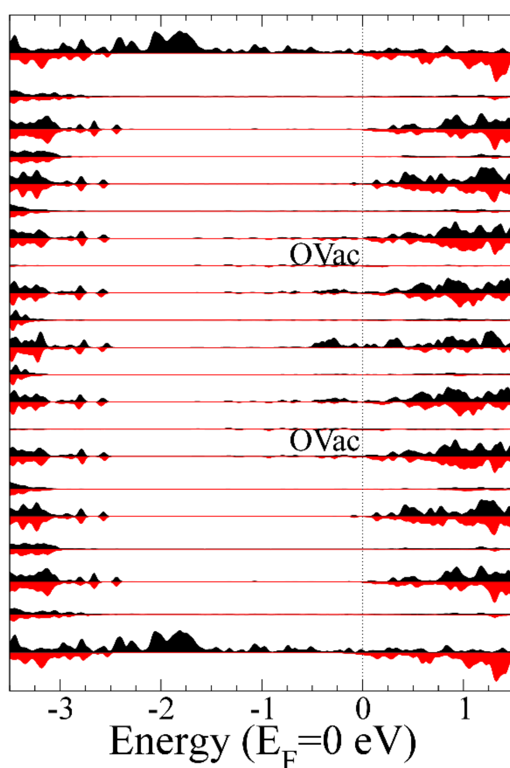

Figure 4.23 Calculated layer-resolved density of states in the BTO region and the two first LSMO planes at each interface for the H-to-H DW configuration promoted by oxygen vacancies. Black curves in the density-of-states plots indicate the majority spin and red curves indicate the minority spin.

In figure 4.23, we can clearly observe a great similarity to figure 4.22 where there is an accumulation of free electron density near the central BTO to screen the polarization charges of a H-to-H DW. However, the great difference is that for the presence of oxygen vacancies we access to the most stable configuration through atomic relaxation, unlike the case without oxygen vacancies which was unstable by 1100 erg/cm^2. So, in both cases, we essentially obtain the same phenomena in which the band bending at the dielectric allows for the population of the conduction band in the center of the BTO. The integration of the electrons from the Ti 3d-orbitals till the Fermi level provides a clearer picture of

the free electron confinement and density associated to the charged ferroelectric domain wall, see figure 4.24.

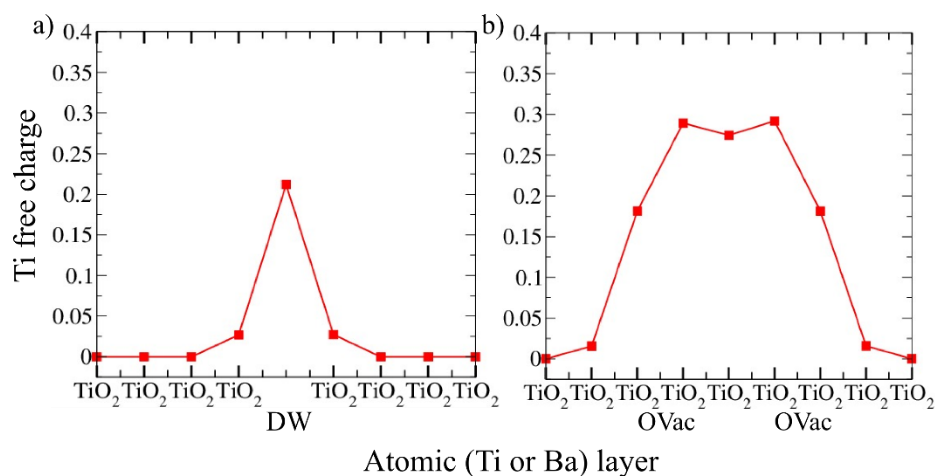

Figure 4.24 Screening charge density profiles for the LSMO/BTO SLs containing a H-to-H domain wall. The screening charge arises from a) the LSMO metallic electrodes (H-t-H forced-configuration), b) the oxygen vacancies which are located at the two Ba planes next-nearest neighbours to the BTO central plane.

In figure 4.24, we can observe that while the region with the highest electron density is the BTO centre, the extension varies from around 1 unit cell in the forced configuration to around 5 units cell when the source of free electrons are the oxygen vacancies. The qualitative picture is clear however the amount of electrons is not precise since it involves approximating the electron integration into spheres centered at atomic positions.

The picture of the H-to-H DW formation and stability due to oxygen vacancies within the BTO is robust against the only parameter we employed in our *ab-initio* calculations which is the U value. Varying the U of the Ti-3d from 4.4 to 1.45 eV give us the PDOS of figure 4.25, which show similar electronic distribution validating the relevance of the oxygen vacancies in the structure and stability of the DW, and the electronic properties of the confined electron gas.

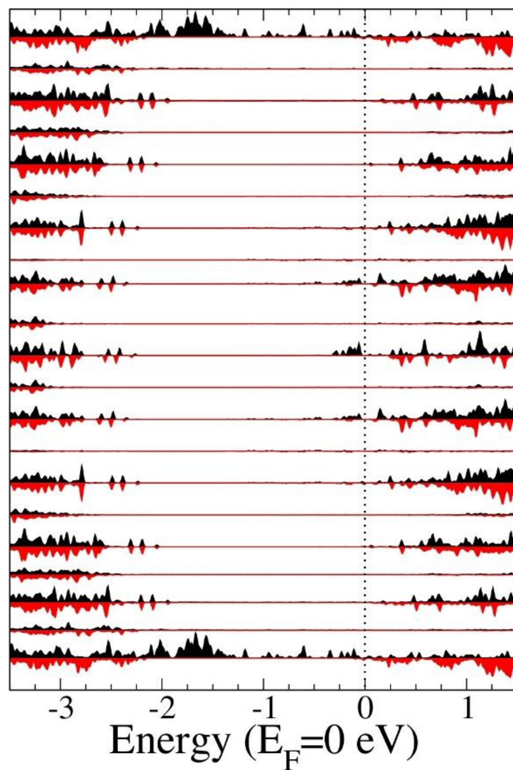

Figure 4.25 Similar to figure 4.23 for $U = 1.45\ eV$ instead of $U = 4.4\ eV$

In order to study the confinement and the orbital nature of the free electron charge we depict in figure 4.26 a similar plot to figure 4.23 but only calculated at the gamma point of the reciprocal lattice.

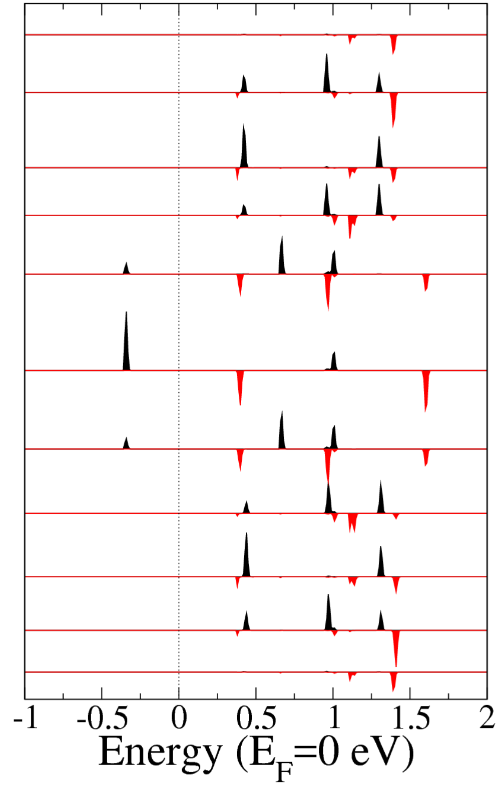

Figure 4.26 Layer-resolved density of states of the d_{xz}, d_{yz} and $d_{3z^2-r^2}$ 3d-Ti orbitals for the oxygen vacancy structure at the gamma point of the BTO conduction band minimum. Black (red) curves in the density-of-states plots indicate the majority (minority) spin.

Figure 4.26 depicts the layer-resolved density of states for the d_{xz}, d_{yz} and $d_{3z^2-r^2}$ 3d-Ti orbitals at the gamma point of the two-dimensional Brillouin zone, for the vacancy configuration. The degenerate d_{xz} and d_{yz} conduction band states quantized by the confining potential of the domain wall show an energy separation in the range of several tens of meV (and thus they should correspond to the resonant levels yielding the conductance oscillations because of resonant tunnelling, whose experiments are explained in chapter 5). These d_{xz} and d_{yz} states have the lowest energy, a low effective mass and hence a high mobility. d_{xy}, $d_{x^2-y^2}$ (mostly localized in a single TiO_2 layer) and $d_{3z^2-r^2}$ orbitals with a higher effective mass are located at higher energies (and therefore they should contribute to the confining potential). The actual energy of the different orbitals and thus their energy separation will depend on the exact shape of the confining potential and in

turn on the actual configuration of the oxygen vacancies. Nevertheless, for the several different oxygen vacancy configurations analysed, the degenerate d_{xy} and d_{yz} states have always the lowest energy, and the energy separation between quantized states is in the range of several tens of meV and close to a constant value. Consequently, tunnelling across the BTO would be assisted by the confined electron states, which would be responsible for the conductance quantization observed in the transport measurements (see sketch in Fig. 4.22). Notice, finally, that DFT calculations show a clear spin polarization ($0.3\ \mu B$ at the Ti central plane) of the confined electronic states (Fig. 4.23), which accounts for the differences in the measured tunnelling conductance in both configurations corresponding to parallel or antiparallel alignment of the electrode magnetic moments.

All these calculations have been employed to publish a collaborative work [19] whose experimental part is included in chapter 5. In that section references to the theoretical results just discussed will be frequently performed.

4.3.2 BTO/Ag (001) super-lattices:

In contrast to the BTO/LSMO (001), Ag does not grow epitaxially on the BTO but it has polycrystalline structure, see figure A5 for STEM micrography, therefore the crystallographic orientation and/or the termination plane may vary, for which we calculate asymmetric supercells containing both TiO_2 and BaO terminations. To check the variability of the properties against crystallographic directions we have calculated symmetric BTO/Ag heterostructures for both the [111] and [001] orientations obtaining qualitatively similar results. Therefore we extrapolate that to the study we will present in asymmetric super-lattices to say we expect no major differences between low indexes BTO/Ag heterostructures. We will consider a BTO/Ag [001] interface model calculation with an asymmetric supercell, with both TiO_2 and BaO terminations of BTO, so we implicitly take into account the variability of interface interactions due to the lack of epitaxial growth of Ag on BTO.

We have performed a c(2x2) in-plane u.c. BTO/Ag [001] SL calculation with the super-lattice containing 5 BTO and 4 Ag unit cells, see figure 4.31 for an atomic sketch. The in-plane lattice parameter is constrained to the experimental STO value 3.905 Å value so both the BTO and Ag are under tensile stress to fit that value by compressing along the out-of-plane direction. We employed 350 eV energy cut off and 3x3x1 k-mesh which is well converged to 450 eV and 5x5x1 k-

mesh respectively. The atomic positions and out-of-plane lattice vectors are allowed to relax till the atomic forces are lower than 15 meV/Å. The employed Hubbard U corrections, as discussed throughout the text, are 4.4 for the Ti unless otherwise specified.

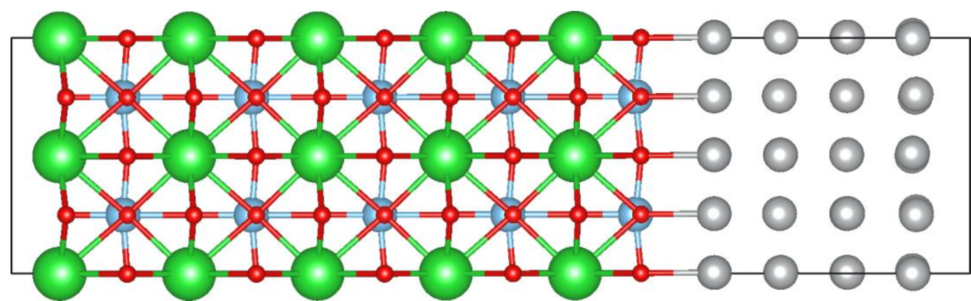

Figure 4.27 c(2x2) supercell of the [001] interface of BTO (left side) and Ag (right side). In order to highlight the atomic displacements the bonds between the oxygen and cations are included. Green, red, blue and grey circles corresponds to Ba, oxygen, Ti and Ag atoms respectively.

After relaxation the ideal BTO/Ag calculation the most important structural features are the appearance of an almost constant ferroelectric displacement of 0.16 Å along the BTO and elongated interfaces distances. The minimum distance between the metal and BTO planes at the TiO_2 and BaO terminated interfaces are 2.44 and 2.37 Å respectively. These distances values compare to 2.10 Ag-oxygen distance in the AgO compound therefore indicating that at the interface is not very strongly bound. These long out-of-plane distances were also relevant in the Ag side to the point that we had to freeze the distance between the two intermediate planes in order to keep it under reasonable values. Similarly the relatively weak interface can also be observed in the PDOS for the ideal BTO/Ag [001], see figure 4.28.

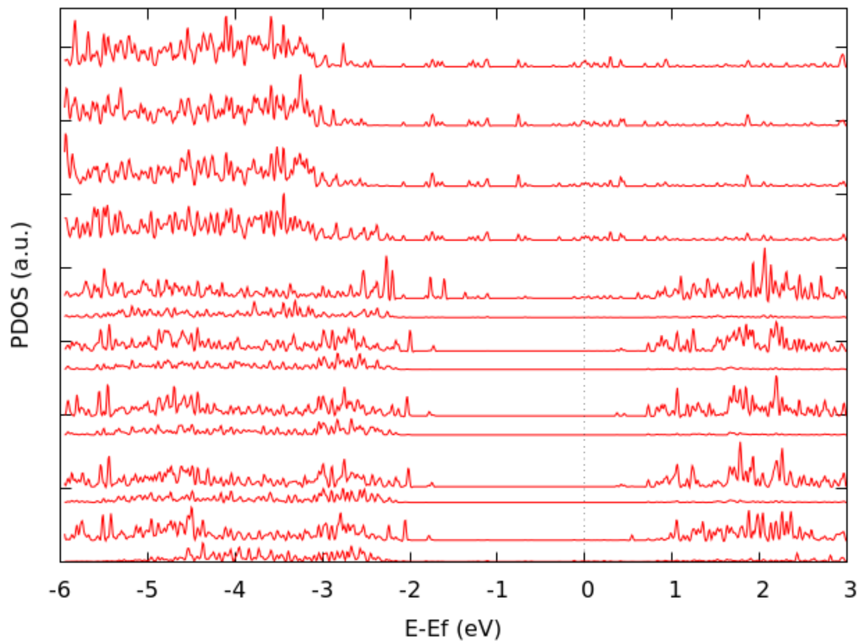

Figure 4.28 PDOS for the ideal BTO/Ag [001] interface along the 4 Ag planes (at the top) and the BTO 5 TiO_2 planes with the BaO termination at the bottom.

In figure 4.28, the BTO show mostly the same electronic feature as in bulk including the interfacial planes, with no occupied valence band BTO states so there is no charge transfer with the Ag. The only slight contribution is some hybridization with the Ag s-orbitals in the energy range [-2, 0] eV below the Fermi level.

We now study the influence of the most relevant defects in each material: oxygen vacancies in the BTO and interstitials in Ag. The PDOS for the same structure including one oxygen vacancy at the third BaO plane is depicted in Figure 4.29.

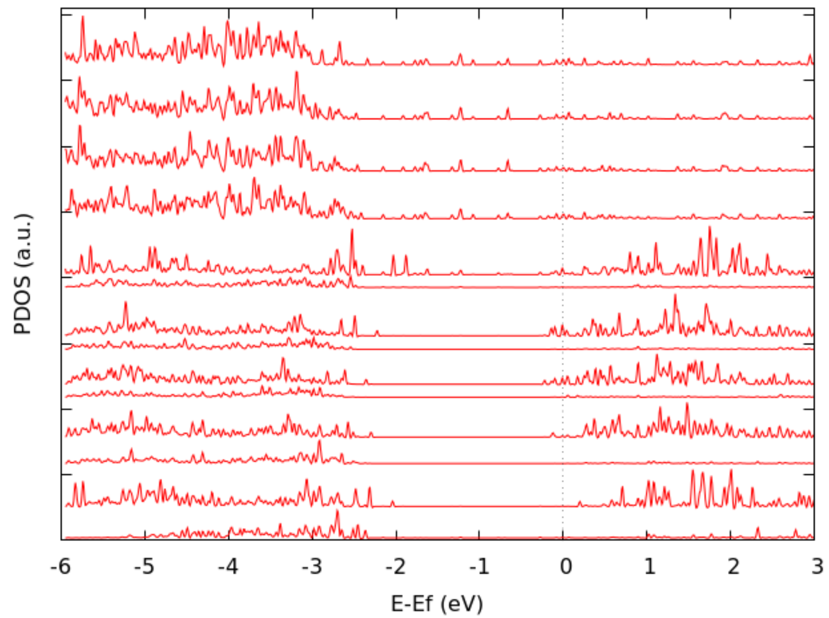

Figure 4.29 Similar PDOS to figure 32 but including oxygen vacancies at the third BaO plane.

We observe that the TiO_2 3d-orbital levels near the vacancy displace towards lower energies till the conduction band slightly populates. The energy location of these levels varies with the theoretical U parameter, being on averaged 0.25 eV for U = 4.4 eV and 0.15 eV for U = 0.0 eV. By virtue of this particular configuration, we can firmly suggest that the existence of oxygen vacancies at the middle plane develops in the BTO occupied electronic states around 0.2 eV below Fermi energy.

Besides the oxygen vacancy in the BTO we have included an insterstitial oxygen between the first and second layer of the Ag, and plot its PDOS in figure 4.30.

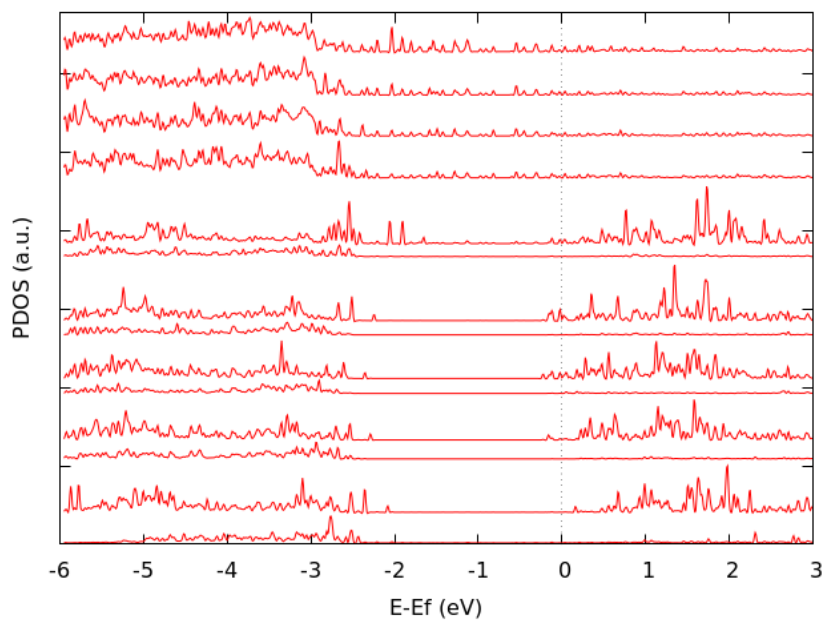

Figure 4.30 Similar PDOS to figure 4.29 but also including oxygen interstitials between the first and second Ag plane respect to the TiO2 terminated interface.

While the presence of the interstitial produces a buckled atomic structure which alters the packing of the Ag the only modification to the electronic states is local to the Silver and it does not differentiates to the interface with only oxygen vacancies in the BTO. While the most important electronic variation is due to the oxygen vacancies at the BTO the interstitials resulting from the oxide catalyst properties of the Ag are essential to allow the reduction of the BTO. As we will see in the experiments explained in chapter 6, the interplay between the oxygen vacancy and ferroelectricity gives rise to a pinning level ascribed to an interface dipole due to a ferroelectricity driven oxygen vacancy ionization; which is thought to be connected with the existence of electronic states near the Fermi level in the BTO obtained in the present DFT calculation.

4.3.3 BTO/Co (0001) super-lattices:

For the BTO/Co (0001) super-lattices the employed Hubbard U corrections, as discussed thought the text, is 4.4 for the Ti and 2.0 eV for the metallic Co. Similarly to the Ag the Co is a polycrystal at the interface with the BTO [001] so we expect to have a variety of termination planes and orientations depending on the interface region. We have employed an asymmetric super-lattice

to account for that variability with $\sqrt{2}x\sqrt{2}$R45º in-plane cell and containing 5 BTO and 5 Co units cells. Again the in-plane u.c. is constrained to the STO value. This interface involves the lowest degree of commensurability due to the fact that the Co show a hcp structure in bulk, as commented in chapter 6, while the BTO and STO have in-plane squared symmetry. This result into a strong relaxation pattern specifically in the Co in order to accommodate not only to the substrate size but also to its symmetry, see figure 4.31.

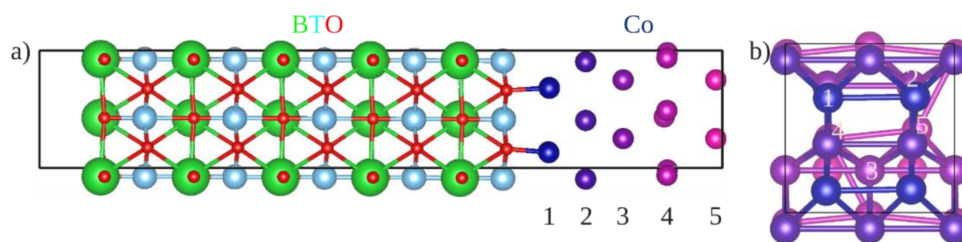

Figure 4.31 Atomic sketch of the asymmetric $\sqrt{2}x\sqrt{2}$R45º ideal BTO/Co [0001] model viewed from the a) [010], b) only Co [001] orientation. The depicted bonds correspond to oxygen bonds. Green, red, light blue and corresponds to Ba, oxygen, Ti respectively. Co atoms are depicted in a colour gradation from dark blue to pink to illustrate the depth effect.

In figure 4.31, we observe that the Co strongly relax specially along the in-plane directions changing the equilateral triangle shape into a scalene one or rectangle. The oxygen at the BTO instead of showing a constant ferroelectric displacement to the cation plane, as for the BTO-Ag interface, it moves away from the Co interfaces, see figure 4.31 near the Co 1º and 5º planes.

The PDOS for such model of the BTO-Co [001] heterostructure is presented in figure 4.32 where we again find that the interface interaction with the BTO is mostly due to the hybridization of the Co d-orbitals, but no charge transfer or mechanism evidencing a strong link between both materials.

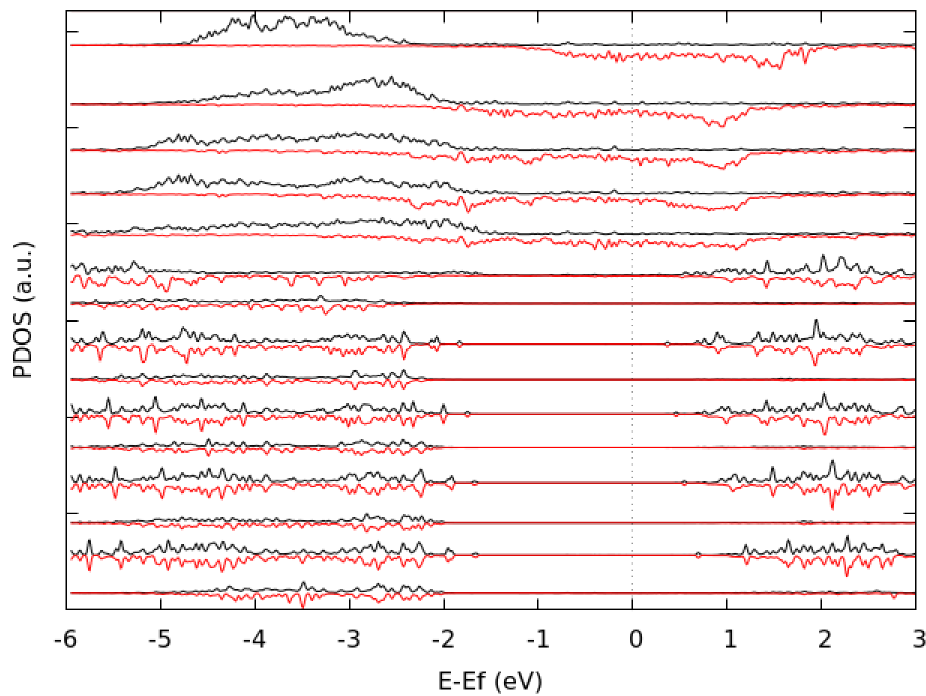

Figure 4.32 PDOS for the ideal BTO-Co [001] interface, illustrated in figure 4.31, along the 5 Co planes (at the top), then the TiO_2 termination (6th curve from the top) and the 5 BTO with the BaO termination at the bottom.

We have then included one oxygen vacancy in the middle of the BTO (third Ba plane) and plot the corresponding PDOS in figure 4.33, depicting the negative transfer magnetoresistance displayed in figure 6.19.

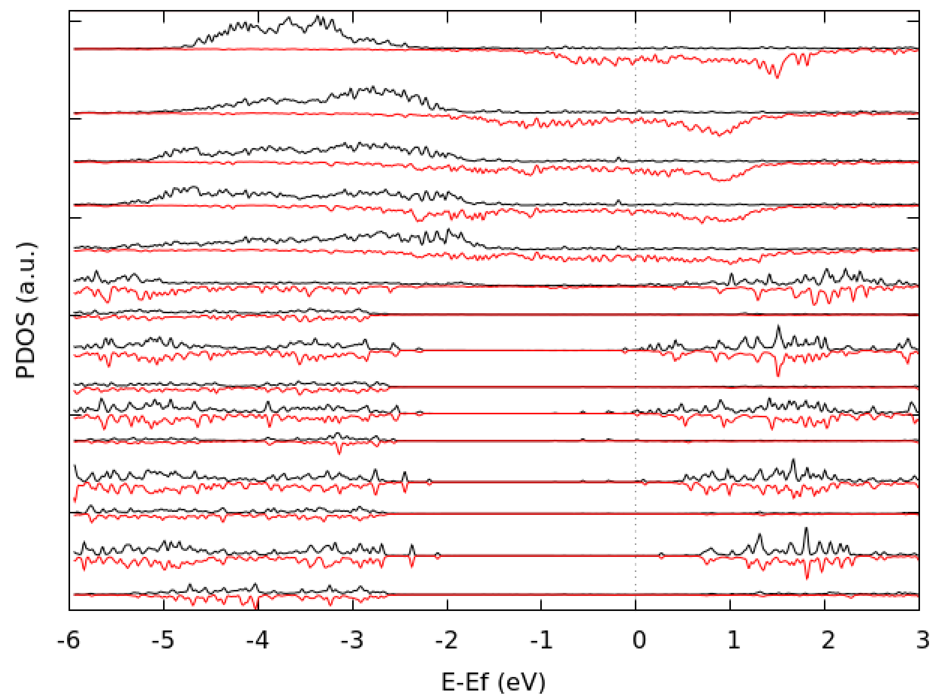

Figure 4.33 Similar PDOS to figure 4.32 but including an oxygen vacancy at the 3rd Ba plane. Besides we have considered the Co high oxygen affinity and its high reactivity to form Cobalt oxides at the interface with the BTO, as discussed in chapter 6. CoO is strongly correlated material and high enough Hubbard U is required to describe the system in its correct AFM insulator phase. We have employed U = 6 eV as discussed in section 4.2.2. This interface involves the lowest degree of commensurability due to the fact that the Co show a hcp structure in bulk, while the BTO and CoO have in-plane squared symmetry constrained to the STO lattice. This result into a strong relaxation pattern specifically in the Co and CoO in order to accommodate substrate sizes in BTO, Co and CoO and symmetries in CoO, see figure 4.34.

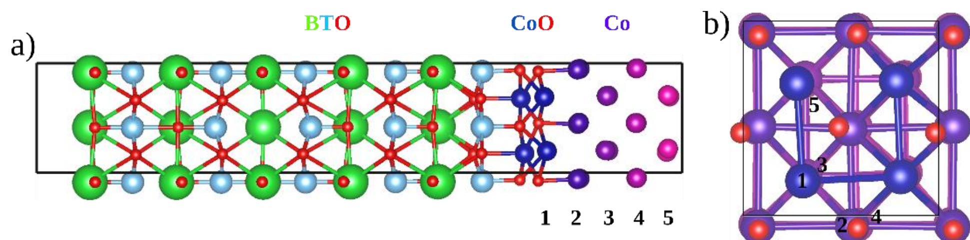

Figure 4.34 Atomic sketch of the asymmetric$\sqrt{2}x\sqrt{2}$R45° BTO/Co [0001] model viewed from the a) [010], b) only Co and CoO along [001]. The depicted bonds correspond to a) oxygen bonds, b) Co-

Co bonds. Green, red, light blue and corresponds to Ba, oxygen, Ti respectively. Co atoms are depicted in a colour gradation from dark blue to pink to illustrate the depth effect.

In figure 4.34, we observe that the Co strongly relax specially along the in-plane directions changing the equilateral triangle shape into a scalene one or rectangle. The oxygen at the BTO instead of showing a constant ferroelectric displacement to the cation plane, as for the BTO-Ag interface, it moves away from the Co interfaces, see figure 4.34 near the 1 and 5 planes.

The PDOS corresponding to the oxygen vacancy at the BTO and the CoO layer at the interface is depicted in Figure 4.35, showing the positive transfer magnetoresistance displayed in figure 6.20.

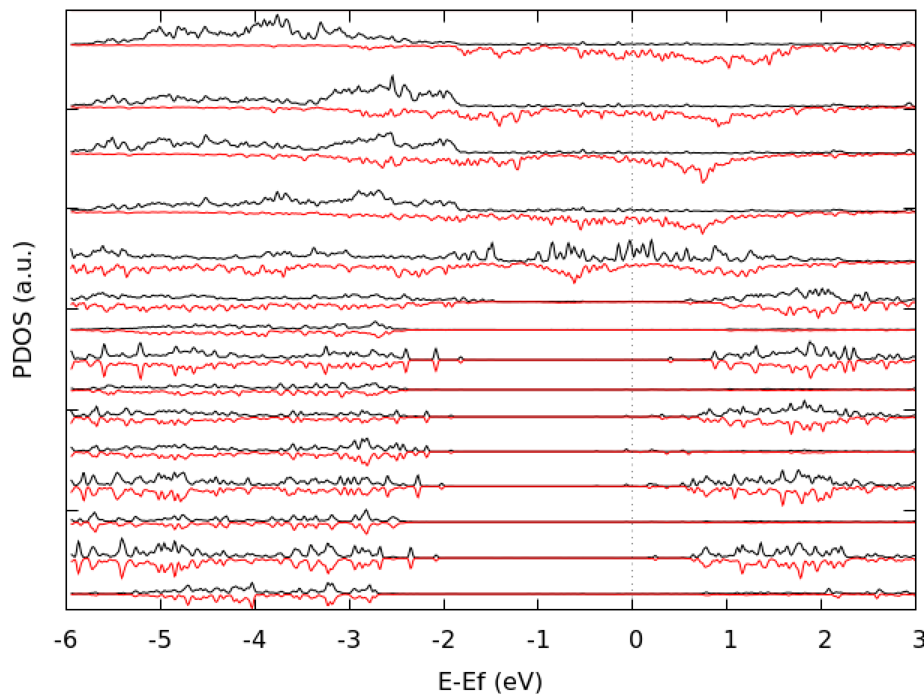

Figure 4.35 Similar PDOS to figure 4.36 but including an oxygen vacancy at the 3rd Ba plane and a full CoO layer at the 5th Co plane, as depicted in figure 4.34.

Notice in figure 4.35 that the CoO plane (fifth plane from the top) show larger population from the majority spin in comparison to the CoO AFM insulator phase and to the larger population from the minority spin in metallic Co, see figure 4.4. The formation of the oxidized Co phase at the interface with BTO will therefore strongly impact the transport properties of the BTO-Co based heterostructures as

will be discussed in chapter 6. Besides, notice the development of a state associated to the oxygen vacancy, by the middle BTO planes, which occur at around 100 meV, as shown in figures 6.13 and 6.14. This state will also grant specific properties to the systems, particularly regarding the activation barrier dependency on the temperature. In figure 6.11, impedance spectroscopy measurements will be performed to highlight the Coulomb Blockade effect [40, 41] in the LSMO/BTO/Co tunnel junctions devices.

Furthermore, the $BaTiO_3/Co$ interface depicts the negative Tunnel Magneto Resistance ($TMR < 0$) measured in direct current (DC) in figure 6.19; which stems from the negative spin polarization in the Fermi level of the hcp Co atomic layers.

The $BaTiO_3/Co$ interface with the added CoO monolayer depicts the positive Tunnel Magneto Resistance ($TMR > 0$) measured in direct current in (DC) in figure 6.20; which stems from the positive spin polarization in the Fermi level of the hcp CoO and the close-oxygen-vacancy TiO_2 atomic planes.

The oxygen vacancy induced positive spin polarization is due to the ($U - J = 4.4\ eV$) Hubbard correction energy value for Ti; given in order to take implicitly into consideration the bottom electrode $La_{0.7}Sr_{0.3}MnO_3$ energy correlations transferred to oxygen vacancies through Ti atoms [42]. In other words, oxygen vacancies could mediate exchange coupling by tunnelling their charge and spin through Ti^{3+} cation [43], resembling a double exchange extrapolated to a ferroelectric insulator barrier because the electrons trapped in oxygen vacancies colour centres are able to localize its charge and spin. Similarly, it is of common knowledge that chemical doping [44, 45] induces changes in bonding angle and thus, triggering variations in the Exchange Energy J magnitude, which gives rise to wide magnetic behaviour; more specifically antiferromagnetism, positive and negative spin polarization in the Fermi level and so on.

To sum up, the LSMO/BTO/Co memristor tunnel junction exhibits sign change in the transfer magneto-resistance (TMR), reflecting the sign change in the spin polarization (at the Fermi level) in the BTO/Co interface because this interface is sensitive enough to the ferroelectric polarization and defect distribution. DFT calculations show that the sign change in BTO/Co interface stems from the competition between the Co atoms exchange interaction suppressed by the CoO monolayer ($U - J = 6.0\ eV$) and the oxygen vacancies colour centres exchange

interaction mediated by Ti^{3+} $(U - J = 4.4\ eV)$ ions, resembling double exchange interaction in an insulator ferroelectric BTO barrier.

Nevertheless, our current VASP simulations could not account for the difference in the coercive magnetic fields in the Tunnel Magneto Resistance (TMR) measurements at the High and Low Resistance States. All things considered, our current VASP simulations could give an explanation to the sign change of the Tunnel Magneto Resistance after switching between the Low and the High Resistance Sates. In conclusion, more accurate density functional theory (DFT) calculations will be needed.

4.4 References

[1] Cohen AJ, Mori-Sánchez P, Yang W. "Insights into current limitations of density functional theory". Science (2008).

[2] S. L. Dudarev, G. A. Botton, S. Y. Savrasov, Z. Szotek, W. M. Temmerman and A. P. Sutton. "Electronic Structure and Elastic Properties of Strongly Correlated Metal Oxides from First Principles: LSDA + U, SIC-LSDA and EELS Study of UO2 and NiO". Phys. stat. sol. (a) 166, 429 (1998).

[3] Kresse, G. & Hafner, J. "Ab initio molecular dynamics for liquid metals". Phys. Rev. B 47, 558–561 (1993).

[4] Kresse, G. & Furthmüller, "J. Efficient iterative schemes for ab initio total-energy calculations using a plane-wave basis set". Phys. Rev. B 54, 11169–11186 (1996).

[5] Kresse, G. & Joubert, D. "From ultrasoft pseudopotentials to the projector augmented-wave method". Phys. Rev. B 59, 1758–1775 (1999).

[6] Dudarev, S. L., Botton, G. A., Savrasov, S. Y., Humphreys, C. J. & Sutton, A. P. "Electron-energy-loss spectra and the structural stability of nickel oxide: an LSDA +U study". Phys. Rev. B 57, 1505–1509 (1998).

[7] Wheeler P. Davey. "Precision Measurements of the Lattice Constants of Twelve Common Metals". Phys. Rev. 25, 753 (1925).

[8] Phillip Christopher, Honglian Xin & Suljo Linic. “Visible-light-enhanced catalytic oxidation reactions on plasmonic silver nanostructures”. *Nat. Chem.* volume 3, pages 467–472 (2011).
[9] Jean-Paul Crocombette, Henri de Monestrol, and F. Willaime. “Oxygen and vacancies in silver: A density-functional study in the local density and generalized gradient approximations”. Phys. Rev. B 66, 024114 (2002).

[10] *Kittel, Charles (1986). Introduction to Solid State Physics (6th ed.). John Wiley & Sons. ISBN 0-471-87474-4.*

[11] F. Vincent, and M. Figlarz, *C. R. Hebd. Seances Acad. Sci.*, 1967, 264C, 1270.

[12] A Chemist's Guide to Density Functional Theory, 2nd Edition. Wolfram Koch, Max C. Holthausen. ISBN: 978-3-527-30372-4. Oct 2001.

[13] Dagotto, E. “*Nanoscale Phase Separation in Manganites”* (Springer-Verlag, Heidelberg, 2002).

[14] Michele Pavone, Ana B. Muñoz-García, Andrew M. Ritzmann, and Emily A. Carter. “First-Principles Study of Lanthanum Strontium Manganite: Insights into Electronic Structure and Oxygen Vacancy Formation”. *J. Phys. Chem. C* 2014 *118* (25), 13346-13356 DOI: 10.1021/jp500352h

[15] Sonali Saha, T. P. Sinha, and Abhijit Mookerjee. “Electronic structure, chemical bonding, and optical properties of paraelectric $BaTiO_3$”. Phys. Rev. B 62, 8828 (2000).

[16] Zhao-Xu Chen, Yi Chen, and Yuan-Sheng Jiang. “DFT Study on Ferroelectricity of $BaTiO_3$”. *J. Phys. Chem. B*, 2001, 105 (24), pp 5766–5771. DOI: 10.1021/jp0032558

[17] Roman Wahl, Doris Vogtenhuber, and Georg Kresse. “$SrTiO_3$ and $BaTiO_3$ revisited using the projector augmented wave method: Performance of hybrid and semilocal functionals”. Phys. Rev. B 78, 104116 (2008).

[18] H. H. Wieder. “Electrical Behavior of Barium Titanate Single Crystals at Low Temperatures”. Phys. Rev. 99, 1161 (1955).

[19] Gabriel Sanchez-Santolino, Javier Tornos, David Hernandez-Martin, Juan I. Beltran, Carmen Munuera, Mariona Cabero, Ana Perez-Muñoz, Jesus Ricote, Federico Mompean, Mar Garcia-Hernandez, Zouhair Sefrioui, Carlos Leon, Steve

J. Pennycook, Maria Carmen Muñoz, Maria Varela and Jacobo Santamaria. “Resonant electron tunnelling assisted by charged domain walls in multiferroic tunnel junctions”. Nat. Nano. (2017). DOI: 10.1038/NNANO.2017.51

[20] K. van Benthem, C. Elsässer and R. H. French (2001). *"Bulk electronic structure of $SrTiO_3$: Experiment and theory"*. J. Applied Phys. 90: 6156. doi:10.1063/1.1415766.

[21]. Okamoto, S., Millis, A. J. & Spaldin, N. A. “Lattice relaxation in oxide heterostructures: $LaTiO_3$/$SrTiO_3$ superlattices”. Phys. Rev. Lett. 97, 056802 (2006).

[22]. Li, J. C., Beltrán, J. I. & Carmen Muñoz, M. “Multiorbital structure of the two-dimensional electron gas in LaAlO3 /SrTiO3 heterostructures. The formation of a dxy ferromagnetic sheet”. Phys. Rev. B 87, 075411 (2013).

[23] R. Resta, M. Posternak, and A. Baldereschi. “Towards a Quantum Theory of Polarization in Ferroelectrics: The Case of KNbO3”. Phys. Rev. Lett. 70, 7 (1993).

[24] Duan, C.-G., Sabirianov, R. F., Mei, W.-N., Jaswal, S. S. & Tsymbal, E. Y. “Interface effect on ferroelectricity at the nanoscale”. Nano Lett. 6, 483–487 (2006).

[25] G. H. Kwei, A. C. Lawson, and S. J. L. Billinge. “Structures of the ferroelectric phases of barium titanate”. J. Phys. Chem. 97, 2368 (1993).

[26] G. Shirane, H. Danner, and P. Pepinsky. “Neutron Diffraction Study of Orthorhombic $BaTiO_3$”. Phys. Rev. 105, 856 (1957).

[27] Ghosez, P., Michenaud, J. & Gonze, X. “Dynamical atomic charges: the case of ABO3 compounds”. Phys. Rev. B 58, 6224–6240 (1998).

[28] K. Terakura, T. Oguchi, A. R. Williams, and J. Kübler. “Band theory of insulating transition-metal monoxides: Band-structure calculations”. Phys. Rev. B 30, 4734 (1984).

[29] W. L. Roth. “Magnetic Structures of MnO, FeO, CoO, and NiO”. Phys. Rev. 110, 1333 – Published 15 June 1958.

[30] https://www.vasp.at/vasp-workshop/slides/magnetism.pdf

[31] J.-H. Park, E. Vescovo, H.-J. Kim, C. Kwon, R. Ramesh & T. Venkatesan. "Direct evidence for a half-metallic ferromagnet". *Nature,* 392, pages 794–796 (1998).

[32] G.Niu, S.Yin, G.Saint-Girons, B.Gautier, P.Lecoeur, V.Pillard, G.Hollinger, B.Vilquin. "Epitaxy of BaTiO3 thin film on Si (0 0 1) using a SrTiO3 buffer layer for non-volatile memory application". Microelectronic Engineering, 88, 7 (2011).

[33] J. Fujioka, A. Doi, D. Okuyama, D. Morikawa, T. Arima, K. N. Okada, Y. Kaneko, T. Fukuda, H. Uchiyama, D. Ishikawa, A. Q. R. Baron, K. Kato, M. Takata & Y. Tokura. "Ferroelectric-like metallic state in electron doped BaTiO3". Nature, Sci. Rep. (2015).

[34] H. Pinto, M. Yoshino, M. Morinaga, A. Stashans, R. Nieminen, Bull. Soc. Discrete Variational Japan 14 (2001) 114.

[35] Vladislav Borisov, Sergey Ostanin and Ingrid Mertig. "Two-dimensional electron gas and its electric control at the interface between ferroelectric and antiferromagnetic insulator studied from first principles". Physical Chemistry Chemical Physics 19, 2015.

[36] A. Savoia, D. Paparo, P. Perna, Z. Ristic, M. Salluzzo, F. Miletto Granozio, U. Scotti di Uccio, C. Richter, S. Thiel, J. Mannhart, and L. Marrucci. "Polar catastrophe and electronic reconstructions at the $LaAlO_3/SrTiO_3$ interface: Evidence from optical second harmonic generation". Phys. Rev. B 80, 075110 (2009).

[37] A. Ohtomo & H. Y. Hwang. "A high-mobility electron gas at the $LaAlO_3/SrTiO_3$ heterointerface". *Nature* 427, pages 423–426 (2004).

[38] S. Gariglio, M. Gabay, and J.-M. Triscone, "Research Update: Conductivity and beyond at the $LaAlO_3/SrTiO_3$ interface", APL Materials 4, 060701 (2016).

[39] Massimiliano Stengel, Pablo Aguado-Puente, Nicola A. Spaldin, and Javier Junquera. "Band alignment at metal/ferroelectric interfaces: Insights and artifacts from first principles". Phys. Rev. B 83, 235112 (2011).

[40] Pham Nam Hai, Shinobu Ohya, Masaaki Tanaka, Stewart E. Barnes & Sadamichi Maekawa. "Electromotive force and huge magnetoresistance in magnetic tunnel junctions". Nature 458 (2009).

[41] O. G. Udalov, N. M. Chtchelkatchev, and I. S. Beloborodov. “Coupling of ferroelectricity and ferromagnetism through Coulomb blockade in composite multiferroics”. Phys. Rev. B 89, 174203 (2014).

[42] Weiwei Li et al. “Oxygen-Vacancy-Induced Antiferromagnetism to Ferromagnetism Transformation in $Eu_{0.5}Ba_{0.5}TiO_{3-\delta}$ Multiferroic Thin Films”. Nat. Sci. Rep. (2013).

[43] N.C. Bristowe, J. Varignon, D. Fontaine, E. Bousquet & Ph. Ghosez. “Ferromagnetism induced by entangled charge and orbital orderings in ferroelectric titanate perovskites”. Nat. Comm. (2015).

[44] W. S. Lee et al. “Role of Lattice Coupling in Establishing Electronic and Magnetic Properties in Quasi-One-Dimensional Cuprates”. Phys. Rev Lett. 110, 265502 (2013).

[45] Xavier Rocquefelte, Karlheinz Schwarz & Peter Blaha. “Theoretical Investigation of the Magnetic Exchange Interactions in Copper (II) Oxides under Chemical and Physical Pressures”. Nat. Sci. Rep. (2012).

Chapter 5: Resonant Tunnelling across Ferroelectric Quantum Wells in Charged Domain Walls

5.1 Methods

The samples are ultrathin epitaxial $La_{0.7}Sr_{0.3}MnO_3/BaTiO_3$ (15/11) unit cells super-lattices grown on top of $SrTiO_3$ (100) substrates using a high pressure (3.2 mbar) and high temperature (750º C) sputtering deposition system [34]. Aberration-corrected scanning transmission electron microscopy (STEM) annular bright field (ABF) images were obtained in an aberration corrected Nion UltraSTEM200 equipped with a 5th-order corrector operated at 200KV and a Gatan Quantum Electron Energy-Loss Spectrometer (EELS). Spectrum images were also obtained using a Nion UltraSTEM100 [35] equipped with a 5th-order corrector and a GatanEnfina EEL Spectrometer, operated at 60KV. For spectrum imaging, the electron beam is scanned along the region of interest and an EEL Spectrum is acquired in every pixel, along with the simultaneous Annular Dark Field (ADF) signal. The probe forming aperture was approximately 30 mrad while the EELS collection semi-angle was 48 mrad. Random noise in the EEL Spectrum images was removed using principal-component analysis [36]. The specimens were prepared by conventional mechanical grinding and polishing and Ar ion milling.

Magnetic tunnel junctions (MTJs) are fabricated from [LSMO (25 nm) / BTO (4.4 nm) / LSMO (25 nm)] tri-layers using standard UV optical lithography and ion milling. The samples are patterned into micron size ($9 \times 18\mu m^2$ and $5 \times 10\mu m^2$) rectangle shape pillars and measured their magneto-transport properties. Typically, 40% of junctions per sample could be measured, which represents a large success ratio of the patterning process.

Aberration corrected STEM-EELS is used in order to study the ferroelectric polarization and the electronic properties in Multiferroic complex oxide heterostructures. Using the Annular Bright Field (ABF) imaging mode, which is

sensitive to light atoms as oxygen, the atomic column position have been measured for all species in the ferroelectric layer and the relative displacement between Ti and O have been quantified, which is related to the ferroelectric polarization. The fine structure of Ti $L_{2,3}$ edge, have been also studied, quantifying the oxidation state, and as a result, the occupation level of Ti 3d band.

The formation of a free-electron gas at charged domain walls (CDW) in $BaTiO_3$ (BTO) [37]. It has also been reported an improvement of ferroelectric properties as electromechanical response [38] due to the presence of charge domain walls (CDW).

5.2 Experimental Results

Magnetic tunnel junctions with active ferroelectric barriers [1] have shown novel technological opportunities related to the separate control of polarization and magnetization. The four resistance states resulting from the (in plane) parallel or antiparallel relative alignment of magnetization vectors of the electrodes for each (out of plane) direction of the polarization vector could expand the possibilities for data storage or enable complex logic operations [2]-[4]. Large changes of the tunnelling electro-resistance occur upon polarization switching [5]-[7] of small ferroelectric domains with polarization vectors parallel to the (uncharged) domain walls. This allows continuously tuning the resistance of the barrier in a multiplicity of domain-controlled memresistance states [8]. In this PhD dissertation, multiferroic tunnel junctions, whose ferroelectric barriers show a completely different domain state with charged domain walls, were examined.

The breakdown of the space inversion symmetry in polar ferroelectrics allows for 180º domain walls with oppositely directed polarization vectors, which tend to be parallel to the polar axis to avoid the build-up of bound charge. Although rare, 180º head-to-head (or tail-to-tail) charged domain are possible, yet at a higher energy cost due to the polarization charges at the wall. In proper ferroelectrics, the existence of charged domain walls (DWs) depends on the availability of free carriers to screen the bound charge, which sets a length scale of the order of 10 nm for the width of the wall (as opposed to 1 nm for a neutral DW). Charged domain walls have been recently shown in bulk samples as the result of poling fields directed at an angle with the stable polarization direction [37, 38]. There are evidences of charged domain walls in ultrathin $BaTiO_3$ (BTO) layers in

multiferroic tunnel junctions. In order to reach this goal, advanced electron microscopy techniques are used to measure the ferroelectric polarization unit cell by unit cell and reveal the real structure and complexity of domain walls in these multiferroic heterojunctions [12]. Charged domain walls are enabled by the presence of oxygen vacancies, which nucleate at the $BaTiO_3$ (BTO) layer to accommodate the large epitaxial mismatch strain, and have a donor character supplying the charge carriers necessary to screen the polarization charges at the domain wall. Furthermore, there are evidences of the domain wall itself providing confined electronic states which enable resonant tunnelling transport between the electrodes, which is modulated by the strong electric field developing in an ultrathin barrier at moderated voltages in a transport experiment.

5.3 Quantum oscillations in tunnelling conductance.

Multiferroic tunnel junctions were obtained by combining ferromagnetic manganite $La_{0.7}Sr_{0.3}MnO_3$ (LSMO) electrodes with ferroelectric $BaTiO_3$ (BTO) barriers in LSMO (10 nm)/BTO (4.4 nm)/LSMO (25nm) tri-layers grown by high pressure oxygen sputtering. BTO layers of this thickness were checked to be ferroelectric by the piezo-force-microscopy (PFM). This system is known to be epitaxial with atomically sharp interfaces. Optical lithography is used to pattern micron size ($9 \times 18 \mu m^2$ and $5 \times 10 \mu m^2$) rectangle shape pillars using standard UV optical lithography and ion milling. Silver electrodes were evaporated to measure perpendicular transport. Intensity-Voltage (I-V) curves (Figure 1) showed the strongly non-linear behaviour characteristic of tunnelling transport. The different thickness of the ferromagnetic electrodes enabled stablishing well defined parallel and antiparallel states of the magnetic electrodes in magnetic field scans due to their different coercitivities (coercive magnetic fields). Surprisingly, the low temperature tunnelling conductance (measured using a dc current set up) exhibits pronounced oscillations indicating resonant transport through discrete unoccupied states of the confined electron gas (see figure 5.1).

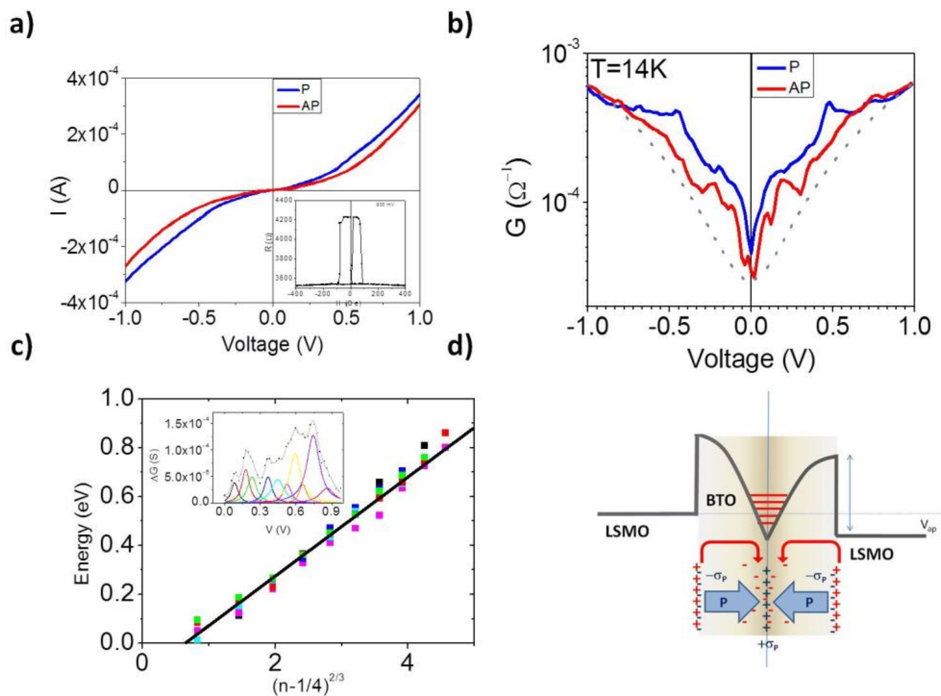

Figure 5.1 Tunnelling transport measurements**.** A Tunneling current as a function of applied bias at parallel (blue curve) and antiparallel (red curve) magnetic state at 14 K. The inset shows the junction resistance versus applied magnetic field sweeping from 4200 Oe to -4200 Oe (black) and from -4200 Oe to 4200 Oe (red) at 14 K measured at 800 mV. B Differential conductance obtained as the numerical derivative of current vs. voltage at parallel (blue curve) and antiparallel (red curve) magnetic state at 14 K. C The inset shows the oscillations maxima, identified by subtracting a parabolic envelop from the experimental differential conductance curves. D Energy levels and band bending scheme.

These quantum oscillations fade out when temperature is increased (Figure 5.1 BIS) and they also disappear when a large voltage is used to switch the ferroelectric polarization (Figure 5.2), indicating that the feature responsible for the presence of confined electronic states in the barrier can be removed by a strong polarizing electric field.

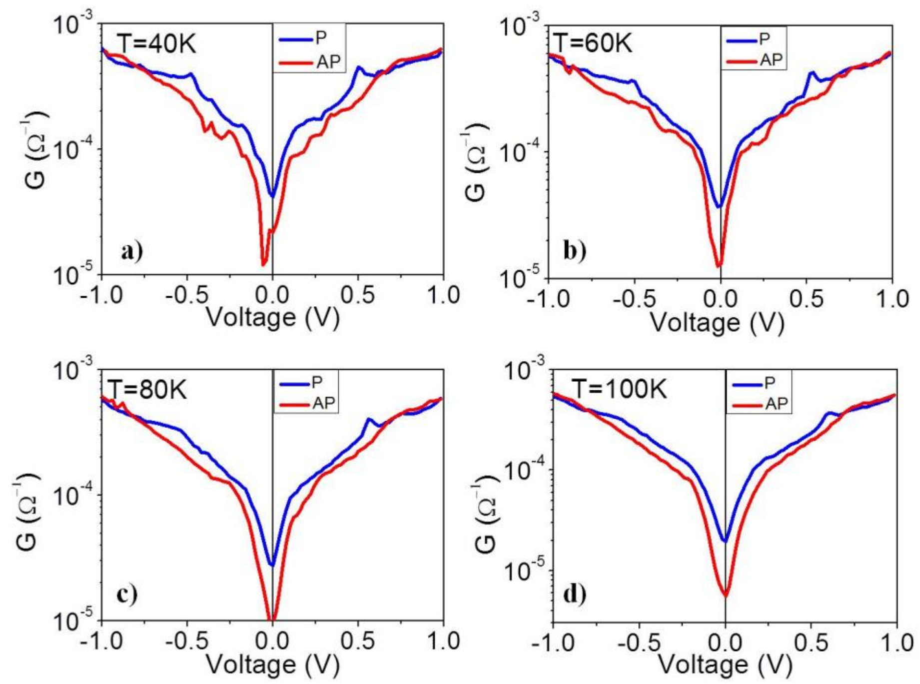

Figure 5.1 BIS Temperature dependence of the conductance oscillations**.** Differential conductance obtained as the numerical derivative of current vs. voltage at parallel (blue curve) and antiparallel (red curve) magnetic state at 40 K (a), 60 K (b), 80 K (c) and 100 K (d).

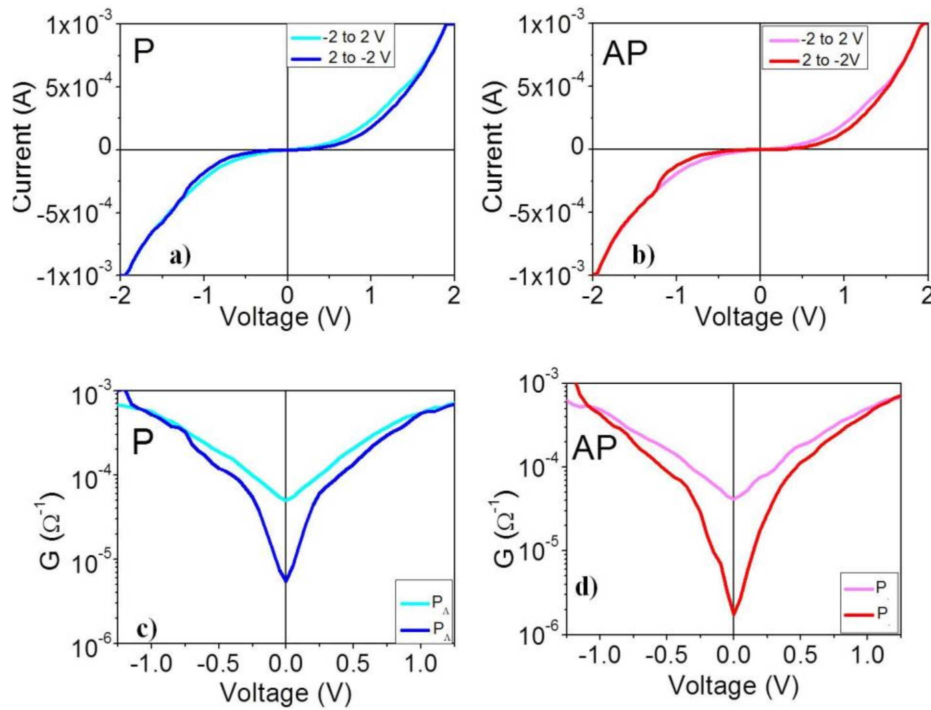

Figure 5.2 Ferroelectric switching of the barrier. Differential conductance obtained as the numerical derivative of current vs. voltage at parallel (blue curves) and antiparallel (red curves) at 40 K. Different curves in each panel correspond to ferroelectric polarization pointing up (dark colour) and pointing down (light colour). Notice that the application of a strong electric field to switch the polarization erases the conductance oscillations.

This feature could consist of mobile defects or structural distortions affecting the local electronic properties or perhaps a domain wall. It is reasonable to think that the energy separations of the conductance oscillations at low temperatures, $\Delta E = (70 - 90) meV$, reflects the possibility of the presence of a two-dimensional electron gas (2DEG) confined within extremely narrow regions within the ferroelectric layer. In order to get further insights into the nature of this resonant tunnelling rate in the ferroelectric barrier, techniques capable of studying structure, chemistry and electronic properties with atomic resolution in real space are essential.

5.4 Fitting of tunnelling conductance peaks

The method to obtain the fitting of tunnelling conductance peaks will be explained in detail. According to references [39], the resonant tunnelling transmission coefficient presents a Lorentzian shape peak, as it will be detailed below:

$$T(E) \approx T_{pk}\left[1+\left(\frac{E-E_{pk}}{\frac{1}{2}\Gamma}\right)^2\right]^{-1}$$

Where the resonance is centred on E_{pk}. Γ is the full width at half-maximum (FWHM), given by the expression:

$$\Gamma = \frac{dE}{dk}\frac{dk}{d\phi}\phi_0 = \frac{\hbar v}{2a}(T_L + T_R)$$

Being ϕ the phase of the interference pattern within the well. The condition for resonance, in other words, the requirement for constructive interference within the quantum well:

$$\phi = 2ka + \rho_L + \rho_R = 2n\pi$$

Through the program Origin Lab, the parabolic envelope of the curves of Figure 5.2 was subtracted, and making use of the Origin Tool Multiple Peak Fit, it is possible to fit the curve choosing the Lorentzian Peak, the curves in the Figure S5.1 are obtained:

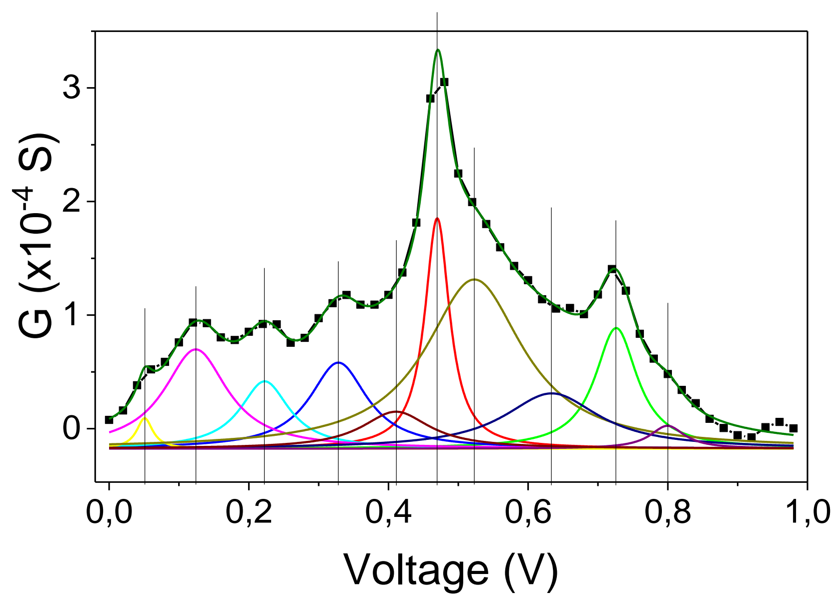

Figure S5.1 Resonant quantum discrete levels lorentzian fitting after subtracting parabolic envelope.

Collecting maxima positions in function of n – 0.5 index, the linear fit in figure S5.2 is obtained

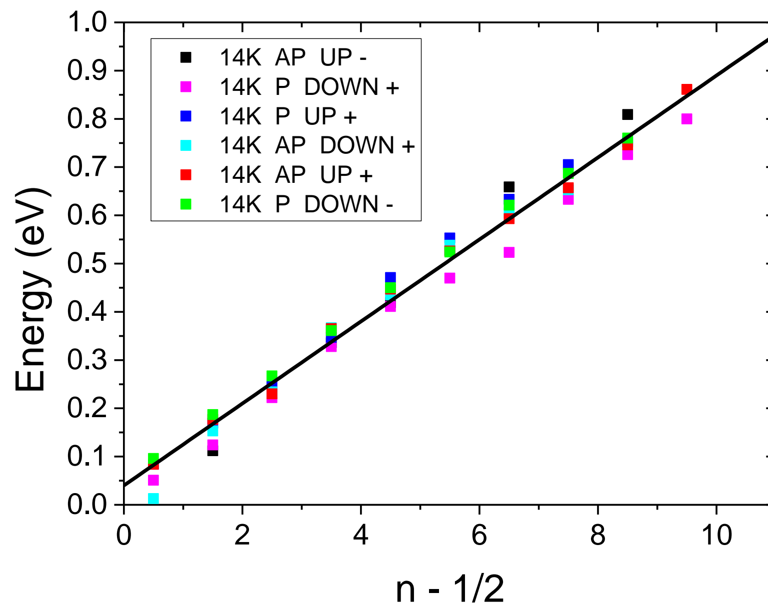

Figure S5.2 Resonant quantum discrete levels parabolic well fitting.

5.5 Measurement of ferroelectric polarization.

To measure the local ferroelectric polarization with atomic resolution, Annular Bright Field (ABF) imaging on a number of LSMO/BTO tri-layers and super-lattices. Atomic resolution imaging in the aberration corrected transmission electron microscope (TEM) provides a path to image light atoms such as oxygen [13], specially by annular bright field (ABF) imaging in the scanning transmission electron microscope (STEM) [14] [15]. Combining ABF images with electron energy-loss spectroscopy (EELS), allow to study not only the structural distortions, but also the chemical and electronic properties of these systems. Here is an example of a super-lattice consisting of a stacking of 17 unit cells of $La_{0.7}Sr_{0.3}MnO_3$ and 11 unit cells of $BaTiO_3$ (two repetitions) grown on top of a $SrTiO_3$ (STO) substrate. Figure 3a shows cross-sectional ABF images of this sample. The growth is epitaxial and coherent, and the different layers are fully strained to the $SrTiO_3$ (STO) in-plane lattice parameter. Such strain will impose a constraint for the ferroelectric polarization in the $BaTiO_3$ (BTO) layer; while the

$BaTiO_3$ bulk lattice parameter is 4.04 Å, the $SrTiO_3$ value is 3.905 Å. Hence, the $BaTiO_3$ (BTO) suffers a 3.34% in-plane compressive strain that makes the unit cell to expand in the out-of-plane direction, forcing the ferroelectric polarization to align preferentially along this axis [16]. Figure 5.3 (b) shows a magnified view of the area highlighted in Figure 5.3 (a). The interfaces between the LSMO and BTO layers are marked by blue dashed lines. Oxygen atoms are visible in this image. In order to reduce random noise and be able to quantify the Oxygen atom positions, a Fourier filter mask is used [17]. From the analysis of such filtered images (Figure 5.3 (c)), it is possible to obtain the atomic column coordinates. Any displacements can be quantified by using an iterative process, looking for the maximum intensity for each column in Annular Bright Field (ABF) images with reversed contrast [18], [19].

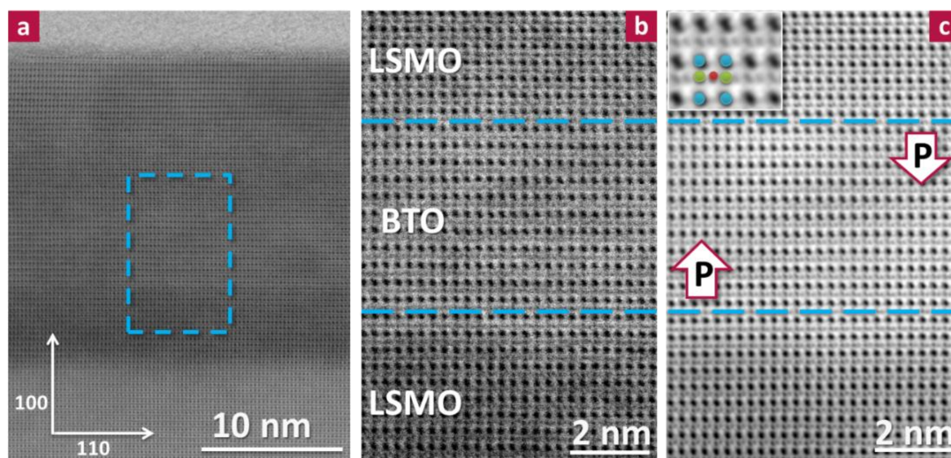

Figure 5.3 Cross-sectional STEM images of a $La_{0.7}Sr_{0.3}MnO_3$ / $BaTiO_3$ super-lattice. a Annular Bright Field (ABF) image of the different layers in the super-lattice. b Amplified image from the area highlighted with a blue rectangle in a. The blue dashed lines denote the interfacial planes. **c** FFT filtered image obtained from b where the oxygen atoms are clearly visible. The inset shows a unit cell scheme in the [1 1 0] orientation with Ba, Ti and O atoms (blue, green, red respectively).

On the one hand, it is noticeable that the oxygen columns in the first planes of the BTO layer are displaced downwards relative to the Ti columns (i.e., towards the bottom LSMO/BTO interface). On the other hand, in the last atomic planes near the top BTO/LSMO interface, the oxygen columns are displaced upwards relative to the Ti columns. The arrows mark the local polarization resulting from this structural configuration. This finding implies that, somewhere through the layer,

there is an inversion of the polarization direction and, hence, a head-to-head domain wall.

5.6 Revealing the presence of a charged H-to-H DW

Having obtained the atomic column coordinates for all atomic species in the image, it is possible to calculate the relative displacement along the out-of-plane axis of oxygen and titanium columns related to the barium sub-lattice, which is used as a reference. This relative displacement (δz) is proportional to the ferroelectric polarization [20]. Figure 5.4 (a) depicts a schematic of a BTO unit cell in the 110 direction, where the relative displacement between oxygen and titanium is indicated. Figure 5.4 (b) shows a false colour map of (δz) for the BTO layer superimposed to the image in Figure 5.3 (c), where each pixel correspond to the (δz) value measured in every unit cell.

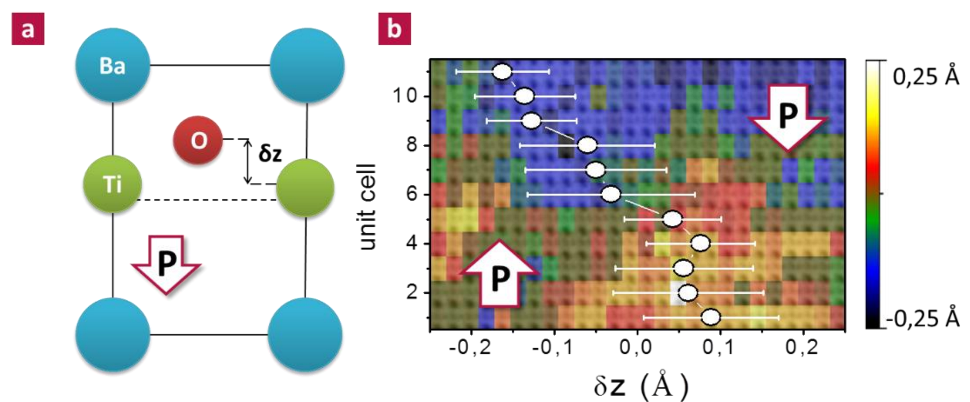

Figure 5.4 Unit cell mapping of the ferroelectric polarization displacements in the BTO layer. A Scheme of a BTO unit cell in the [110] orientation showing the relative displacement (δz) between Ti and O for a polarization down configuration. The horizontal dashed line represents the middle of the unit cell. B δz map from the BTO layer in image 1c, each pixel correspond to one unit cell. Superimposed is the averaged δz Ti-O relative displacement obtained from image b. The error bars represent the standard deviation. The origin in the y axis corresponds to the bottom LSMO/BTO interface.

The absolute values of the displacements measured on the order of $(0.1 - 0.2)$ Å, consistent with previous studies [12], [21], [22]. By mapping these δz values, it is possible to track the local polarization in a quantitative manner unit cell by unit

cell. The trend is an inhomogeneous polarization along the ferroelectric layer, with positive values near the bottom interface and negative values close to the top interface. The graph superimposed in figure 5.4 (b) exhibits the laterally averaged values (along the interface), which clearly demonstrates the sign change in the local polarization. Additionally, the measurements indicate that there is a Head-to-Head (H-to-H) Domain Wall within the ultrathin (11 unit cells) ferroelectric layer, with a polarization vector which changes from positive at the bottom interface, to negative at the top interface. The smooth polarization gradient would in principle suggest that the width of the wall may be of the order of 2 nm. Notice, however, that this polarization is averaged over the thickness of the cross-section sample and also over the size of the spectrum image. Looking at line scans in polarization maps in Figure 5.4, regions where a negative-to-positive change in the value of polarization occurs within nearest neighbours are found; suggesting that, in fact, the domain wall is rough locally (Figure 5.4 (b)).

Notwithstanding such local inhomogeneity, average values of the local polarization across the ferroelectric layer are estimated. Since a Head-to-Head Domain Wall is detected approximately at the centre of the ferroelectric layer and a relative displacement between Titanium and Oxygen atoms of $\delta_{O-Ti} = 0.012 \pm 0.002\ nm$ at the edges of the ferroelectric barrier, the local polarization can be calculated in terms of the ionic displacements within the unit cell using the Born effective charges:

$$P(z) = \frac{e}{V}\sum_{m=1}^{N} Z_m^* \, \delta z_m$$

Where V is the volume of the unit cell, δz_m is the displacement of the mth atom respect to its position in the centrosymmetric cell. The Born charges, Z_m^* reported for $BaTiO_3$ [23] are 2.83 and 5.81 for Ba and Ti cations, respectively, and -1.95 and -4.73 for O anions in the TiO_2 and BaO planes respectively. Making use of an average oxygen charge defined as $\overline{Z_m^*} = -\frac{4.73+2\ 1.95}{3} = -4.3$, the local polarization can be determined in terms of the Ti-O relative displacement measured from the Annular Bright Field (ABF) images as P= 22 C/(m^2 nm)* δ_{O-Ti} (nm). For a displacement δ_{O-Ti}= 0.012 nm (see Figure 5.3). This calculation yields a value of P= 0.27 C/m^2 very close to the bulk polarization of $BaTiO_3$ (0.26 C/m^2).

Such a Head-to-Head Domain Wall implies the build-up of polarization charge at the domain wall which must be screened by free charges. The electronic thickness

of a charged domain wall is essentially determined by the availability of free carriers to screen its bound charge. In un-doped semiconductor ferroelectrics, the screening charge results from charge activation over the forbidden energy gap, E_{gap} of the ferroelectric, which requires strong band bending until the bottom of the conduction band falls below the Fermi level. The creation of a Charged Domain Wall thus involves an energy of $E_{CDW} \cong 2\frac{P_0 E_{gap}}{e}$, where P is the equilibrium polarization at both sides of the domain wall (DW). For $BaTiO_3$, endowed with a $P_0 = 0.26\ {}^{C}/_{m^2}$, and an energy gap of $E_{gap} = 3.2\ eV$. Then, charged domain walls have a large energy cost $E_{CDW} \cong 1600\ {}^{erg}/_{cm^2}$, in comparison with $E_{NDW} \cong 2.5\ {}^{erg}/_{cm^2}$ typically needed for the neutral domain walls (NDW) in $BaTiO_3$. Thus, screening sets a length scale for the width of the barrier which can be estimated to be of the order of the Thomas – Fermi screening length (the length scale for charge in-homogeneities). For intrinsic $BaTiO_3$, with an effective density of states at the conduction band of $n_i = 10^{18}\ cm^{-3}$, the width of the charged domain wall can be calculated to be in the range 10 – 20 nm. Thus, it is particularly puzzling that a 2 nanometres thick, Head – to – Head, energetically expensive, Charged Domain Wall (CDW) is found in the 4.4 nanometres thick $BaTiO_3$ tunnel barrier with a polarization vector directed in the (001) crystalline direction (which typically yields neutral domain walls). Furthermore, the very narrow width of the Head – to – Head domain wall implies that free charges are available to screen the polarization charges.

5.7 Screening of the DW charges by oxygen vacancies.

In the following it is high time to argue that oxygen vacancies at the $BaTiO_3$ layer are the source of the screening charges. In virtue of this assumption, it is necessary to make use of Electron Energy Loss Spectroscopy (EELS) in order to search for free charges whose signature are the changes in the Ti oxidation state. From the study of the occupation of the 3d band of titanium, which affects the crystal field splitting in the L_2 and L_3 edges Electron Energy Loss Spectroscopy (EELS) fine structure [24], evidences suggesting the presence of large amounts of oxygen vacancies in the ferroelectric barrier are found. Then, analysing the fine structure of titanium $L_{2,3}$ edges, it is possible to quantify the titanium oxidation state using a multiple linear least – square (MLLS) fit to two reference spectra for bulk

$LaTiO_3$ (Ti^{3+}) and $BaTiO_3$ (Ti^{4+}) [25]. The fitting results provide the statistical weights for each reference spectra, which help calculate the relative proportion of Ti^{3+} to Ti^{4+}. Then, the Ti oxidation state was obtained for each measured spectra, producing 2D maps of the Ti oxidation state through the $BaTiO_3$ layers [26]. Figure 5a shows a Z-contrast image of the super-lattice with the Ti oxidation state map for the $BaTiO_3$ layer, obtained through the Multiple Linear Least – Square (MLLS) fit method, superimposed in the image. A slight, but significant, reduction in the oxidation state can be noticed well into the $BaTiO_3$ layer. In order to appreciate this kind of behaviour with more detail, the values have been laterally averaged for each pixel in the map, and the resulting profile is depicted in Figure 5.5 (B).

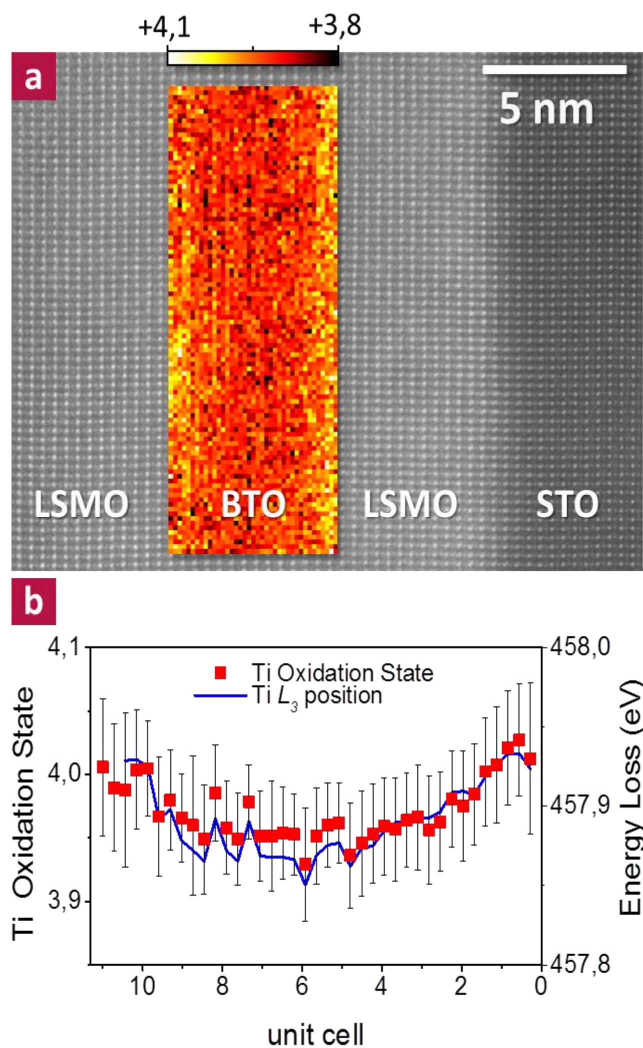

Figure 5.5 Titanium oxidation state quantification in the BTO layer by EELS. A Z-contrast image of the $La_{0.7}Sr_{0.3}MnO_3$ / $BaTiO_3$ super-lattice. The inset shows the titanium oxidation state map from the BTO layer. B Averaged titanium oxidation state value from the inset in image A (red squares). The error bars represent the standard deviation. The blue curve represents the energy loss value for the Ti L_3 edge. The origin in the y axis corresponds to the bottom LSMO/BTO interface.

Notice that in both interfaces the Ti oxidation state is near the nominal +4 value, while inside the layer, as light reduction to $\approx +3.95$ is observed. The error bars in Figure 5.5 (B) correspond to the statistical deviation of the measurement. In addition, a chemical shift (blue curve in Figure 5.5 (B)) of the Ti $L_{2,3}$ edges is also measured, which demonstrates a slight reduction in the Ti oxidation state [27].

Since Ti has a 4+ nominal oxidation state in $BaTiO_3$, the average Ti oxidation state of 3.95+ at the center of the layer results from 5% of Ti atoms with a 3+ oxidation state, which corresponds to a maximum concentration of charge carriers supplied by oxygen vacancies of $n = 8 \times 10^{20}\ cm^{-3}$. Single ionized oxygen vacancies are known are known to produce a level in the semiconducting gap at 0.4 eV below the conduction band edge. Assuming that each vacancy supplies one electron (doubly ionized states have a larger energy cost) and that free electrons are uniformly distributed across the barrier as the Electron Energy Loss Spectroscopy (EELS) image suggests, an estimate of the electronic thickness of the domain wall of 2 – 3 nm can be made. Notice also that for this electron doping, the Thomas – Fermi screening length is in the range of 1 nm [28], which again provides the correct length scale for the width of the Domain Wall (1 nm at each side of the Domain Wall). It is important also to notice that, although these levels of doping may appear high, $BaTiO_3$ is known to retain its ferroelectric ground-state with charge densities in excess of $n = 2 \times 10^{21}\ cm^{-3}$ [28], [29].

A subject of great interest is on the origin of this large density of oxygen vacancies. The large expansion of the lattice and strong strain gradients occurring at the $BaTiO_3$ interfaces provide a clue to the origin of the large density of oxygen vacancies found in the $BaTiO_3$ [30]. Uniformly strained layers, with in-plane lattice parameters clamped to the square lattice of the $SrTiO_3$ substrate, cell volume conservation (Poisson effect) imposes severe constraints to lattice deformations. Since typically the lattice expands around oxygen vacancies due to the enhanced repulsion between B site cations, nucleation of oxygen vacancies are a mechanism to release the large amount of elastic energy stored in uniformly strained structures and is thus likely to occur at compressively strained interfaces.

5.8 Discussion

The presence of a Head-to-Head Domain Wall in the ferroelectric barrier is connected to pinning of the ferroelectric polarization by interface dipoles due to symmetrical $LaO+$ termination of both manganite layers (evidenced by EELS). Both, symmetrical interface terminations [31] together with the donor character of the LaO plane at both interfaces conspire to stabilize a Head-to-Head Domain Wall as theoretically proposed earlier.

The ionization of oxygen vacancies at the $BaTiO_3$ layer contributes stabilizing the Charged Domain Wall by screening the polarization charges. Negative polarization charges at the interfaces are screened by (positive) ionized oxygen vacancies, while the electrons transferred to the core of the Domain Wall (DW) screen the build-up of positive bound charge. The ionized oxygen vacancies gives rise to a band bending at the $BaTiO_3$, which can be approximated by a parabolic (or triangular) potential well by assuming that the oxygen vacancies are uniformly distributed. This fact would result in an electric field inside the $BaTiO_3$ layer with a roughly linear dependence from zero at the centre towards its maximum value close to the interfaces. The band bending necessary to have the oxygen vacancies ionized at $E_D = 0.4\, eV$ below the conduction band in the $BaTiO_3$, allows calculate this electric field to be of the order of $E_{conf} = \frac{E_D}{ew} = 2 \times 10^6\ V/_{cm}$.

Back to the explanation of the quantum resonant tunnelling, the data proof that a 2D Electron Gas (2DEG) is formed at the 4.4 nm thick $BaTiO_3$ layer. The charge transferred from the ionized oxygen vacancies is about 0.05 electrons per unit cell, and therefore to a carrier density of about $n_{2D} \cong 3 \times 10^{18}\ m^{-2}$, which is in fact the electronic charge needed to compensate the polarization charge $2P \approx 0.5\ C/_{m^2}$. The discrete energy spectrum stems from the splitting of the two degenerate d_{xz} , d_{yz} bands while the d_{xy} band (with a negligible energy splitting) will be pushed below the Fermi level due to its large effective mass along the z direction. This electron gas is similar to those reported at the surface of $SrTiO_3$ single crystals and also at the $LaAlO_3/SrTiO_3$ interface [33]. The main assumption made in this physical system is that the ferroelectric charged domain wall (CDW) can be assimilated to a triangular (or parabolic) confining potential (see sketch in Figure 1d) which arises from the band bending which uncovers the screening charges from the oxygen vacancies. Maxima were identified by subtracting a parabolic envelope from the experimental differential conductance curves. Figure 1c shows the voltage positions of the conductance maxima at different temperatures obtained experimentally from the conductance plots of Figure 1 in front of the positions expected from a triangular well. Positions of the maxima are quite equally separated and thus fit very well into the theoretical expression corresponding to a triangular (parabolic) well potential, what allows obtain an estimate of the confining electric field. From the experimental energy separation of about $\Delta E \approx 80\, meV$ between the conductance oscillations, the electric field E can be estimated using the relation:

$$E_n = \left[\frac{3}{2}\pi\left(n - \frac{1}{4}\right)\right]^{2/3} \left[\frac{(eE\hbar)^2}{2m^* m_0}\right]^{1/3} \qquad E_n = \hbar\omega_0\left(n + \frac{1}{2}\right) = \Delta E\left(n + \frac{1}{2}\right)$$

Where E is the confining electric field and m^* is the effective mass for the electrons in the $BaTiO_3$ ferroelectric tunnelling barrier. Imposing an effective mass $m^* = 1$, a value of $E \approx 1.7 \times 10^6 \; V/_{cm}$ is calculated close to the $BaTiO_3$ interfaces (at a distance z = 2nm from the potential minima), which is in good agreement with our qualitative estimate.

Notice finally that the intensity of the conductance oscillations changes for the magnetic alignment (parallel or antiparallel) of the electrodes suggesting a certain degree of spin polarization of the screening charges. This fact can be understood if one realizes that the donor electron nature of oxygen vacancies at the interface with the $La_{0.7}Sr_{0.3}MnO_3$ may be in fact spin-polarized.

In summary, it is shown that the electronic confinement of the ferroelectric quantum well of the Head-to-Head domain wall (DW) completely determines the tunnelling transport in the magnetic tunnel junctions. This milestone traces a new avenue for future devices concepts in oxide electronics exploiting the electronic structure of ferroelectric Head-to-Head charged domain walls (CDW).

5.9 References

[1] J. P. Velez, G. -G. Duan, J. D. Burton, A. Smogunov, M. K. Niranjan, E. Tosatti, S. S. Jaswal, and E. Y. Tsymbal, "Magnetic tunnel junctions with ferroelectric barriers: prediction of four resistance States from first principles". *Nano Lett*, 9, 1, pp. 427–32, (2009).

[2] V. Garcia, S. Fusil, K. Bouzehouane, S. Enouz-Vedrenne, N. D. Mathur, A. Barthélemy, and M. Bibes, "Giant tunnel electroresistance for non-destructive readout of ferroelectric states". *Nature*, 460, 7251, pp. 81–4, (2009).

[3] A. Gruverman, D. Wu, H. Lu, Y. Wang, H. W. Yang, C. M. Folkman, M. Y. Zhuralev, D. Felker, M. R. Zchovski, C.-B. Eom and E. Y. Tsymbal, "Tunneling

electroresistance effect in ferroelectric tunnel junctions at the nanoscale". *Nano Lett*, 9, 10, pp. 3539–43, (2009).

[4] P. Maksymovich, S. Jesse, P. Yu, R. Ramesh, A. P. Badorf and S. V. Kalinin, "Polarization control of electron tunneling into ferroelectric surfaces". *Science*, 324, 5933, pp. 1421–5, (2009).

[5] V. Garcia, M. Bibes, L. Bocher, S. Valencia, F. Kronast, A. Crassous, X. Moya, S. Enouz-Vedrenne, A. Gloter, D. Imhoff, C. Deranlot, N. D. Mathur, S. Fusil, K. Bouzehouane and A. Barthélemy, "Ferroelectric control of spin polarization". *Science*, 327, 5969, pp. 1106–10, (2010).

[6] Z. Wen, C. Li, D. Wu, A. Li and N. Ming, "Ferroelectric-field-effect-enhanced electroresistance in metal/ferroelectric/semiconductor tunnel junctions". *Nat. Matter.* 12, 7, pp. 617–21, (2013).

[7] Y. W. Yin, J. D. Burton, Y.-M. Kim, A. Y. Borisevich, S. J. Pennycook, S. M. Yang, T. W. Noh, A. Gruverman, X. G. Li, E. Y. Tsymbal, and Q. Li, "Enhanced tunnelling electroresistance effect due to a ferroelectrically induced phase transition at a magnetic complex oxide interface". *Nat. Matter.* 12, pp. 1–6, (2013).

[8] A. Chanthbouala, A. Crassous, V. Garcia, K. Bouzehouane, S. Fusil, X. Moya, J. Allibe, B. Dlubak, J. Grollier, S. Xavier, C. Deranlot, A. Moshar, R. Proksch, N. D. Mathur, M. Bibes, and A. Barthélemy, "Solid-state memories based on ferroelectric tunnel junctions". *Nat. Nanotechnol.*, vol. 7, no. 2, pp. 101–4, Feb. 2012.

[9] G. Catalan, J. Seidel, R. Ramesh, and J. F. Scott, "Domain wall nanoelectronics". *Rev. Mod. Phys.*, vol. 84, no. 1, pp. 119–156, Feb. 2012.

[10] J. Seidel, L. W. Martin, Q. He, Q. Zhan, Y.-H. Chu, A. Rother, M. E. Hawkridge, P. Maksymovich, P. Yu, M. Gajek, N. Balke, S. V. Kalinin, S. Gemming, F. Wang, G. Catalan, J. F. Scott, N. A. Spaldin, J. Orenstein, and R. Ramesh, "Conduction at domain walls in oxide multiferroics". *Nat. Matter.* 8, 3, pp. 229–34, (2009).

[11] E. K. H. Salje, "Multiferroic domain boundaries as active memory devices: trajectories towards domain boundary engineering". *Chemphyschem*, 11, 5, pp. 940–50, (2010).

[12] C.-L. Jia, S.-B. Mi, K. Urban, I. Vrejoiu, M. Alexe, and D. Hesse, "Atomic–scale study of electric dipoles near charged and uncharged domain walls in ferroelectric films". *Nat. Matter.* 7, 1, pp. 57–61, (2008).

[13] C. Jia and K. Urban, "Atomic–resolution measurement of oxygen concentration in oxide materials". *Science* 303, March, pp. 2001–2004, (2004).

[14] S. D. Findlay, N. Shibata, H. Sawada, E. Okunishi, Y. Kondo, T. Yamamoto, and Y. Ikuhara, "Robust atomic resolution imaging of light elements using scanning transmission electron microscopy" *Appl. Phys. Lett.*, vol. 95, no. 19, p. 191913, (2009).

[15] S. D. Findlay, N. Shibata, H. Sawada, E. Okunishi, Y. Kondo, and Y. Ikuhara, "Dynamics of annular bright field imaging in scanning transmission electron microscopy". *Ultramicroscopy*, 110, 7, pp. 903–23, (2010).

[16] L. Kim, J. Kim, D. Jung, J. Lee, and U. V. Waghmare, "Polarization of strained $BaTiO_3/SrTiO_3$ artificial super-lattice: First principles study". *Appl. Phys. Lett.*, 87, 5, 052903, (2005).

[17] Y. Kim, J. Yeong, J. Kim, and Y. Kim, "Image Processing of Atomic Resolution Transmission Electron Microscope Images". *J. Korean Phys. Soc.*, 48, 2, pp. 250–255, (2006).

[18] Y. Gong, Z. Liu, A. R. Lupini, G. Shi, J. Lin, S. Najmaei, Z. Lin, A. L. Elías, A. Berkdemir, G. You, H. Terrones, M. Terrones, R. Vajtai, S. T. Pantelides, S. J. Pennycook, J. Lou, W. Zhou, and P. M. Ajayan, "Band gap engineering and layer-by-layer mapping of selenium-doped molybdenum disulfide". *Nano Lett.*, 14, 2, pp. 442–9, (2014).

[19] H. J. Chang, S. V. Kalinin, A. N. Morozovska, M. Huijben, Y.-H. Chu, P. Yu, R. Ramesh, E. A. Eliseev, G. S. Svechnikov, S. J. Pennycook, and A. Y. Borisevich, "Atomically resolved mapping of polarization and electric fields across ferroelectric/oxide interfaces by Z-contrast imaging". *Adv. Mater.* 23, 21, pp. 2474–9, (2011).

[20] Y. Wang, M. K. Niranjan, K. Janicka, J. P. Velez, M. Y. Zhuravlev, S. S. Jaswal, and E. Y. Tsymbal, "Ferroelectric dead layer driven by a polar interface". *Phys. Rev. B*, 82, 9, 094114, (2010).

[21] C. L. Jia, V. Nagarajan, J.-Q. He, L. Houben, T. Zhao, R. Ramesh, K. Urban, and R. Waser, “Unit-cell scale mapping of ferroelectricity and tetragonality in epitaxial ultrathin ferroelectric films”. *Nat. Mater.* 6, 1, pp. 64–9, (2007).

[22] M. Chisholm, W. Luo, and M. Oxley, “Atomic-scale compensation phenomena at polar interfaces”. *Phys. Rev. …*, pp. 1–5, (2010).

[23] P. Ghosez, J. Michenaud, and X. Gonze, “Dynamical atomic charges: The case of ABO_3 compounds”. *Phys. Rev. B*, 58, 10, pp. 6224–6240, (1998).

[24] E. Stoyanov, F. Langerhorst, and G. Steinle-Neumann, “The effect of valence state and site geometry on Ti $L_{2,3}$ and O K electron energy loss-spectra of Ti_xO_y phases”. *Am. Mineral.* 92, 4, pp. 577–586, (2007).

[25] J. Garcia-Barriocanal, F. Y. Bruno, A. Rivera-Calzada, Z. Sefrioui, N. M. Nemes, M. Garcia-Hernández, J. Rubio-Zuazo, G. R. Castro, M. Varela, S. J. Pennycook, C. Leon, and J. Santamaria, “Charge Leakage’ at $LaMnO_3/SrTiO_3$ interfaces”. *Adv. Mater.* 22, 5, pp. 627–32, (2010).

[26] G. Sánchez-Santolino, J. Tornos, F. Y. Bruno, F. A. Cuellar, C. Leon, J. Santamaria, S. J. Pennycook, and M. Varela, “Characterization of Surface metallic states in $SrTiO_3$ by means of aberration corrected electron microscopy”. *Ultramicroscopy*, 127, pp. 109–113, (2012).

[27] M. Yoshiya and Y. Tanaka, “First principles calculation of chemical shifts in ELNES/NEXAFS of titanium oxides”. *J. Phys. …*, 3217, (1999).

[28] Y. Wang, X. Liu, J. D. Burton, S. S. Jaswal, and E. Y. Tsymbal, “Ferroelectric Instability Under Screened Coulomb Interaction”. *Phys. Rev. Lett.* 109, 24, p. 247601, (2012).

[29] T. Kolodiazhnyi, M. Tachibana, H. Kawaji, J. Hwang, and E. Takayama-Muromachi, “Persistence of Ferroelectricity in $BaTiO_3$ through the Insulator-Metal Transition”. *Phys. Rev. Lett.* 104, 14, 147602, (2010).

[30] Y.-M. Kim, J. He, M. D. Biegalski, H. Ambaye, V. Lauter, H. M. Christen, S. T. Pantelides, S. J. Pennycook, S. V. Kalinin, and A. Y. Borisevich, “Probing oxygen vacancy concentration and homogeneity in solid-oxide fuel-cell cathode on the subunit-cell level”. *Nat. Mater.* 11, 10, pp. 888–94, (2012).

[31] C.-G. Duan, R. F. Sabirianov, W.-N. Mei, S. S. Jaswal, and E. Y. Tsymbal, "Interface Effect on Ferroelectricity at the Nanoscale". *Nano Lett.*, 6, 3, pp. 483–487, (2006).

[32] X. Wu, and D. Vanderbilt, "Theory of hypothetical ferroelectric super-lattices incorporating head-to-head and tail-to-tail 180º domain walls". *Phys. Rev. B*, 73, 2, 020103, (2006).

[33] A. F. Santander-Syro, O. Copie, T. Kondo, F. Fortuna, S. Pailhès, R. Weht, X. G. Qiu, F. Bertran, A. Nicolaou, A. Taleb-Ibrahimi, P. Le Fèvre, G. Herranz, M. Bibes, N. Reyren, Y. Apertet, P. Lecoeur, A. Barthélémy, and M. J. Rozenberg, "Two-dimensional electron gas with universal sub-bands at the Surface of $SrTiO_3$". *Nature*, 469, 7329, pp. 189–93, (2011).

[34] M. Varela, Z. Sefrioui, and D. Arias, "Intracell changes in Epitaxially Strained $YBa_2Cu_3O_{7-x}$ Ultrathin Layers in $YBa_2Cu_3O_{7-x}/PrBa_2Cu_3O_7$ Super-lattices". *Phys. Rev Lett.* 83, 19, pp. 3936–3939, (1999).

[35] O. L. Krivanek, G. J. Corbin, N. Dellby, B. F. Elston, R. J. Keyse, M. F. Murfitt, C. S. Own, Z. S. Szilagyi, and J. W. Woodruff, "An electron microscope for the aberration-corrected era". *Ultramicroscopy*, 108, 3, pp. 179–95, (2008).

[36] M. Bosman, M. Watanabe, D. T. L. Alexander, and V. J. Keast, "Mapping chemical and bonding information using multivariate analysis of electron energy-loss spectrum images". *Ultramicroscopy*, 16, 11–12, pp. 1024–1032, (2006).

[37] T. Sluka, A. K. Tangantsev, P. Bednyakov, and N. Setter, "Free-electron gas at charged domain walls in insulating $BaTiO_3$". *Nat. Commun.* 4, 1808, (2013).

[38] T. Sluka, A. K Tangantsev, D. Damjanovic, M. Gureev, and N. Setter, "Enhanced electrochemical response of ferroelectrics due to charge domain walls". *Nat. Commun.* 3, 748, (2012).

[39] "The physics of low dimensional semiconductors". John H. Davies.

Chapter 6: Oxygen Vacancy Control of a Ferroelectric Memristor

6.1 Introduction

The study of the novel electronic states appearing in (both) structurally and chemically sharp interfaces between correlated oxides has become one of the paradigms of an emerging field [5]. Oxygen vacancies, however, are defects difficult to detect and in many cases also to avoid in these perovskite oxides [6], and have drastic effects on materials properties through their associated strain and doping fields [3]. In this paper we make use of the generation and transport of oxygen vacancies through electrochemical interface reactions at electrochemically inert contacts to modify the electric response of the ultrathin barrier of a ferroelectric tunnel junction. Our approach breaks the current paradigm of nominally perfect ("power point") oxide interfaces [5] and exploits the unavoidable defects at interfaces [6] to tailor electronic states. Novel functionalities result from the merging of two well-known phenomena, namely resistive switching driven by the generation and transport of oxygen vacancies and tunnelling electroresistance, due to the switching of the ferroelectric polarization.

In many oxides, resistive switching relies on valence changes associated with the generation and transport of oxygen vacancies across a layer of a semiconducting/insulating transition metal oxide [2, 7- 9]. An electroforming process is required which involves the generation of oxygen vacancies at the anode (typically an inert electrode such as Pt, Ag, Au, etc.) through the reduction process driven by the migration of O^{2-} ions [2, 8- 11] and positively charged vacancies drift towards the cathode where are neutralized by electrons supplied by the cathode modify the conducting properties over a layer termed virtual cathode. Resistive switching is attributed to the growth of this virtual cathode which eventually shorts cathode and anode (as in the Valence Change Model (VCM) [12 - 15]); or to the modification of the contact (Schottky) barrier (Contact Resistance Model (CRM) [16 - 19]).

Although resistive switching is a relatively well-known phenomenon, its incorporation to the ultrathin tunneling barriers of a ferroelectric tunnel junction is shown here to be the source of exciting behaviors. Magnetic tunnel junctions with ferroelectric barriers have focused much interest in recent years due to the possibility of modulating the tunneling resistance by the orientation (up or down) of the ferroelectric polarization in what is called tunneling electroresistance (TER) [4]. Notably, a giant electroresistance has been theoretically predicted [4, 20] and experimentally observed [21–29] for ferroelectric capacitors with metal electrodes with different screening lengths. Some works have shown that electroresistance is solely determined by the domain structure of the ferroelectric (defining multiple memresistance states) [21]. Typically this approach relies on the use of narrow (100 ns or less) pulse sequences to switch ferroelectric polarization and avoid the drift of oxygen vacancies. Other authors have shown large hysteretic resistance changes in ferroelectric tunnel junctions resulting from the drift of oxygen vacancies, [30]. Furthermore, samples produced with high intentional concentration of oxygen vacancies display reversed polarity (resistive) switching to the ferroelectric switching found in similar samples with low vacancy concentration [31]. Both type of switchings have even been found in the same sample, but appearing independently at different voltage ranges [32, 33]. There is an interesting open question on the possible interplay between both phenomena as it could be the source of novel electroresistance effects resulting from the coupling between ferroelectric polarization and charged defects.

Here we explore the interplay between ferroelectric (electroresistance) and oxygen vacancy (resistive) switching by using a radically new approach. By applying *strong continuous dc* fields, electrochemical reactions are promoted in a ferroelectric ultrathin layer we are able to control the generation and transport of oxygen vacancies across it and explore their effect on the switching of the ferroelectric polarization. We demonstrate a strong coupling between ferroelectric polarization and ionized oxygen vacancies. The manipulation of the oxygen vacancies profile at the interfaces of the ferroelectric barrier modifies the screening mechanism of ferroelectric polarization, and vice versa, ferroelectric polarization triggers a strong modulation of the ionized vacancies concentration at the oxide/ferroelectric interface.

6.2 Experimental Results

We have grown ferroelectric $BaTiO_3$ (BTO) on Sr doped La manganite $La_{0.7}Sr_{0.3}MnO_3$ (LSMO) epitaxially deposited onto (001) $SrTiO_3$ (STO) substrates using a high (3.2 mbar pure oxygen) pressure and high-temperature (750 °C) sputtering deposition system [38]. Target to substrate distance was set to 1.5 cm such that the highly confined oxygen plasma was tangent to the substrate.

These LSMO/BTO interfaces are sharp both structurally and chemically as shown by scanning transmission electron microscopy (STEM) high angle annular dark field (HAADF) imaging combined with electron energy-loss spectroscopy (EELS) elemental maps (see Figures 6.1 (a-c)).

Aberration-corrected scanning transmission electron microscopy (STEM) high angle annular dark field (HAADF) and annular bright field (ABF) images were obtained in an aberration-corrected Nion UltraSTEM 200 equipped with a 5th-order aberration corrector and a Gatan Enfinium EEL spectrometer operated at 200 kV. The specimens were prepared by conventional mechanical grinding and polishing and Ar ion milling.

The bilayers are flat and continuous over lateral distances of the order of hundreds of nm, as displayed in the low magnification HAADF image. Figure 6.1(a) exhibits a contrast reversed atomic resolution annular bright field (ABF) image of a LSMO/BTO interface from a SrTiO3(100)//25 nm $La_{0.7}Sra_{0.3}MnO_3$ (LSMO) / 10 nm $BaTiO_3$ bilayer, prepared in cross section down the [110] projection. Since this imaging mode is sensitive to light species [34], O columns can be imaged, and their coordinates can be quantified by looking for the center of mass of intensities for each column [35]. This way, the relative displacement (δz) along the out-of-plane direction for the O/Ti atomic columns can be measured, as described previously [31]. Local polarization P(z) was obtained from the atomic displacements measured from annular bright field images using the Born charges, as described previously [35]. By tracking the local values of the δz parameter, which are in the 0.1-0.2 Å range, the local polarization can be estimated and mapped in a cell-by-cell fashion (as shown in Fig. 6.1(b)).

The polarization of as-grown samples take values close to the bulk polarization of BTO and shows preferred down- orientation, probably due to the accumulation of oxygen vacancies at the surface [36, 37].

Atomic force microscopy imaging shows that the surface topography reproduces the one unit cell thick substrate terraces evidencing a 2D growth (see Figure 1 (d)). Piezoelectric force microscopy (PFM) using amplitude and phase contrast indicate a ferroelectric groundstate and the possibility to 'write' up or down polarization states using few volts tip bias (see Figures 6.1 (e-h)).

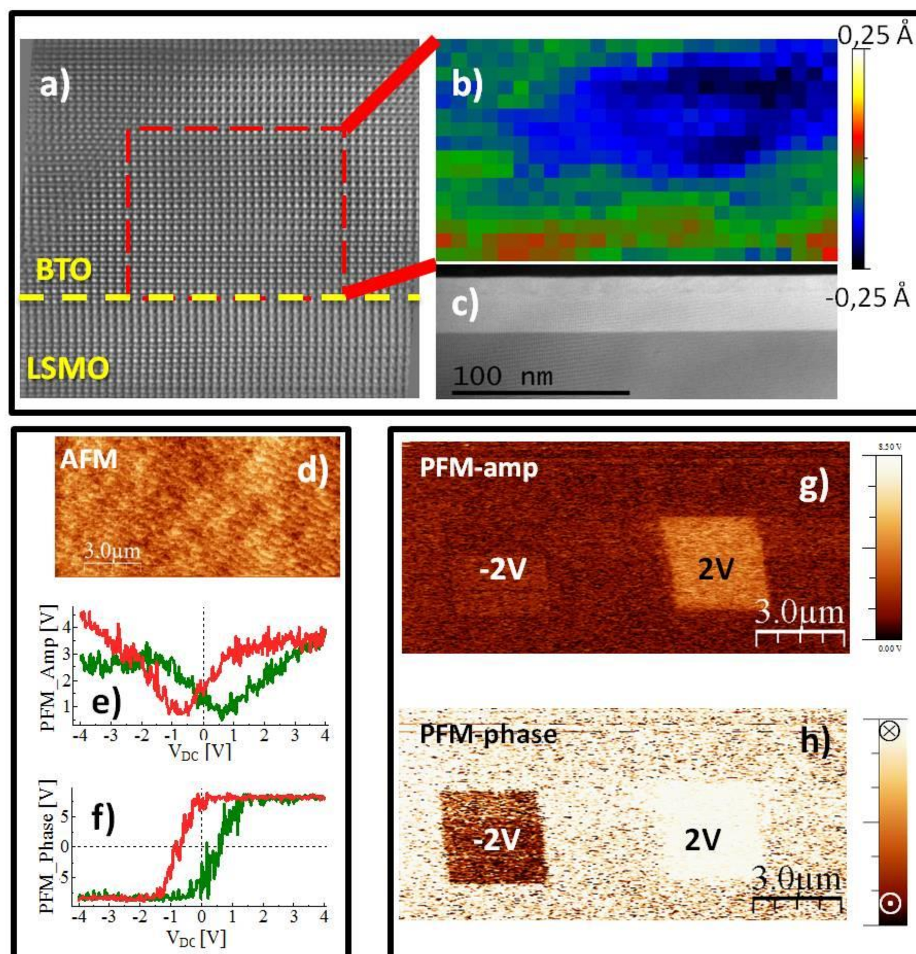

Figure 6.1 Interface structure. High resolution electron microscopy of a SrTiO3(100)//25 nm $La_{0.7}Sr_{0.3}MnO_3$ (LSMO) / 10 nm BaTiO3 sample. a) Contrast reversed ABF image of a cross section sample down the [110] direction which allows measuring the Ti-O displacements to estimate polarization. b) δz map from the region within the red square. c) Low magnification HAADF image showing flat layers and interfaces over large lateral distances. d) AFM image showing atomically flat surfaces displaying STO surface terraces. Piezoresponse (amplitude (e) and phase (f)) hysteresis loop measured on a selected location of the sample. Amplitude (g) and phase (h) PFM images showing that stable polarization states can be written with the PFM tip using small voltages.

Metal (Ag) / $BaTiO_3$ (4nm) / $La_{0.7}Sr_{0.3}MnO_3$ (25 nm) micron-size pillars were fabricated by using conventional optical lithography techniques and ion milling. With such a small barrier thickness electron transport is governed by tunneling through the oxide barrier as previously shown in symmetric $La_{0.7}Sr_{0.3}MnO_3$ (10 nm) / $BaTiO_3$ (4nm) / $La_{0.7}Sr_{0.3}MnO_3$ (25 nm) magnetic tunnel junctions [35]. Ag and LSMO have very similar work functions (4.7 eV and 4.8 eV respectively), and thus both are expected to build up similar contact barriers given by the energy difference between the work function of the metal and the electron affinity of the BTO insulator (3.8 eV), see sketch in figure 6.2 (a). The selection of the Ag electrode serves the purpose of generating oxygen vacancies [38]. Ag is an inert electrode known to promote anodic reduction of BTO as described by the following reaction:

$$O^{2-} \rightarrow \frac{1}{2} O_2 \text{ (gas)} + 2e^- + V_O^{\cdot\cdot}$$

where $V_O^{\cdot\cdot}$ denotes a doubly ionized oxygen vacancy in Kröger-Vink notation. This reaction governs the forming process by which charged oxygen vacancies are generated under the anode and are driven by the electric field to the cathode where they accumulate. Electrons to compensate charge neutrality are supplied by the LSMO cathode. Oxygen vacancies have thus a doping effect associated with their donor character and their accumulation forms a virtual cathode at the LSMO surface with deeply modified conducting properties (see sketch in figure 2 (b)).

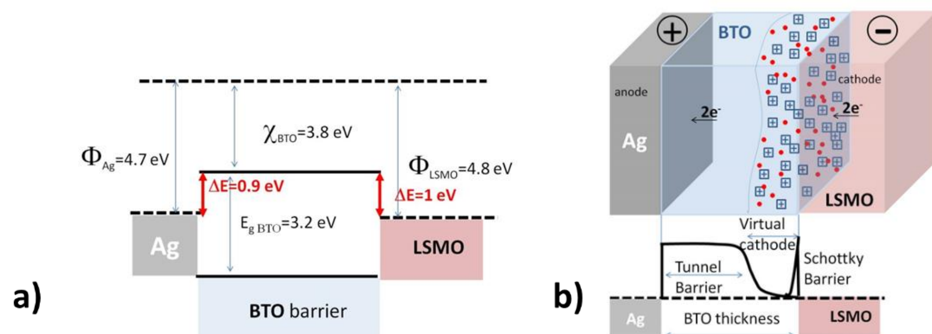

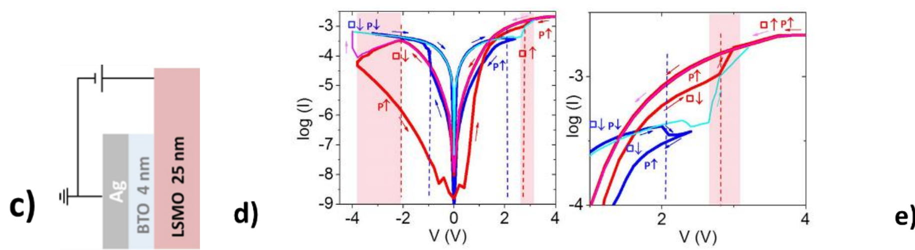

Figure 6.2 Resistive and ferroelectric switching of Ag/BTO/LSMO bilayers. a) Sketch illustrating ideal Schottky contact barriers at the interfaces of an Ag/BTO/LSMO sample. b) Sketch of a virtual cathode formed at the LSMO due to the accumulation of oxygen vacancies generated at the Ag interface and transported across the BTO. Electrons supplied by the LSMO to restore charge neutrality dope the BTO at the interface and depress the tunneling barrier at the Schottky contact with the LSMO (see lower sketch illustrating the conduction band profile). d) IV curves of an Ag/BTO/LSMO sample measured at 100 K. Positive (negative) voltages correspond to electric fields pointing up (down), see device connection scheme in panel c). Blue curves after applying a strong -6 V negative voltage (electric field pointing down). Red curves have been measured after applying strong +6 V positive voltages e). Larger amplitude sweeps cyan curve (with negative starting voltage) and light magenta curve (with positive starting voltage) switch between the two families of curves (blue and red).

We have measured IV curves at temperatures comprised between 20 and 100 K after forming processes in -6 to -8 V negative voltages. We will describe the behavior of the 100 K data as representative of the whole data set (see Figure 6.2). Since transport is dominated by tunneling through the BTO barrier, little changes were observed (as shown later) when temperature is decreased. The top Ag electrode was grounded (see sketch in figure 6.2 (c)), so that positive (negative) voltages correspond to electric fields pointing up (down). Red (blue) curves in figure 6.2 (d) correspond to an initial resistance state written by electric fields pointing up (down) applied after forming. Electric field sweeps from both initial states show two sequential switching fields (voltages). Strong irreversibilities in the IV curves (see figure 6.2 (d)) result from reverse voltage sweeps after crossing the first switching field. On the other hand larger voltage amplitude sweeps across the second switching field allow switching between curves families (red and blue) with different initial resistance states (written in up or down fields). See for an example the light blue curve in figure 6.2 (d), which starts in the blue curve at negative voltages and switches into the red curve. Conversely, the light magenta curve starts in the red curve at positive voltages and switches into the blue curve at sufficiently negative voltages.

Notably, the presence of two different sequential switching fields is a unique feature which evidences the independent switching of oxygen vacancies and of the ferroelectric polarization. For clarity, Supplementary Figure S6.1 shows Figure 6.2 (d) replotted in a linear scale in to better identify the switches at positive voltages. As it will become apparent below, both processes can be distinguished since the switching of oxygen vacancies involves their generation or annihilation, a process which is slowed down at low temperature yielding more gradual switching than the ferroelectric polarization which is typically more abrupt. Moreover, as described below both phenomena produce resistance switches of different signs, yielding eight-like (blue curves) and counter-eight-like (red curves) IV loops.

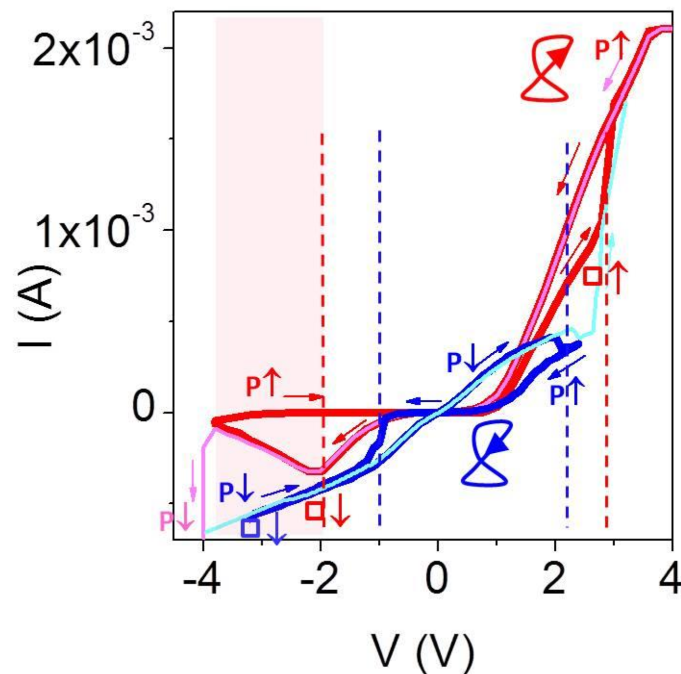

Figure S6.1 Resistive and ferroelectric switching of Ag/BTO/LSMO bilayers. IV curves of an Ag/BTO/LSMO sample measured at 100 K as in Figure 6.2 (c) but displayed in a linear scale to have a better perspective of the resistance switches at positive voltages.

Strong initial electric fields pointing down (blue curves in Figure 6.2 (d) at large negative voltages) force ferroelectric polarization to point down and drive oxygen vacancies generated at the Ag electrode towards the (bottom) LSMO interface. IV

curves (blue curves in Figure 6.2) are tunnel-like for this initial write field. The abrupt switch to a higher resistance state occurring at 2V corresponds to the switching of the ferroelectric polarization to point up (see the enlarged view of the positive voltage region in Figure 6.2 (e)). The resistance increase can be understood within the interface polarization model [20], as a result of the increase of the average barrier height when polarization points away from the LSMO electrode with the longest screening length. Analysis of IV curves at low voltages with the Brinkman model for a trapezoidal tunnel barrier [39] yielded barrier heights of 0.2 and 0.36 eV for down and up polarization respectively. The height of the tunnel barrier is determined by the distance from the Fermi level to the edge of the BTO conduction band. The Fermi level lies above the relatively deep donor level of the oxygen vacancies (0.4 eV below conduction band edge) which are weakly ionized at the low temperatures of the experiment. At large voltages current is limited by a series resistance due to the doping of the LSMO electrode due to the transfer of oxygen vacancies (which are shallow donors for LSMO). For initial electric fields pointing down, the large series resistance results from the compensation of manganite holes by the electrons supplied by oxygen vacancies and transferred across the interface. Further increasing voltage (see light blue curve in figures 6.2 (d) and 6.2 (e)) produces a gradual switch into the red curve which as discussed below is associated with the switching of oxygen vacancies towards the top (Ag) interface.

Electroresistance loops measured by recording the resistance at low voltages (10 mV) after writing in high voltage loops of figure 6.2 (d) show a positive electroresistance at positive voltages which supports the assignment of the low field switches to the inversion of the ferroelectric polarization (see figure 6.3 (a)). Large values of the electroresistance were obtained in the range 10^4 – 10^5 % as expected from the large interface asymmetry due to the different contacts, in agreement with the giant electroresistance effects previously discussed in ferroelectric capacitors with metal electrodes with different screening lengths [20]. The sketches in Figure 6.3 (a) illustrate the increase of the tunnel barrier for polarization pointing up (away from the LSMO electrode with longer screening length than Ag due to its lower carrier density).

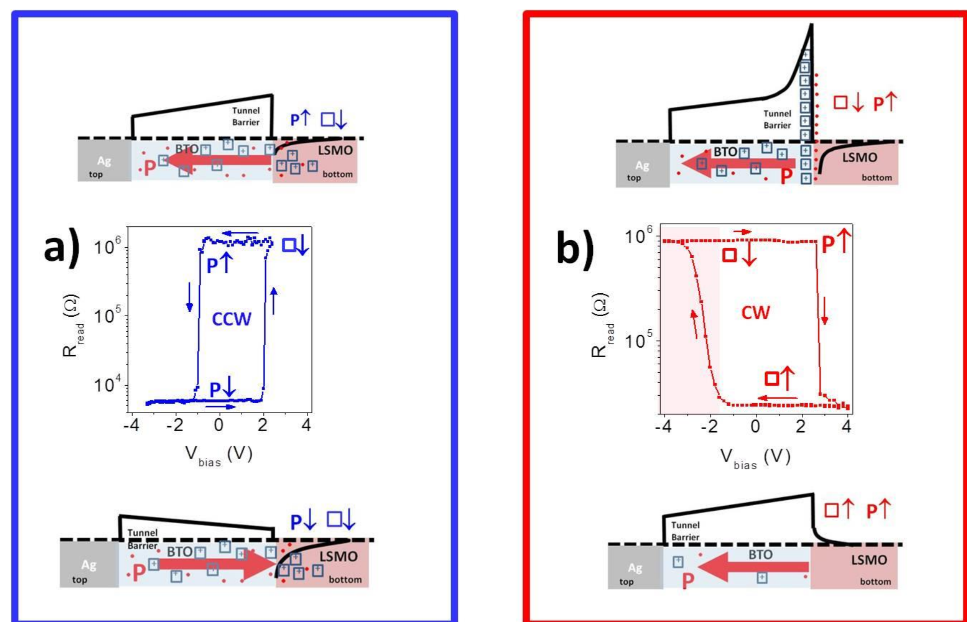

Figure 6.3 Oxygen vacancy driven change of the sign of the electroresistance. Electroresistance loops of an Ag/BTO/LSMO bilayer with initial state 'written' with electric field pointing down (vacancies down) (a), and with electric fields pointing up (vacancies up) (b). Upper and lower sketches in panel (a) illustrate the modulation of the tunnel barrier due to the asymmetric screening at the interfaces according to the interface polarization model [23].

On the other hand, initial electric fields pointing up force ferroelectric polarization to point up and push oxygen vacancies towards the Ag metal (top) interface (red curves in Figure 6.2 (d) at large positive voltages). IV curves between positive voltages down to -2 V are tunnel like with larger barrier heights close to 0.7 eV (as obtained from the analysis with the Simmons model) indicating the depletion of the BTO barrier from oxygen vacancies. Furthermore, notice that in this configuration, the series resistance is the smallest indicating stronger hole doping of the LSMO. The picture emerges that the positive write voltages annihilate oxygen vacancies.

Sweeps towards more negative voltages (V < -2 V) result first in a gradual cross over from tunnel- into Schottky-like IV curves denounced by a strong suppression of the current at negative voltages. See also Figure 6.2 (d) reproduced in linear scale as Supplementary Figure S6.1. This process occurs over a very wide voltage range (marked with a pink shaded rectangle in Figure 6.2 (d)) and its very gradual nature is a strong indication that it is due to the electrochemical generation of oxygen vacancies, slowed down at the low temperatures of the experiment, and

not to the reversal of the ferroelectric polarization which typically occurs with sharper coercive fields. The Schottky barrier builds up at the bottom interface (reversed biased for negative voltages) and results from the accumulation of oxygen vacancies there. If voltage is now reversed, diode–like IV curves are found until at positive voltages resistance switches back to the initial tunnel-like curve. This switching is also gradual and coincides with the high voltage switch of the light blue curves into the red curves (oxygen vacancies drift towards top Ag electrode). Notice also that its level is well above the positive switch which we have ascribed to the switching of the ferroelectric polarization in the blue curves (see enlarged view of Figure 6.2 (e)). It is thus natural to conclude that in the red curves ferroelectric polarization remains always pointing up and to ascribe the high voltage switch to the (partial) annihilation of oxygen vacancies at the top Ag electrode.

The onset of the Schottky regime produces a strong resistance increase at negative voltages. This increase is so large that hysteretic electroresistance loops cannot be measured at low voltage. The resistance loops corresponding to switching of oxygen vacancies (red curves in Figure 6.2 (d)) were measured at a level of 0.7 V necessary to achieve a measurable resistance in the high resistance state (see Figure 6.3 (b)). Oxygen vacancy hysteretic resistance loops measured at low voltage are clock-wise compared to ferroelectric electroresistance loops which are anti-clock-wise, indicating a different underlying mechanism. We can thus define an oxygen-vacancy-electroresistace driven by the generation and accumulation of oxygen vacancies at the bottom interface. Its sign (negative in this system) is opposite to the (positive) ferroelectric electroresistance, and its size can also be very large due to the build-up of a Schottky barrier, yielding near "infinite" electroresistance at low voltage due to the reversed bias conduction of a 0.5 eV barrier building up. Such "negative" electroresistance is not expected from ferroelectric switching further supporting our interpretation in terms of the switching of oxygen vacancies.

Comparing the switching behavior of (Ag)BTO/LSMO bilayers with symmetric LSMO/BTO/LSMO trilayers provides further support to the role of oxygen vacancy generation at the Ag/BTO interface. Symmetric LSMO/BTO/LSMO tunnel junctions from [LSMO 25 nm)/BTO (4.4 nm)/LSMO 10 nm] trilayers using standard UV optical lithography and ion milling. Samples are patterned into micron size (9x18 μm^2 and 5x10 μm^2) rectangle shape pillars with silver electrodes evaporated to measure perpendicular transport whose geometry and thickness are equal to the bottom LSMO and BTO layers of the bilayers showed nearly

symmetric IV curves displaying very weak irreversibility (see Supplementary Figure S6.2). This finding indicates that although the mixed valence of the manganite allows for redox processes at the interface and structural vacancies may exist at the interfaces there is not significant oxygen vacancy generation in this voltage range. The small electroresistance observed in the low voltage resistance loops is ascribed to the reversal of the ferroelectric polarization, possible accompanied by the drifting of (native) oxygen vacancies (see inset to figure S6.2).

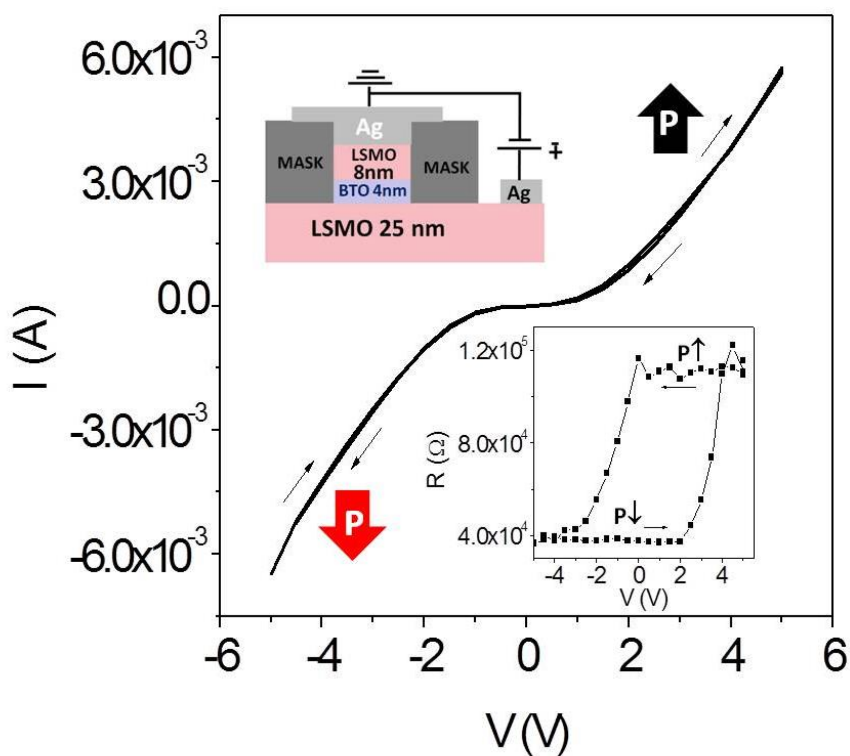

Figure S6.2 Electroresistance of LSMO/BTO/LSMO trilayers. IV curves cycling the voltage between -5 and +5 V of a symmetric LSMO/BTO/LSMO trilayer (see sketch in upper inset). The lower inset shows the electroresistance loop using a 10 mV reading voltage after applying the 'write' voltages of the loop of the main panel.

Measurements at different temperatures in the range 20-100 K produced very small changes in the IV curves and in the electroresistance loops. Figure 6.4 shows a series of IV curves at different temperatures in separate plots for initial up and

down write fields as well as low voltage electroresistance loops. The weak temperature dependence can be understood on the basis of the transport being dominated by tunnelling across the ultrathin ferroelectric and allows ruling out interpretations in terms of filamentary Ag conduction which would render the low resistance state metallic [40, 41]. The small differences observed in the crossover into the Schottky regime indicate that temperature plays a role in the kinetics of the vacancy generation reaction.

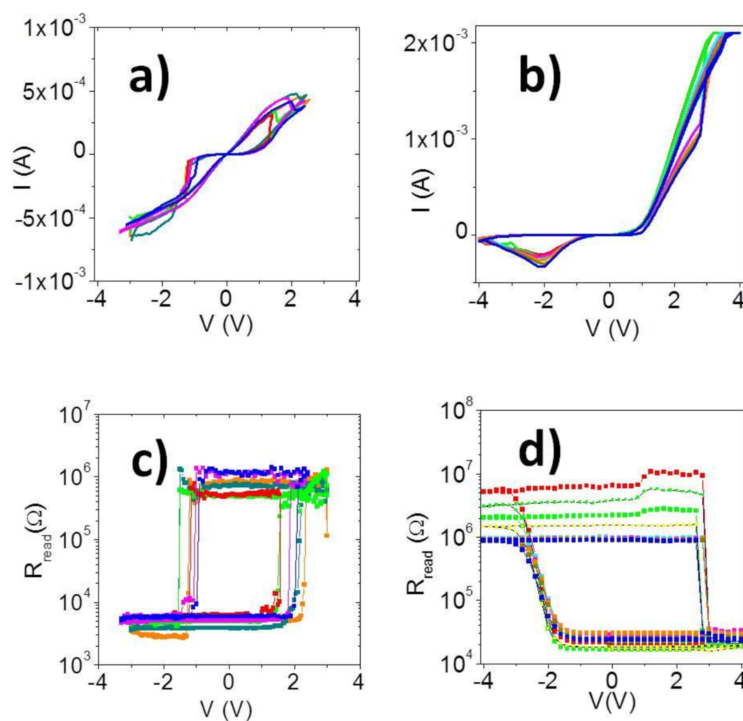

Figure 6.4 Temperature dependence of the IV curves (4(a) and 4(b)) and of electroresistance loops (panels (b) and (c)). For initial fields pointing down (panels (a) and (c)) temperatures are: red (20 K), green, magenta (80 K) and blue (100 K). For initial fields pointing up (panels (b) and (d)) measured temperatures are (red (30 K), green (45 K), cyan (75 K), magenta (80 K), orange (85 K), olive (90 K) and blue (100 K). To better illustrate the temperature dependence of the high resistance level in panel (d) data at 35 K (small green symbols) and 55 K (small yellow symbols) have been added.

Notice that the resistance switches at the onset of the Schottky barrier (negative voltage flank of the resistance loops in Figure 6.4 (d)) are very gradual and extend over a wide voltage range (also marked with a pink shaded rectangle in the figure 6.3 (b)). This gives rise naturally to a memristive response with multiple high-

resistance states controlled by the maximum bias (before sweep direction is reversed) of the minor loops along its negative flank. See figure 5. The high resistance level is controlled by the gradual built up of space charge giving rise to the Schottky barrier, and in fact, the voltage asymmetry of the loop can be used to estimate the voltage drop (height) in the barrier, of the order of 0.7 volts after inspection of figure 6.5.

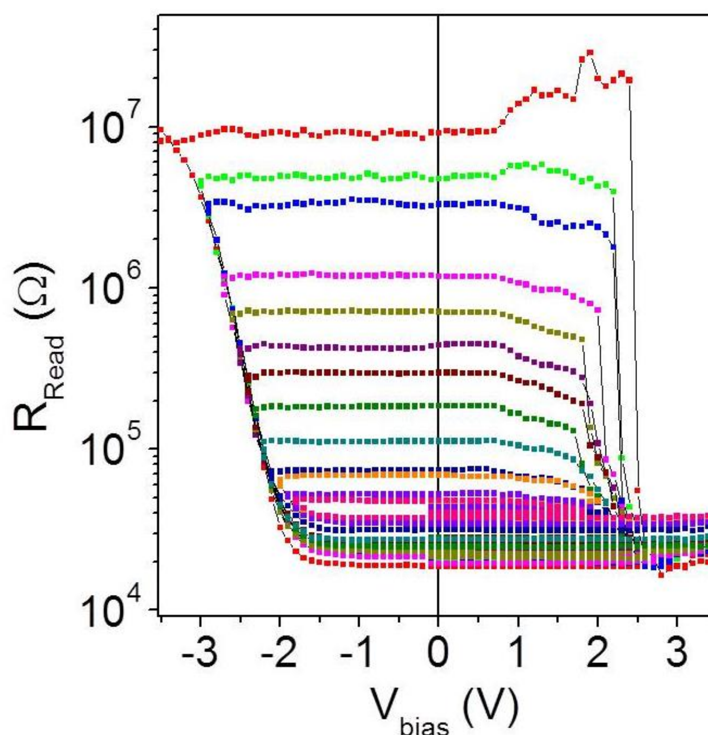

Figure 6.5 Memristive resistance loops. Resistance loops measured at 15 K. Resistance was recorded at 0.7 volts after different bias (´write´) voltages as shown in the x axis. The different high resistance states result from different maximum voltages along the negative voltage flank of the hysteresis loop.

6.3 Discussion

We now discuss the formation of the Schottky barrier. Notice that it starts building up in a state where, after application of large positive voltages, the barrier has been

depleted from oxygen vacancies and ferroelectric polarization has been driven to point in the up direction. The depletion of oxygen vacancies causes the observed increase of the tunnel barrier as illustrated in the lower sketch of Figure 6.3 (b). The Schottky barrier forms at the onset of oxygen vacancy generation at negative voltages. Its very formation indicates a high level of ionization of the oxygen vacancy levels. Moreover, the stabilization of the polarization-up state in high negative voltages constitutes an evidence of the screening of polarization charges by oxygen vacancies. I.e., the positive charges of the ionized oxygen vacancies compensate the negative polarization charges at the bottom interface corresponding to the ferroelectric polarization pointing up. This high level of ionization is caused by the interplay between vacancy generation and compensation of polarization charges. Oxygen vacancies generated at the Ag electrode enter the BTO layer in a charged state, and driven by the electric field, they reach the interface where they are trapped by the negative polarization charges. Neutralizing electrons supplied by the bottom LSMO electrode accumulate at the LSMO side of the interface building up the Schottky barrier (and annihilating the screening holes of the negative polarization charges in the tunnel regime prior to vacancy generation). See upper sketch in Figure 3 (b). Assuming that oxygen vacancies accumulate in a narrow $\delta = 1nm$ thick layer at the BTO interface to screen the $\sigma_P = 1.6 \times 10^{14}\ cm^{-2}$ sheet carrier density corresponding to the bulk polarization of the BTO and using $\varepsilon_r = 100$ for the relative permittivity of the BTO the height of the barrier V_b can be estimated from $\frac{\sigma_P}{\varepsilon_r} = \frac{V_b}{d}$ to be V_b =1 V. The picture emerges that, the formation of the Schottky barrier is the signature of the screening of ferroelectric polarization by charged oxygen vacancies. This mechanism stabilizes the up-polarization up to relatively large negative fields of -4V, above which the Schottky barrier collapses and polarization switches. It can be observed from the IV curves that once the Schottky barrier has been formed, further increasing negative voltage (see magenta curve) produces an abrupt switch of the resistance to reach the state (blue curves at negative voltages) corresponding to the ferroelectric polarization pointing down and non-blocked weakly ionized oxygen vacancies. I.e. the switch occurring at large negative voltage involves a) the switching of ferroelectric polarization and b) a sudden change in the ionization of oxygen vacancies accompanied with a redistribution (as evidenced by the large series resistance).

This result evidences a strong interplay between oxygen vacancies and ferroelectric polarization which couples their switching. Notice that the accumulation of oxygen vacancies at the bottom interface stabilizes the up

polarization which now switches at a voltage of nearly -4 V instead of the -1 V coercive voltage. Conversely, the polarization pointing down triggers the accumulation of ionized oxygen vacancies which give rise to the Schottky barrier.

A direct confirmation of this scenario is obtained from the measurements of low voltage capacitance. Frequency dependent capacitance and conductance were measured using a HP 4285 impedance analyzer in the frequency range 1 kHz – 100 kHz on samples patterned in the form of micron size pillars using low voltage (20 mV) excitation ac signals. Voltage was swept in a hysteresis loop sequence (see Figure 6.6) after applying a positive initial 'write' voltage (polarization pointing up and barrier depleted from oxygen vacancies). A hysteretic capacitance was measured whose switching is dominated by the accumulation of oxygen vacancies at the BTO/LSMO interface. The increase of the capacitance (and the decrease of the conductance) observed at moderate negative (write) voltages, results from the accumulation of the charged vacancies to compensate the negative polarization charges at one side of the interface and the accumulation of electrons at the LSMO side in the same amount to restore charge neutrality, building an interface dipole. The size of the dipole can be estimated from the capacitance hysteresis as $\Delta C = \frac{\Delta Q}{\Delta \phi}$ which relates the increment of the capacitance (5 10^{-11} pF) to the barrier height and the charge stored at one side of the interface. $\Delta \phi = \frac{e\delta\sigma_p}{\varepsilon}$. Using 40 for the high field value of the relative permittivity, an effective value of the barrier of 0.5 V is estimated using the charge density 1.6 10^{14} cm^{-2} corresponding to the polarization charges of the BTO. For positive voltages the reversed electric field (now pointing up) eventually sweeps the oxygen vacancies out of the Schottky barrier restoring the tunneling regime, and giving rise to a conductance increase and a decrease of the capacitance.

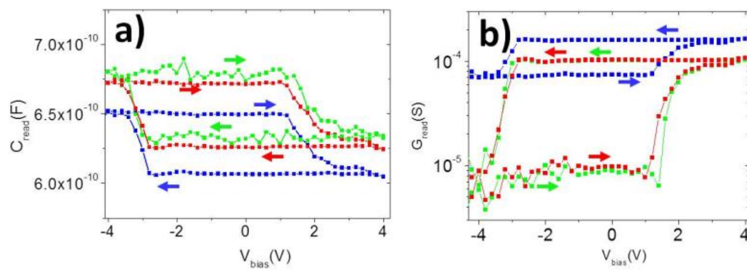

Figure 6.6 Hysteretic capacitance in the Schottky regime. (a) Capacitance and conductance (b) recorded at 100 K at various frequencies: of 1 kHz (green symbols), 10kHz (red symbols) and 100 kHz (blue symbols) read at low voltages (20 mV) after sweeping the 'write' voltage in an hysteresis loops sequence.

Physically, this result can be understood in the framework of models where ferroelectric polarization is compensated / screened at interfacial Schottky barriers building at interfaces due to the accumulation of defects [42 -43]. These models rely on the existence of an ultrathin dead layer of thickness δ inside the space charge region at the ferroelectric side [43] where potential drops bending the bands of the ferroelectric. This dead layer is always present due to incomplete screening of polarization charges although it may result also from the presence of defects [43].

In summary, we have shown the interplay between electric field driven oxygen vacancy generation and polarization switching in a ferroelectric tunnel barrier with a redox active electrode. We have demonstrated that the screening of polarization by charged oxygen vacancies, increases the ionization of the donor level associated with oxygen vacancies well above the level set by thermodynamic equilibrium. Ferroelectric driven ionization builds up an interface dipole which controls tunnel transport yielding a nearly infinite electroresistance. Moreover, the interplay between electrochemical processes involving ion motion and electronic processes in a single device opens interesting new avenues not only for novel memory applications but eventually for emulation of neuron activity and its integration in neuromorphic computing networks.

As a parenthetical remark, it is noted a weak Mem-Capacitor behavior in Figure 6.6. According to reference [42], the necessary condition to obtain a memory capacitor is a reversible chemical reaction controlled by an electric field. In the proposed particular case, the electric field create interstitial oxygen atoms in the face-centered cubic silver electrode leaving behind oxygen vacancies in the Barium Titanate barrier, because of the different charge carrier mobilities between the interstitial oxygen atoms and the oxygen vacancies, the mem-capacitor effect is warranted. Thus, an additional electric field is needed to remove the interstitial oxygen atoms from the fcc silver electrode in order to recombine them with the oxygen vacancies in the Barium Titanate tunnel barrier. The border traps can be estimated using this expression [43]:

$$\Delta N_{2D} \sim \frac{1}{qA} \int_{V_1}^{V_2} |C_B - C_F| dV$$

Using Figure 6.6, and dividing ΔN_{2D} by $BaTiO_3$ barrier thickness, the volume concentration of oxygen vacancies is obtained:

$$\Delta N_{3D} = 7.5 \times 10^{20} cm^{-3}$$

The electric field associated with the interface dipole from the interplay between the ferroelectric polarization and the oxygen vacancy ionization is the following:

$$E_{F-P} = \frac{P}{\varepsilon_0 \chi} \cong 3.7 \times 10^7 \, {}^{V}\!/_{m}$$

Multiplying this electric field by the tunnel barrier thickness of approximately 4 nm:

$$\Delta U \cong 0.15 \; eV$$

Obtaining the change in the barrier height due to the change of the ferroelectric polarization.

Figures 4.29 and 4.30, the density of states (DOS) depicts a localized state 150 meV on the left of the Fermi energy possibly ascribed to an interface pinning dipole level as a result of the interplay between the ferroelectricity and the oxygen interstitial-vacancy pair.

6.4 Ferroelectric Memristor with transition metal top Electrodes

We have performed memristor hysteresis and impedance spectroscopy measurements using other metals as top electrodes: Cobalt, Tantalum, and Nickel. The idea behind this experiment is tailoring the generation of oxygen vacancies through the oxidation threshold of the metal which changes between -1,8eV for Co to -3eV for Pt (see table 6.1 for work functions and redox/absorb thresholds for the selected electrodes).

Metal	Schottky Voltage	TER 1kHz 50K	REDOX/Absorb Threshold Voltage	Work Function
Ag	+0,8V	14,35	-2V	4,73eV
Co	+1,0V	189,55	-1,8V	5eV
Ta	+1,2V	742,82	-3,8V	4,2 eV ($TaSi_2$)
Pt	+0,8V	214,07	-3V	6,35eV

Table 6.1. Values of Schottky voltage, TER Ratio, Oxidation threshold and Work function for Ag, Co, Ta [66] and Pt.

6.4.1 LSMO/BTO/Cobalt

Cobalt has a very low oxidation enthalpy and it is very prone to be oxidized to form the CoO native oxide generating oxygen vacancies in $BaTiO_{3-\delta}$ ferroelectric barrier. The switching of oxygen vacancies gives rise to the hysteretic conductance curves displayed in figures 6.7 and 6.8 which depends strongly on frequency. Hysteretic conductance curves are associated to the switching of oxygen vacancies as inferred from the anticlock-wise sense of the loops (see discussion in preceding paragraphs). Recent literature [40, 41] has discussed that surface interfacial defect states and the pinning of the domain walls by the ionization-deionization of oxygen vacancies could play a relevant role in the frequency dependence of the Write and Read Conductance Measurements.

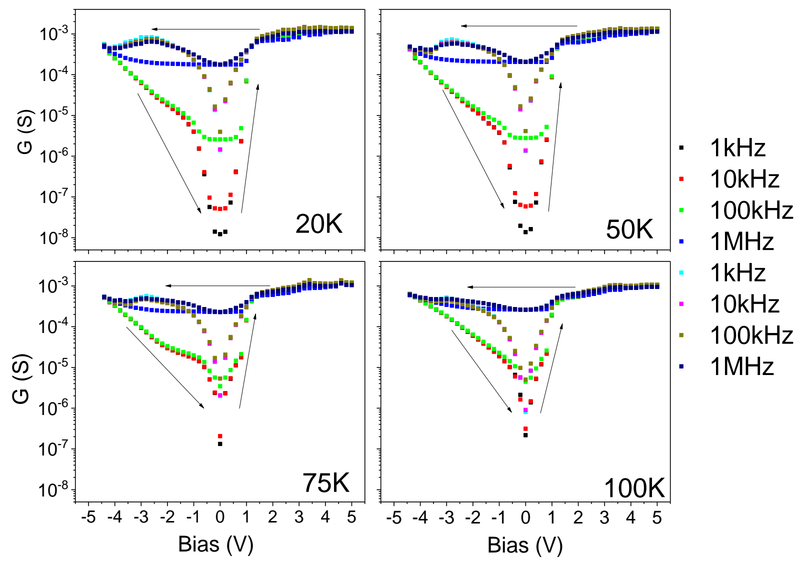

Figure 6.7 'Write' differential Conductance measurements LSMO/BTO/Co at 20, 50, 75 and 100 K.

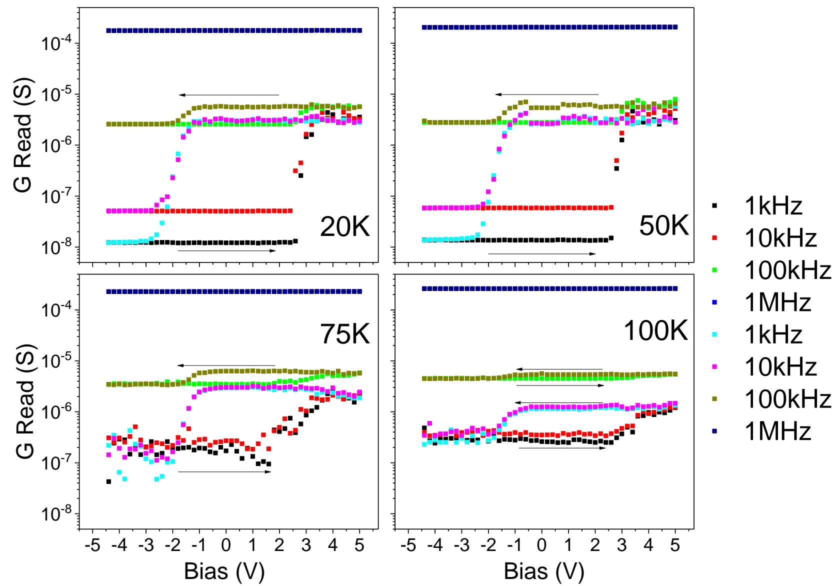

Figure 6.8 'Read' differential Conductance measurements LSMO/BTO/Co at 20, 50, 75 and 100 K.

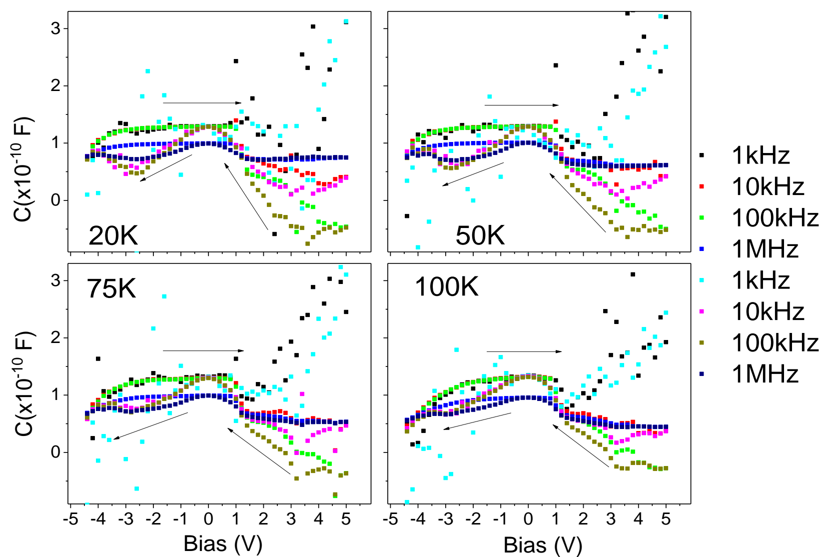

Figure 6.9 Write differential Capacitance measurements LSMO/BTO/Co at 20, 50, 75 and 100 K.

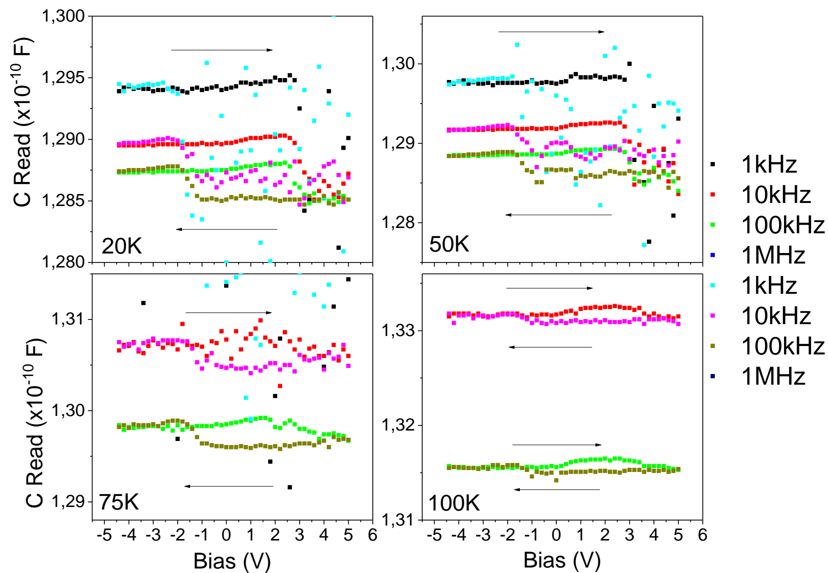

Figure 6.10 Read differential Capacitance measurements LSMO/BTO/Co at 20, 50, 75 and 100 K.

Note the decrease of the memristive hysteresis behaviour while increasing the temperature and also the strong dispersion of the Write and Read differential Conductance with the change of frequency. The low amplitude hysteretic capacitance (memcapacitor) behavior [42] displayed in figure 6.10 is analogous to

the one found in LSMO/BTO/Ag junctions and described in the previous section. In order to get information on the energy scales involved in charge trapping-detrapping mechanisms (interfacial defect states energy), impedance spectroscopy measurements have been performed.

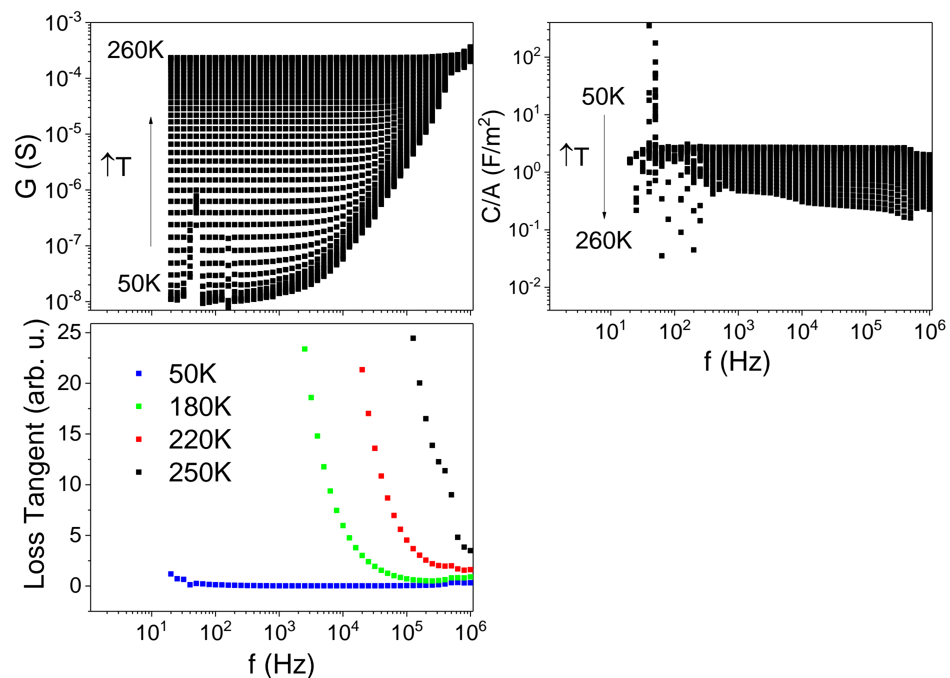

Figure 6.11 G vs f curves at temperature ranged from 50K to 260K at 5K interval (Top Left Hand Corner). C/A vs f curves at temperatures in the same range (Top Right Hand Corner). $\tan\delta$ vs f curves at different temperatures (Bottom Left Hand Corner).

Figure 6.11 shows the frequency dependence of conductance curves at different temperatures. A conductivity plateau is found at low frequency which increases with temperature. At the same time capacitance decreases with temperature in a way that the loss tangent remains constant at low temperature. This behavior has been ascribed to Coulomb-Blockade of electrons trapped at oxygen vacancy centers. Note the flat shape of the $\tan\delta$ vs frequency curves at T = 50K displayed in the lower panel of figure 6.11. To examine the temperature dependence of the low frequency conductance, conductance values at $100\,Hz$ extracted from the upper panel of figure 6.11 have been plot as a function of temperature in an Arrhenius fashion. See Figure 6.12.

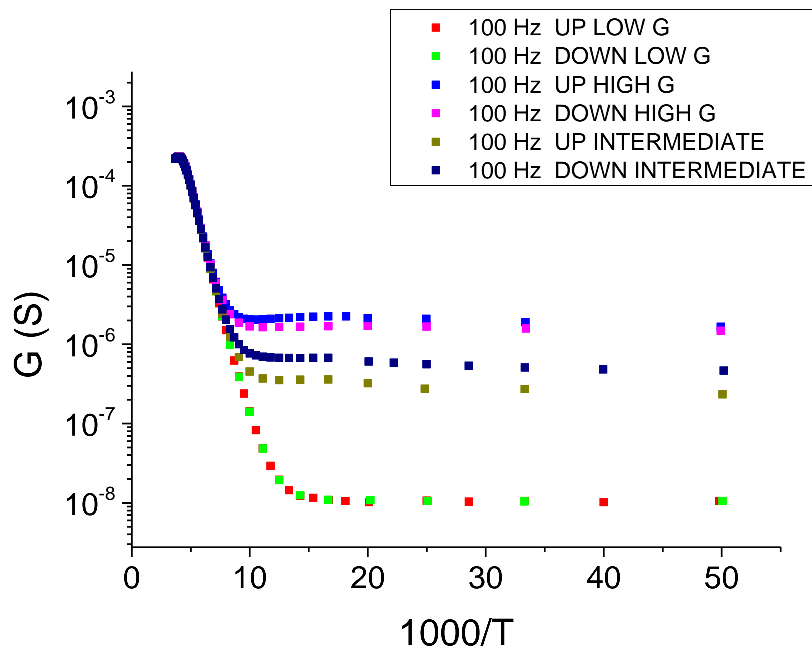

Figure 6.12 Conductance at 100 Hz as a function of temperature of a tunnel junction LSMO/BTO/Co polarized to low conductance state (-5V LOW G green and yellow symbols), and to high conductance state (+9V HIGH G light blue and magenta symbols) and intermediate conductance state (-2.1V INTERMEDIATE olive and royal blue symbols).

Notice that there are two clearly separated regimes. At high temperatures there is a temperature activated regime which crosses over to a temperature independent regime at low temperatures. Linear fits to the activated portions (see Figure 6.13). In the range from 100K until 220K, G vs 1000/T curve was fitted to obtain the thermal activation energy:

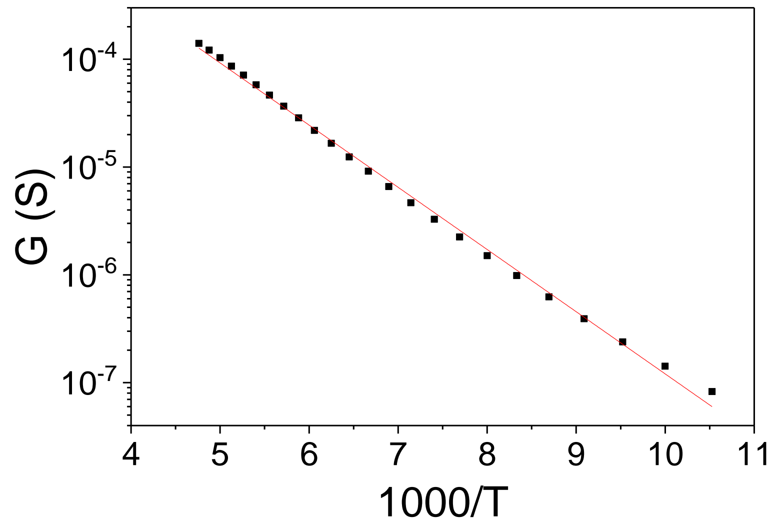

Figure 6.13 Conductance activated behaviour in the high temperature regime (see Figure 6.12). The thermal activation energy is 116meV.

The thermal activation energy was calculated through the equation:

$$G = G_0 exp\left(-\frac{\Delta E_{TAE}}{k_B T}\right)$$

Where ΔE_{TAE} is the thermal activation energy $\Delta E_{TAE} = (115.7 \pm 1.3) meV$

The thermal activation energy of the impedance measurements is in the order of 100 meV. This value is one order of magnitude below the values characteristic of the ionic diffusion process by oxygen vacancies (1 eV). The thermal activation energy in the order of 100 meV found is thus ascribed to an electronic process. A possibility is an electron-electron Coulomb repulsion $\left(E_C = \frac{e^2}{C_0}\right)$ energy. A measure of the screening Coulomb energy per electron is obtained by dividing this energy by 2 (repulsion is a cooperative effect involving 2 electrons). Thus, Charging Energy $\left(E_C = \frac{e^2}{2C_0}\right)$ in the order of 50 meV, in good agreement with the estimates by Maekawa [44, 45]. Further interesting information is obtained from the crossover frequency from a frequency independent to power law dependent conductance behaviour (obtained from figure 6.11). Cross over frequencies were obtained from the values at which conductance was doubles respect to the plateau

values. Cross over frequencies displayed an activated behaviour as shown in Figure 6.14.

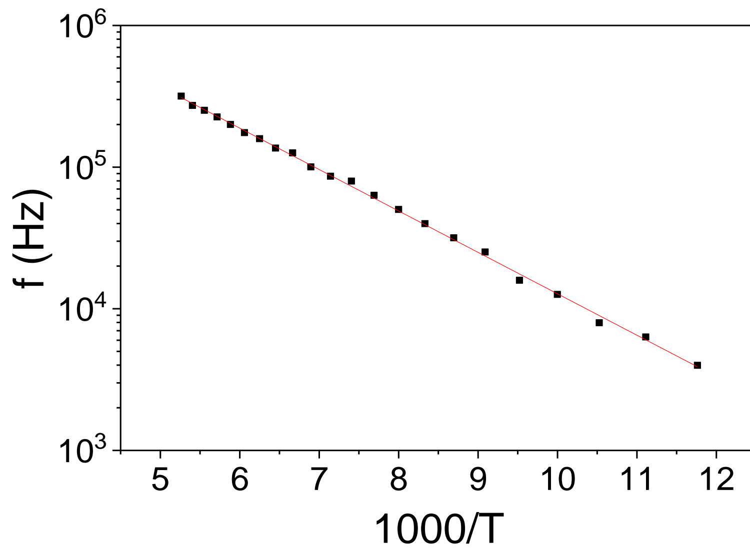

Figure 6.14 Temperature dependence of the cross over frequency (see text). The thermal activation energy is 58 meV.

In this particular case, the thermal activation energy was obtained from the expression:

$$f = f_0 exp\left(-\frac{\Delta E_{TAE}}{2k_B T}\right)$$

Where ΔE_{TAE} is the thermal activation energy $\frac{\Delta E_{TAE}}{2} = (57.8 \pm 0.7)meV$

These values are the same as the activation energies obtained for the low frequency plateaus. And can thus be identified with $\frac{\Delta E_{TAE}}{2}$ the Charging Energy $\left(E_C = \frac{e^2}{2C_0}\right)$, the screening Coulomb repulsion energy per electron. I.e., the energy scale found from first principles simulations which we have ascribed to the localized level of the density of states 100 meV below the fermi energy, and may reflect the hindering of electron transfer across the tunnel barrier. (See figure 6.25). C_0 , the capacitance associated to an oxygen vacancy hosting a localized electron can be thus estimated from the charging energy to be:

$$C_0 = 1.38 \times 10^{-18}\, F$$

The total oxygen vacancy concentration N can then be inferred from the following expression [44]:

$$C = NC_0$$

where $N_{3D} = \frac{N}{V}$ is the volume concentration of oxygen vacancies:

$$N_{3D} = 3.27 \times 10^{20} cm^{-3}$$

This doping concentration, slightly below 1%, yields a sheet carrier density of $1.44 \times 10^{14} cm^{-2}$ is at the level necessary to screen the bulk polarization of the BTO (0.26C/m^2). The interesting possibility can be inferred that the oxygen vacancies can be generated precisely to screen the ferroelectric polarization of the BTO.

This issue brings about a natural question, if it is possible to estimate with reasonable precision the REDOX potential in this solid state device. In order to address this problem, differential conductance measurements in increasing voltage bias amplitude were performed (see figure 6.15). Figure 6.15 displays conductance changes by cycling (and gradually increasing) voltage in the memresistance state. Conductance changes are ultimately caused by the electric field control of the oxidation of the Co electrode and the formation of oxygen vacancies in the BTO. We are thus indirectly probing the REDOX potential of our system.

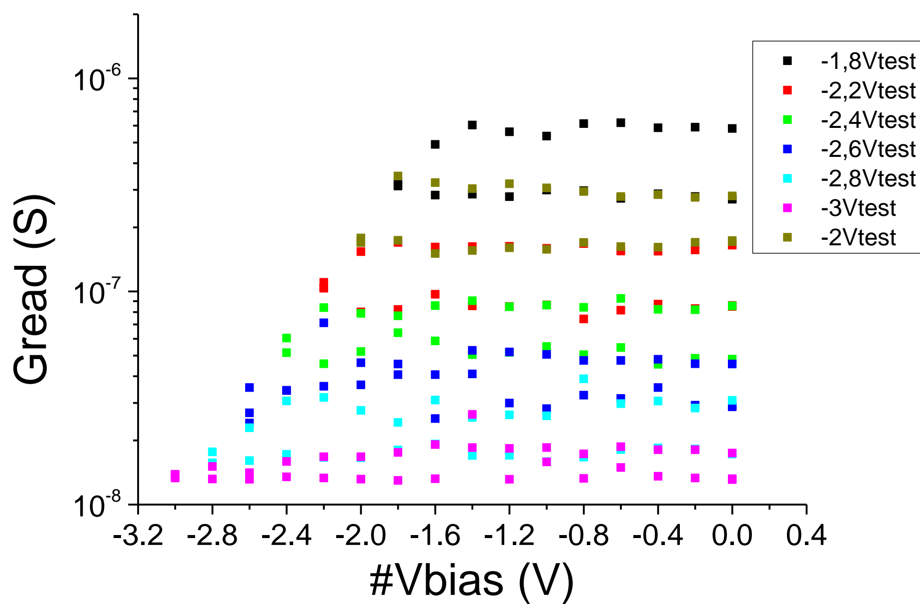

Figure 6.15 Gread vs Vbias Hysteresis Half Loop. Are the oxygen vacancy formation voltage/tension controlled by?

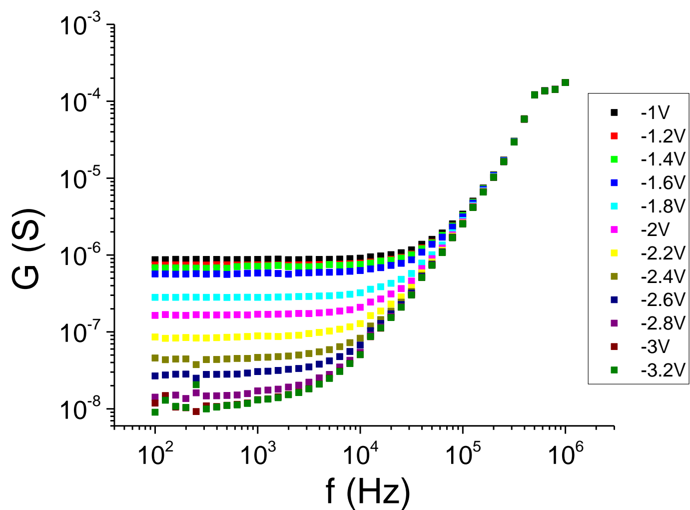

Figure 6.16 After each hysteresis half loop, differential conductance measurements were performed at 10mV oscillation varying the frequency. Are these measurements activated by previous bias voltage?

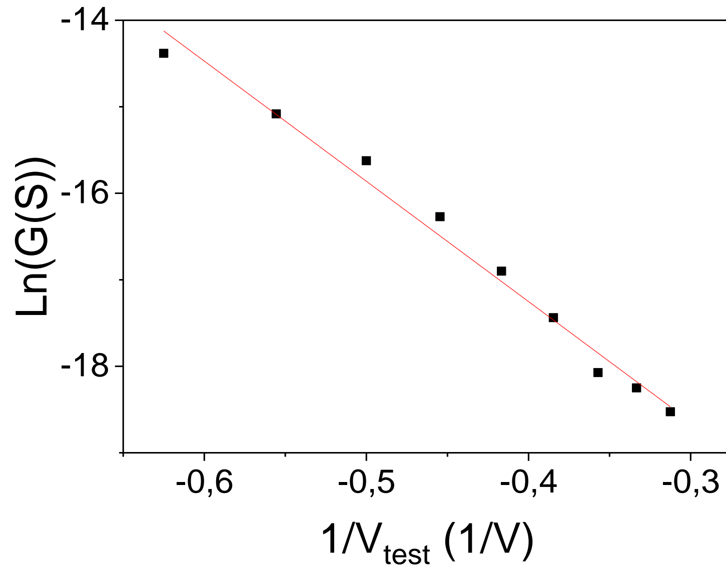

Figure 6.17 Fitting the 100Hz conductance measurements in function of the inverse of previous bias voltage applied. The REDOX potential is estimated in 13.90 eV. This value is very similar to the hydrogenic-like binding energy associated with oxygen vacancy formation.

To sum up, after fitting the 100Hz conductance data, the REDOX potential (the energetic cost of produce an oxygen vacancy in $BaTiO_3$ and an oxygen interstitial in Co) is estimated in 13.90 eV. This value is a measure of the needed to remove/ionize an electron from a hydrogen atom. In other words, the energy calculated by this fitting could be ascribed to the hydrogenic-like binding energy associated with oxygen vacancy formation in this solid state device. According to reference [50], an electron associated with a particular defect will be confined in a hydrogenic orbital (such as an exciton) whose energy is given by the following equation:

$$E_B = \left(\frac{m^*}{m\varepsilon^2}\right) R_\infty$$

Being $R_\infty = 13.6\ eV$ the Rydberg constant, m^* is the effective mass of electrons and ε is the high-frequency dielectric constant.

Despite the Co work function, approximately 5 eV, the surface states associated to interfacial defects induced by the REDOX reaction play a relevant role by which Bardeen [51] proposed that the Fermi level of the semiconductor (in our case the $BaTiO_3$ ferroelectric tunnel barrier) is “pinned” by surface states to the originally

charge neutrality level. These states are not only real surface states but also localized states induced in the band gap of the ferroelectric tunnel barrier by metallic cobalt in our case.

Hysteretic conductance was also obtained from DC measurements (see figure 6.19 displaying the 'read' resistance values measured at an excitation voltage of 10 mV). These loops displayed the same anti clockwise conductance change found in the ac measurements. The cross over from the tunnel –like to Schottky –like behaviour is responsible for the very large amplitude of the memresistance loops. The Low Resistance State (LRS) is governed by the recombination (annihilation) of oxygen vacancies in the $BaTiO_3$/Co interface by disolving the CoO layer which turns into metallic Co and reduces the resistance. On the other hand the high Resistance state (HRS) is driven by the oxidation of the Co and the accumulation of oxygen vacancies at the BTO/LSMO interface.

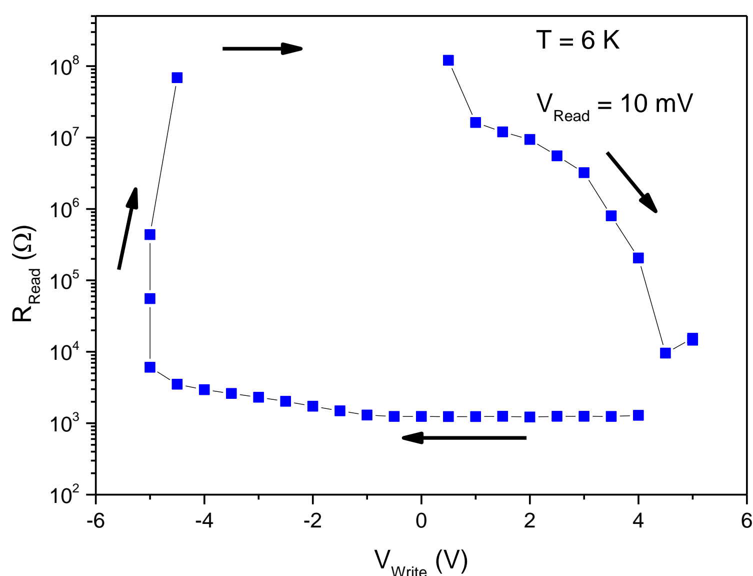

Figure 6.18 'Read' resistance loop of a LSMO/$BaTiO_3/Co$ junction at low temperature (6 K).

Additionally, magnetotransport properties of tunnel junction were measured to obtain the tunnelling magnetoresistance, TMR. Low voltage resistance was

measured while sweeping a magnetic field in the plane of the layers in an hysteresis loop sequence. Two markedly different behaviors where obtained for the low (LRS) and high (HRS) resistance levels. While TMR in the LRS was negative (see Figure 6.19), positive TMR was measured in the HRS (see Figure 6.20). Also a significant increase of the coercivity was found in the HRS indicating a modification of the magnetic state of the interface triggered by resistance switching. The negative TMR in the low resistance state can be discussed in terms of the negative spin polarization in the Fermi level of Co and the competition with the Hubbard U and Exchange interaction J induced in the electron trapped in oxygen vacancies.

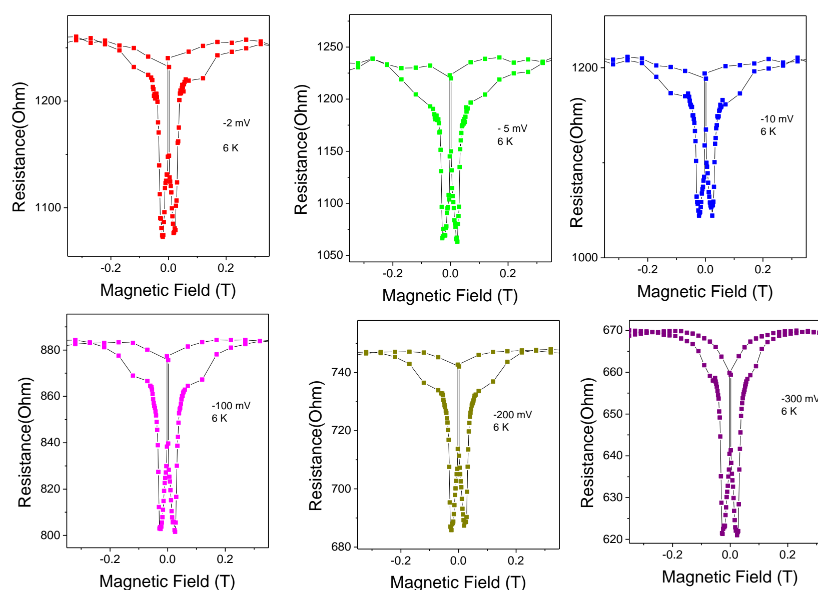

Figure 6.19 Negative Tunnel MagnetoResistance (TMR) in the Low Resistance State (LRS).

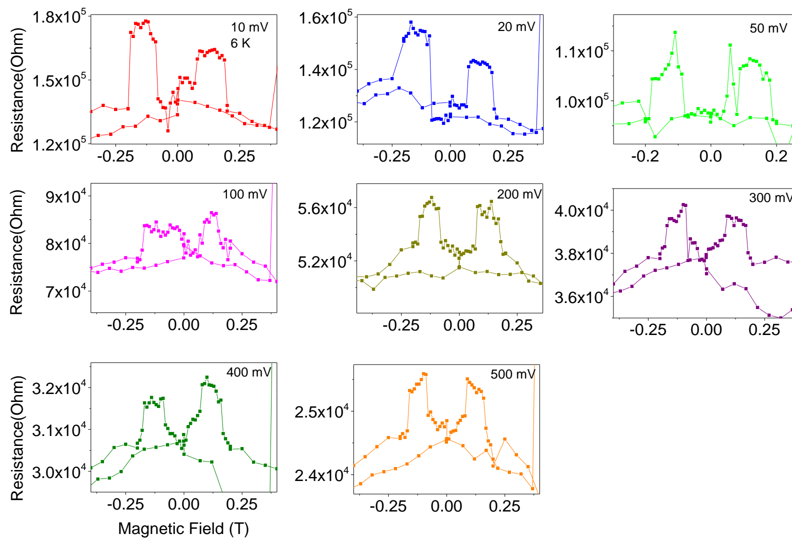

Figure 6.20 Positive Tunnel Magnetoresistance (TMR) in the High Resistance State (HRS) in the order of $10^5\Omega$.

By means of Density Functional Theory (DFT), we will gain insight about the role played by the switching oxygen vacancies in the spin polarization of the Fermi level. To clarify this, atomistic model of $BaTiO_3/Co$ interface have been performed in VASP simulations, whose associated density of states (DOS) is attached in figure 6.21.

This calculations capture the negative spin polarization at the $BaTiO_3/Co$ interface, which gives rise to the negative Tunnel Magneto Resistance ($TMR < 0$) measured in direct current (DC). I.e., we conclude that the negative magnetoresistance stems from the negative spin polarization in the Fermi level of the hcp Co atomic layers.

On the other hand, when oxygen ions are driven towards the Co interface by the strong external electric field, a CoO oxide layer is formed, which affects deeply the magnetic state of the interface. A CoO monolayer was added to the $BaTiO_3/Co$ interface and a DFT simulation was performed, whose density of states (DOS) is attached in figure 6.23. To clarify the role of electronic correlations in oxygen vacancies through Ti and interstitial oxygens through Co in the spin

polarization of the Fermi level, we assumed $U - J = 4.4\ eV$ in Ti and $U - J = 6.0\ eV$ in the CoO oxide monolayer.

The $BaTiO_3/Co$ interface with the added CoO monolayer displays a positive spin polarization in the Fermi level due to the hcp CoO and the close-oxygen-vacancy TiO_2 atomic planes. Also we found a positive spin polarization of the oxygen vacancy induced by the $(U - J = 4.4\ eV)$ Hubbard correction energy value for Ti. An interesting possibility is that the origin of Ti induced correlations and magnetism is driven by the bottom electrode $La_{0.7}Sr_{0.3}MnO_3$ energy correlations transferred to oxygen vacancies through Ti atoms [46]. In other words, oxygen vacancies could mediate exchange coupling by charge and spin tunnelling through Ti^{3+} cation [47], resembling a double exchange scenario in a ferroelectric insulator barrier driven by tunnelling, in which electrons trapped in oxygen vacancies are able to localize its charge and spin but transmit magnetic interactions to their neighbours by tunnelling processes. In addition, it is well known that chemical doping [48, 49] induces changes in bonding angle and may thus trigger variations in the Exchange Energy J magnitude and give rise to deep changes in magnetic states, (ferro- vs antiferromagnetism, or positive vs negative spin polarization).

The positive spin polarization at the Fermi Level in presence of the CoO layer is thus responsible for the positive Tunnel Magneto Resistance $(TMR > 0)$ measured in direct current (DC), however, our current VASP simulations could not account for the difference in the coercive magnetic fields in the Tunnel Magneto Resistance (TMR) measurements at the High and Low Resistance States.

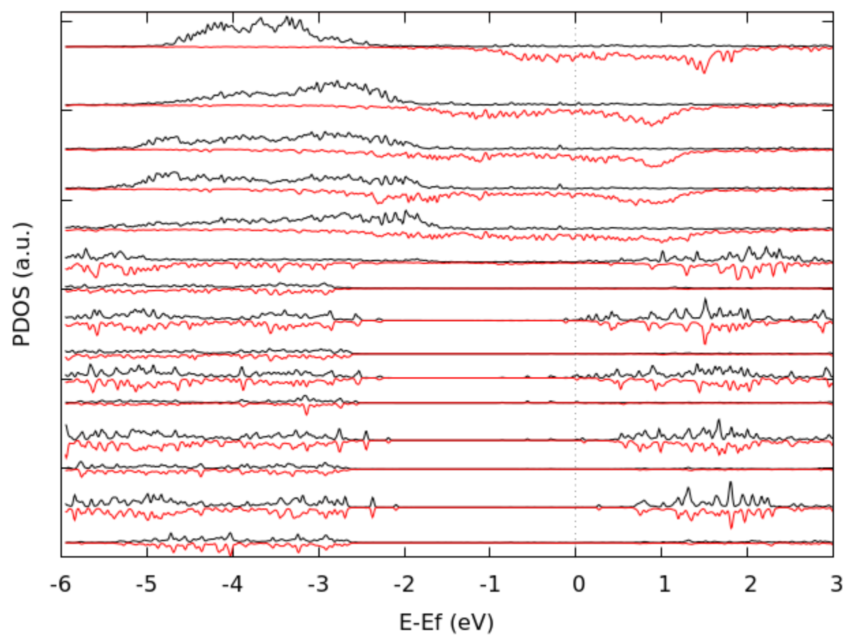

Figure 6.21 Total DOS BTO/Co interface with an oxygen vacancy in the 3º BaO plane.

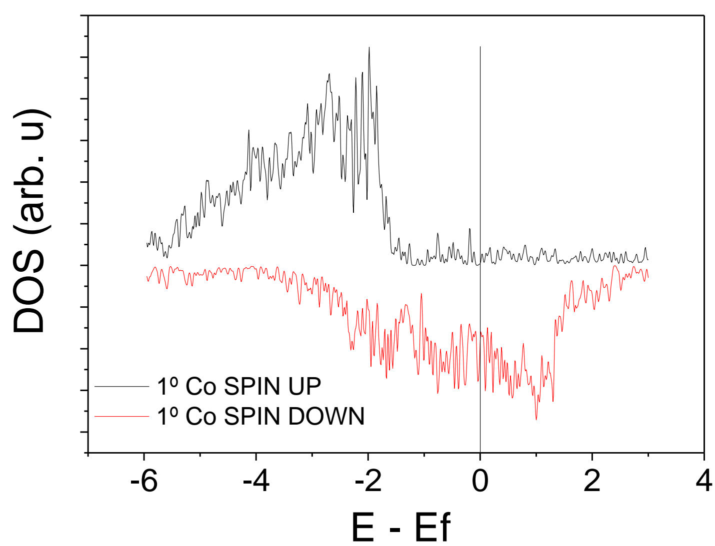

Figure 6.22 Enlarged view of the spin polarized DOS at the first Co plane showing negative spin polarization.

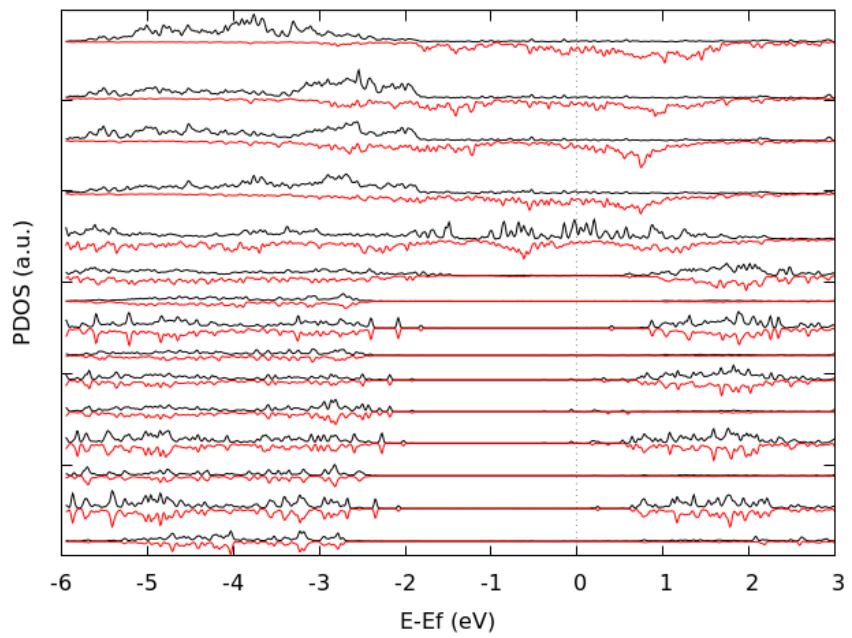

Figure 6.23 Total DOS BTO/Co interface with a CoO layer and an oxygen vacancy in the 3º BaO plane.

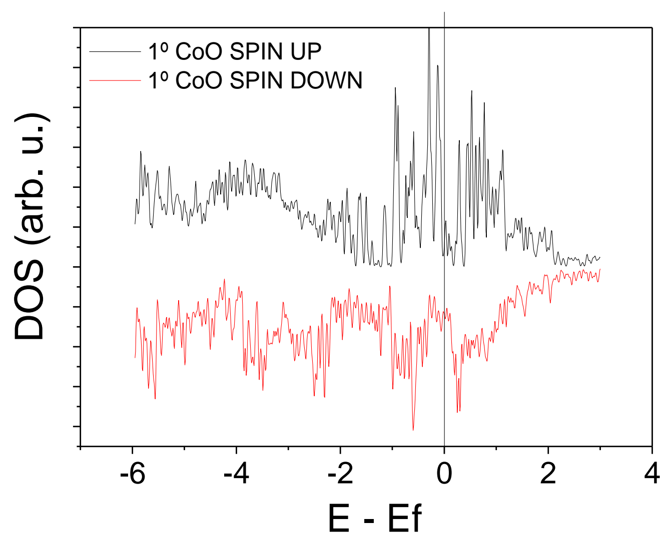

Figure 6.24 Enlarged view of the spin polarized DOS at the first CoO plane showing positive spin polarization.

.

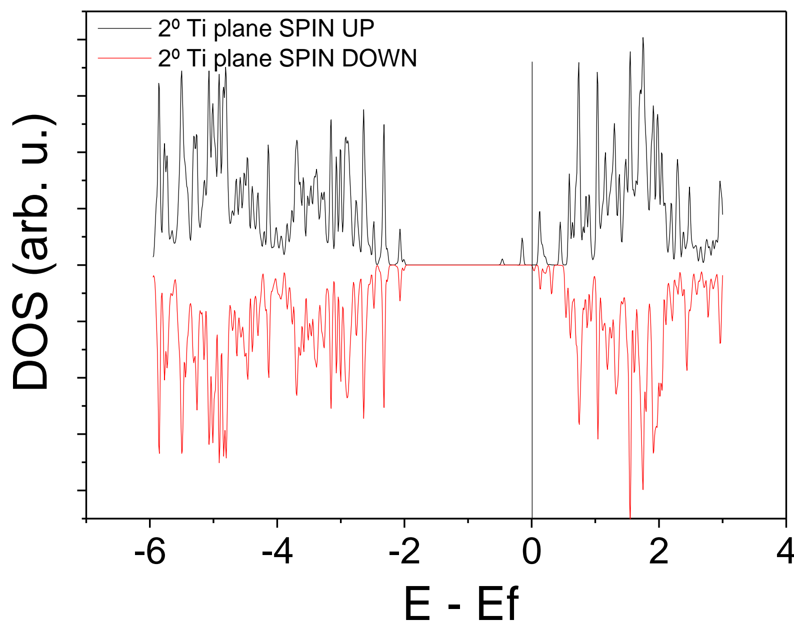

Figure 6.25 Total DOS enlargement in the 2º TiO_2 plane. Note the positively spin-polarised localised level at 130 meV below the Fermi level. It corresponds to the thermal activation energy of the differential conductance and ascribed to the Coulomb charging energy.

Comparing figures 6.22 and 6.24, it is noted the sign change in the spin-polarized density of states (DOS) at the Fermi level from the negative spin polarization of metallic Co at the Fermi level to the positive spin polarization of the CoO monolayer at the Fermi level.

This problem has been tackled in recent literature [52–55]. Specifically, J. Moodera´s [56] research group was the first who measured a positive spin polarization in Co with $SrTiO_3$ barriers, attributing to a $SrTiO_3$ amorphous layer. Previously, E. Tsymbal et al. [57] made surface DFT calculations in bcc iron displaying a positive spin polarization at the Fermi energy induced by an oxygen over-layer; which was ascribed to hybridization of the iron $3d$ orbitals with the oxygen $2p$ orbitals, jointly to the strong exchange splitting of the former results in exchange-split bonding and antibonding oxygen states. These antibonding states are partially occupied for the majority spins but are almost unoccupied for the minority spins, leading to the aforementioned behaviour. Recently, M. Alexe´s [58] research group measured tunnel magnetoresistance (TMR) electrically modulated by ferroelectric domains in a magnetic FeRAM hybrid tunnel junction.

Our DFT calculations show that oxygen vacancies are a necessary ingredient for the inversion of the spin polarization. I.e., if we calculate the effect of a CoO over-layer in absence of oxygen vacancies, the spin polarization at the Fermi level drops to zero and a gap opens, but no inversion of the spin polarization is observed. Our research studies of the sign change of tunnel magnetoresistance ascribed to the combined action of the cobalt oxidation in CoO (Mott insulator) and the formation of oxygen vacancies in the $BaTiO_3$ ferroelectric barrier with trapped electrons which localises spin and charge. Localized spins screen partially the ferroelectric dipole moment and transmit the magnetic interaction to the CoO layer by tunnelling, and thus give rise to magnetoelectric coupling.

In summary, our current VASP DFT simulations provide a feasible explanation to the sign change of the Tunnel Magneto Resistance upon switching between the Low and the High Resistance Sates.

To address the possible role of the oxidation enthalpy of the metal electrode in the process of oxygen vacancy formation, we have conducted a series of test experiments with different metals.

6.4.2 LSMO/BTO/Ta

Tantalum has a very low oxidation enthalpy and it is very prone to be oxidized forming two native oxides (TaO_2 and Ta_2O_5) leaving oxygen vacancies in $BaTiO_{3-\delta}$ ferroelectric barrier. Direct evidence for the formation of this oxides has been obtained by photoemission spectroscopy [59]. The dynamics of oxygen vacancy formation gives rise to hysteretic conductance curves as shown in figures 6.26 and 6.27.

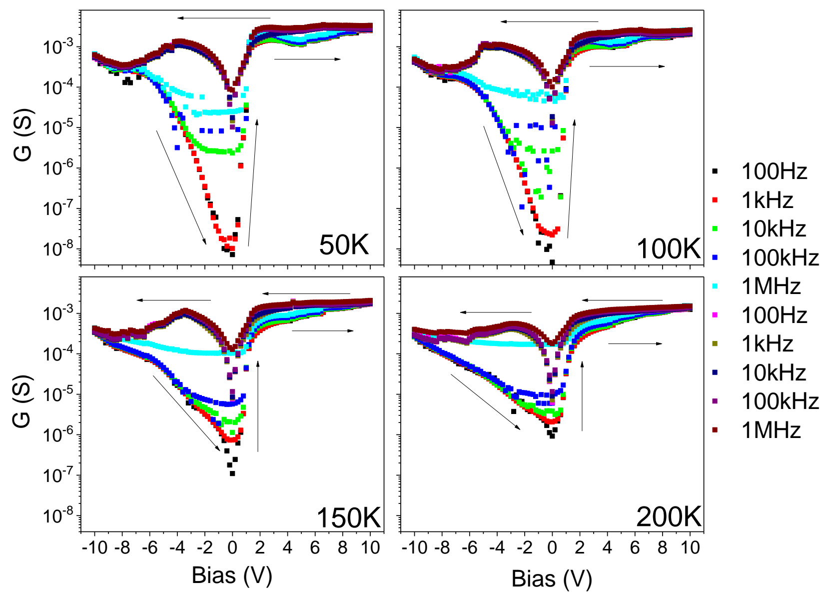

Figure 6.26 Write differential Conductance measurements LSMO/BTO/Ta; 50, 100, 150 and 200K.

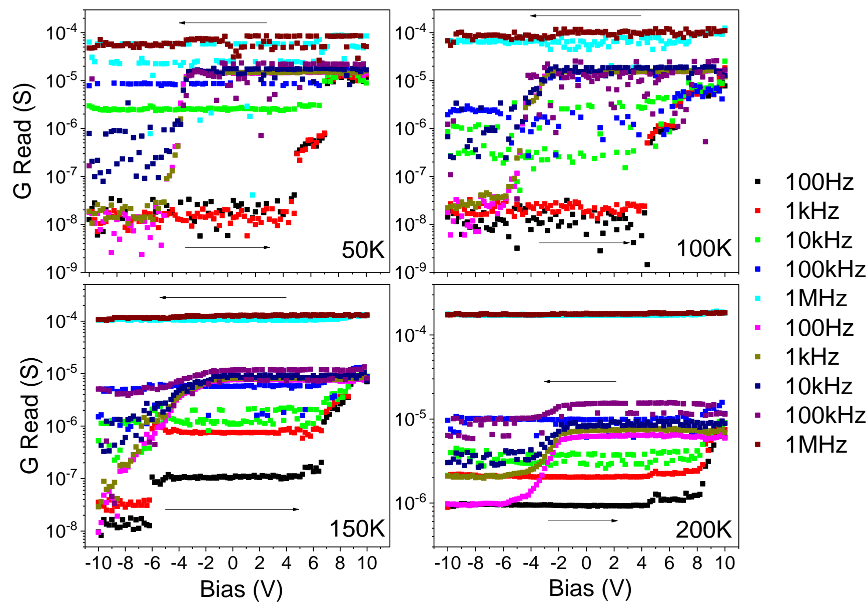

Figure 6.27 Read differential Conductance measurements LSMO/BTO/Ta; 50, 100, 150 and 200K

.

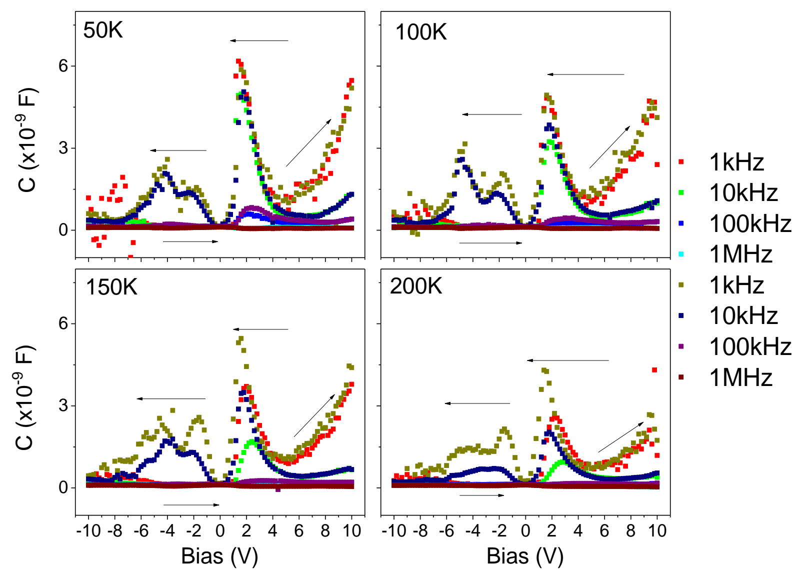

Figure 6.28 Write differential Capacitance measurements LSMO/BTO/Ta; 50, 100, 150 and 200K.

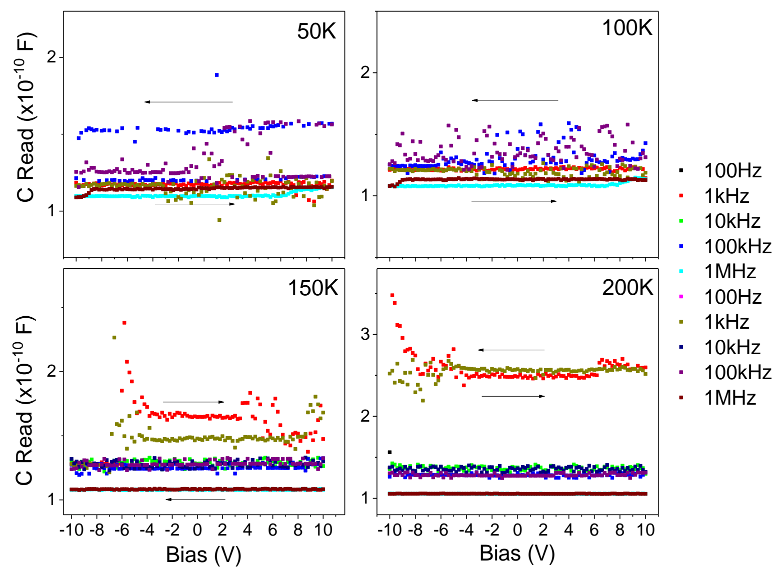

Figure 6.29 Read differential Capacitance measurements LSMO/BTO/Ta; 50, 100, 150 and 200K.

Despite the low work function of Tantalum (4.22 eV), a wide voltage range of ±10 V was used to warrant saturation of the conductance states. Oxidation of the Ta

electrode occurs probably owing through two consecutive coupled REDOX chemical reactions:

$$Ta + O_2 \leftrightarrow TaO_2 \qquad (1)$$

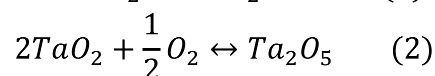

$$2TaO_2 + \frac{1}{2}O_2 \leftrightarrow Ta_2O_5 \qquad (2)$$

Notice that the positive flank of the conductance hysteresis loops of figure 6.27 exhibits an intermediate plateau indicating the annihilation of oxygen vacancies from two different Ta oxides. We conjecture that both REDOX chemical reactions are coupled or controlled by $BaTiO_3$ barrier ferroelectricity. In other words, oxygen vacancies associated to REDOX reaction (1) are generated, and ferroelectric dipoles “partially switch” to saturate in the first plateau. After, new oxygen vacancies associated to REDOX reaction (2) are generated for negative voltages, and consequently ferroelectric dipoles “switch again” to saturate completely to the extreme low conductance state. The same reasoning could be followed conversely for positive voltages recombining the oxygen vacancies in $BaTiO_{3-\delta}$ with the oxidized tantalum in order to recover the $BaTiO_3$ without oxygen vacancies and the metallic Tantalum.

The write differential capacitance exhibited pronounced maxima at voltage values corresponding to the coercivity observed in conductance loops. Capacitance at the maxima reached very large values in the nF range. These large values of the capacitance are typically ascribed to electrochemical reactions. The presence of two consecutive capacitance peaks at each voltage flank supports the formation / annihilation of two different oxides.

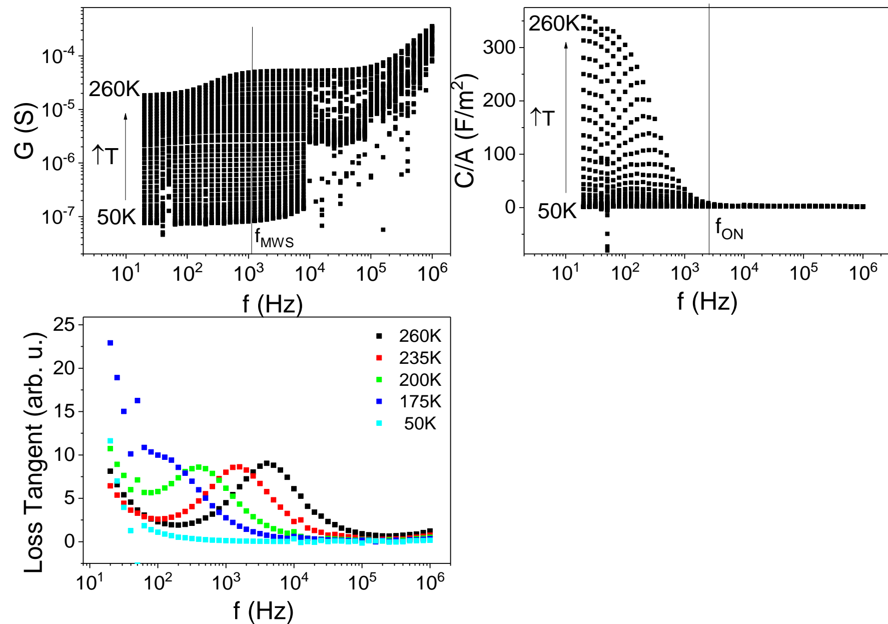

Figure 6.30 G vs f curves at temperatures ranged from 50K to 260K at 5K interval (Top Left Hand Corner). C/A vs f curves at temperatures in the same range (Top Right Hand Corner). Note the Maxwell-Wagner-like trend in the sense of increasing the capacitance in very low frequencies while increasing temperature correlated with the increasing of conductance while increasing temperature. $\tan\delta$ peak maxima shift different temperatures (Bottom Left Hand Corner). When $\omega \to 0 \Rightarrow tan\delta \to \infty$ and constitutes the foremost signature of Maxwell-Wagner-Sillars Relaxation.

Further support to the formation of an oxide interlayer resulting from the generation of oxygen vacancies we have measured the frequency dependence of the conductance and the capacitance in the low conductance state where oxygen vacancies and thus the interfacial oxide have been created. As depicted in figure 6.30, when temperature increases, the differential conductance increases in the whole frequency measured range while the differential capacitance steeply increases only in the low frequency range (from 20Hz until 1kHz). We can understand the enhancement of the differential capacitance as a Maxwell-Wagner-Sillars polarization effect characteristic of heterogeneous media. Note also that the loss tangent exhibits a low frequency increase which does not occur in the Debye relaxation. The main difference between Debye relaxation and the Maxwell-Wagner-Sillars relaxation is based on the loss tangent dispersion with the frequency:

In the former, when $\omega \to 0 \Rightarrow tan\delta \to 0$

In the latter, when $\omega \rightarrow 0 \Rightarrow tan\delta \rightarrow \infty$

In the present system, the Maxwell-Wagner-Sillars polarization coexists with the memristive behaviour in the high frequency limit. Thus, the impedance spectroscopy is the result of the combined effects between Maxwell-Wagner-Sillars polarization and the memristive effect and should be taken into consideration upon determining the Maxwell-Wagner-Sillars frequency f_{MWS} starting the conductance plateau.

The Maxwell-Wagner-Sillars polarization effect was quoted in recent scientific literature [60 - 64] and associated with interfacial effects and heterogeneity in composite materials. In the present case, the aforementioned effect is probably due to the heterogeneity of the $BaTiO_3/Ta$ interface; whose space charge layer is prone to have formed segregated oxides in the tantalum grain boundaries (TaO_2 and Ta_2O_5, whose contributions in dielectric permittivity are given by ε_{TaO_2} and $\varepsilon_{Ta_2O_5}$), which seems to interact with the ferroelectric dipoles in $BaTiO_3$ tunnel barrier, as discussed in the analysis of the write differential capacitance maxima in function of voltage bias.

Analogous to the previous subsection, we select the differential conductance curve in function of temperature extracting only the $f = 100Hz$ from the impedance spectroscopy data:

In the range from 100K until 220K, G vs 1000/T curve was fitted to obtain the thermal activation energy:

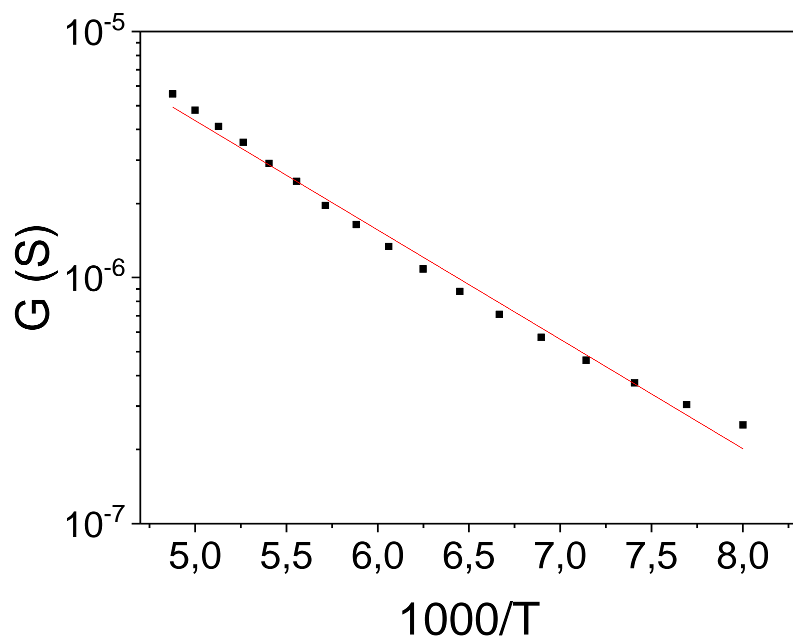

Figure 6.31 The thermally activated behaviour of the conductance measured at 100 Hz. Activation energy is 88 meV.

In order to estimate the REDOX potential, differential conductance measurements in increasing voltage bias amplitude were performed.

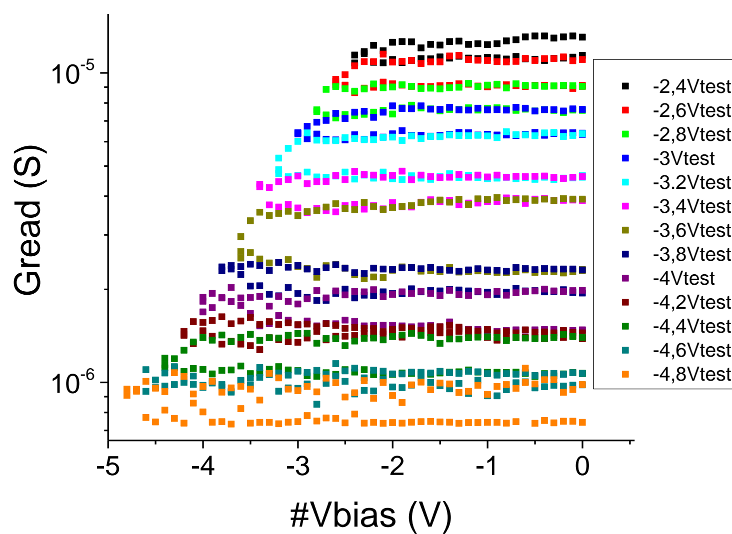

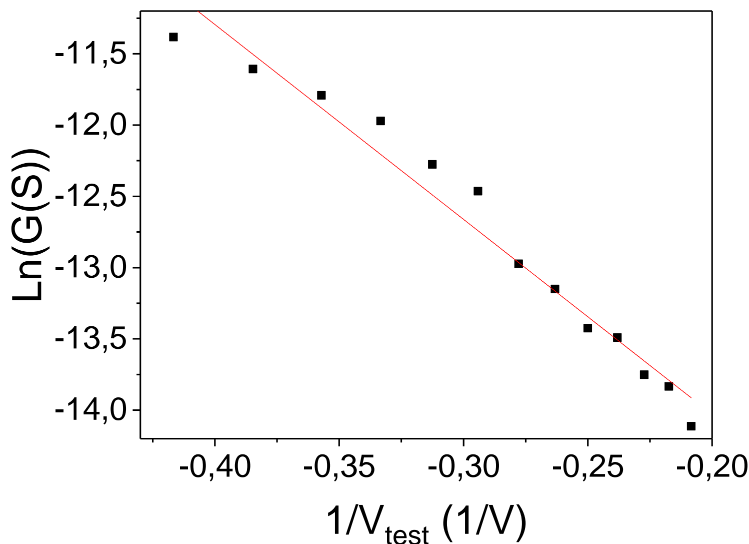

Figure 6.32 Gread vs Vbias Hysteresis Half Loop (Top). Conductance measured at 100 Hz as a function of the inverse write bias voltage (Bottom). The line is a linear fit. The REDOX potential is estimated to be 13.66 eV.

After fitting the 0Vbias data points, the REDOX potential (the average energetic cost of produce the oxygen vacancies in $BaTiO_3$ and oxygen interstitial atoms in Ta forming TaO_2 and Ta_2O_5) is estimated to be 13.67 eV. This value is very similar to the 13.6 eV needed to remove/ionize an electron from a hydrogen atom. In other words, the energy calculated by this fitting could be ascribed to the hydrogenic-like binding energy associated with oxygen vacancy formation in this solid state device.

6.4.3 LSMO/BTO/Pt

Despite its large work function (6.36 eV), Pt is catalytic oxide able to adsorb a monolayer of oxygen at its surface [65] as discussed by Stanley Williams and col. using a sandwich of Pt$/TiO_2(12nm)/Pt$. In our case, Pt oxygen adsorption leaves an oxygen vacancy in $BaTiO_{3-\delta}$ ferroelectric barrier. These induced oxygen vacancies give rise to behaviors similar to those observed previously with low work function oxides as Co or Ta. Hysteretic write and read conductance and

capacitance curves are displayed in figures 6.33 and 6.34 and 6.35 and 6.36 respectively.

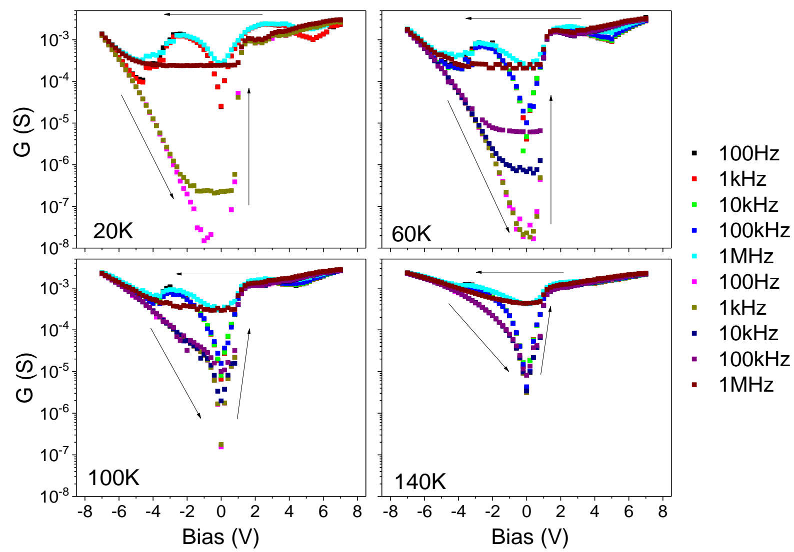

Figure 6.33 Write differential Conductance measurements LSMO/BTO/Pt; 20K, 60K, 100K and 140K.

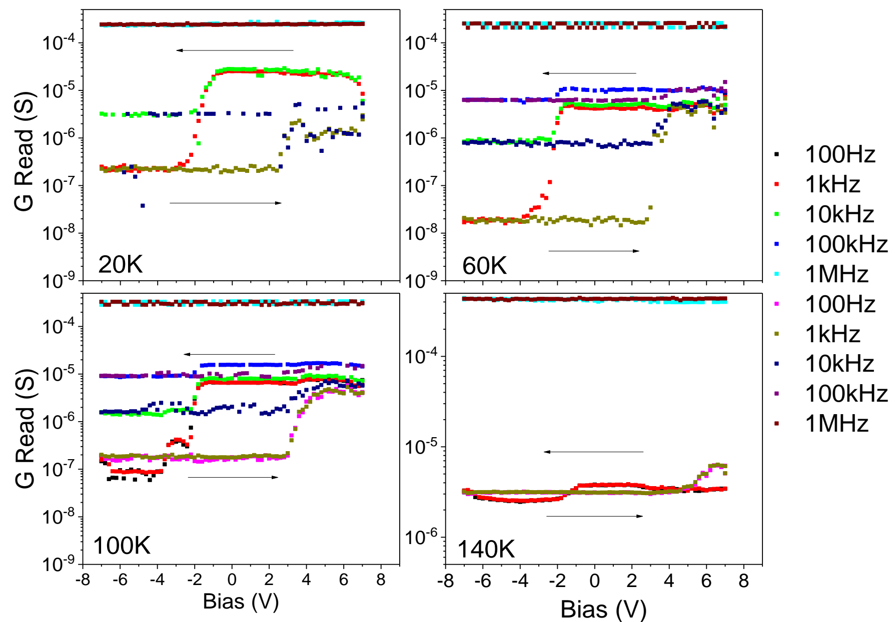

Figure 6.34 Read differential Conductance measurements LSMO/BTO/Pt; 20K, 60K, 100K and 140K.

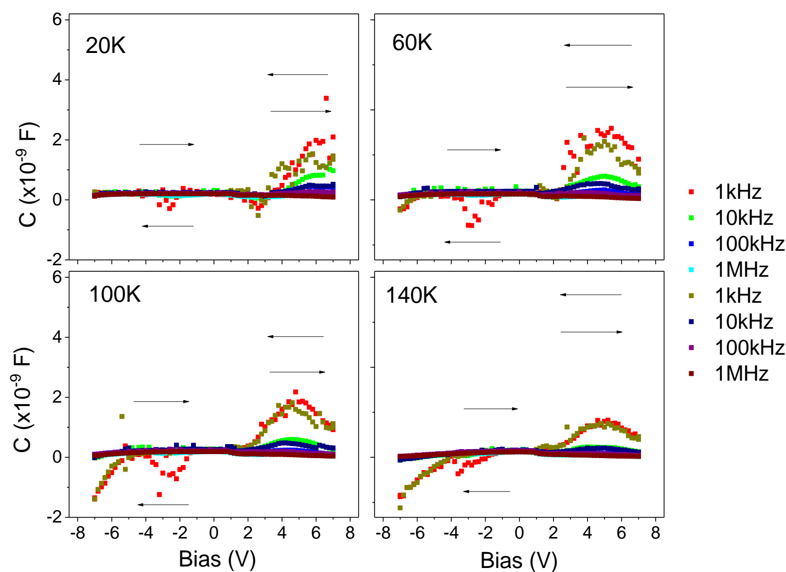

Figure 6.35 Write differential Capacitance measurements LSMO/BTO/Pt; 20K, 60K, 100K and 140K.

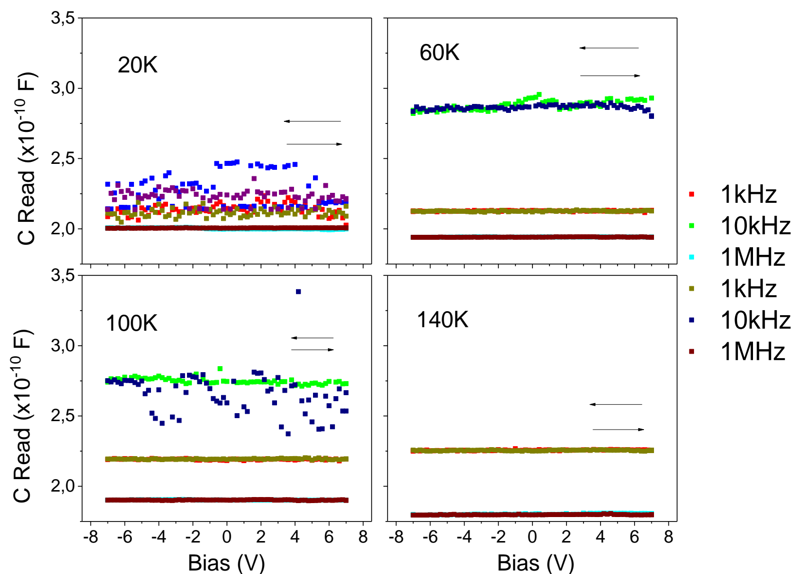

Figure 6.36 Read differential Capacitance measurements LSMO/BTO/Pt at 20K, 60K and 100K.

An interesting observation is that conductance loops are symmetric with both flanks of the differential conductance loop occurring in the same voltage range. On the other hand, notice that the conductance loops sample with an oxidizing

electrode are strongly asymmetric mostly in the positive voltage range. The process occurring at positive voltage range is the annihilation of oxygen vacancies by the reduction of the oxide. The picture emerges that the generation of oxygen vacancies in our BTO tunnel barrier is controlled by the oxidation kinetics of the electrode. When the vacancy annihilation process is limited by the reduction of the oxide, this process requires larger voltages the more stable are the oxides as it is in fact observed for the case of Ta with the lowest oxidation enthalpy of the series of electrodes analysed.

6.5 References

[1] B. C. H. Steele and A. Heinzel, "Materials for fuel cell technologies". *Nature* 414, 345 (2001).

[2] E. D. Wachsman and K. T. Lee, "Lowering the temperature of the oxide fuel cell". *Science* 248, 935 (2011).

[3] Waser, R. & Aono, M. "Nanoionics-based resistive switching memories". *Nat. Mater.* 6, 833–840 (2007).

[4] G. I. Meijer. Who Wins the Nonvolatile Memory Race? *Science* 319, 1625 (2008).

[5] Sergei V. Kalinin and Nicola A. Spaldin "Functional Ion Defects in Transition Metal Oxides". *Science* 341, 858 (2013).

[6] Hwang, H. Y. *et al.* "Emergent phenomena at oxide interfaces". *Nat. Mater.* 11**,** 103–13 (2012).

[7] J.N. Eckstein "Watch out for the lack of oxygen". *Nat. Mater*. 6, 473 (2007).

[8] R. Waser et al. "Redox-Based Resistive Switching Memories". *Adv. Mater.* 21, 2632 (2009).

[9] J. J Yang, D. B. Strukov and D. R. Stewart, "Memristive devices for computing". *Nat. Nanotech.* 8, 13 (2013).

[10] K. Szot, W. Speier, G. Bihlmayer, R. Waser. "Switching the electrical resistance of individual dislocations in single-crystalline $SrTiO_3$". *Nat. Mater.* 2006, 5, 312.

[11] R. Waser, R. Dittmann, G. Staikov, K. Szot. "Redox-Based Resistive Switching Memories –Nanoionic Mechanisms, Prospects, and Challenges". *Adv. Mater.* 2009, 21, 2632.

[12] Yang, J. J. *et al.* "The mechanism of electroforming of metal oxide memristive switches". *Nanotechnology* 20, 215201 (2009).

[13] Jeong, D. S., Schroeder, H., Breuer, U. & Waser, R., "Characteristic electroforming behavior in Pt/TiO_2/Pt resistive switching cells depending on atmosphere". *J. Appl. Phys.* 104, 123716 (2008).
[14] Watanabe, Y. et al. "Current-driven insulator–conductor transition and nonvolatile memory in Chromium–doped $SrTiO_3$ single crystals". *Appl. Phys. Lett.* 78, 3738–3740 (2001).
[15] Rozenberg, M. J., Inoue, I. H. & Sanchez, M. J. "Nonvolatile memory with multilevel switching: a basic model". *Phys. Rev. Lett.* 92, 178302 (2004).
[16] Chen, X., Wu, N., Strozier, J. & Ignatiev, A. "Spatially extended nature of resistive switching in perovskite oxide thin films". *Appl. Phys. Lett.* 89, 063507 (2006).
[17] Nian, Y. B., Strozier, J.,Wu, N. J., Chen, X. & Ignatiev, A. "Evidence for an oxygen diffusion model for the electric pulse induced resistance change effect in transition-metal oxides". *Phys. Rev. Lett.* 98, 146403 (2007).
[18] Sawa, A., Fujii, T., Kawasaki, M. & Tokura, Y. "Hysteretic current–voltage characteristics and resistance switching at a rectifying Ti/$Pr_{0.7}Ca_{0.3}MnO_3$ interface". *Appl. Phys. Lett.* 85, 4073–4075 (2004).
[19] Fujii, T., Kawasaki, M., Sawa, A. & Akoh, H. "Hysteretic current–voltage characteristics and resistance switching at an epitaxial oxide Schottky junction $SrRuO_3$/$SrTi_{0.99}Nb_{0.01}O_3$". *Appl. Phys. Lett.* 86, 012107 (2005).
[20] A. Sawa. "Resistive switching in transition metal oxides". *Mater. Today* 11, 28 (2008).
[21] J. J. Yang, M. D. Pickett, X. Li, D. A. A. Ohlberg, D. R. Stewart, R. S. Williams. "Memristive switching mechanism for metal/oxide/metal nanodevices". *Nat. Nanotechnol*., 3, 429 (2008).
[22] J. P. Velev, C.-G. Duan, J. D. Burton, A. Smogunov, M. K. Niranjan, E. Tosatti, S. S. Jaswal, and E. Y. Tsymbal, "Magnetic tunnel junctions with ferroelectric barriers: prediction of four resistance States from first principles"., *Nano Lett.*, 9, 1, pp. 427–32, (2009).
[23] M. Y. Zhuravlev, R. F. Sabirianov, S. S. Jaswal, and E. Y. Tsymbal. "Giant Electroresistance in Ferroelectric Tunnel Junctions". *Phys. Rev. Lett.* 94, 246802 (2005); E. Tsymbal and H. Kohlstedt. "Tunneling Across a Ferroelectric". *Science* 313, 181 (2006).
[24] V. Garcia, S. Fusil, K. Bouzehouane, S. Enouz-Vedrenne, N. D. Mathur, A. Barthélémy, M. Bibes. "Giant tunnel electroresistance for non-destructive readout of ferroelectric states". *Nature 460*, 81 (2009).

[25] P. Maksymovych , S. Jesse , P. Yu , R. Ramesh , A. Baddorf, S. V. Kalinin, "Polarization Control of Electron Tunneling into Ferroelectric Surfaces". *Science 324*, 1421 (2009).
[26] A. Gruverman , D. Wu , H. Lu , Y. Wang , H. W. Jang , C. M. Folkman, M. Rzchowski , C.-B. Eom, E. Y. Tsymbal. "Tunneling Electroresistance Effect in Ferroelectric Tunnel Junctions at the Nanoscale". *Nano Lett. 9*, 3539 (2009).
[27] D. Pantel, S. Goetze, D. Hesse, M. Alexe. "Room-Temperature Ferroelectric Resistive Switching in Ultrathin $Pb(Zr_{0.2}Ti_{0.8})O_3$ Films". *ACS Nano* 2011, *5*, 6032.
[28] D. Pantel , H. Lu , S. Goetze , P. Werner , D. J. Kim , A. Gruverman , D. Hesse , M. Alexe, "Tunnel electroresistance in junctions with ultrathin ferroelectric $Pb(Zr_{0.2}Ti_{0.8})O_3$ barriers". *Appl. Phys. Lett.* 2012, *100*, 232902. ; D. Pantel, S. Goetze , D. Hesse , M. Alexe. "Reversible electrical switching of spin polarization in multiferroic tunnel junctions". *Nat. Mater.* 2012, *11*, 289.
[29] L. Jiang, W. S. Choi , H. Jeen , S. Dong , Y. Kim , M.-G. Han , Y. Zhu , S. Kalinin , E. Dagotto , T. Egami , H. N. Lee. "Tunneling Electroresistance Induced by Interfacial Phase Transitions in Ultrathin Oxide Heterostructures". *Nano Lett.* 2013, *13*, 5837.
[30] Z. Wen, L. You, J. Wang, A. Li, D. Wu. "Temperature-dependent tunneling electroresistance in Pt/BaTiO3/SrRuO3 ferroelectric tunnel junctions". *Appl. Phys. Lett.* 2013, *103*, 132913.
[31] Z. Wen, C. Li, D. Wu, A. Li, N. Ming. "Ferroelectric-field-effect-enhanced electroresistance in metal/ferroelectric/semiconductor tunnel junctions". *Nat. Mater. 12*, 618 (2013).
[32] A. K. Tagantsev, CZ Pawlaczyk, K. Brooks and N. Setter, "Built in electric field assisted nucleation and coercive fields in ferroelectric thin fims". *Integrated Ferroelectrics* 4, 1 (1994).
[33] A. K. Tagantsev and G. Gerra "Interface-induced phenomena in polarization response of ferroelectric thin films". *Journal of Applied Physics* 100, 051607 (2006).
[34] Jongmyung Yoo, Jeonghwan Song and Hyunsang Hwang. Effect of cation amount in the electrolyte on characteristics of Ag/TiO_2 based threshold switching devices. Nanotechnology 29 (2018) 365707 (5pp).
[35] Greta Radaelli, Diego Gutiérrez, Florencio Sánchez, Riccardo Bertacco, Massimiliano Stengel, and Josep Fontcuberta. "Large Room-Temperature Electroresistance in Dual-Modulated Ferroelectric Tunnel Barriers". *Adv. Mater.* 27, 2602 (2015).
[36] P. W. M. Blom, R. M. Wolf, J. F. M. Cillessen, and M. P. C. M. Krijn. "Ferroelectric Schottky Diode". *Phys. Rev. Lett.* 73, 2107 (1994).

[37] L. Pintillie and M. Alexe, “Metal-ferroelectric-metal heterostructures with Schottky contacts. I. Influence of the ferroelectric properties”. *J. Appl. Phys.* 98, 124103 (2005).
[38] L. Pintillie, I. Boerasu, M. J. M. Gomes, T. Zhao, R. Ramesh, and M. Alexe. “Metal-ferroelectric-metal structures with Schottky contacts. II. Analysis of the experimental current-voltage and capacitance-voltage characteristics of $Pb(Zr,Ti)O_3$ thin films”. *J. Appl. Phys.* 98, 124104 (2005).
[39] S. Farokhipoor and B. Noheda. “Screening effects in ferroelectric resistive switching of $BiFeO_3$ thin films”. *Apl. Mater.* 2, 056102 (2014).
[40] Rickard Fors, Sergey I. Khartsev, and Alexander M. Grishin. “Giant resistance switching in metal-insulator-manganite junctions: Evidence for Mott transition”. *Phys. Rev B* 71, 045305 (2005).

[41] Yang Bai, Tuomo Siponkoski, Jani Peräntie, Heli Jantunen, and Jari Juuti. “Ferroelectric, pyroelectric, and piezoelectric properties of a photovoltaic perovskite oxide”. *Appl. Phys. Lett.* 110, 063093 (2017).

[42] Qianxi Lai, Lei Zhang, Zhiyong Li, William F. Stickle, R. Stanley Williams, and Yong Chen. “Analog memory capacitor based on field-configurable ion-doped polymers”. *Appl. Phys. Lett.* 95, 213503 (2009).
[43] D. K. Chen, R. D. Schrimpf, D. M. Fleetwood, K. F. Galloway, S. T. Pantelides, A. Dimoulas, G. Mavrou, A. Sotiropoulos, and Y. Panayiotatos. “Total Dose Response of Ge MOS Capacitors with HfO2/Dy2O3 Gate Stacks”. IEEE Trans. Nuclear Sci. 54(4):971 - 974
[44] Pham Nam Hai, Shinobu Ohya, Masaaki Tanaka, Stewart E. Barnes & Sadamichi Maekawa. “Electromotive force and huge magnetoresistance in magnetic tunnel junctions”. Nature 458 (2009).

[45] O. G. Udalov, N. M. Chtchelkatchev, and I. S. Beloborodov. “Coupling of ferroelectricity and ferromagnetism through Coulomb blockade in composite multiferroics”. Phys. Rev. B 89, 174203 (2014).

[46] Weiwei Li, Run Zhao, Le Wang, Rujun Tang, Yuanyuan Zhu, Joo Hwan Lee, Haixia Cao, Tianyi Cai, Haizhong Guo, Can Wang, Langsheng Ling, Li Pi, Kuijuan Jin, Yuheng Zhang, Haiyan Wang, Yongqiang Wang, Sheng Ju & Hao Yang. “Oxygen-Vacancy-Induced Antiferromagnetism to Ferromagnetism Transformation in $Eu_{0.5}Ba_{0.5}TiO_{3-\delta}$ Multiferroic Thin Films”. Nat. Sci. Rep. (2013).

[47] N.C. Bristowe, J. Varignon, D. Fontaine, E. Bousquet & Ph. Ghosez. "Ferromagnetism induced by entangled charge and orbital orderings in ferroelectric titanate perovskites". Nat. Comm. (2015).
[48] W. S. Lee et al. "Role of Lattice Coupling in Establishing Electronic and Magnetic Properties in Quasi-One-Dimensional Cuprates". Phys. Rev. Lett. 110, 265502 (2013).
[49] Xavier Rocquefelte, Karlheinz Schwarz & Peter Blaha. "Theoretical Investigation of the Magnetic Exchange Interactions in Copper (II) Oxides under Chemical and Physical Pressures". Nat. Sci. Rep., (2012).
[50] J. M. D. COEY, M. VENKATESAN AND C. B. FITZGERALD. "Donor impurity band exchange in dilute ferromagnetic oxides". Nat. Mater. 4 (2005).
[51] M. Dawber, K. M. Rabe, J. F. Scott. "Physics of thin-film ferroelectric oxides". Rev. Mod. Phys. 77 (2005).
[52] E. Y. Tsymbal, A. Sokolov, I. F. Sabirianov, and B. Doudin. "Resonant Inversion of Tunneling Magnetoresistance". Phys. Rev. Lett., 90 186602 (2003).
[53] M. Ye. Zhuravlev, E. Y. Tsymbal, and A. V. Vedyayev. "Impurity-Assisted Interlayer Exchange Coupling across a Tunnel Barrier". Phys. Rev. Lett., 94 026806 (2005).
[54] J. P. Velev, K. D. Belashchenko, D. A. Stewart, M. van Schilfgaarde, S. S. Jaswal, and E. Y. Tsymbal. "Negative Spin Polarization and Large Tunneling Magnetoresistance in Epitaxial Co|SrTiO3|Co Magnetic Tunnel Junctions". Phys. Rev. Lett. 95 216601 (2005).
[55] Chun-Gang Duan, S. S. Jaswal, and E. Y. Tsymbal. "Predicted Magnetoelectric Effect in Fe/BaTiO3 Multilayers: Ferroelectric Control of Magnetism". Phys. Rev. Lett. 97 047201 (2006).
[56] Andy Thomas and Jagadeesh S. Moodera. "Evidence for positive spin polarization in Co with $SrTiO_3$ barriers". J. Appl. Phys. 97, 10C908 (2005).
[57] E. Yu. Tsymbal, I. I. Oleinik, and D. G. Pettifor. "Oxygen-induced positive spin polarization from Fe into the vacuum barrier". J. Appl. Phys. 87, 5230 (2000).
[58] Zheng-Dong Luo, Geanina Apachitei, Ming-Min Yang, Jonathan J. P. Peters, Ana M. Sanchez, and Marin Alexe. "Bi-ferroic memristive properties of multiferroic tunnel junctions". Appl. Phys. Lett., 112, 102905 (2018).
[59] J. Y. Zhang, I. W. Boyd, "Ultraviolet annealing of thin films grown by pulsed laser deposition," Appl. Surf. Sci. 154-155, 17 (2000).
[60] D. O'Neill, R. M. Bowman, and J. M. Gregg. "Dielectric enhancement and Maxwell–Wagner effects in ferroelectric superlattice structures". Appl. Phys. Lett., 77, 10, (2000).

[61] G. Catalan, D. O'Neill, R. M. Bowman, and J. M. Gregg. "Relaxor features in ferroelectric superlattices: A Maxwell–Wagner approach". Appl. Phys. Lett., 77, 19, (2000).
[62] Xu Ning, Pu Yong Ping, and Wang Zhuo. "Large Dielectric Constant and Maxwell–Wagner Effects in BaTiO3/Cu Composites". J. Am. Ceram. Soc., 95 [3] 999–1003 (2012).
[63] M. Samet, V. Levchenko, G. Boiteux, G. Seytre, A. Kallel, and A. Serghei. "Electrode polarization vs. Maxwell-Wagner-Sillars interfacial polarization in dielectric spectra of materials: Characteristic frequencies and scaling laws". J. Chem. Phys. 142, 194703 (2015).
[64] N. Ortega, Ashok Kumar, R. S. Katiyar, and J. F. Scott. "Maxwell-Wagner space charge effects on the $Pb(Zr,Ti)O_3 - CoFe_2O_4$ multilayers". Appl. Phys. Lett., 91, 102902 (2007).
[65] Dmitri B. Strukov, Gregory S. Snider, Duncan R. Stewart & R. Stanley Williams. "The missing memristor found". Nature 453 (2008).

[66] https://patents.google.com/patent/US6835639B2/en

Chapter 7: Final Conclusions and Prospective Research Lines

The main findings of this dissertation are summarized here. We performed an analysis of the interplay between ferroelectricity, ferromagnetism, domain structure and memristive response in magnetic tunnel junctions. In order to reach this objective, we grew epitaxial heterostructures combining ferromagnetic manganites $La_{0.7}Ca_{0.3}MnO_3$ (LCMO), $La_{0.7}Sr_{0.3}MnO_3$ (LSMO) to be used as bottom electrode; the Mott/Anderson insulator $PrBa_2Cu_3O_{7-\delta}$ (PBCO) and ferroelectric barium titanate $BaTiO_{3-\delta}$ for use as a tunnel barrier and different metals (Ag, Co, Ta, Pt) to be deposited as top electrodes. We found hysteretic response in transport properties which may not be explained with the Schottky model in simple terms because the ferroelectricity interacts with interface defects

such as oxygen vacancies modifying their ionization and changing and the Schottky barrier. To gain more insight into the understanding of the hysteretic memristive behaviour, several experimental techniques were combined with density functional theory simulations by VASP. The main findings of this work can be summarized as follows:

- The LCMO/PBCO/Ag tunnel junction resistive switching behaviour directly probe the tunneling routes across the CuO_2 planes providing a direct connection to the Fehrenbacher and Rice model for cuprates. We have found evidence for the presence of the insulating gap of 4 eV mentioned above between the Pr^{IV} states and the Cu^{III} states. This is in agreement with the Fehrenbacher and Rice model stating that the absence of conductivity of the Cu–O chains is due to the O vacancies excluding the possibility to circumvent the CuO_2 planes via the tunneling of charge carriers through the Cu–O chains.

- The conduction mechanism of the LCMO/PBCO/Ag tunnel junctions is predominantly the tunneling of electrons assisted by traps localized in the CuO chains in the PBCO barrier. The Low Resistance State of the LSMO/PBCO/Ag tunnel junction was examined by fitting IV curves to the Child-Langmuir law (analogous to the electron conduction in a plane parallel vacuum diode in the ballistic conduction regime) and to the Fowler-Nordheim quantum tunneling.

- We found a free-electron gas in 180º Head-to-Head charged domain walls (CDW) in $BaTiO_3$ barriers in LSMO/BTO/LSMO tunnel junctions. We obtained evidence for confined electronic states which enable resonant tunnelling transport between the electrodes. Low temperature tunnelling conductance (measured using a dc current set up) exhibits pronounced oscillations indicating resonant transport through discrete unoccupied states of the confined electron gas, which is modulated by the strong electric field developing in an ultrathin barrier at moderated voltages in a transport experiment.

- We found a weak Mem-Capacitor behavior in LSMO/BTO/Ag memristor tunnel junctions occurring as a consequence of reversible interfacial chemical reaction controlled by an electric field. In the particular LSMO/BTO/Ag memristor, the electric field create interstitial oxygen

atoms in the face-centered cubic silver electrode leaving behind oxygen vacancies in the Barium Titanate barrier. The different charge carrier mobilities of the interstitial oxygen atoms and the oxygen vacancies, give rise to locally charged defects giving rise to the mem-capacitor effect.

- We found evidence of the coupling of oxygen vacancies to ferroelectric polarization in LSMO/BTO/Co memristor tunnel juntions. This gives rise to a t_{2g} localized electronic state resulting from the Coulomb-Blockade-like screening of the ferroelectric polarization. Experimental evidence is obtained from the highly anomalous decrease of the capacitance while increasing temperature which correlates with the increase of conductance when temperature is increased. Furthermore, the flat shape of the loss tangent vs frequency further support the purely electronic Coulomb-Blockade-like regime (T = 50K).

- The LSMO/BTO/Co memristor tunnel junction exhibits sign change in the tunnel magneto-resistance (TMR) driven by the switching of the ferroelectric polarization. This reflects the sign change in the spin polarization (at the Fermi level) in the BTO/Co interface triggered by the ferroelectric polarization and the defect distribution. DFT calculations show that the sign change in BTO/Co interface stems from the competition between the Co atoms exchange interaction suppressed by the CoO monolayer ($U - J = 6.0$ eV) and the oxygen vacancies colour centres exchange interaction mediated by Ti^{3+} ions ($U - J = 4.4$ eV). Tunnel transport mediated by the oxygen vacancy centers resemble a double exchange interaction in an insulator ferroelectric BTO barrier.

- Experiments conducted using top electrodes with different work functions did not show not a linear relationship between the barrier height and the work function of the transition metals involved (Ag, Co, Ta and Pt). The Schottky barrier detected in IV curves is at the BTO/LSMO interface and it is caused by doping effects associated to the accumulation of oxygen vacancies. Oxygen vacancy formation is controlled by the oxidation of the electrode driven by the applied electric field. The LSMO/BTO/Ta memristor tunnel junction couple ferroelectricity and oxygen vacancy formation to two consecutive REDOX chemical reactions of metallic Ta to TaO_2 oxide and Ta_2O_5 oxide. Heterogeneity due to the formed oxide layers caused the memristor to display Maxwell-Wagner-Sillars relaxation effect. Finally, we found the electric field necessary to annihilate oxygen

vacancies (positive coercivity of conductance hysteresis loops) scales with the (absolute value of the) oxidation enthalpy of the top electrode, indicating that the process is limited by the electric field induced reduction of the interfacial electrode oxide. This constitutes a first evidence of memristive response governed by electric field controlled electrochemical reactions at the interface with the electrode.

- As a final outlook into future experiments, it would be highly interesting to work with the recently developed scanning transmission electron microscope (STEM) sample holders which allow applying electric field pulses in situ and take annular bright field (ABF) images and electron energy loss spectroscopy (EELS) measurements combined to examine real time valence changes and eventually also ensuing structural modifications associated to the REDOX chemical reactions controlling resistive switching.

Appendix 1. Surfaces:

The most simple system in which the strain conditions of a substrate place a decisive role are thin film surfaces. After discussing the BTO bulk properties in this sub-section we study the electronic and structural properties of the BTO surface under the strain condition of the STO in-plane. BTO surface can be considered as an intermediate step towards the BTO-metal interfaces, which we will address in the next section, and will give us the opportunity to introduce the different supercell models we will use in both STO-constrained calculations. In parthicular we will discuss the role of the U correction and surface plane termination on the structural and electronic properties.

A.1.1 BTO-surfaces:

As mentioned for the bulk $U = 4.4\,eV$ value is suitable to exhibit a ferroelectric distortion value similar to the experimental results under the STO in-plane constrain (see figure 4.7). In order to study the effect of oxygen vacancies we will perform different calculation in-plane unit cells (u.c.) as c(1x1) and c(2x2) to see the effect of the oxygen vacancies concentration. All calculated cells contain 7 TiO_2 planes along the [001] direction, which is the δ distortion direction, and the number of BaO planes will be either 6, 7 or 8 for the symmetric TiO_2 termination (TiO_2-symm), stoichiometric (Stoich) or symmetric BaO (BaO-symm) termination respectively, see figure 17. The vacuum space we included to avoid interaction from one side of the slab to the other is at least 10 Å. Since the conduction bands mainly comes from the TiO_2 planes while the BaO planes mostly contribute to the valence band each termination will exhibit different electronic and structural properties. Besides, for the Stoich calculation (one termination is TiO_2 while the

other is BaO) we have checked that the corrections to the formation of the electric dipole moment are reduced.

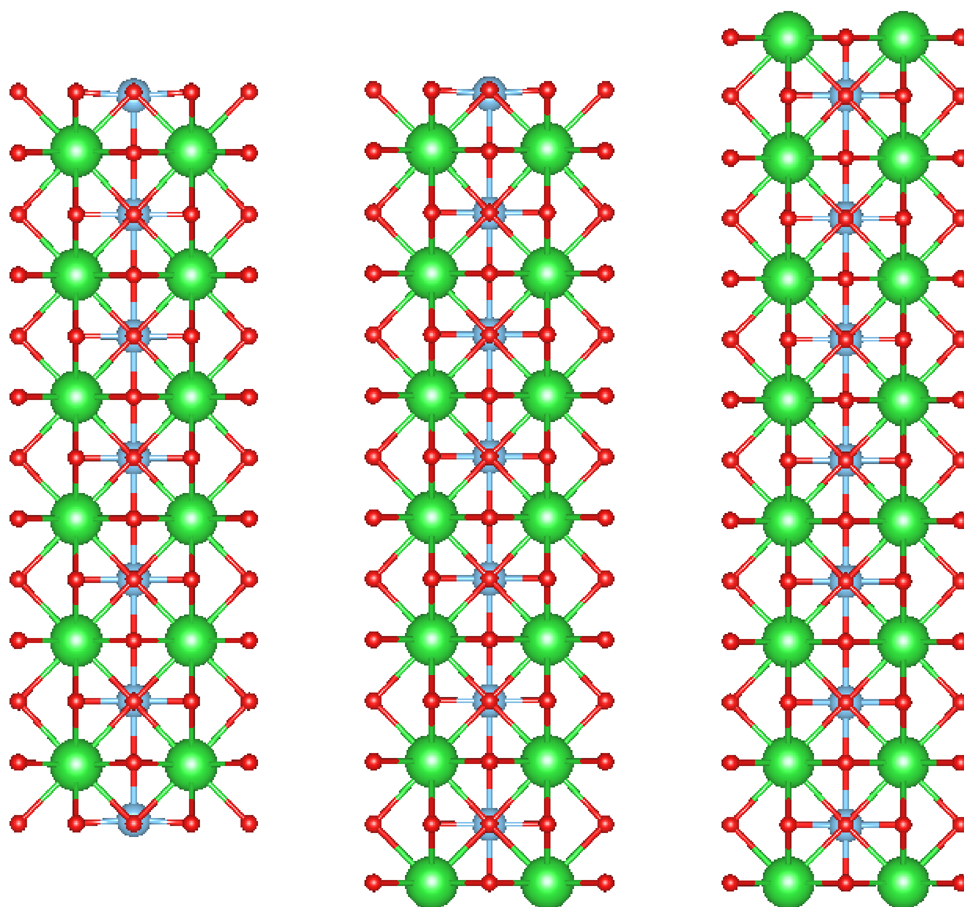

Figure A1 c(1x1) Relaxed surface cells for different atomic terminations: a) symmetric TiO_2 (symm-TiO_2), b) stoichiometric (stoich), c) symmetric BaO termination (symm-BaO). No U was applied.

A first inspection to figure A1 show that the relaxation of the TiO_2 terminated surfaces, such as symm-TiO_2 slab, is different from BaO terminated, symm-BaO. For the former the oxygens (Ti) tend to displace towards (away from) the surface, which can be considered as a region (1 or 2 TiO_2 planes) where there is an intrinsic formation of a ferroelectric distortion (δ). Similar results have been obtain by Pruneda el at. for the $La_{1-x}Sr_xMnO_3$ surface, and which have been explained by Tsymbal as related to the surface oxidation states due to unsaturated

bonds. Contrary to the TiO_2 termination the BaO termination does not induce any ferroelectric distortion near by the surface.

Another feature that affects the structural distortions are the oxygen vacancies. But to account for a diluted concentration we have to go beyond c(1x1) in-plane calculations to c(2x2). This allows including more degrees of freedom, and more adequately describe the atomic relaxations near the oxygen vacancies when they are located either at the TiO_2 or at the BaO most superficial plane, see figure A2.

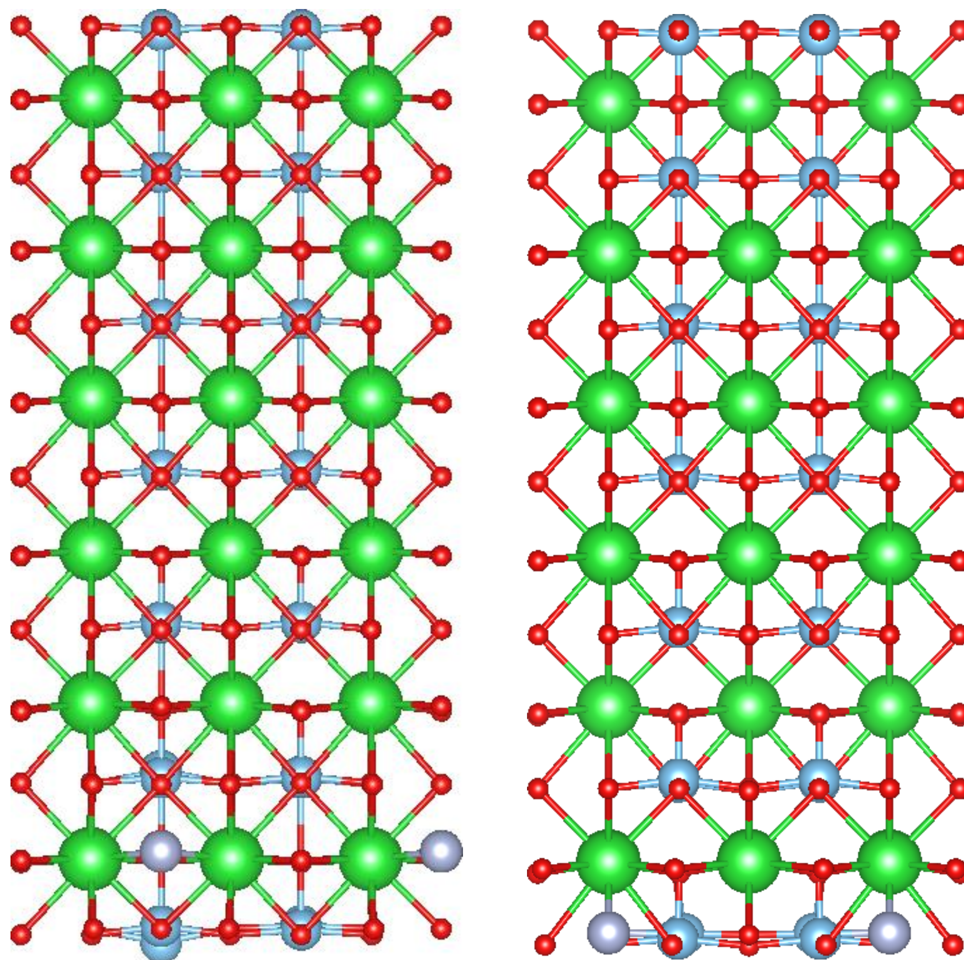

Figure A2 Atomic sketch of the U = 0.0 calculation for the TiO_2 symmetric slab with oxygen vacancies (grey circles) in the BaO surface plane (left) or TiO_2 surface plane (right).

We observe in figure A2 that while the relaxation pattern away from the oxygen vacancy denotes high in-plane symmetries, such as c(1x1) or large $\sqrt{2}x\sqrt{2}$ R45º near the vacancy the relaxation is more complex and require a c(2x2) in-plane cell. The presence of the vacancy triggers strong relaxations, which extends around 2 unit cells for the cations while 4-5 u.c. for the oxygen network.

In order to rationalize the depth effect in the different simulations we depict in figure A3 the δ displacements as a function of the 7 TiO_2 planes for different values of the U correction and various c(1x1) surface models: TiO_2-symm, stoich and BaO-symm.

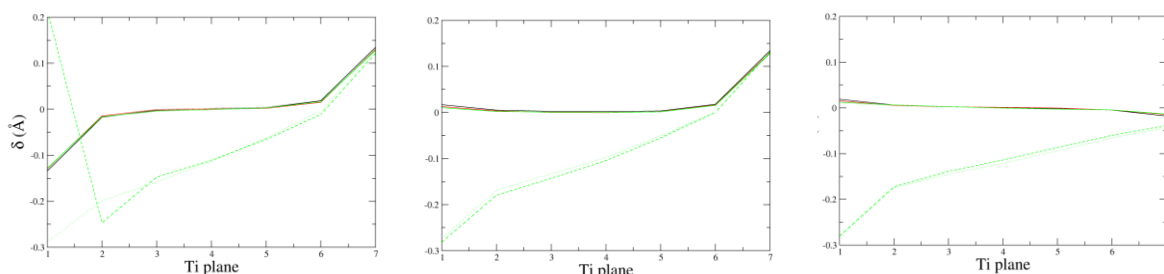

Figure A3 δ displacements as a function of the TiO_2 planes for two oxygen vacancy locations (dashed in BaO and dotted in TiO_2 planes with constant U = 4.4 eV) and different U values for non-vacancy cases (continuous black, red and green lines corresponds to 0.0, 2.0 and 4.4). This is depicted for c(1x1) calculations: a) TiO_2-symm, b) Stoich, c) BaO-symm. In the Stoich case the right interface corresponds to TiO_2 termination while the left to the BaO termination.

We observe in figure A3 that for the non-OVac cases, the U corrections (continuous lines) do not influence on the δ displacement which only differs from zero within 1 uc of a TiO_2 terminated surface. The values, 0.1 in the right surface and -0.1 in the left surface indicates that the oxygen moves towards the surface while the Ti move away from it. The BaO termination shows no δ displacement (right figure A3). However when including the oxygen vacancies the δ displacement profile is deeply modified. On averaged the oxygen moves toward the surface by almost 0.3 Å, except for the vacancy location at the BaO plane in the TiO_2 termination for which it moves 0.2 Å away from the surface. The most stable oxygen vacancy location is at the TiO_2 plane by 52, 256 and 38 meV for the TiO_2-symm, Stoich and BaO-symm for U=4.4 eV, respectively. The large value

for the Stoich calculation is reduced around 93 meV when taking into consideration the dipole correction. The larger stability of the OVac at the TiO_2 plane, regardless of the surface termination, contrast to the most stable case in bulk of the BaO plane. A more realistic model than a c(1x1) in-plane may be required.

We now consider the c(2x2) calculations which allows for an oxygen vacancy concentration 4 times lower than at the c(1x1) and more relaxation degrees of freedom. See figure A2 for an atomic sketch of the TiO_2 surface termination, which is closer to the real defect configurations. In figure A4, we depict the δ for the different c(2x2) surface terminations, oxygen vacancy locations and U values.

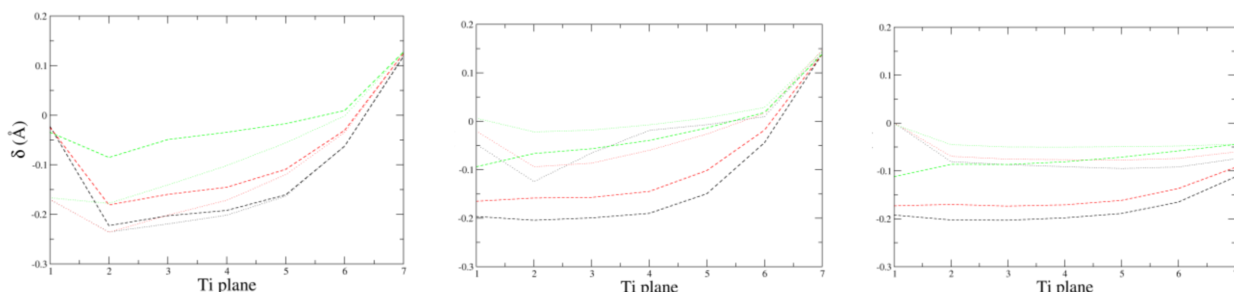

Figure A4 δ values for oxygen vacancies in c(2x2) surface models: a) TiO-symm (left), b) Stoich (middle) and c) BaO-symm (right) including oxygen vacancies at the BaO or TiO_2 plane respectively in dashed or dotted lines at the leftmost surface. U values for 0.0, 2.0 and 4.4 are included as black, red and green lines. In the Stoich case the right interface corresponds to TiO_2 terminations while the left to the BaO termination.

In figure A4 the location of the oxygen vacancy is at the leftmost surface for each calculation: TiO_2-symm (left), Stoich (middle) and BaO-symm (right). Contrary to the surface calculations without vacancies, in the vacancy calculations of figure A3 the U value influences the δ displacement magnitude, which gradually flattens as the U is increased. This occurs throughout the inner planes of the slab while the most superficial ones tends to be pinned, spatially at the TiO_2-terminations. The flattening agrees with the trend observed for the bulk since increasing the U very effectively reduces the δ value. Besides the δ trend is kept with the U. Notice that OVac at BaO planes induce larger δ distortions than at TiO_2 planes. These latter planes when at the surface most location (numbers 1 and 7) pin

the delta value which do not change altering U. Additionally, comparing the δ results between c(1x1) versus the c(2x2) in-plane u.c. sizes we conclude that they are very similar but for two features. Near the oxygen vacancy (left size in figure 4.19 and 4.20) the value is different and the convergence to the distortion δ thought-out the slab is more gradual in the c(2x2) case. This evidences that it is not required very big in-plane cell size to obtain a correct description of the oxygen vacancies and the role of its location in different surface models.

From the energetics point of view, particularizing for the c(2x2) in-plane all the most stable oxygen vacancy location is at the BaO plane, as in bulk, except for the TiO_2-symm calculation which stabilizes the oxygen vacancy at the TiO_2 plane, see table A1.

Energy	U	Termination
1.48	0.0	BaO-symm
0.82	0.0	Stoich
-1.51	0.0	TiO2-symm
0.96	2.0	BaO-symm
0.60	2.0	Stoich
-1.10	2.0	TiO2-symm
0.39	4.4	BaO-symm
0.29	4.4	Stoich
-0.21	4.4	TiO2-symm

Table A1 Total energy of a c(2x2) calculations of oxygen vacancies at the interfacial TiO_2 plane, minus the total energy at the BaO plane, as a function of the U value and surface termination.

In table A1 increasing the U value do not alter the most stable oxygen vacancy position for a surface model but it only reduces the energy difference. This can be understood as due to the fact that the δ displacements difference between the two oxygen vacancy locations is reduced as U is increased, see figure A4, again reducing the tetragonality towards the cubic symmetry.

These results show that there are structural features, some are intrinsic to the surface and other are related to the oxygen vacancy, that can be reasonably studied in c(2x2) models and both persist when varying the U values and oxygen vacancy locations. These do not affect qualitatively but only quantitatively in the form the δ curves approach to the boundary surface conditions where the surface termination and/or oxygen vacancy positions impose the structural and electrostatic constrains.

Appendix 2. ABF $BaTiO_3$/Ag interface:

We attach an Annular Bright Field (ABF) Transmission Electron Microscopy (TEM) image of $BaTiO_3$/Ag interface. Notice that silver grows polycrystalline and an amorphous layer is observed between the silver and barium titanate regions.

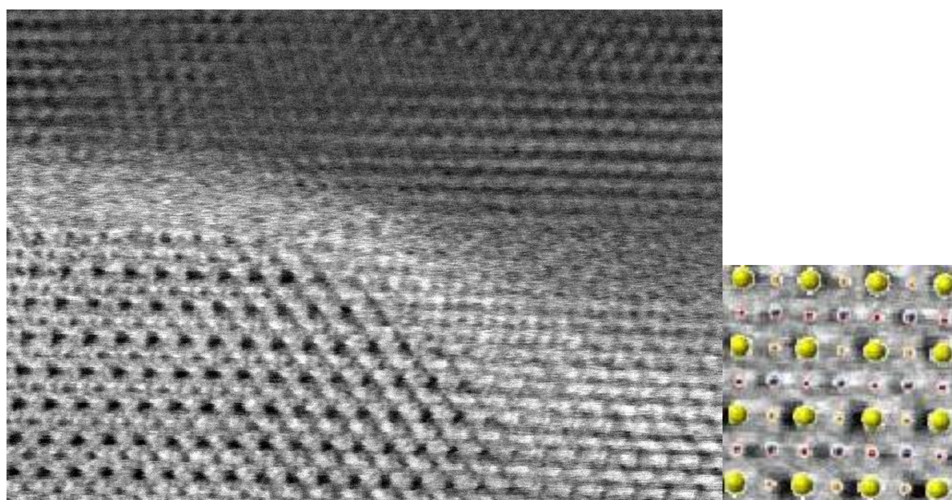

Figure A5. ABF TEM images BTO/Ag interface.

The publications associated to this PhD dissertation are the following:

- Xiao Shen, Timothy J. Pennycook, David Hernandez-Martin, Ana Pérez, Yevgeniy S. Puzyrev, Yaohua Liu, Suzanne G. E. te Velthuis, John W. Freeland, Padraic Shafer, Chenhui Zhu, Maria Varela, Carlos Leon, Zouhair Sefrioui, Jacobo Santamaria, and Sokrates T. Pantelides. "High On/Off Ratio Memristive Switching of Manganite/Cuprate Bilayer by Interfacial Magnetoelectricity". Adv. Mater. Interfaces 2016, 3, 1600086.
- Gabriel Sanchez-Santolino, Javier Tornos, David Hernandez-Martin, Juan I. Beltran, Carmen Munuera, Mariona Cabero, Ana Perez-Muñoz, Jesus Ricote, Federico Mompean, Mar Garcia-Hernandez, Zouhair Sefrioui, Carlos Leon, Steve J. Pennycook, Maria Carmen Muñoz, Maria Varela, and Jacobo Santamaria. "Resonant electron tunnelling assisted by charged domain walls in multiferroic tunnel junctions". Nat. Nanotechnol. 10 (2017).
- D. Hernandez-Martin, F. Gallego, J. Tornos, J. I. Beltran, C. Munuera, M. Cabero, F. Cuellar, D. Arias, G. Sanchez-Santolino, F. J. Mompean, M. Garcia-Hernandez, A. Rivera-Calzada, S. J. Pennycook, M. Varela, M. C. Muñoz, Z. Sefrioui, C. Leon, and J. Santamaria. "Oxygen vacancy control of a ferroelectric memristor". To be published.
- Fabian A. Cuellar, David Hernandez-Martin, Javier Tornos, Fernando Gallego, Gloria Orfila, Alberto Rivera-Calzada, Zouhair Sefrioui, Carlos Leon, and Jacobo Santamaria. "Interface Magnetism in $La_{0.7}Ca_{0.3}MnO_3/PrBa_2Cu_3O_7$ Epitaxial Heterostructures". Phys. Status Solidi A 2018, 1800265.
- J. Tornos, F. Gallego, S. Valencia, Y. H. Liu, V. Rouco, V. Lauter, R. Abrudan, C. Luo, H.Ryll, Q. Wang, D. Hernandez-Martin, G. Orfila, M. Cabero, F. Cuellar, D. Arias, F. J. Mompean, M. Garcia-Hernandez, F. Radu , T. R. Charlton, A. Rivera-Calzada, Z. Sefrioui, S. G. E. te Velthuis, C. Leon, and J. Santamaria. "Ferroelectric control of interface spin filtering in multiferroic tunnel junctions". Sent to Phys. Rev. Lett. To be published.